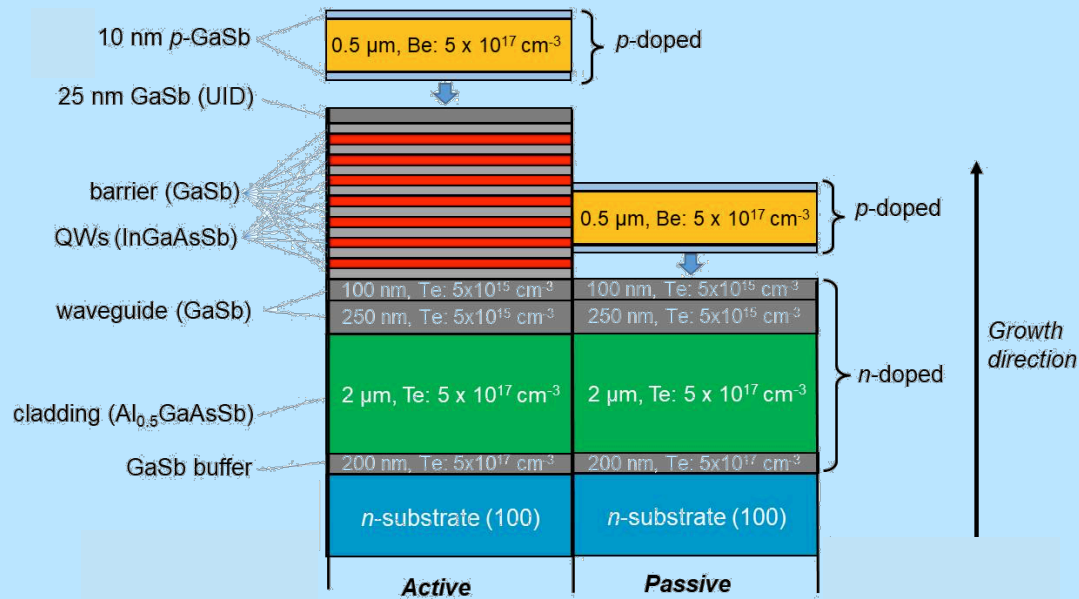


Research in Optoelectronics (A)



2018 Reprints of
Professor Larry A. Coldren
and Collaborators

ECE Technical Report 19-01
Department of Electrical & Computer Engineering
University of California, Santa Barbara

Research in Optoelectronics (A)

Reprints published in 2018

by

Professor Larry A. Coldren

and Collaborators

Published as

Technical Report # ECE 19-01

of

The Department of Electrical & Computer Engineering

The University of California

Santa Barbara, CA 93106

Phone: (805) 893-4486

Fax: (805) 893-4500

E-mail: coldren@ece.ucsb.edu

<http://www.ece.ucsb.edu/Faculty/Coldren/>

Introduction:

In 2018 Professor Coldren was a co-author on eighteen publications that will be listed in this compendium. All of the work involves photonic devices and integrated circuits on III-V compound semiconductor materials as well as their integration into small sub-systems. The characterization of these devices and circuits within systems environments is also included in some cases.

As in the past, the reprints have been grouped into several areas. As in recent years, most of these are within **I. Photonic Integrated Circuits** (PICs): subcategories called out are *A. Reviews and Overviews*, *B. Low-Power Optical Phase Locked Loops*, *C. GaSb-based PICs*, *D. PICs for Free-Space Links and LIDAR*, and *E. Signal Processing*. Within a second category, **II. Widely-Tunable Vertical-Cavity Surface-Emitting Lasers (VCSELs)**, there are four more papers.

The work was performed with funding from several federal grants and some gift funds from industry. Much of the work at UCSB was done in collaboration with other faculty, and the work on Signal Processing (**IE.**) was carried out in Prof. Yao's group at the Univ. of Ottawa with some devices we created some years ago, while the widely-tunable VCSEL work (**II.**) was led by Prof. Chang-Hasnain of UC-Berkeley.

Sub-section (**IA.**) contains summaries from three invited presentations on indium phosphide-based photonic-integrated-circuits (PICs). Copies of the presentation slides are included for the Micro-Optics Conference Plenary talk in Taipei. In (**IB.**), a single paper is included on our continuing work on low-power integrated heterodyne optical phase-locked loops (OPLLs). Sub-section (**IC.**) contains two conference papers on GaSb-based PICs, where for the first time we describe efforts to perform MBE regrowth to form active-passive interfaces to make monolithic tunable lasers and other multiple-section photonic ICs in the near-mid-IR wavelength range. Sub-section **ID.** lists seven papers which summarize numerous efforts on free-space communication and LIDAR led by Prof. Klamkin, mostly funded by NASA grants. Prof. Yao continues to study our active micro-ring filters in sub-section **IE.**, this time exploring the possibility of optical dynamic memories.

The second major section, **II. Widely-Tunable VCSELs**, lists four papers on VCSELs with a MEMs upper mirror which provides a secondary air cavity above the semiconductor structure to tune the wavelength of the device. By adjusting the coupling region between the two cavities the tuning range is extended by (in my words) creating an anti-resonant configuration in the middle of the tuning range. This work is led by Prof. Chang-Hasnain of UC-Berkeley.

III. Collaborating Students

| | |
|-----------------|-----------------------|
| H. Zhao | UCSB, Klamkin Group |
| B. Song | UCSB, Klamkin Group |
| Y. Liu | UCSB, Klamkin Group |
| B. Isaac | UCSB, Klamkin Group |
| F. Sang | UCSB, Klamkin Group |
| M. Pendharkar | UCSB, Palmstrom Group |
| S.T.S. Brunelli | UCSB, Klamkin Group |
| K. T. Cook | UC Berkeley |
| J. Qi | UC Berkeley |
| J. Kapraun | UC Berkeley |
| E. Kolev | UC Berkeley |

Table of Contents:

I. Photonic Integrated Circuits

A. Reviews and Overviews

- Shamsul Arafin** and Larry A. Coldren, "Advanced InP Photonic Integrated Circuits for Communication and Sensing" *IEEE Journal of Selected Topics in Quantum Electronics*, **24**, (1), pp. 1-12, (Jan.-Feb. 2018). INVITED PAPER 1
- L. A. Coldren**, "Photonic integrated circuits for coherent communication and sensing," *Proc. Micro-Optics Conference*, Paper A-1, Taipei, (Oct., 2018). PLENARY 13
- J. Klamkin**, H. Zhao, B. Song, Y. Liu, B. Isaac, S. Pinna, F. Sang, and L. A. Coldren, "Indium Phosphide Photonic Integrated Circuits: Technology and Applications," *Proc. 2018 IEEE BiCMOS and Compound Semiconductor Integrated Circuits and Technology Symposium (BCICTS)*, San Diego, CA, pp. 8-13 (Oct., 2018). PLENARY 37

B. Low-Power Optical-Phase-Locked Loops

- Arda Simsek**, Shamsul Arafin, Seong-Kyun Kim, Gordon B. Morrison, Leif A. Johansson, Milan L. Mashanovitch, Larry A. Coldren, and Mark J. W. Rodwell, "Evolution of Chip-Scale Heterodyne Optical Phase-Locked Loops Toward Watt Level Power Consumption," *J. Lightwave Technology*. **36**, 258-264 (Jan., 2018). 43

C. GaSb-based PICs

- A.P. McFadden**, S. Arafin, M. Pendharkar, L. Coldren and C.J. Palmstrøm, "MBE Growth of Quaternary AlGaAsSb/InGaAsSb Heterostructures for Tunable Lasers with 2.2-2.6 μ m Emission Wavelength," SPIE 2018 Light science workshop, Santa Barbara, (April, 2018) 50
- S. Arafin**, A. P. McFadden, M. Pendharkar, C. J. Palmstrøm and L. A. Coldren, "Recent progress on GaSb-based photonic integrated circuits," *Proc. 14th International Conference on Mid-Infrared Optoelectronics*, paper WeM13, MIOMD- 2018, Flagstaff, AZ, USA, (Oct. 2018). 52

D. PICs for Free-Space Links and LIDAR

- H. Zhao**, S. Pinna, B. Song, L. Megalini, S. S. Brunelli, L. Coldren, and J. Klamkin, "High-Power Integrated Indium Phosphide Transmitter for Free Space Optical Communications," in *Conference on Lasers and Electro-Optics*, OSA Technical Digest (online) (Optical Society of America, 2018), paper JW2A.52 (May, 2018). 54
- S. Pinna**, B. Song, L. A. Coldren, and J. Klamkin, "Vernier Transceiver Architecture for Side-Lobe-Free and High-Entendue LiDAR," in *Conference on Lasers and Electro-Optics*, OSA Technical Digest (online) (Optical Society of America, 2018), paper ATu3R.3 (May, 2018). 56
- H. Zhao**, S. Pinna, B. Song, L. Megalini, S. T. Š. Brunelli, L. Coldren, and J. Klamkin, "Integrated Indium Phosphide Transmitter for Free Space Optical Link," in *Advanced Photonics 2018 (BGPP, IPR, NP, NOMA, Sensors, Networks, SPPCom, SOF)*, OSA Technical Digest (online) (Optical Society of America, 2018), paper ITu4B.6 (July, 2018). 58
- H. Zhao**, S. Pinna, B. Song, Simone Tommaso, Suran Brunelli, B. Isaac, F. Sang, L.A. Coldren, and J. Klamkin, "Widely Tunable Integrated Laser Transmitter for Free Space Optical Communications," *Proc. 2018 IEEE International Semiconductor Laser Conference (ISLC)*, Santa Fe, NM, Paper MC5, (Sept, 2018). 60
- H. Zhao**, S. Pinna, B. Song, L. Megalini, Simone Tommaso Suran Burnelli, L.A. Coldren, and J. Klamkin. "3-Gbps Free Space Optical Link Based on Integrated Indium Phosphide Transmitter," *Proc. 2018 IEEE Photonics Conference (IPC)*, paper WA1, Reston, VA, (Oct., 2018). 62
- Brandon Isaac**, Bowen Song, Sergio Pinna, Shamsul Arafin, and Larry Coldren. "Indium Phosphide Photonic Integrated Circuit Transmitter with Integrated Linewidth Narrowing for Laser Communications and Sensing." *Proc. 2018 IEEE International Semiconductor Laser Conference (ISLC)*, paper MC7, (Sept, 2018). 64
- H. Zhao**, Sergio Pinna, Bowen Song, Ludovico Megalini, Simone Tommaso Suran Brunelli, Larry Coldren, and Jonathan Klamkin "Indium Phosphide Photonic Integrated Circuits for Free Space Optical Links," in *IEEE Journal of Selected Topics in Quantum Electronics*, vol. 24, no. 6, pp. 1-6, (Nov.-Dec. 2018). 66

E. Signal Processing

- Jiejun Zhang**, Robert S. Guzzon, Larry A. Coldren, and Jianping Yao, "Optical dynamic memory based on an integrated active ring resonator," *Opt. Letters*, **43**, 4687-4690 (Oct., 2018) 72

II. Widely-Tunable VCSELs

- P. Qiao**, K. T. Cook, J. Qi, L. A. Coldren, and C. J. Chang-Hasnain, "Wide, Continuously Swept VCSEL Using a Novel Air-Cavity-Dominant Design," in *Optical Fiber Communication Conference*, OSA Technical Digest (online) (Optical Society of America, 2018), paper Th11.7 (Mar., 2018). 76
- J. Kapraun**, J. Qi, J. Wang, P. Tingzon, K. Cook, E. Kolev, L. A. Coldren, and C. J. Chang-Hasnain, "Air-Cavity Dominated HCG-VCSEL with a Wide Continuous Tuning," in *Conference on Lasers and Electro-Optics*, OSA Technical Digest (online) (Optical Society of America, 2018), paper STu3Q.5 (May, 2018). 79
- K. T. Cook**, Pengfei Quio, Jipeng Qi, Wang, Larry A Coldren, Connie J Chang-Hasnain "Air Cavity Dominant VCSELs with a Wide Wavelength Sweep," paper STu3Q. 5, *Proc. 2018 Conference on Lasers and Electro-Optics (CLEO)*, San Jose, CA, 2018, pp. 1-2 81
- K. T. Cook**, P. Qiao, J. Qi, L. A. Coldren and C. J. Chang-Hasnain, "Physics of Widely Tunable VCSELs with Coupled Cavities," paper TuP43, *Proc. 2018 IEEE International Semiconductor Laser Conference (ISLC)*, Santa Fe, NM, USA, (Sept., 2018) 91

I. Photonic Integrated Circuits

A. Reviews and Overviews

Advanced InP Photonic Integrated Circuits for Communication and Sensing

Shamsul Arafin, *Senior Member, IEEE*, and Larry A. Coldren, *Life Fellow, IEEE*

(Invited Paper)

Abstract—Similar to the area of microelectronics, InP-based photonic integrated circuits (PICs) in the optical domain as a counterpart are also seeing a clear exponential development. This rapid progress can be defined by a number of active/passive components monolithically integrated on a single chip. Given the probability of achieving low-cost, compact, robust, and energy-efficient complex photonic systems, there have been significant achievements made in realizing relatively complex InP-PICs in recent years. The performance of these complex PICs is reaching a stage that can enable a whole new class of applications beyond telecom and datacom. A great deal of effort from both academia and industry has made the significant advances of this technology possible. This development has resulted in a positive and profound impact in many areas including sensing, medical diagnostics, metrology, and consumer photonics. This review paper will mainly discuss the recent, in particular since 2012, progress and findings obtained out of current academic and industry research activities for InP-PICs. Major emphasis will be given to the high-performance and complex PICs that have been reported by the scientific community in this time period. A prospect for further development of this photonic integration in InP-platforms is also briefly described.

Index Terms—Photonic integrated circuits, integrated optics, optical transceivers, optical filters, beam sweeping, optical phase-locked loop.

I. INTRODUCTION

OVER the past couple of decades, photonic integrated circuits (PICs) have delivered on much of the promise to provide reductions in size, weight and power over discrete solutions [1], [2]. In many cases, improvements in reliability, cost and even performance have been observed, although cost improvements require some significant production volume, and performance improvements only come if the integrated elements work well on the chosen integration platform. In fact, for some applications, some compromise in PIC performance may be tolerable, if improvements in the other mentioned aspects are achieved.

For active PICs, in which optical gain is required, such as those requiring lasers or semiconductor-optical-amplifiers

Manuscript received May 8, 2017; revised June 30, 2017; accepted September 15, 2017. Date of publication September 20, 2017; date of current version October 6, 2017. This work was supported in part by DARPA-MTO under the DODOS Project and in part by the National Science Foundation under Grant 1402935. (Corresponding author: Shamsul Arafin.)

The authors are with the Department of Electrical and Computer Engineering, University of California, Santa Barbara, CA 93106 USA (e-mail: sarafin@ucsb.edu; coldren@ucsb.edu).

Color versions of one or more of the figures in this paper are available online at <http://ieeexplore.ieee.org>.

Digital Object Identifier 10.1109/JSTQE.2017.2754583

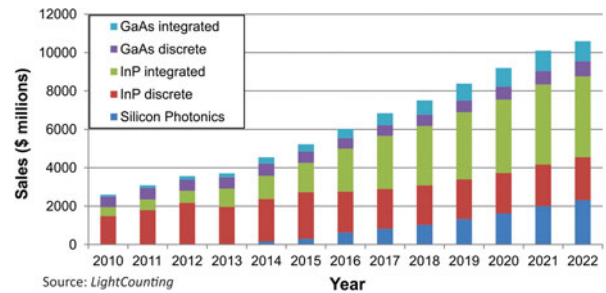


Fig. 1. A bar chart for the transceiver market history from 2010 and projection towards 2022. Reproduced with permission from [14].

(SOAs), it is most desirable to choose an integration platform that naturally provides gain, such as one based on a III-V semiconductor. For the low-loss or low-dispersion fiber optic windows at 1550 nm and 1310 nm, respectively, this III-V material platform has been based upon InP. Early InP-PICs containing both active and passive components at emission wavelengths of 1550 nm [3]–[5] and 1310 nm [6], [7] were reported and their potential for enabling applications in the area of fiber optics were also described.

Despite the great versatility of InP-based monolithic integration, a single waveguide platform cannot be utilized here for a single function. This often leads to restrictions in performance and applicability. However, this intrinsic problem can be circumvented by complex fabrication or additional regrowth steps [8].

The alternative to a pure monolithic InP-platform is to employ some sort of hybrid or heterogeneous solutions, in which a gain block or layer is incorporated with an otherwise passive PIC platform. This has been done by using a discrete InP-gain chip optically coupled to the passive PIC as well as by wafer bonding InP layers directly to the passive PIC. Microdisk lasers by Spuesens *et al.* [9], ring lasers by Liang *et al.* [10], multiwavelength AWG lasers by Kurczveil *et al.* [11], an optical transmitter by Srinivasan *et al.* [12] and a transceiver by Fedeli *et al.* [13] are some of the exemplary reports on InP-based lasers and SOAs integrated with silicon-photonics in recent years.

Although the PIC literature has been dominated by silicon photonics and these hybrid solutions in the past few years, it is important to point out that the commercial sales of PICs continues to be dominated by InP-based solutions. Fig. 1 gives a bar chart of the sales of optical transceivers in the recent past along with projections for the next five years at this writing (2017)

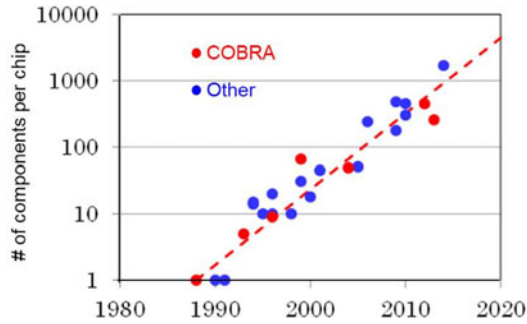


Fig. 2. Evolution of chip complexity measured as the number of components per chip over time. Figure was based on the data from [18].

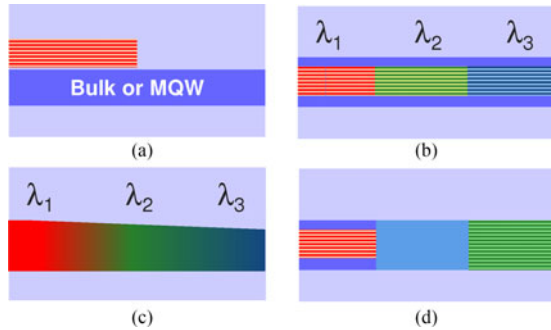


Fig. 3. Several active-passive waveguide integration approaches, (a) offset-quantum wells, (b) QW intermixing, (c) selective area growth, and (d) butt-joint regrowth. Courtesy: Lumentum.

[14]. Such transceivers dominate the optical component market. There is an additional $\sim \$1$ B in sales over this time period for optical amplifiers and passives that is relatively flat. As can be observed, InP PICs currently provide the largest sales component, and they are projected to continue to be the dominant component, perhaps for the next decade or so. This is why the current and future research on InP-PICs is justified.

There have been a few excellent and comprehensive reviews on InP-based PICs and its generic integration technology recently published [15]–[19]. In this paper, we have chosen to focus on the more recent advances on InP-PICs, being suitable for coherent communication and sensing applications, which have not been covered in the prior reviews.

Nevertheless, it is worthwhile including a chart from [18] that indicates the growth in the number of components per chip over time, and this is shown as Fig. 2. It shows the complexity development over forty years. Interestingly, there are other charts for optical communication PICs that show plots of data capacity per chip in Gbps which also have nearly the very same trend line [20]. So, the title could just as well be “Data Capacity/Chip (Gbps)”.

To get started with the body of this paper, we first will briefly review the current thinking on active-passive waveguide integration techniques, critical for active PICs, in Section II. There continue to be a number of choices, but there appears to be some agreement on the tradeoffs. Then in Section III, a brief sampling of recent commercial PIC advances gives an example of the status of a decades-old PIC design as well as much more complex and highly functional PICs available today; then moving on to

Section IV where a review of analog functionalities gives examples of recent programmable filters and signal processing elements not discussed in prior reviews. Section V, entitled sensing by beam sweeping and light detection and ranging (LiDAR), introduces a novel coherent transceiver PIC, and gives a summary of prior results from some of its elements; finally in Section VI, optical phase-locked loops (OPLL) for low-cost/power coherent receivers and synthesis, the advantages of the close integration of coherent receiver PICs with feedback electronics is explored in a couple of applications.

II. RECENT THINKING ON ACTIVE-PASSIVE INTEGRATION

Prior to discussing the various advanced InP-PICs, recently developed by industry and academia, it is important to provide a short overview of the integration technology platforms that they have used. It is desirable for these platforms to enable the monolithic integration of different active and passive components with a minimal compromise in the performance of the individual components. As illustrated in Fig. 3, several commonly used integration platforms include offset quantum wells, quantum well intermixing (QWI), selective area growth, and butt-joint regrowth [2]. Among these platforms, the butt-joint regrowth technique is most popular with the more established industries due to its ultimate design flexibility [17]. Since the multiple active and passive waveguide structures are created in different growth steps, a large flexibility in the material composition, number and width of quantum wells and doping can be provided in each section. However, this benefit comes with additional growth steps. For a complex PIC, it could require five or more regrowths to achieve the desired multiple bandgaps, perhaps resulting low yield in the devices, if extreme precision is not available.

Offset quantum well (OQW) and quantum well intermixing (QWI) are other two integration platforms which tend to be more widely used in academic research and industries where the availability of epitaxial growth equipment is not available, or where regrowth technology is not well developed. In both cases, an unpatterned cladding regrowth [2] is performed with only a small or negligible height change between the active and passive regions, and this regrowth can usually be performed by commercial vendors. One of the disadvantages of this technique is that the doping concentrations in the active and the passive cladding layers are the same, introducing higher absorption losses in the transparent regions.

Multiple bandgaps are possible in the QWI process by multiple etching and annealing steps, but the in OQW case, double (again planar) regrowths are generally necessary for three bandgaps. QWI has also been used at surfaces to increase the bandgap of active regions and thus make transparent regions that might otherwise be absorbing because of surface recombination inhibiting carrier build-up to a transparency level. Especially in Al-containing materials of high-power lasers, facet damage is a well-known consequence [21]–[22], and this can also show up as unwanted ‘active’ absorption loss in other structures.

The final integration platform, selective area growth (SAG), is used commercially in electroabsorption modulator

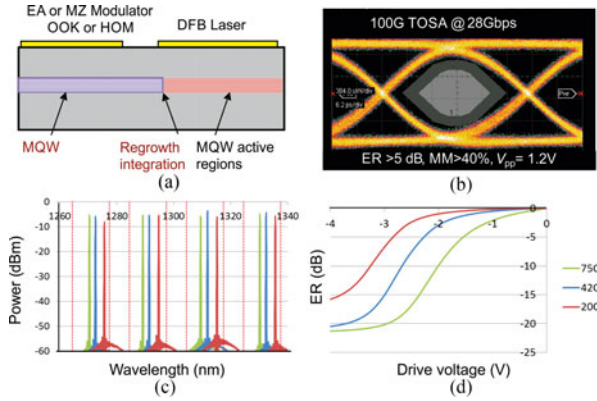


Fig. 4. (a) DFB laser with an integrated modulator for optical transceivers in metro or datacenters, (b) eye diagram measured at $V_{pp} = 1.2$ V; $ER > 5$ dB, (c) optical spectra-100 gigabit ethernet (GbE) CWDM4, and (d) transfer function of EAM optimized for uncooled applications. Courtesy: Lumentum.

(EAM)/distributed feedback (DFB)-laser PICs [23], and is particularly interesting because multiple-bandgap devices can be grown in a single step by just changing the width of dielectric-coated regions beside the waveguide regions-to-be during the initial epitaxial growth. Because precursors will not decompose and grow on the substrate over the coated regions, they ‘pile-up,’ diffuse laterally, and provide for a thicker growth beside the coated regions. The width of the coated regions determines the amount of the increase in thickness, and for QWs, the reduction in effective bandgap. For quaternary growth on InP, there are limitations on the compositional range over which this can be accomplished, due to the need to approximately lattice match.

This technique is also currently being used in combination with butt-joint regrowth in some commercial devices. This allows some regrowth steps to be eliminated, where the doping levels can be the same in some adjacent regions [24].

III. SAMPLING OF RECENT COMMERCIAL INP-PIC ADVANCES

This section will focus on a short overview of several different types of InP-PICs by commercial vendors, which will show the recent advances, PIC complexity and technological maturity. In addition to these commercial PICs, there have been also a quite bit of successful academic or foundry works recently reported in this area [25]–[27].

Fig. 4(a) illustrates a recent state-of-the-art example of one of the oldest PIC concepts, which dates back to the mid-1980’s [28], [29]. This is a simple DFB laser with EAM integrated on a single chip of InP. The integration avoids any chip-to-chip coupling optics with associated losses, expense, and reliability issues, and the bandgap of the modulator is adjusted to be appropriately offset from the wavelength of the laser during fabrication [30], [31]. With proper design, the device can operate over a wide temperature range by only offsetting the DC bias voltage. Applications are for datacom, perhaps in data centers.

The commercial vendor, Lumentum successfully demonstrated such InP-based PICs and its eye diagrams were measured at 28 Gbps for a transmitter optical subassembly (TOSA) calibrated at 0 dBm time averaged output power per channel, as presented in Fig. 4(b). This is a major step forward

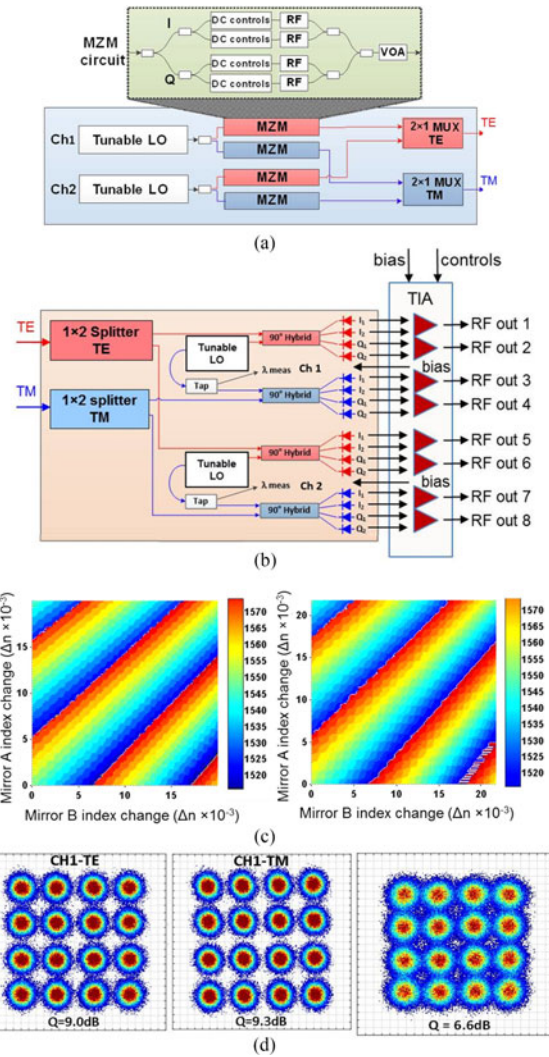


Fig. 5. (a) 2-Channel Tx PIC architecture, (b) 2-Channel Rx PIC and TIA ASIC architecture, (c) laser tuning maps of Tx. Each map shows the laser output wavelength as a function of the estimated effective index change on the two mirror sections, and (d) recovered constellations at 88 Gbd \times 16 QAM from a reference Tx, EDFA, 80 km fiber and Rx PIC wire-bonded to a TIA receiver (left); 88 GBaud 16 QAM constellation after propagation over 80 km of SMF from a Tx PIC to a Rx PIC wire-bonded to a TIA receiver (right). Courtesy: Infinera.

in terms of low requirements on the drive voltage, ensuring compatibility with low power dissipation modulator drivers and improving the power budget of the transceivers. The spectral characteristics of electroabsorption modulated laser (EML) based $4\lambda \times 25$ Gbps coarse wavelength division multiplexing (CWDM)-TOSA are presented in Fig. 4(c). Fig. 4(d) shows the typical transfer function of the EAM optimized for uncooled applications. The slope of the transfer function exceeded 10 dB/V, providing high modulation efficiency with low insertion loss.

Fig. 5 shows recent results from Infinera’s multi-channel widely-tunable coherent transmitter (Tx) and receiver (Rx) PICs, which together form a flexible high-capacity link. With 2 Channels > 700 Gb/s per channel (via 88 Gbaud, 16-QAM dual-polarization modulation) over 80 km was demonstrated. That is, a total capacity of 1.4 Tbps could be available using

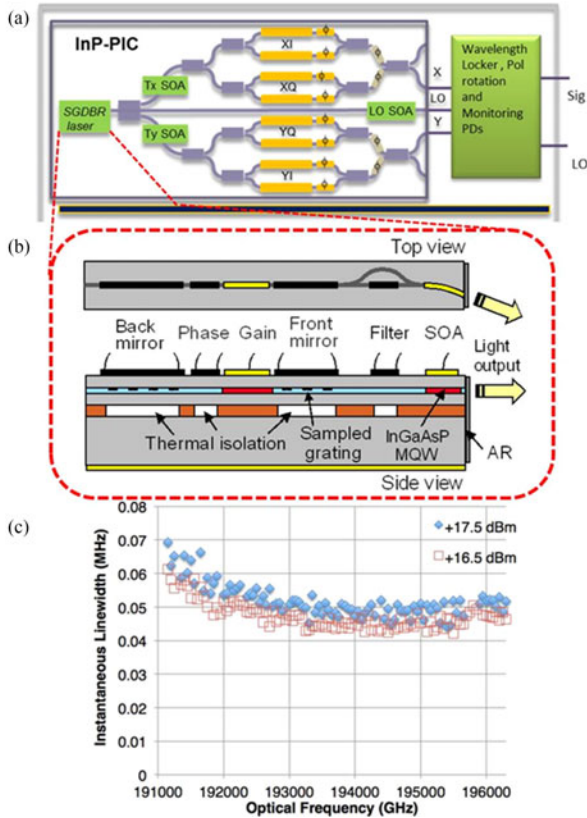


Fig. 6. (a) Schematic layout of monolithic InP-PIC consisting of thermally tuned narrow linewidth C-band tunable SG-DBR laser, dual-polarization I - Q modulators, and three SOAs, (b) schematic of a monolithic widely-tunable SGDBR laser utilizing high-efficiency thermal index tuning design, and (c) linewidth as a function of optical frequency. Courtesy: Lumentum.

both channels. Tuning across the entire C-band in both the Tx and Rx insures arbitrary wavelength reconfigurability [20], [32].

Both Tx and Rx chips have a two channel design. The Tx chip incorporates two independent widely-tunable lasers, each split into two nested Mach-Zehnder modulators (MZM) for I - Q modulation of a TE and TM-to-be channel. Each MZM can run up to 88 Gbaud with various modulation formats. The two TE or TM channels are combined at the output of the chip.

The Rx chip has TE and TM inputs, each of which are split into two channels. The outputs of two widely-tunable LO lasers are each divided in two and one half combined with a TE and the other a TM output from the two splitters by a 90° hybrid. The four outputs (I , I' , Q , and Q') of the four 90° hybrids become the four sets of outputs to the electronics for the TE and TM channel modes of the two channels.

Infinera plans to incorporate modules with these PICs within their future optical communication systems, as with their other PIC-based systems. That is, the Rx and Tx modules containing the PICs described in Fig. 5 will not be externally available as standalone products.

Fig. 6 illustrates Lumentum's single-channel widely-tunable Tx PIC, configured for advanced modulation format TE and TM transmission, which also provides an output for the LO of a co-located Rx [33]. Of particular interest is the widely tunable laser, which has very desirable output characteristics.

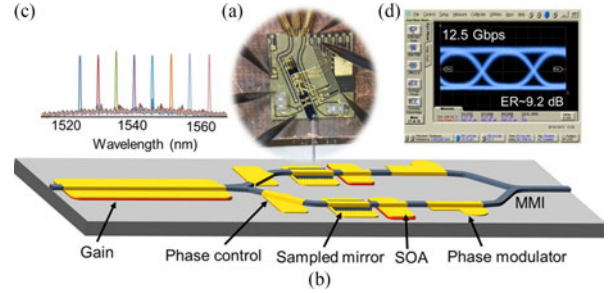


Fig. 7. (a) Microscope image of InP-PIC as a tunable interferometric transmitter mounted on the AlN carrier and wirebonded, (b) schematic layout of such a PIC with integrated traveling-wave modulators, (c) optical spectra of the on-chip SG-DBR laser lasing at different mirror super-modes, and (d) eye diagram measurements of the PIC for 12.5 Gbps operations. Courtesy: Freedom photonics.

The output power exceeds 50 mW; the linewidth is less than 70 kHz; and the side-mode suppression ratio is greater than 50 dB across the entire C-band. No other integrated widely-tunable laser competes with these characteristics. The nested MZM is similar in design to that described above following Fig. 5. Also of note is that Lumentum makes available such widely-tunable Tx modules of this design [33], [34].

In addition to a high-performance InP-PIC-based transmitter, demonstrated by Freedom Photonics Inc. [35], a new and novel form of widely-tunable transmitter is recently reported [36]. This transmitter, shown in Fig. 7, is based on a type of dual-output Y-branch laser, a pair of high-speed phase modulators, and a multimode-interference (MMI) coupler to complete a MZM at what would have been the dual output side of the laser [36]. Compared to the existing technology, such a compact and cost-effective transmitter achieves the functionality of an integrated widely-tunable laser with a MZM, a so called integrated laser Mach-Zehnder (ILMZ), to provide controllable chirp outputs, etc., but much more elegantly. By only adding a phase modulator at the end of each Y-branch laser output arm followed by the combining MMI, the ILMZ is complete.

Fig. 7 shows a photo of a mounted device, a device schematic, superimposed spectrum, and an eye diagram. A tuning range of 50 nm was observed; The SMSR was 50 dB; the eye was taken at 12.5 Gbps with an extinction ratio of > 9 dB; over 80 km reach observed in standard SMF-28 fiber. The phase modulators used in this work used a bulk electro-optic effect. Improved responses are expected with quantum well designs.

Fig. 8 illustrates the ability to integrate multiple widely-tunable transmitters and combined into a single output on a single chip. These were SGDBR lasers followed by SOAs and EAMs, and then finally combined in a 4×1 wide-band power combiner. The PIC operates well at 55°C for reduced TEC power. SOAs enable variable optical attenuator (VOA) and blanking functions for high-speed switching between lasers. Eye diagrams illustrate full functionality of the PIC.

IV. ANALOG FUNCTIONALITIES

In RF-photonic and analog fiber optic links and systems, two key components, a linear optical modulator and a tunable

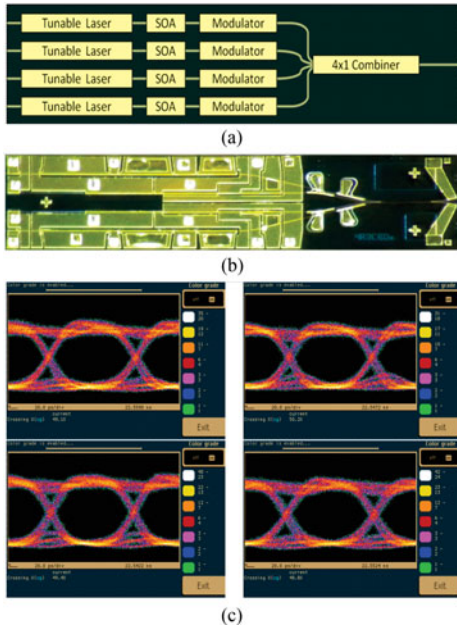


Fig. 8. (a) Schematic layout of a quad-transmitter using InP-PICs, (b) microscope image of the monolithic InP C-band tunable transmitter with single output waveguide, and (c) eye diagram measurements of the all transmitters. Courtesy: Freedom Photonics.

optical filter can be important for reducing the signal distortion and achieving a high dynamic range. Linear modulation of RF directly onto the optical wave is desired in a number of applications. Analog RF-photonic links for antenna remoting is one example. In this case, optical fibers can replace microwave cables between the equipment bay and the antenna, perhaps on ships or airplanes, where size, weight and transmission loss are important. Key criteria are overall link loss, noise figure, bandwidth, and dynamic range. To meet these criteria, ring-assisted MZI (RAMZI) modulators, proposed in 2003 [37], have been used in InP- PICs [38], [39].

In an analog RF-photonic system, an optical tunable filter is also highly desirable as the second key component. It is often desired to incorporate optical filters to isolate flexible communication channels or weaker portions of the optical spectrum near stronger ones received for more detailed analysis. Fig. 9 outlines results from a multi-section active ring-resonator filter PIC formed on InP.

For testing, a coherent heterodyne RF photonic link is formed as shown in Fig. 9(a). In such a system, a photonic carrier signal is phase modulated using the RF input. The modulated carrier signal goes through the InP-PIC filter to be evaluated. A strong local oscillator (LO) laser down-converts the InP-PIC-filtered optical signal through a balanced detection receiver.

Tunable bandwidth and tunable center frequency RF photonic filters were developed by Norberg *et al.* [40] and Guzzon *et al.* [41]. Cascaded and coupled-ring bandpass filters were fabricated and demonstrated in this study, showing high levels of tunability and near-ideal filter shapes. Fig. 9(b) shows a schematic of a third-order coupled-ring bandpass filter. The tunable coupling between two neighboring rings and between the outer ring and the bypass waveguide was realized using four

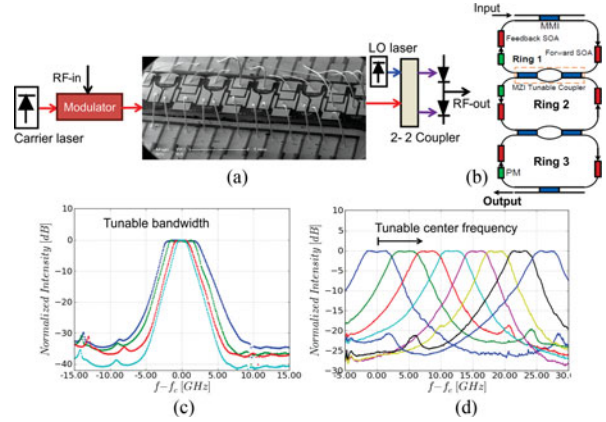


Fig. 9. (a) Test set-up for PIC filter, and balanced receiver. The optical signal is in red, RF electrical signals in black, and LO in blue, (b) schematic representation of third-order coupled-ring filter. MMIs are in blue, SOAs in red, and phase modulators (PMs) in green, (c) 3rd order tunable bandwidth result, and (d) center frequency tunability demonstrated using a 2nd order bandpass filter. Reproduced with permission from [40].

tunable couplers each consisting of two multimode interference couplers and two PMs. Fig. 9(c) gives results of bandwidth adjustment, and Fig. 9(d) shows the tuning of the center frequency in a two-section coupled-ring configuration.

The optimal Spur-free Dynamic Range (SFDR) and Noise Figure (NF) was obtained with the SOA gains adjusted such that the overall filters had near zero net insertion loss. SOAs were designed with separation layers between the waveguides and active regions to increase their saturation levels to ~ 19 dBm. In this case, the NF and SFDR were measured to be ~ 4 dB and ~ 115 dB-Hz^{2/3}, respectively. These are very good numbers, and quite unexpected with SOAs included within the filters, but it turns out that removing the insertion loss is more important than the ASE added by the SOAs.

In today's optical communication links, signal processing is still performed digitally using electrical systems. This standard digital signal processing requires electronic sampling, optical-to-electrical and electrical-to-optical conversions to reconstruct the signal in the receiver side. This is mainly due to the fact that digital signal processing in the electrical domain suffers from the limited speed due to much lower electronic sampling rate. By contrast, equivalent signal processing in the optical domain offers the advantages of relieving the inherent time-bandwidth constraints in electrical systems. Therefore, implementing signal processing directly in the optical domain in these optical links will eliminate the necessity of electronic sampling, OE and EO conversions, paving the way for achieving power-efficient and high-speed signal processing [42].

Considering this, Liu *et al.* [43] used the same integrated multi-section active ring filters described in Fig. 9 above to perform reconfigurable signal processing functions, including temporal integration, temporal differentiations and Hilbert transformation. Fig. 10(a) shows a fabricated InP-PIC used in this study. Two active microring resonators and a bypass waveguide, as schematically shown in Fig. 10(b), were utilized. To obtain on-chip reconfigurability, six semiconductor optical amplifiers (SOAs) and five current-injection phase modulators (PMs) in

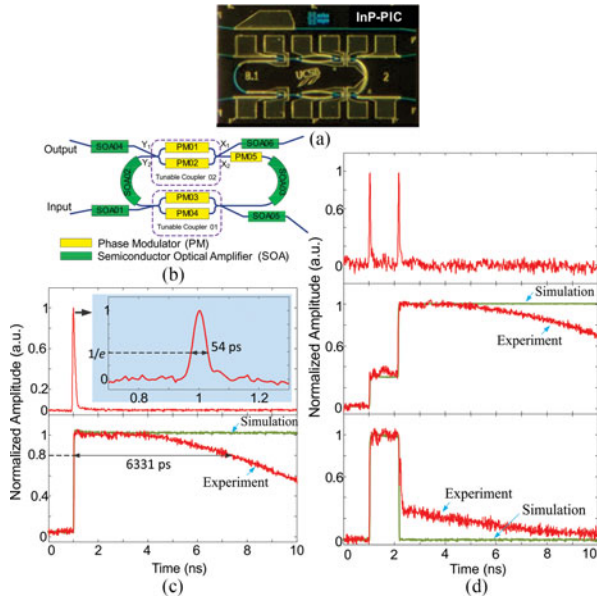


Fig. 10. (a) Microscope image of the processed on-chip photonic temporal integrator prototype based on InP-PICs, (b) its schematic illustration, (c) the experimental results, where the input Gaussian pulse with a temporal width of 54 ps (top); the integral of the Gaussian pulse with an integration time window of 6331 ps (bottom), and (d) the input in-phase doublet pulse (top); the integral of the in-phase doublet pulse (middle); the integral of the out-of-phase doublet pulse (bottom). Reproduced with permission from [43].

the unit cell [43] were used. In this way, a photonic temporal integrator with ultra-high power efficiency and a continuously tunable operating wavelength was achieved.

The authors tested the operation of such an InP-PIC based signal processor that was configured as a photonic temporal integrator. By configuring the photonic temporal integrator with the injection currents to the SOAs and PMs in the ring, a high Q-factor of 31×10^6 was achieved and the ring was still under the lasing threshold. As shown in Fig. 10(c), the temporal integral of the input Gaussian pulse is realized. The presented photonic integrator provided a time-bandwidth product of ~ 100 , which is far better than an advanced electronic integrator.

The authors also tested the integration of an in-phase doublet pulse by the proposed photonic temporal integrator. In Fig. 10(d), the integrator sums up the area of the in-phase doublet, giving two steps corresponding the area of the first pulse and the area of the first and the second pulses. With a π -phase shift (out-of-phase), a memory resetting function is performed by the integrator.

In addition to the use of InP-PIC based optical filters and re-configurable signal processors in analog RF-photonic systems, other types of PICs show a number of analog functionalities, including optical arbitrary waveform generation (OAWG) [44]. Such analog PICs for OAWG have found applications in areas of optical communications and arbitrary optical/RF waveform generation. In late 2011, a monolithically integrated OAWG based on InP-PICs with access to 1 THz of optical bandwidth was demonstrated [45].

In this study, the authors demonstrated an optical waveform shaper that can manipulate the amplitude and phase of a stable

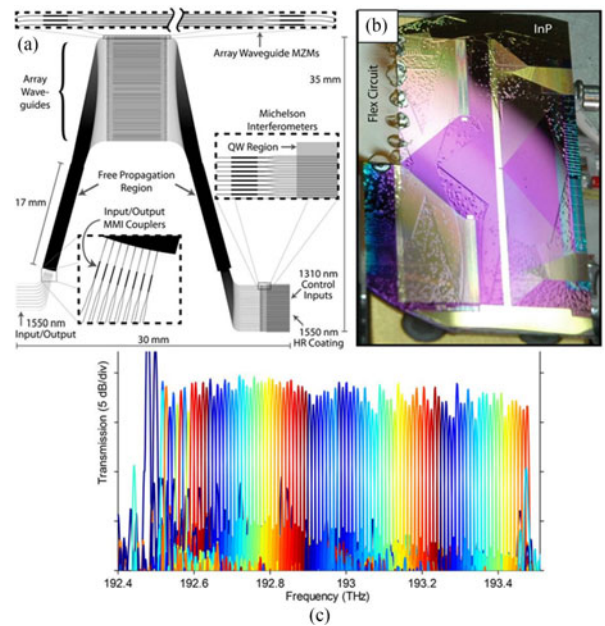


Fig. 11. (a) Mask layout of a single 100-channel \times 10-GHz OAWG device, (b) two fabricated InP devices from a single 2-inch wafer with a flex circuit attached to one device, and (c) single-pass 100-channel \times 10-GHz AWG output spectrum after phase-error correction. Reproduced with permission from [45].

optical frequency comb (OFC) on a line-by-line basis. These InP-based OAWG devices consisted of a 100-channel arrayed-waveguide grating (AWG) spaced at 10 GHz with 100 Michelson interferometers, 200 QW phase modulators and 400 electro-optic MZMs in twin configurations on a single 2 inch wafer.

The mask layout of OAWG devices with an overall dimension of $3 \text{ cm} \times 3.5 \text{ cm}$ is shown in Fig. 11(a). Two fully-processed devices are shown in Fig. 11(b) where the upper device was a mirror image of the lower one. Devices with a cleaved-facet at the left side used a 2×1 MMI coupler as the 1550-nm input and output. The input/output side is zoomed-in and the detail of each MMI coupler is shown in the inset. The AWG contained 400 arrayed waveguides and, each had an electro-optic MZM. Each of the 100 AWG outputs had a Michelson interferometer consisting of a 2×1 MMI splitter/combiner, as shown in the inset of Fig. 11(a). The interferometer arms had a 1-mm-long QW phase modulator and an HR/AR-coated cleaved-facet mirror with a reflectivity of 86% at 1550 nm and 6% at 1310 nm.

The successful operation of OAWG devices requires high adjacent channel isolation resulting low crosstalk for the MUX and overlapping passbands for the DEMUX. Fig. 11(c) shows the measured single-pass AWG transmission for all 100 AWG outputs after phase-error correction (TE polarization). The data were taken by moving a fiber to each AWG output channel and making a measurement with the Optical Vector Network Analyzer. Each output was recorded and the average channel bandwidth of 6 GHz was reported. The average calculated crosstalk values were measured to be 15.1 dB. This represents one of the largest area InP-PICs ever fabricated.

Despite of the academic proof-of-principle, it is an open question whether such a very large InP-PIC based AWG can be

mass-fabricated, even in more mature foundry technologies, due to the large number of long waveguides.

V. SENSING BY BEAM SWEEPING AND LIDAR

Optical beam generation, shaping and steering based on optical-phased array (OPA) technology are currently of significant research interests due to lots of emerging applications, including free-space optical communication, 3D imaging and mapping in LiDAR systems and autonomous cars [46]. Over the last couple of years, considerable research effort has been made for the development of highly-integrated and reduced size, weight and power consumption beam steering systems utilizing PICs. Several beam steering demonstrations based on PICs using either InP- [47]–[49] or silicon platforms [50] are already reported.

Recently, Guo *et al.* demonstrated 2-D optical beam steering with an InP-PIC using the scheme of 1-D OPA plus wavelength tuning with surface-emitting gratings [47]–[49]. In this case, the 1-D OPA scans the beam laterally, while axial scanning is achieved by varying the wavelength of a widely-tunable laser via the surface-emitting grating. An InP platform was chosen because all of the active and passive components necessary for the desired rapid 2-D beam steering could be integrated on a single PIC. This includes the rapidly-reconfigurable and widely-tunable laser for axial scanning, the high-power SOAs for sufficient power to all waveguide elements of the OPA, and efficient and rapidly-tunable phase shifters for each waveguide of the OPA. In this case, a SGDBR laser was chosen and forward-biased current-injection phase-shifters were selected.

Fig. 12(a) shows the layout of the SWEEPER-PIC. It utilized 32-element OPA. The free-space splitter was fed by either an SGDBR with ~ 45 nm of wavelength tuning or an external laser input. The free-space splitter excited 32 waveguides that flared out over a width of ~ 3.5 mm to spread the heat from the following phase-shifters and SOAs. Each waveguide had a separately contacted phase-shifter and SOA. The waveguides were then brought back together in a non-uniformly spaced array to suppress sidelobes, as shown in Fig. 12(b).

The grating region was covered with a metal layer spaced by effectively one wavelength above the waveguide in the medium to enhance the bottom emission, and this was slightly off of normal to avoid back reflections. Fig. 12(c) shows intensity scans of the one-dimensional (1D) far-field both longitudinally (axially) and laterally, whereas Fig. 12(d) presents 3D plots of the optimized far-field patterns. There was an on-chip monitor array for each channel after grating. The PIC contained 104 diodes in total. Beam steering angle range of 6° in the longitudinal direction and 12° in the lateral direction were reported with the on-chip laser. Wider longitudinal sweeping was possible with an off-chip laser.

More recently, there have been some ongoing research efforts to demonstrate a LiDAR system based upon the SWEEPER concept. For this, a more complex InP transceiver PIC is being explored as well as its integration with a Si-photonics emitter PIC. Fig. 13(a) illustrates the concept [51]. In this case, the InP-PIC transceiver is flip-chip bonded to the Si-photonics

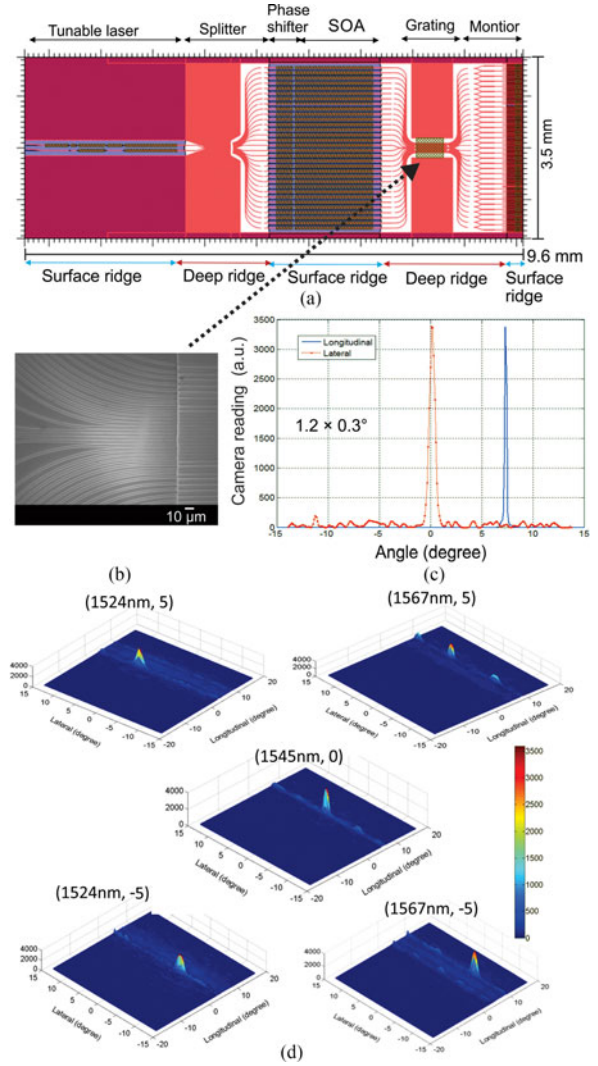


Fig. 12. (a) Schematic and (b) mask layout of the InP-PIC for $32 \times N$ surface emitting grating phase array, and (b) SEM images of waveguide feeds from splitter and into grating arrays, (c) one-dimensional, and (d) three-dimensional plot of the far-field patterns for some critical angles in the longitudinal and lateral directions, wavelength controlling the longitudinal direction and phase shifters controlling the lateral direction. Reproduced with permission from [49].

(SOI)-PIC, and light is coupled to a waveguide on the SOI, where the optical splitter, phase-shifter (modulator) array and 1-D grating surface-emitting waveguide array (OPA) exists. Electrical contacts to the InP-PIC are also made to the SOI-PIC. The SOI in turn, is flip-chipped to a Si-interposer which contains the drive and control electronics for both the InP-PIC transceiver and the SOI-phase modulators. The InP-PIC transceiver, illustrated more explicitly in Fig. 13(b), contains an asymmetric MZ (AMZ) filter and detectors for a wavelength locker as well as couplers and detectors for a coherent receiver in addition to the widely-tunable SGDBR laser. With the addition of external feedback electronics from the AMZ filter detectors to the phase tuning section of the laser, the locker selects and stabilizes the laser to specific wavelengths across its widely-tunable spectrum. These wavelengths correspond to directions in the far-field for the resulting optical beam. Also, thermal transients can be eliminated following a wavelength tuning event. Finally, the AMZ

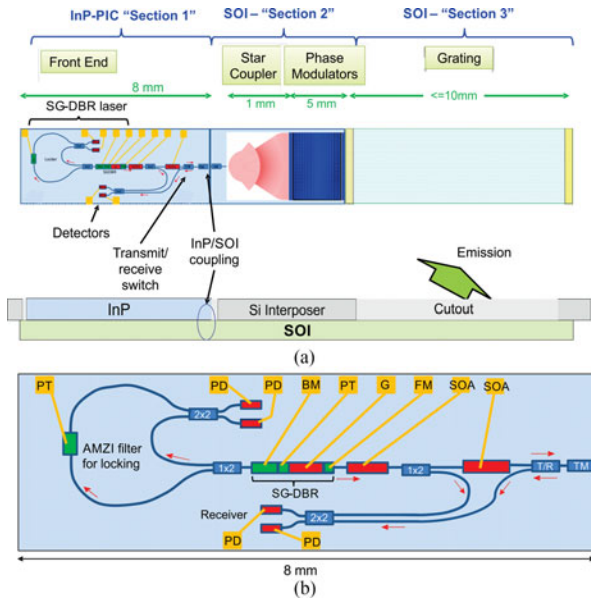


Fig. 13. (a) Hybrid integration of InP-transceiver PIC with a SOI-emitter PIC on a Si-Interposer, and (b) schematic layout of the InP-PIC. (BM = back mirror, FM = front mirror, G = gain, PD = photodiode, PT = phase tuner, SOA = semiconductor optical amplifier, TM = turning mirror, T/R = transmit/receive.)

filter is also tunable by the addition of a phase shifter in one of its arms—upper left-most contact pad in Fig. 13(b). This provides for a possible continuous ramping of the output frequency of the laser while it is locked, enabling an frequency modulated continuous wave (FMCW) type of LiDAR to be implemented [51].

The coherent receiver is formed by coupling a portion of the SGDBR's output to the receiver coupler as the LO, where it is combined with a portion of the return echo from the SOI emitter/receiver stage. For the FMCW case, these waves mix in the two receiver photodiodes to provide the heterodyne current to the external receiver electronics. The frequency of the return wave is slightly different from the present SGDBR value, because of the delay and the frequency sweep rate of the laser. For example, if the laser were to be swept at a rate of $100 \text{ MHz}/\mu\text{s}$ and the delay of the return echo was $1 \mu\text{s}$, then the heterodyne difference frequency would be 100 MHz , and this would then determine the distance to the object causing the echo.

The viability of the coherent LiDAR PIC of Fig. 13 is supported by the fact that some of its key elements have already been successfully demonstrated. For example, the very important wavelength locker, which both stabilizes the wavelength output and enables wavelength chirping, has been demonstrated before using InP-PICs. As shown in Fig. 14, AMZI filters have been integrated with SGDBRs, and with feedback electronics shown vast improvements in wavelength stability [52], [53]. In fact, this prior work shows the same design as incorporated within Fig. 13. The InP-PIC consists of a widely-tunable SG-DBR laser, a 60 GHz free spectral range (FSR) AMZI, and waveguide detectors monolithically integrated on the InP platform. A microscope image of the PIC can be seen in Fig. 14(b) together with a circuit schematic. The basic idea of such wavelength locking is that the optical frequencies of the

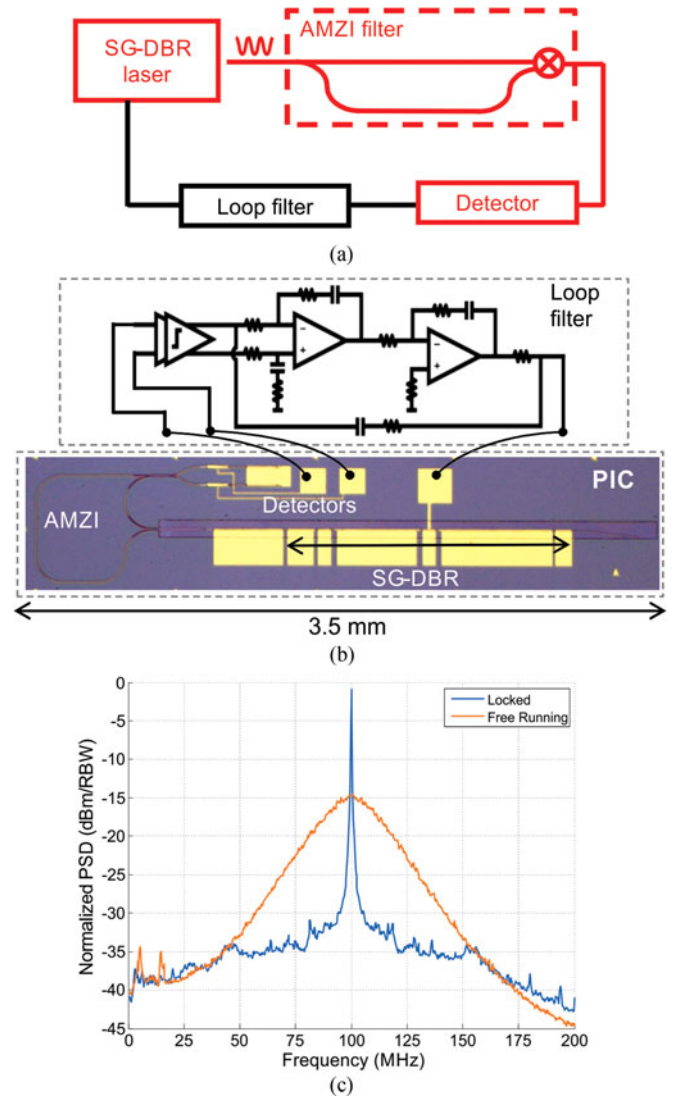


Fig. 14. (a) Schematic of the frequency lock loop system using an InP-PIC, (b) micrograph of the InP-PIC with a schematic of the feedback electronics including loop filter and (c) ESA spectra of the free running and locked SGDBR laser. The 3-dB linewidth after locking is 150 kHz . Reproduced with permission from [52].

SG-DBR laser can be stabilized by locking at the zero-crossings of the on-chip AMZI filter. The high-gain of the feedback loop provides an error signal to the laser tuning phase section that forces the wavelength to shift until there is essentially no input current to the circuit. If the gain is sufficiently high even frequency noise that would cause a natural dithering about this operating point is significantly suppressed. This latter effect is shown in Fig. 14(c), where the linewidth is reduced from an initial value of several MHz down to 150 kHz with frequency locking.

Another building block in the LiDAR system of Fig. 13 is the efficient coupling of light from the InP transceiver PIC to-and-from the SOI emitter PIC [54]–[56]. With flip-chip bonding, vertical coupling is required. A technique, employing a grating coupler on the SOI waveguide and a TIR reflector within the InP-PIC, has been recently explored [57]. Fig. 15(a) illustrates

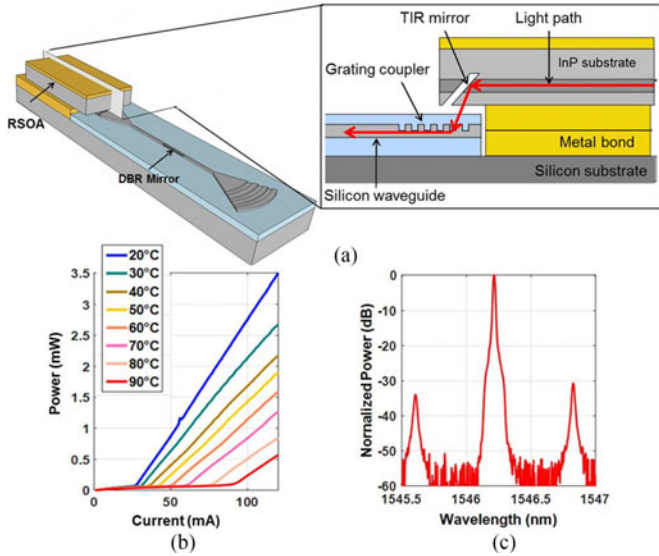


Fig. 15. (a) 3D schematic of the InP-PIC bonded to the silicon substrate for 3D integrated hybrid silicon laser, and a cross-sectional schematic is zoomed-in, illustrating vertical coupling using turning mirror, (b) temperature dependent LIV curves and (c) lasing spectrum of the hybrid laser. Reproduced with permission from [56].

this technique schematically. As a matter of fact, this approach is based on the flip-chip integration of InP-PICs containing total internal reflection (TIR) turning mirrors for surface emission. In refs. [54]–[57], light was coupled to the SOI waveguides through surface grating couplers, as shown in Fig. 15(a). Fig. 15(b) shows the temperature dependent continuous-wave LIV characteristics. The maximum operating temperature of these devices was 90°C. Devices showed reasonably good wall-plug efficiency due to an excellent heat management. Fig. 15(c) show the lasing spectra of the hybrid laser at a bias current of 60 mA, measured at room temperature. Devices exhibit single-mode operation with a side-mode suppression ratio (SMSR) of 30 dB or greater.

VI. OPLL FOR COHERENT RECEIVERS AND FREQUENCY SYNTHESIS

Although coherent communication in today's optical links is being used, it is mainly based on the high speed analog-to-digital converter (ADC) and digital signal processor (DSP) to recover the phase information, which makes the receiver power-hungry and less cost-effective. Therefore, it is currently of significant interest to develop compact, efficient and cost-effective analog coherent optical receivers that do not require ADC or DSP. In 2012, a highly-integrated 'analog coherent' optical receiver using InP-PICs was achieved [58], [59]. A homodyne optical phase-locked loop (OPLL) technique with a Costas loop was employed in such a receiver. A photonic IC, an electrical IC, and a hybrid loop filter were developed to build a stable homodyne OPLL. Finally, the binary phase-shift keying (BPSK) receiver based on Costas loop exhibited error-free ($BER < 10^{-12}$) up to 35 Gbps with no latency. The integrated Costas receiver has its advantage in better phase noise suppression, high BER, small footprint, power efficiency and cost-effectiveness.

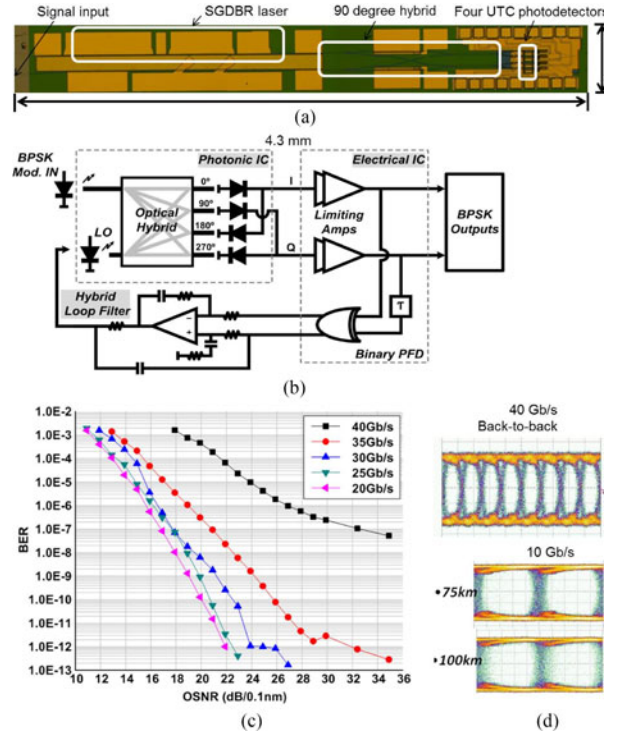


Fig. 16. (a) Microscope image of the InP-PIC used for developing OPLL systems, (b) schematic of the Costas loop based phase-locked coherent BPSK receiver using this PIC, (c) bit error rate (BER) vs optical signal-to-noise ratio (OSNR) curves of the receiver, measured at the data rates from 20–40 Gbps, and (d) eye diagrams of received data at 40 Gbps for a back-to-back experiment as well as at 10 Gbps after 75 and 100 km fiber propagation. Reproduced with permission from [58].

The fully-processed PIC based on the InGaAsP/InP platform used in this study is shown in Fig. 16(a). The PIC included a widely tunable SG-DBR laser with a 40 nm wavelength span by current injection into front and back mirrors and a phase-tuning section diode. The received signal from the reference laser and LO laser were mixed by an integrated 90° optical hybrid and down-converted by four uni-traveling carrier PDs for I - Q electrical outputs. The fabricated optical hybrid had $\pm 2\%$ imbalanced outputs and the PDs exhibited a 3-dB bandwidth of 30 GHz and 18 mA saturation current at -5 V.

The general architecture of the optical Costas loop-based analog coherent optical receiver is shown in Fig. 16(b). The I - Q signals were detected by four high speed photodetectors, which not only converted the optical signal to electrical signal, they also acted as low pass filters. The mixer was realized by a delay line and an XOR gate, which act together as a quadri-correlator phase/frequency detector (PFD). The error signal from the PFD fed back to the laser tuning section through the loop filter.

The authors measured the bit-error-rate (BER) and eye diagrams of the received BPSK data. The BER measurement was carried out at the bit rates of 20, 25, 30, 35, and 40 Gbps. By varying the VOA, the optical signal-to-noise ratio (OSNR) from the EDFA output changes, and therefore the BERs are measured at different OSNR. The results are shown in Fig. 16(c). The measured eye diagrams at 40 Gbps for the back-to-back experiment are shown in Fig. 16(d), from which we can see the eyes are

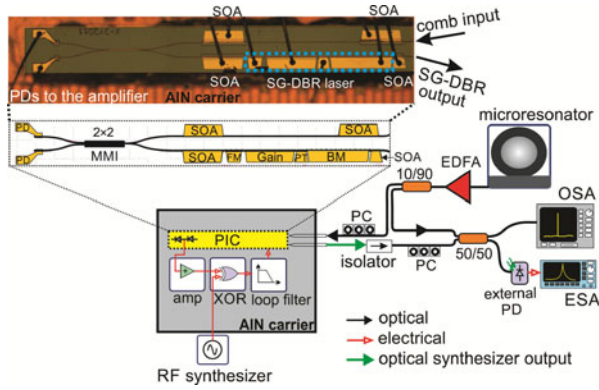


Fig. 17. The test setup of the optical synthesizer using heterodyne OPLL locking scheme. A microscope picture of the fully fabricated PIC mounted on AIN carrier with wirebonding shown at the top. (amp: amplifier, BM: back mirror, ESA: electrical spectrum analyzer, EDFA: erbium doped fiber amplifier, FM: front mirror, MMI: multimode interference, OSA: optical spectrum analyzer, PC: polarization controller, PT: phase tuner, PD: photodetector, PIC: photonic integrated circuit, SOA: semiconductor optical amplifier). Reproduced with permission from [63].

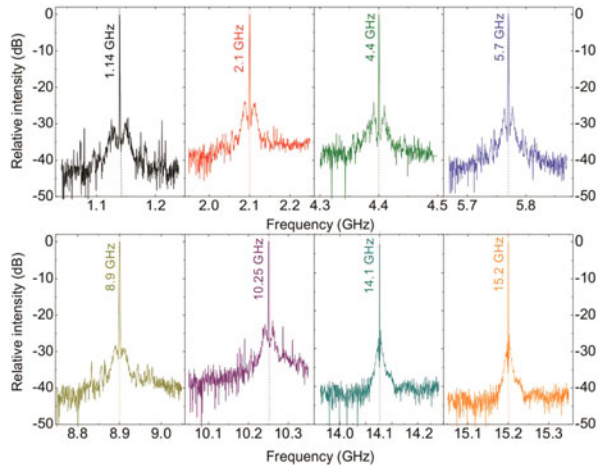


Fig. 18. Offset locking at frequencies up to 15.2 GHz, showing the locking range of the OPLL system using InP-PIC.

fairly open even at 40 Gbps, exhibiting superior performance of error-free ($BER < 10^{-12}$) up to 35 Gbps. For long propagation through 75 km and 100 km of optical fiber, the eye diagrams of the received 10 Gbps BPSK data are shown in Fig. 16(d).

Recently, chip-scale optical frequency synthesizers are of significant research interest for enabling a number of potential applications, including optical spectroscopy, LiDAR, and optical frequency metrology. There have been ongoing extensive efforts among the scientific community to develop such highly-integrated optical frequency synthesis systems [60]–[62].

Very recently, the experimental demonstration of a chip-scale optical frequency synthesizer was reported [63], [64]. One of the key building blocks in such synthesizers was InP-based PICs that include widely-tunable LO-laser, input waveguide for the light injection from the master oscillator (MO), couplers and on-chip high-speed photodetectors (PDs), monolithically integrated. The system was developed by offset phase-locking the on-chip widely tunable SG-DBR laser to a magnesium fluoride (MgF_2) microresonator-based optical frequency comb

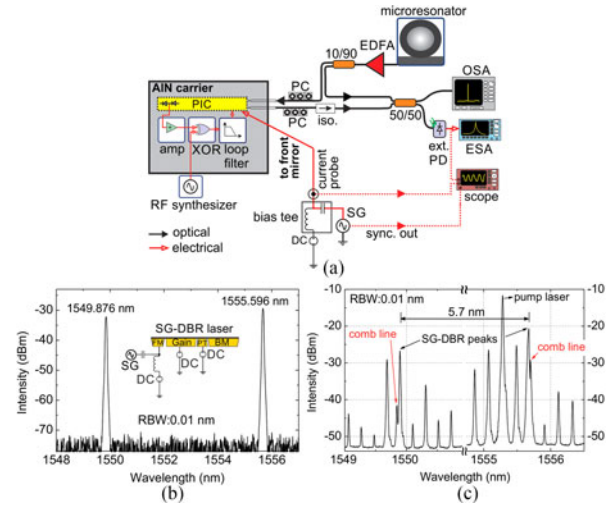


Fig. 19. (a) The test setup for measuring the switching speed of our OFS, (b) the optical spectrum of SG-DBR laser when the current into the front mirror is modulated to result wavelength switching of 5.7 nm, and (c) superimposed optical spectra of comb output and SG-DBR laser, where both comb peaks separated by 0.024 nm from their corresponding SG-DBR laser peaks can be resolved. (BM = back mirror, DC = direct current, EDFA = erbium doped fiber amplifier, ext. PD = external photodetector, FM = front mirror, PIC = photonic integrated circuit, PC = polarization controller, PT = phase tuner, RBW = resolution bandwidth). Reproduced with permission from [63].

using OPLL technology. Fig. 17 shows the experimental setup used in this study to confirm the phase-locking the SG-DBR laser in the InP-PIC to the optical comb. Despite the tuning range of the on-chip laser was ~ 50 nm, the coverage of the synthesizer was limited by the comb span, defined by the comb lines intensity exceeding -50 dBm. The balanced PDs integrated in the InP-PIC were mainly responsible for generating differential phase error signals between the SG-DBR laser and a particular comb line to be locked to.

In order to achieve the continuous tuning between comb lines, the developed synthesizer system had a bandwidth exceeding half of the comb's free-spectral-range (FSR). Thus any desired optical frequencies between comb lines could be generated. This was experimentally verified by determining the offset locking range of the heterodyne OPLL system. Fig. 18 shows the RF spectra of the phase-locked on-chip laser with various offsets. By changing the RF reference frequency, the SG-DBR frequency was shifted with an offset up to a frequency of 15.2 GHz relative to the comb line and the heterodyne OPLL phase locked the LO laser to the comb.

It was also demonstrated that the SGDBR output could jump from being locked to one comb line to another many comb lines away. For that, the current into the front mirror in the laser was modulated by a square wave signal with a frequency of 800 kHz and 50% duty cycle. The square-wave signal into the front mirror modulates the lasing wavelength between two values with a separation of ~ 5.72 nm (715 GHz), corresponding to 27 comb lines. The wavelength switching rate between these two values was much faster than the spectrum capturing rate the optical spectrum analyzer (OSA). Therefore, both wavelength values on the OSA are observed simultaneously, as shown in Fig. 19(b). The dc offset and amplitude of the square wave were set to

values that result in two output wavelengths of SG-DBR lasers. In order to measure the switching speed, the output wavelengths of the laser beat against two comb lines, generating a RF beat note with the same frequency. The superimposed-optical spectra of comb output and laser at these two specific states are shown in Fig. 19(c). By offset phase locking the SG-DBR laser to the comb lines, the complete operation of the optical frequency synthesis was achieved

VII. CONCLUSION

InP-PIC technology has matured, expanded and accelerated at a great speed within the last 20 years. Its technological capability is progressed in a way that can impact every field imaginable. This advancement is primarily made by monolithically integrating and then successfully demonstrating a wide range of photonic functions on the same chip. In addition to the development of high-performance next generation telecom/datacom transceivers, the scientific community is focusing on the realization of InP PIC-based complicated and useful photonic systems that can enable lots of real-world applications in the areas including sensing, imaging and high-speed signal processing.

Despite this advancement of InP-PIC technology, further efforts are still required to reduce the assembly complexity of InP-PICs. Since InP-PICs often are interfaced with electronics and other integrated optical and micro-optical systems, this necessitates a flexible packaging technology that can handle not only low-cost and high-volume demands, but also high-performance components. Hybrid packaging is one of the most popular ways to combine the processed chips in a package and/or on an interposer. On-chip integration of InP-PICs and CMOS electronics is another important area of research that promises to provide a high-performance system with a greatly reduced cost.

A number of InP-based foundry platforms are already established and the open access to these foundries facilitates the development of novel photonic ASICs. With all these past, current and future efforts, it is certain that this InP-PIC technology will move further ahead in the next decade or so. Beyond the areas of telecom and datacom, this maturing technology and its fast advances are then expected to influence our daily lives and socio-economic infrastructure.

REFERENCES

- [1] D. F. Welch *et al.*, "The realization of large-scale photonic integrated circuits and the associated impact on fiber-optic communication systems," *J. Lightw. Technol.*, vol. 24, no. 12, pp. 4674–4683, Dec. 2006.
- [2] L. A. Coldren *et al.*, "High performance InP-based photonic ICs—A tutorial," *J. Lightw. Technol.*, vol. 29, no. 4, pp. 554–570, Feb. 2011.
- [3] K. Kudo *et al.*, "1.55- μm wavelength-selectable microarray DFB-LD's with monolithically integrated MMI combiner, SOA, and EA-modulator," *IEEE Photon. Technol. Lett.*, vol. 12, no. 3, pp. 242–244, Mar. 2000.
- [4] P. Bernasconi *et al.*, "Monolithically integrated 40-Gb/s switchable wavelength converter," *J. Lightw. Technol.*, vol. 24, no. 1, pp. 71–76, Jan. 2006.
- [5] B. Mason, J. Barton, G. A. Fish, L. A. Coldren, and S. P. DenBaars, "Design of sampled grating DBR lasers with integrated semiconductor optical amplifiers," *IEEE Photon. Technol. Lett.*, vol. 12, no. 7, pp. 762–764, Jul. 2000.
- [6] D. Tsou, S. Zaytseva, A. Paucharda, S. Hummela, and Y.-H. Lo, "InP-based three-dimensional photonic integrated circuits," in *Proc. SPIE, Adv. Microelectron. Device Technol.*, 2001, vol. 4600, pp. 10–13.
- [7] M. R. Gokhale *et al.*, "Uncooled, 10 Gb/s 1310 nm electroabsorption modulated laser," in *Proc. Opt. Fiber Commun.*, Atlanta, GA, USA, Mar. 2003, p. PD42-P1-3.
- [8] J. W. Raring *et al.*, "40 Gbit/s photonic receivers integrating UTC photodiodes with high- and low-confinement SOAs using quantum well intermixing and MOCVD regrowth," *Electron. Lett.*, vol. 42, no. 16, pp. 942–943, 2006.
- [9] T. Spuesens *et al.*, "Improved design of an InP-based microdisk laser heterogeneously integrated with SOI," in *Proc. Group IV Photon.*, San Francisco, CA, USA, Sep. 2009, pp. 202–204.
- [10] D. Liang *et al.*, "Optimization of hybrid silicon microring lasers," *IEEE Photon. J.*, vol. 3, no. 3, pp. 580–587, Jun. 2011.
- [11] G. Kurczveil *et al.*, "An integrated hybrid silicon multiwavelength AWG laser," *IEEE J. Sel. Topics Quantum Electron.*, vol. 17, no. 6, pp. 1521–1527, Nov./Dec. 2011.
- [12] S. Srinivasan *et al.*, "Hybrid silicon devices for energy-efficient optical transmitters," *IEEE Micro*, vol. 33, no. 1, pp. 22–31, Jan./Feb. 2013.
- [13] J. M. Fedeli *et al.*, "Silicon photonics transceivers with InP on Si lasers," *Mater. Res. Soc.*, vol. 1559, pp. 1–11, 2013.
- [14] LightCounting, "Integrated optical devices," Rep., 2017. [Online]. Available: <https://www.lightcounting.com/Silicon.cfm>
- [15] P. R. A. Binetti *et al.*, "Indium phosphide photonic integrated circuits for coherent optical links," *IEEE J. Quantum Electron.*, vol. 48, no. 2, pp. 279–291, Feb. 2012.
- [16] G. Gilardi and M. K. Smit, "Generic InP-based integration technology: Present and prospects [invited]," *Prog. Electromagn. Res.*, vol. 147, pp. 23–35, 2014.
- [17] M. Smit *et al.*, "An introduction to InP-based generic integration technology," *Semicond. Sci. Technol.*, vol. 29, no. 8, 2014, Art. no. 083001.
- [18] K. A. Williams *et al.*, "InP photonic circuits using generic integration [invited]," *Photon. Res.*, vol. 3, no. 5, pp. B60–B68, 2015.
- [19] K. Ławniczuk *et al.*, "Open access to technology platforms for InP-based photonic integrated circuits," *Adv. Opt. Technol.*, vol. 4, no. 2, pp. 157–165, 2015.
- [20] M. Lauer mann *et al.*, "Multi-channel, widely-tunable coherent transmitter and receiver PICs operating at 88 Gbaud/16-QAM," in *Proc. Opt. Fiber Commun.*, Los Angeles, CA, USA, Mar. 2017, pp. 1–3.
- [21] J. H. Marsh, "Quantum well intermixing revolutionizes high power laser diodes," *Laser Technik J.*, vol. 4, no. 5, pp. 32–35, 2007.
- [22] L. Hou and J. H. Marsh, "Photonic integrated circuits based on quantum well intermixing techniques," *Procedia Eng.*, vol. 140, pp. 107–114, 2016.
- [23] M. Aoki *et al.*, "Novel structure MQW electroabsorption modulator/DFB-laser integrated device fabricated by selective area MOCVD growth," *Electron. Lett.*, vol. 27, no. 23, pp. 2138–2140, 1991.
- [24] [Online]. Available: <https://www.lumentum.com>
- [25] S. Lange *et al.*, "100 GBd intensity modulation and direct detection with an InP-based monolithic DFB laser Mach-Zehnder modulator," in *Proc. Opt. Fiber Commun.*, Los Angeles, CA, USA, Mar. 2017, pp. 1–3.
- [26] N. P. Kelly, L. Caro, M. Dernaika, and F. H. Peters, "Regrowth-free integration of injection locked slotted laser with an electroabsorption modulator," *Opt. Express*, vol. 25, no. 4, pp. 4054–4060, Feb. 20, 2017.
- [27] H. Debrégeas *et al.*, "Record 6dBm electroabsorption modulated laser for 10Gb/s and 25Gb/s high power budget access networks," in *Proc. Opt. Fiber Commun.*, Los Angeles, CA, USA, Mar. 2017, pp. 1–3.
- [28] Y. Kawamura, K. Wakita, Y. Itaya, Y. Yoshikuni, and H. Asahi, "Monolithic integration of InGaAsP/InP DFB lasers and InGaAs/InAlAs MQW optical modulators," *Electron. Lett.*, vol. 22, no. 5, pp. 242–243, 1986.
- [29] M. Suzuki *et al.*, "Monolithic integration of InGaAsP/InP distributed feedback laser and electroabsorption modulator by vapor phase epitaxy," *J. Lightw. Technol.*, vol. LT-5, no. 9, pp. 1277–1285, Sep. 1987.
- [30] Y. Akulova, "InP photonic integrated circuits for high efficiency pluggable optical interfaces," in *Proc. Opt. Fiber Commun.*, Los Angeles, CA, USA, Mar. 2015, pp. 1–3.
- [31] Y. Akulova, "InP photonic integrated circuits for high efficiency optical transceivers," in *Proc. IEEE Photon. Conf.*, San Diego, CA, USA, Oct. 2014, pp. 1–2.
- [32] V. Lal *et al.*, "Extended C-band tunable multi-channel InP-based coherent transmitter PICs," *J. Lightw. Technol.*, vol. 35, no. 7, pp. 1320–1327, Apr. 2017.
- [33] Y. Akulova, "Advances in integrated widely tunable coherent transmitters," in *Proc. Opt. Fiber Commun.*, Anaheim, CA, USA, Mar. 2016, pp. 1–3.

- [34] M. Larson *et al.*, "Narrow linewidth sampled-grating distributed Bragg reflector laser with enhanced side-mode suppression," in *Proc. Opt. Fiber Commun.*, Los Angeles, CA, USA, Mar. 2015, pp. 1–3.
- [35] G. B. Morrison *et al.*, "Optoelectronic transmitter design to enable RF photonic systems," in *Proc. Int. Topical Meeting Microw. Photon.*, Long Beach, CA, USA, Nov. 2016, pp. 325–327.
- [36] M. L. Mashanovitch *et al.*, "A novel widely tunable monolithically integrated transmitter device in indium phosphide," in *Proc. Adv. Photon. IPR*, 2017, Paper IM3A.3.
- [37] X. Xiaobo, J. Khurgin, K. Jin, and F. S. Chow, "Linearized Mach-Zehnder intensity modulator," *IEEE Photon. Technol. Lett.*, vol. 15, no. 4, pp. 531–533, Apr. 2003.
- [38] E. J. Norberg, R. S. Guzzon, S. C. Nicholes, J. S. Parker, and L. A. Coldren, "Programmable photonic lattice filters in InGaAsP-InP," *IEEE Photon. Technol. Lett.*, vol. 22, no. 2, pp. 109–111, Jan. 2010.
- [39] J. S. Fandiño, P. Muñoz, D. Doménech, and J. Capmany, "A monolithic integrated photonic microwave filter," *Nature Photon.*, vol. 11, no. 2, pp. 124–129, 2016.
- [40] E. J. Norberg, R. S. Guzzon, J. S. Parker, L. A. Johansson, and L. A. Coldren, "Programmable photonic microwave filters monolithically integrated in InP-InGaAsP," *J. Lightw. Technol.*, vol. 29, no. 11, pp. 1611–1619, Jun. 2011.
- [41] R. S. Guzzon, E. J. Norberg, and L. A. Coldren, "Spurious-free dynamic range in photonic integrated circuit filters with semiconductor optical amplifiers," *IEEE J. Quantum Electron.*, vol. 48, no. 2, pp. 269–278, Feb. 2012.
- [42] W. Liu *et al.*, "A fully reconfigurable photonic integrated signal processor," *Nature Photon.*, vol. 10, no. 3, pp. 190–195, 2016.
- [43] W. Liu *et al.*, "A photonic temporal integrator with an ultra-long integration time window based on an InP-InGaAsP integrated ring resonator," *J. Lightw. Technol.*, vol. 32, no. 20, pp. 3654–3659, Oct. 2014.
- [44] W. Jiang *et al.*, "A monolithic InP-based photonic integrated circuit for optical arbitrary waveform generation," in *Proc. Opt. Fiber Commun.*, San Diego, CA, USA, Feb. 2008, pp. 1–3.
- [45] F. M. Soares *et al.*, "Monolithic InP 100-channel \times 10-GHz device for optical arbitrary waveform generation," *IEEE Photon. J.*, vol. 3, no. 6, pp. 975–985, Dec. 2011.
- [46] M. J. R. Heck, "Highly integrated optical phased arrays: Photonic integrated circuits for optical beam shaping and beam steering," *Nanophotonics*, vol. 6, no. 1, pp. 93–107, 2017.
- [47] W. Guo *et al.*, "InP photonic integrated circuit for 2D optical beam steering," in *Proc. Int. Photon. Nanofabrication Test.*, Wuhan, China, Nov. 2012, pp. 1–2.
- [48] W. Guo, P. R. A. Binetti, C. Althouse, L. A. Johansson, and L. A. Coldren, "InP photonic integrated circuit with on-chip tunable laser source for 2D optical beam steering," in *Proc. Opt. Fiber Commun.*, Anaheim, CA, USA, Mar. 2013, pp. 1–3.
- [49] W. Guo *et al.*, "Two-dimensional optical beam steering with InP-based photonic integrated circuits," *IEEE J. Sel. Topics Quantum Electron.*, vol. 19, no. 4, Jul./Aug. 2013, Art. no. 6100212.
- [50] J. K. Doyle *et al.*, "Two-dimensional free-space beam steering with an optical phased array on silicon-on-insulator," *Opt. Express*, vol. 19, no. 22, pp. 21595–21604, 2011.
- [51] S. J. M. Paul, J. Bowers, L. A. Coldren, and S. J. B. Yoo, "Photonic integrated circuits for coherent LiDAR," in *Proc. 18th Coherent Laser Radar Conf.*, Boulder, CO, USA, 2016, Paper T12.
- [52] A. Sivananthan *et al.*, "Integrated linewidth reduction of a tunable SG-DBR laser," in *Proc. Conf. Lasers Electro-Opt.*, 2013, Paper CTu1L.2.
- [53] A. Sivananthan *et al.*, "Monolithic linewidth narrowing of a tunable SG-DBR laser," in *Proc. Opt. Fiber Commun.*, Anaheim, CA, USA, Mar. 2013, pp. 1–3.
- [54] B. Song, C. Stagarescu, S. Ristic, A. Behfar, and J. Klamkin, "3D integrated hybrid silicon laser," *Opt. Express*, vol. 24, no. 10, pp. 10435–10444, 2016.
- [55] B. Song *et al.*, "3D integrated hybrid silicon laser," in *Proc. Eur. Conf. Opt. Commun.*, Valencia, Spain, Sep. 2015, pp. 1–3.
- [56] B. Song, L. Megalini, S. Dwivedi, S. Ristic, and J. Klamkin, "High thermal performance 3D hybrid silicon lasers," *IEEE Photon. Technol. Lett.*, vol. 29, no. 14, pp. 1143–1146, Jul. 2017.
- [57] B. Song, Y. Liu, S. Ristic, and J. Klamkin, "Tunable 3D hybrid integrated silicon photonic external cavity laser," in *Proc. Conf. Lasers Electro-Opt.*, San Jose, CA, USA, May 2017, pp. 1–2.
- [58] H.-C. Park *et al.*, "40 Gbit/s coherent optical receiver using a Costas loop," *Opt. Express*, vol. 20, no. 26, pp. B197–B203, 2012.
- [59] M. Lu *et al.*, "An integrated 40 Gbit/s optical Costas receiver," *J. Lightw. Technol.*, vol. 31, no. 13, pp. 2244–2253, Jul. 2013.
- [60] J. E. Bowers *et al.*, "Chip-scale optical resonator enabled synthesizer (CORES) miniature systems for optical frequency synthesis," in *Proc. IEEE Int. Freq. Control Symp.*, New Orleans, LA, USA, Sep. 2016, pp. 1–5.
- [61] M. Lu *et al.*, "A highly-integrated optical frequency synthesizer based on phase-locked loops," in *Proc. Opt. Fiber Commun.*, San Francisco, CA, USA, Mar. 2014, pp. 1–3.
- [62] D. T. Spencer *et al.*, "Towards an integrated photonics optical-frequency synthesizer with <1 Hz residual frequency noise," in *Proc. Opt. Fiber Commun.*, Los Angeles, CA, USA, Mar. 2017, pp. 1–3.
- [63] S. Arafin *et al.*, "Towards chip-scale optical frequency synthesis based on optical heterodyne phase-locked loop," *Opt. Express*, vol. 25, no. 2, pp. 681–695, 2017.
- [64] S. Arafin *et al.*, "Power-efficient Kerr frequency comb based tunable optical source," *IEEE Photon. J.*, vol. 9, no. 3, Jun. 2017, Art. no. 6600814.



Shamsul Arafin (S'08–M'12–SM'17) received the B.Sc. degree in electrical and electronics engineering from Bangladesh University of Engineering and Technology, Dhaka, Bangladesh, in 2005, the M.Sc. degree in communication technology from Universität Ulm, Ulm, Germany, in 2008, and the Ph.D. degree from the Walter Schottky Institut, Technische Universität München, Munich, Germany, in 2012. He is currently an Assistant Project Scientist at the University of California, Santa Barbara (UCSB), Santa Barbara, CA, USA. Prior to joining UCSB, he was

a Postdoctoral Research Scholar in Device Research Laboratory, University of California, Los Angeles, CA, USA. He has authored and coauthored more than 80 papers in leading technical journals and international conferences.

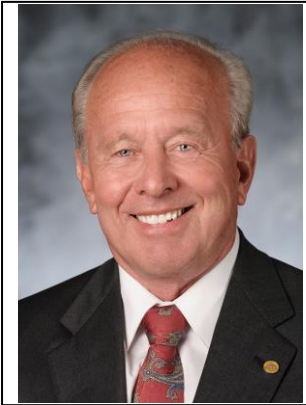


Larry A. Coldren (S'67–M'72–SM'77–F'82–LF'12) received the Ph.D. degree in electrical engineering from Stanford University, Stanford, CA, USA, in 1972. After 13 years in the research area with Bell Laboratories, he joined the University of California at Santa Barbara (UCSB) in 1984. He is currently the Fred Kavli Professor of optoelectronics and sensors and holds appointments with the Department of Materials and the Department of Electrical and Computer Engineering. From 2009 to 2011, he was acting Dean of the College of Engineering. In

1990, he cofounded Optical Concepts, later acquired as Gore Photonics, to develop novel VCSEL technology, and, in 1998, he cofounded Agility Communications, later acquired by JDSU (now Lumentum), to develop widely tunable integrated transmitters. At UCSB, he worked on multiple-section widely tunable lasers and efficient vertical-cavity surface-emitting lasers (VCSELs). More recently, his group has developed high-performance InP-based photonic integrated circuits and high-speed, high-efficiency VCSELs. He has authored or coauthored more than a thousand journal and conference papers, eight book chapters, a widely used textbook, and 63 issued patents. He is a Fellow of OSA, IEE, and the National Academy of Inventors, as well as a member of the National Academy of Engineering. He received the 2004 John Tyndall Award, the 2009 Aron Kressel Award, the 2014 David Sarnoff Award, the 2015 IPRM Award, and the 2017 Nick Holonyak, Jr. Award.

Photonic Integrated Circuits for Coherent Communication and Sensing

Larry A. Coldren
Electrical & Computer Engineering and Materials,
University of California, Santa Barbara, CA 93106
coldren@ucsb.edu



Abstract: Coherent optical receivers and transceivers are currently being actively employed in coherent communication systems as well as in sensor systems such as lidars, optical coherence tomography and other biosensors. Many of these include widely-tunable lasers for local oscillators (LOs) and transmitters. In order to make these more practical and reliable as well as cost effective, photonic integration is also being implemented. Both InP and Si-photonic integration technologies have been involved. Generic coherent receiver photonic IC (PIC) chips can be employed for many of these applications. The author's work has been mainly with the InP-based PICs, which still remain dominant commercially. A recent application of interest for coherent communication links is in data centers for increased dynamic range that would enable optical switching and wavelength routing, but for this application the power dissipation must be very low.

Key to the coherent optical receivers that have been explored in the author's group is the use of an optical phase and frequency locked loop circuit, of a Costa's loop design, in order to avoid power-hungry high-speed analog-to-digital converters (ADCs) and digital signal processors (DSPs), with base rates of 40 Gb/s or more. These OPLL-based, or more correctly OPFLL-based, receivers have been dubbed 'analog coherent' receivers, because of the analog feedback loop that phase locks the LO to the carrier of the incoming signal. With this phase locking, no ADC/DSP is necessary, at least for the low-dispersive links encountered in data centers using 1.3 μm wavelengths. Some low-overhead FEC may be desired to insure error-free operation, but error-free operation with base rates above 35 Gb/s have already been demonstrated without FEC.

Issues with this type of receiver include polarization demodulation. Without the ADC/DSP approach, some other approach is necessary. The currently planned scheme includes the use of dual polarization and QPSK demodulation, so with 'analog coherent' novel circuits are necessary. A discussion of possible approaches will be included in the presentation.

Another recent driver for complex PICs is for low-cost lidars for automotive and drones. A second activity that will be summarized is work that involves the integration of an InP-based transceiver PIC with a Si-photonics-based phased-array optical emitter PIC for FMCW lidar. The emitter waveguides contain surface-emitting gratings, and as the wavelength is swept, the optical beam is swept axially. Lateral sweeping is accomplished by the 1-D phased array. As in the analog-coherent receiver case, close integration of interface electronics with the PICs is key to the successful operation of this system. For FMCW the wavelength is linearly modulated a relatively small amount (few GHz) at each wavelength point, so that the return echo is at a slightly different frequency than the outgoing beam, and the difference frequency can be used to give the distance to the reflection.

The InP-transceiver PIC contains a widely-tunable laser, which can be tuned over many tens of nanometers for wide beam deflection, a locker interferometer that defines the grid of wavelengths (and thus axial beam angles), a means of modulating the interferometer for the FMCW function, a splitter to tap off some output to serve as a Local Oscillator (LO) signal for the on-chip FMCW receiver photodiodes, and a coupler to tap off the return echo and also direct it to the on-chip receiver photodiodes. The linearly chirped LO and delayed return echo light mix in the receiver photodiodes to provide an RF difference frequency, which can be spectrally analysed to obtain distance as well as velocity information.

The presentation will discuss general issues with photonic integration in addition to the above examples.

Photonic-Integrated-Circuits for Coherent Communication and Sensing



Larry A. Coldren
ECE & Materials, UC-Santa Barbara

Major contributions by:
Mike Larson—Lumentum
Chris Doerr—Acacia
Beck Mason—Oclaro
Fred Kish—Infinera
UCSB Collaborators

What's the problem?

MOC 2018

Size, Weight, Power, Cost, Performance, Reliability

Where?

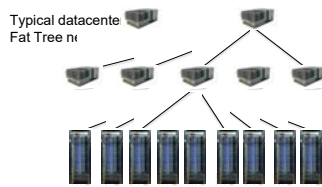
- Communication
 - Long haul
 - Metro, campus
 - Data centers, Supercomputers
- Sensing/instrumentation
- Computing

- 1970's - OEICs on GaAs for high-speed computing
- 1980's – InP photonics/fiber; integration & tunables for **coherent** → **Reach**
- 1990's – Widely-tunables, laser-mods, EDFAs; int. for WDM and cost
- 1990's – VCSELs for datacom and optical interconnection
- 2000 - Bubble: Explosion of strange ideas, bandwidth-demand satisfied by DWDM → crash; but bandwidth needed by 2010.
- 2000's – InP PICs & PLCs expanded and matured; increasing use of VCSELs in high-speed datacom and computing interconnects
- 2006+ – Emergence of Si-PICs with several different goals: low-cost OEICs; high-performance PICs; or stop Moore's-Law saturation
- 2008+ - Use of advanced modulation formats/**coherent receivers for improved Spectral Efficiency** —need for integration at both ends of links
- 2010's – Increased InP-PIC use; maturity of Si-photonics solutions; heterogeneous integration approaches; improved VCSEL link efficiency
- 2018 – **Data-center focus; coherent LIDAR/imaging; InP & Si-PICs in 'volume'**

INTREPID

Clint Schow-PI, J. Buckwalter, L. Coldren, J. Klamkin, A. Saleh – UCSB
K. Schmidtke & 5 others – Facebook

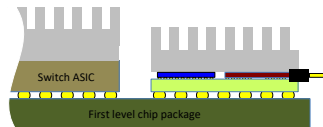
Intelligent Reduction of Energy through Photonic Integration for Datacenters



Facebook OCP Rack "Wedge" ToR switch (ToR = Top of Rack)

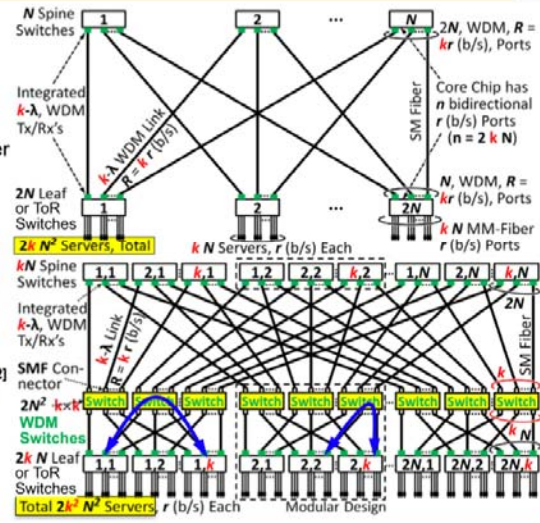


- ▶ **Photonics Integrated into Switch Packages**
 - Points of highest bandwidth concentration
- ▶ **Analog Coherent Links Optimized for Datacenters**
 - Large sensitivity gain → more energy efficient interconnects
 - Enabling technology for WDM, photonic routing and switching
- ▶ **Low-Power VCSEL Links**
 - Ultra-low power connections from servers to ToR or EoR switches
- ▶ **New Network Architectures**
 - Exploring wavelength routing and switching
- ▶ **Transition to Widespread Commercial Availability**
 - Technology demo in live datacenter
 - Open Compute Project (OCP), Telecom Infra Project (TIP)



Datacenter Network Architecture

- ▶ **Aggressive Integration**
 - Analog coherent WDM interfaces, with $k = 4$ to 16 wavelengths
 - Integrated directly into high-radix electronic switch ports
 - Greatly reduced cost, latency, power
- ▶ **Phase 1 Enhancements**
 - Add a layer of $k \times k$ AWGRs^[1]
 - Network scales-out by a factor of k
 - x2-4 increase in energy efficiency, compared to conventional designs
 - Same latency and switch sizes
- ▶ **Phase 2 Enhancements**
 - Replace AWGRs by **WDM switches**^[2]
 - Enabling network configurability, including **direct optical ToR-to-ToR connections**, to match workload
 - Leads to further improvements in energy efficiency and latency



[1] Saleh, "Scaling-out Data Centers Using Photonics Technologies," PS Conference, 2014.
 [2] Saleh, et al, "Elastic WDM Switching for Scalable Data Center Networks," OECC/PS Conference, 2016.

Analog Coherent: Maximizing Energy Efficiency

Direct-Modulation/Direct Detection

$$\text{Detected power} \propto (P_{\text{laser}} \cdot A_{\text{total}})$$

P_{laser} = laser power, A_{total} = total link attenuation

- ▶ RX sensitivity sets link budget, energy efficiency
 - Poor sensitivity = higher transmitter power
- ▶ Sensitivity directly degrades with data rate
 - Problem only getting worse

Field Modulation/Coherent Detection

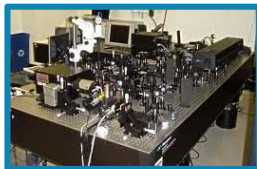
$$\text{Detected power} \propto \sqrt{(P_{\text{laser}} \cdot A_{\text{total}}) \cdot P_{\text{LO}}}$$

P_{LO} = Local Oscillator (LO) power

- ▶ ~20dB improvement in RX sensitivity possible
- ▶ Much greater tolerance to attenuation
 - Looser component specs for yield and cost
 - Ability to compensate for insertion loss of optical routing/switching devices

Optical Phase Locked Loop (OPLL) → Eliminating Power-Hungry DSP

Typical OPLLs prior to 2000
Lab-scale



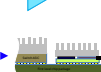
Prior UCSB work

Carrier-scale, single channel



INTREPID

Chip-scale, WDM multi-channel
with simple mux/demux



Photonic and Electronic Integration

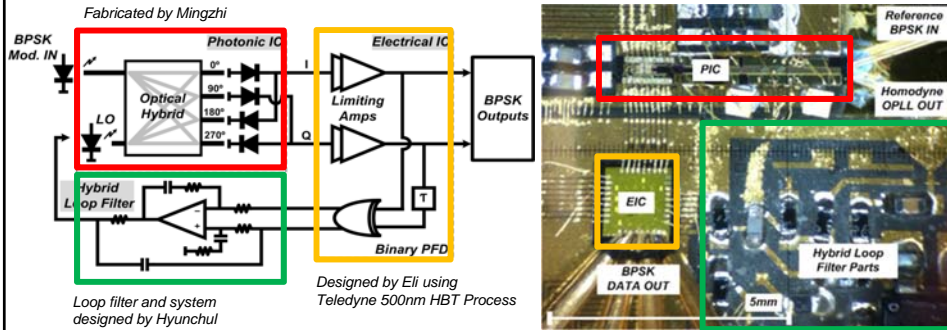
<1000X size
<100X power

<10X size
<10X power



UCSB **Prior Work: Phase Locked Coherent BPSK Receiver**
“Analog Coherent” MOC 2018

OPLL + Costas Loop → 1 cm² footprint



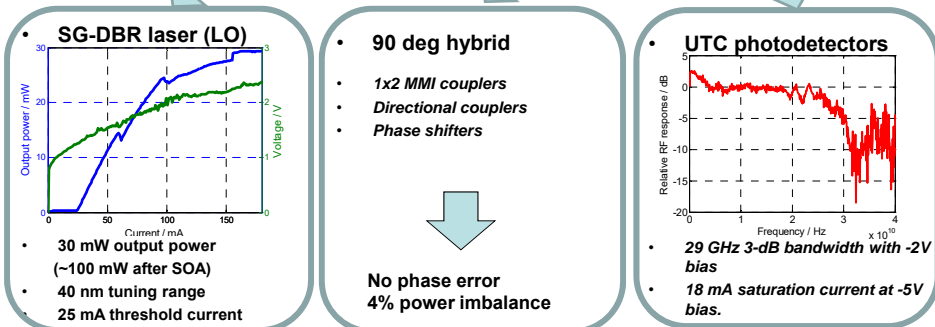
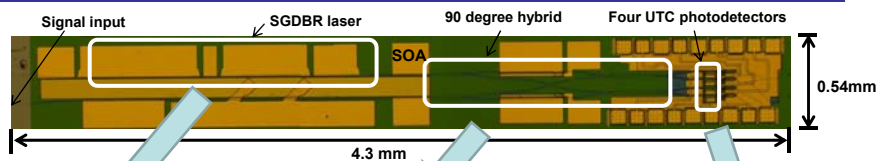
Photonic IC: SGDBR laser, optical hybrid, and un-balanced PDs

Electronic IC: limiting amplifiers and phase & frequency detector (PFD)

Hybrid loop filter: Feed-forward technique, op-amplifier and 0603 SMDs

Mingzhi Lu, et. al., *Optics Express*, Vol. 20, Issue 9, pp. 9736-9741 (2012)

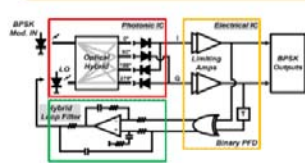
UCSB **InP Widely-tunable Coherent Receiver PIC-2**
(Heterodyne or Intradyn—also for Optical Synthesis) MOC 2018



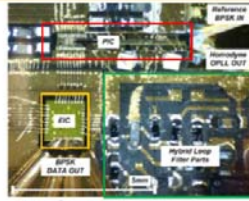
- I and Q outputs normally connected to ADC and DSP for Receiver
- Much lower SWaP-C Optical Phase Locked Loop (OPLL) used

Mingzhi Lu, et. al., *Optics Express*, Vol. 20, Issue 9, pp. 9736-9741 (2012)

Feasibility Established: Analog Coherent OPLLs



- **1.1GHz** closed loop bandwidth
- **120ps** loop propagation delay
- **100kHz** SGDBR-linewidth (*as ref. laser*)
- **-100dBc/Hz@above 50kHz** phase noise
- **600ns** frequency pull-in time
- **<10ns** phase lock time

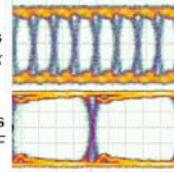


Operation at 1550nm

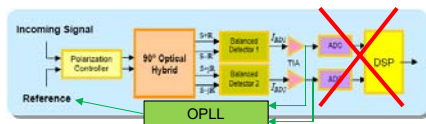
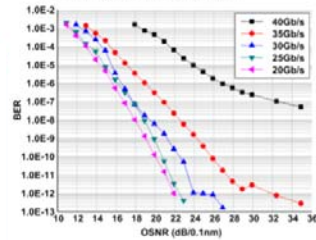
High-Speed Operation:

40 Gb/s
back-to-back

10 Gb/s
25km SMF



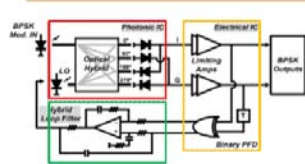
Error-free up to 35Gb/s:



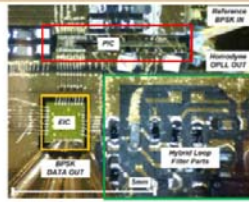
- S. Ristic *et al.*, *JLT* (2010)
- M. Lu *et al.*, *Optics Express*, (2012)
- P. R. A. Binetti *et al.*, *JQE* (2012)
- M. Lu *et al.*, *JLT* (2013)

8

Feasibility Established: Analog Coherent OPLLs



- **1.1GHz** closed loop bandwidth
- **120ps** loop propagation delay
- **100kHz** SGDBR-linewidth (*as ref. laser*)
- **-100dBc/Hz@above 50kHz** phase noise
- **600ns** frequency pull-in time
- **<10ns** phase lock time

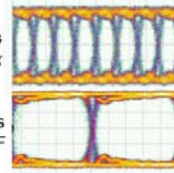


Operation at 1550nm

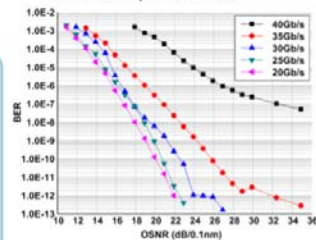
High-Speed Operation:

40 Gb/s
back-to-back

10 Gb/s
25km SMF



Error-free up to 35Gb/s:



INTREPID Focus

- ▶ O-band operation at maximum energy efficiency
- ▶ Co-optimization and tighter integration of photonics and electronics
- ▶ Flip-chip packaging supporting multi-channel WDM scaling

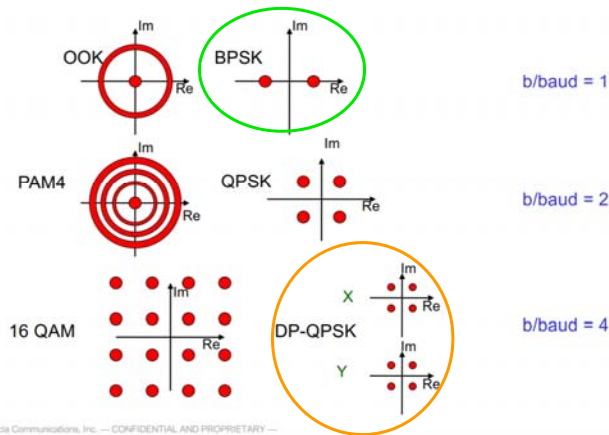


- S. Ristic *et al.*, *JLT* (2010)
- M. Lu *et al.*, *Optics Express*, (2012)
- P. R. A. Binetti *et al.*, *JQE* (2012)
- M. Lu *et al.*, *JLT* (2013)

8

For coherent use Vector modulation:

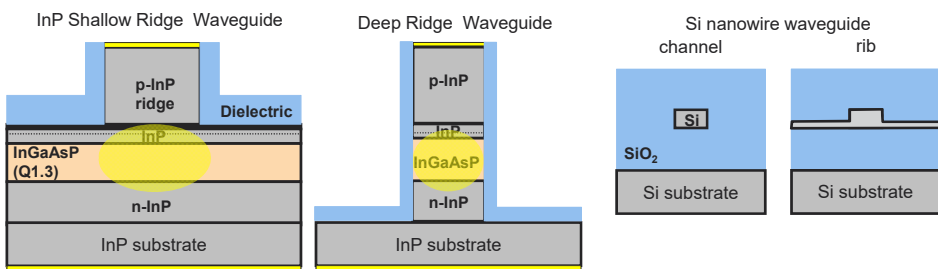
Modulation formats



© 2017 Acacia Communications, Inc. — CONFIDENTIAL AND PROPRIETARY —



Waveguides: InP vs SiP (Lumentum Slides—M. Larson)



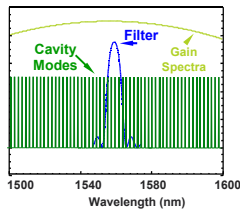
- Ridge width ~2um
- Core thickness 200-300nm
- Moderate index step (3.4 <-> 3.17) $\Delta n \sim 0.2$
- Ridge width ~1.2-1.8um
- Core thickness 200-300nm
- Moderate vertical index step
- Large lateral index step (3.3 <-> 1.45) $\Delta n \sim 2^*$
- Waveguides in both systems are polarization sensitive
- 450 x 220nm typical
- Large index step vertical & lateral (3.5 <-> 1.45) $\Delta n \sim 2$

Passive PIC Elements

| Passive Element | InP | SiP |
|---------------------------|---|---|
| Power Splitter/Combiner | Multimode Interference Couplers (MMIs) | MMIs Directional Couplers Adiabatic Couplers Y Junctions |
| 90 degree hybrid co-mixer | 2x4 MMI cascaded 2x2 couplers | 2x4 MMI cascaded 2x2 couplers |
| Off-chip coupling | Cleaved Facet Spot size converter (vertical/lateral taper) | Spot size converter to SiNx Grating coupler |
| Polarization diversity | hybrid | Polarization Beam Splitter/Rotator (PBSR) |
| Isolator | hybrid | hybrid |

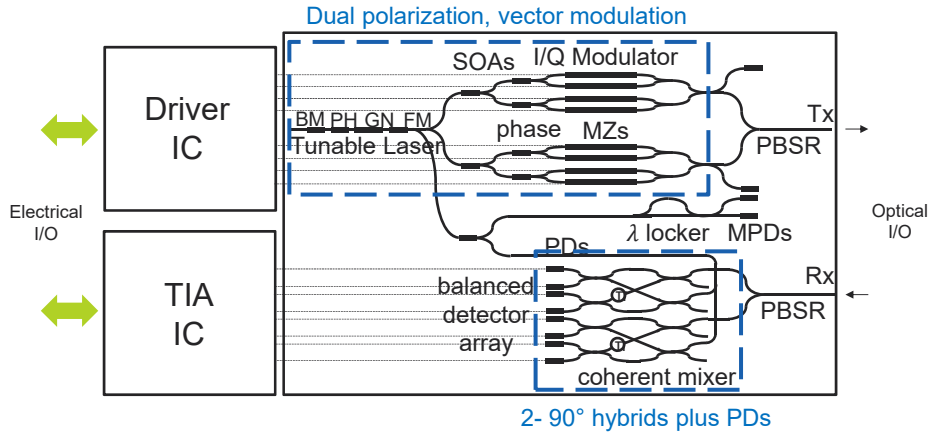
Laser Building Blocks

- Laser source required for transmitter and local oscillator
- Narrow linewidth, high power, full C-band tunable
- Vernier tuning architecture with 2 or more filters to overcome refractive index tuning limitations
- Laser must be temperature stabilized or suffer environmentally-induced frequency drift



| | InP | SiP |
|---------------------|---|--|
| Optical Gain Medium | InGaAsP or InGaAlAs quantum wells | hybrid or heterogeneous |
| Filters / Mirrors | Vertically-etched gratings in InGaAsP waveguide Microring resonators | Micro-ring resonators; Laterally-patterned gratings |
| Tuning mechanism | Carrier injection or thermal (microheater) | Thermal (microheater) |

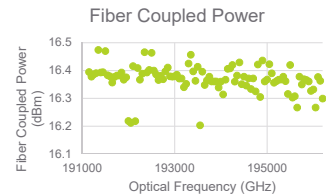
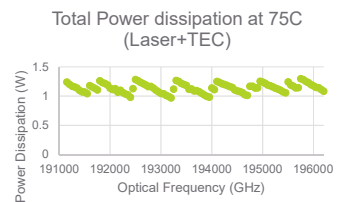
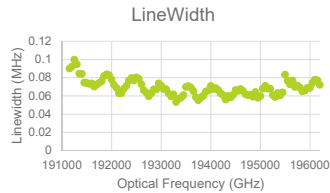
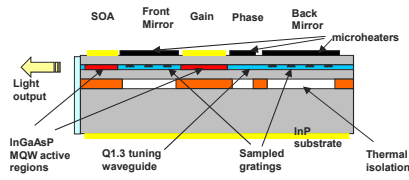
Single or Multiple PICs? InP Practical View (Lumentum)



- Separate Tx and Rx PIC for thermal considerations
 - Laser + Modulator must be temperature controlled; Receiver is uncooled

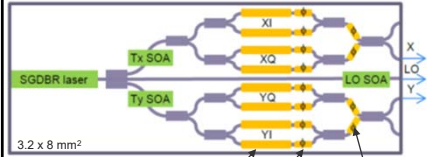
Narrow linewidth thermally tuned Sampled Grating DBR laser in InP (Lumentum)

- Vernier-tuned SGDBR Laser, comb spacing ~700GHz
- +16dBm output power, 100kHz linewidth
- <1.4W P_{diss} at 75C (laser TEC at 52C)



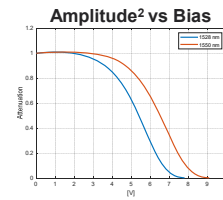
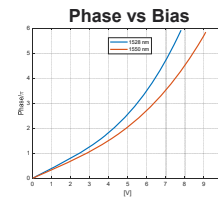
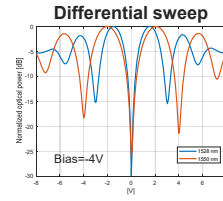
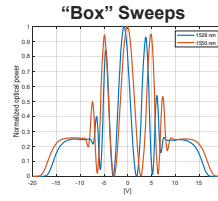
InP Coherent Tx PIC

- Integrated Narrow Linewidth Tunable Laser with Dual Polarization IQ modulator and LO Output



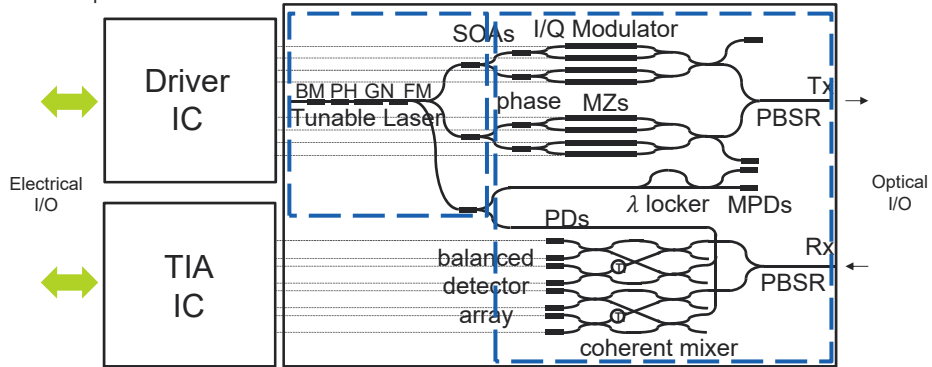
Carry RF data traffic

Maintain I and Q at quadrature
Provide null-bias for each child Mach-Zehnder



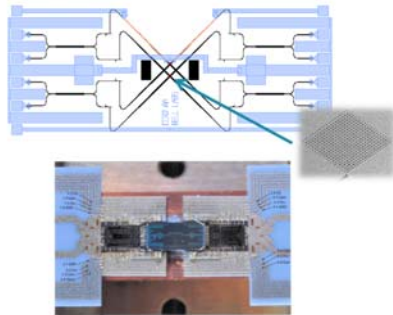
Single or Multiple PICs? SiP Preferred View (Acacia, NTT)

- Separate Tunable Laser PIC from Modulator+Receiver PIC for thermal considerations

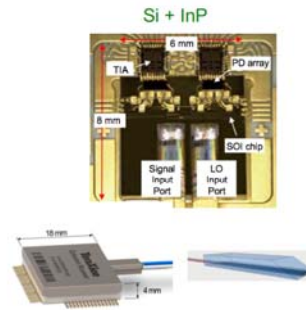


C. Doerr et al., OFC 2016
K. Kikuchi et al., Compound Semiconductor Integrated Circuit Symposium (CSICS), 2017

Early SiPh coherent receivers

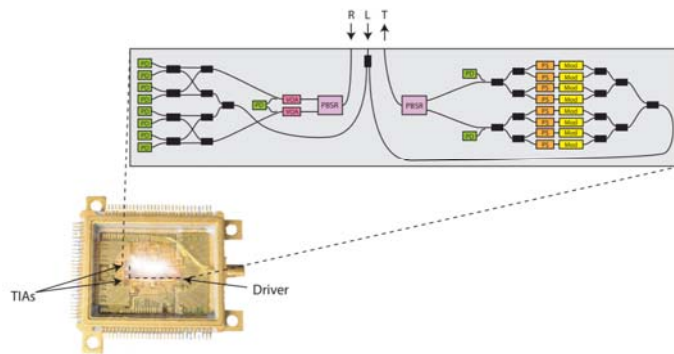


C. R. Doerr, et al., *J. Lightwave Tech.*, vol. 28, pp. 520-525, 2010.
C. R. Doerr, et al., *IEEE PTL*, 2011.



Y. Painchaud, et al., 2013.

Single-chip coherent transceiver



Power consumption = 4.3 W

ASIC-PIC co-packaging

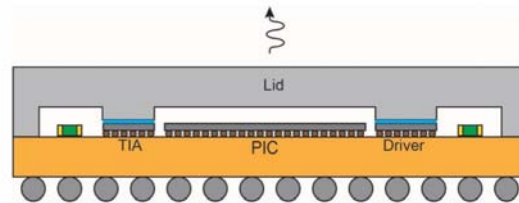
Improved heat dissipation

TuEE.5.pdf

OFC 2018 © OSA 2018

- Heat flows directly from die backside to lid

Very high bandwidth connections

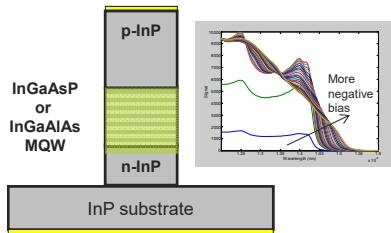


Acacia Communications, Inc. — CONFIDENTIAL AND PROPRIETARY —



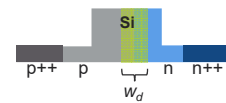
Modulator Material Physics

- InP: Quantum Confined Stark Effect
 - Applied reverse bias causes a redshift of the multiple quantum well excitonic absorption edge
 - $\Delta n \propto V, V^2$



D.A.B Miller, et al., Phys. Rev. Lett., 53 (1984) p. 2174

- SiP: plasma dispersion effect
 - $\Delta n \propto$ carrier concentration $\Delta N, \Delta P$.
 - Carrier concentration is a non-linear function of applied V



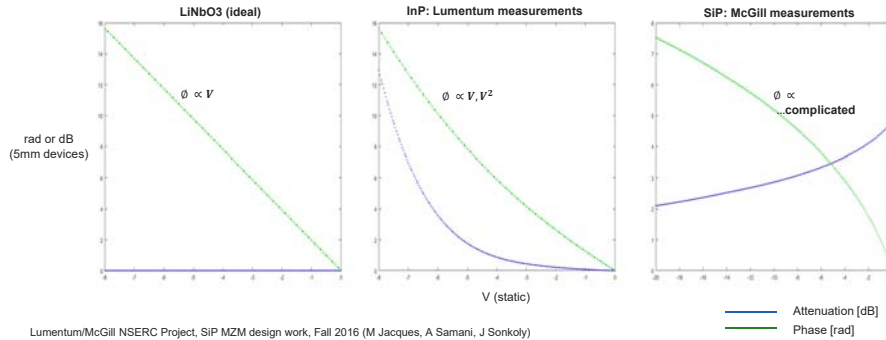
$$\Delta n(\lambda) = -3.64 \times 10^{-10} \lambda^2 \Delta N - 3.51 \times 10^{-6} \lambda^2 \Delta P^{0.8}$$

'Soref' equation. Fitting parameters are empirical

Soref and Bennett. IEEE JQE 23.1 (1987): 123-129.

Phase Shifter Transfer Functions

- Phase & attenuation vs applied voltage for 3 modulator materials
 - InP: nonlinear phase and attenuation (electro-absorption) with increasing reverse bias
 - SiP: complicated phase and attenuation; notice: vertical scale range is 1/2, horizontal scale (V) is 2.5X



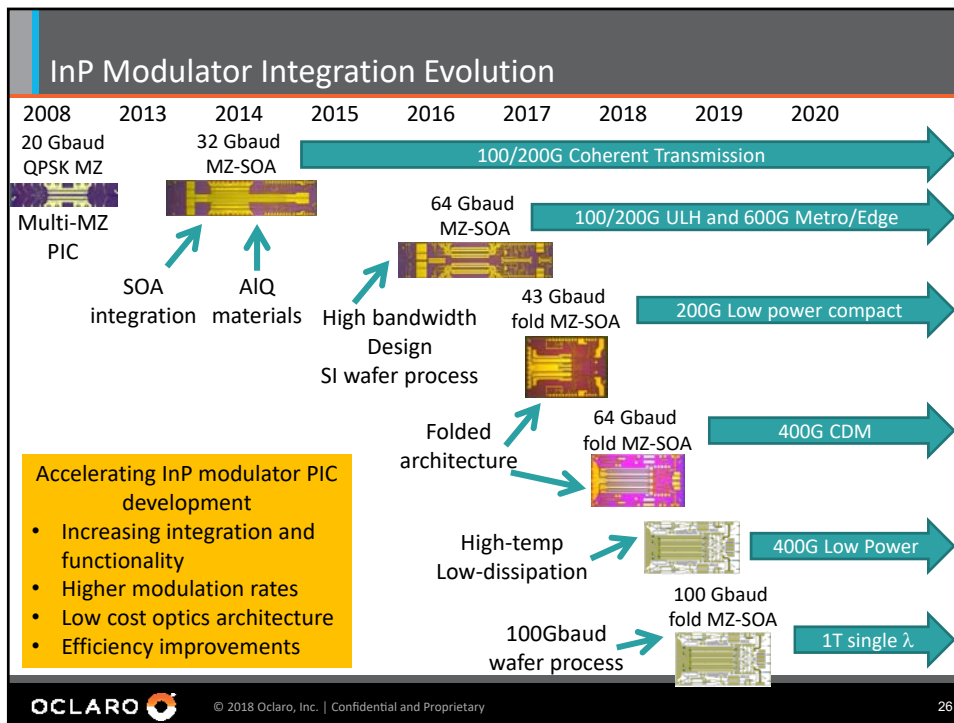
Power Dissipation Budget Comparison: 64 Gbaud DP-16QAM IC-TROSA component level estimate

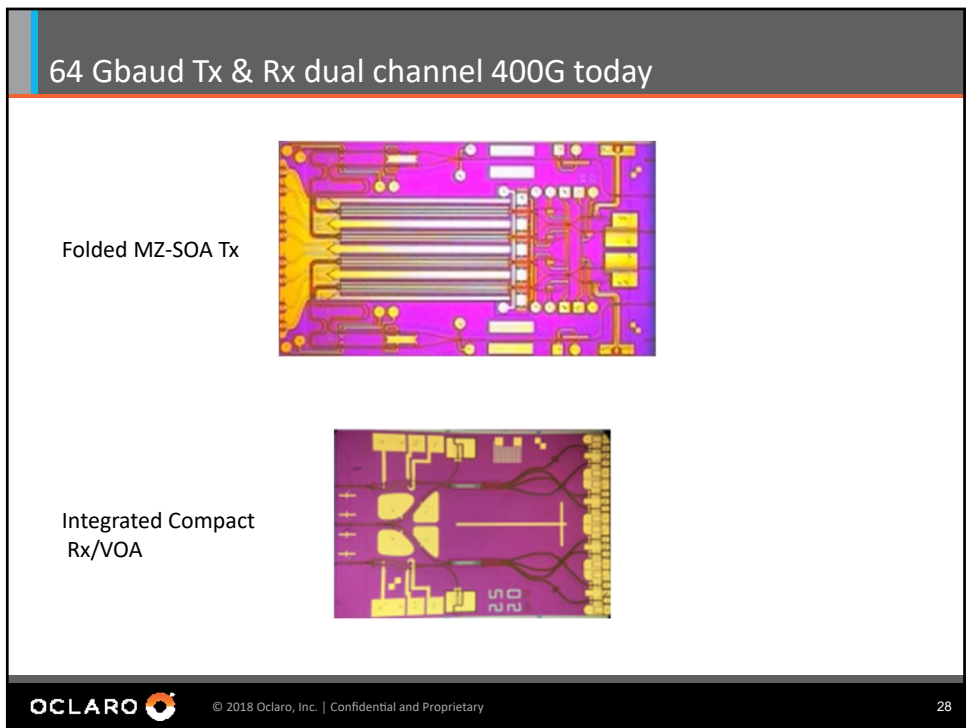
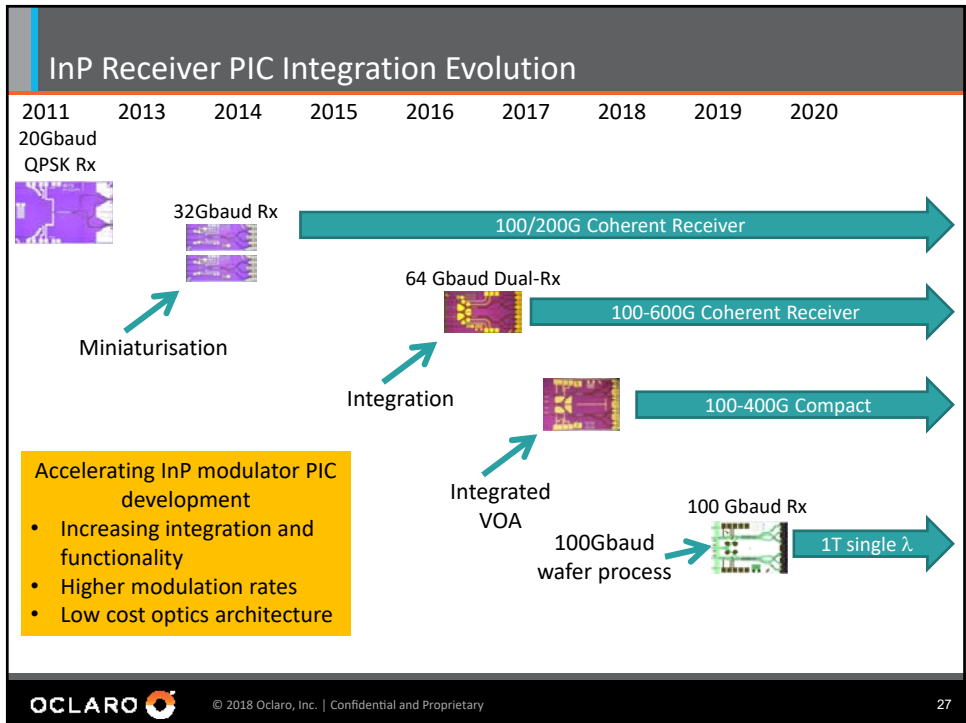
- Conservative estimates for budgetary purpose
- InP PIC + TEC is 3.3W vs. 2.3W for SiP + External Laser: 1W SiP advantage
- SiP solution is disadvantaged by high V_{pp} => high driver power dissipation

| Power dissipation item (max) | InP IC-TROSA Tx PIC + Rx PIC | SiP IC-TROSA TxRx PIC + Laser PIC | Notes |
|------------------------------|------------------------------|-----------------------------------|-------------------------|
| Tx PIC active load (W) | 0.9 | 0.1 | InP case includes laser |
| Tx TEC (W) | 2.4 | 0 | |
| External Laser + TEC (W) | 0 | 2.2 | SiP case only |
| Driver (W) | 1.9 | 3.5 | |
| TIA (W) | 1.1 | 1.1 | |
| Total (W) | 6.3 | 6.9 | maximum |

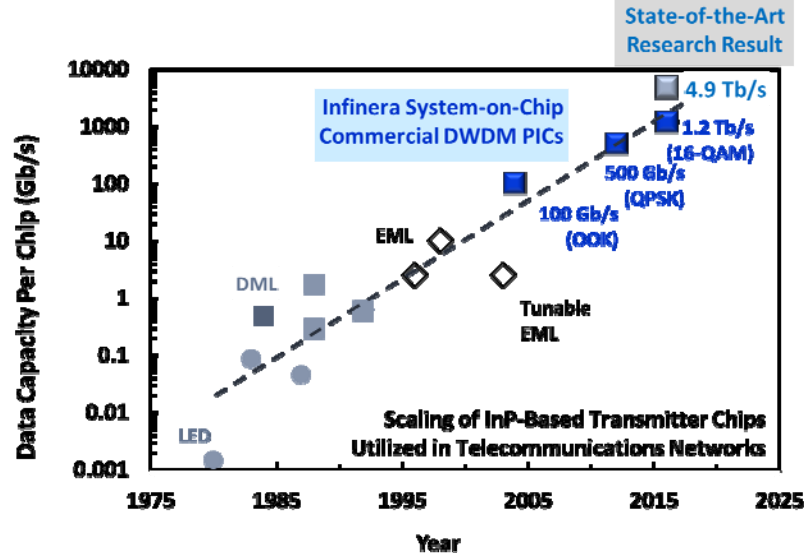
Summary

- As long as laser is temperature sensitive and requires TEC, single PIC solution is unlikely the lowest power dissipation
 - At 1310 may be able to use uncooled laser
- High V_{pi} of SiP modulator is a challenge for driver power dissipation and scaling to higher baud rates
 - SiP modulators may not be good choices within data centers





Data Capacity Scaling in The Network



29 © 2011 Infinera Corporation.



Photonic Module Evolution

Multi-channel DWDM Photonic IC Modules



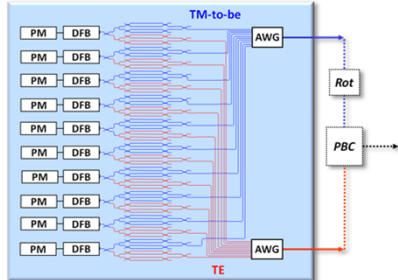
Fig. 21. Scaling of four generations of multi-channel DWDM SOC photonic IC modules. From their first commercial deployment in 2004 to 2016 (12 years), the data capacity of these modules has scaled 24x in roughly the same footprint (images shown to scale).

³⁰ F. Kish, et al, *JSTQE*, 24 (1) 2018

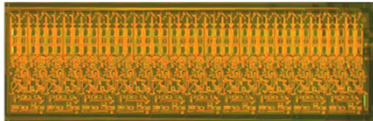


2011: 500 Gb/s PM-QPSK Coherent PICs

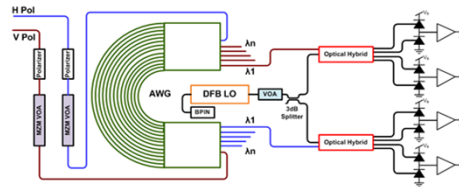
Tx PIC Architecture (5 x 114 Gb/s)



- > 450 Integrated Functions
- 8 Different Integrated Functions



Rx PIC Architecture (5x 114Gb/s)

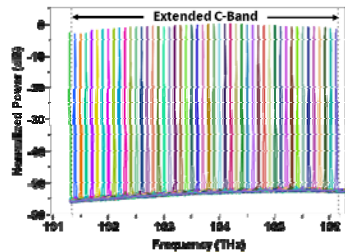
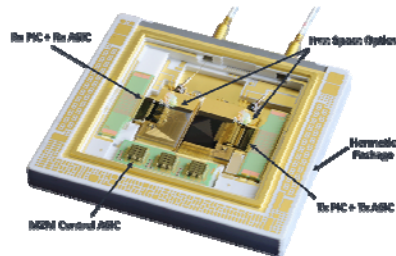


- > 150 Integrated Functions
- 7 Different Integrated Functions

31 © 2011 Infinera Corporation

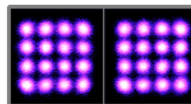
infinera

2016 : 1.2Tbps Extended C-Band tunable coherent 32GBaud/16-QAM coherent Transceiver

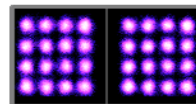


- ▶ 1.2 Tbps, 6-Channel transmitter and receiver PICs in single Module
- ▶ Independent extended C-Band tunable channels
- ▶ 200Gbps per channel (33GBaud/16QAM) capable to 1500km Reach.
- ▶ 44GBaud data rate demonstrated

33GBaud, 16-QAM



44GBaud, 16-QAM



B2B Constellations

32 © 2011 Infinera Corporation

infinera

Back-to-back transmitter constellations on PIC with potential capacity of 4.9 Tb/s

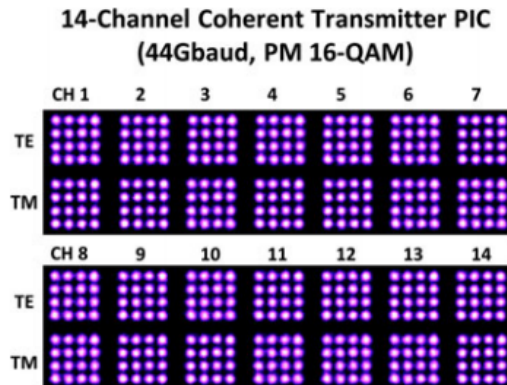


Fig. 19. Back-to-back 44 Gbaud constellations for PM 16-QAM modulation for all 14 channels on a SOC DWDM coherent transmitter PIC (measured using a companion widely tunable multi-channel receiver PIC). The figure shows only the outermost sub-carrier on each polarization for a dual-pol 16-QAM signal. The total capacity of this photonic IC is >4.9 Tb/s.

³³ F. Kish, et al, *JSTQE*, 24 (1) 2018

infinera®

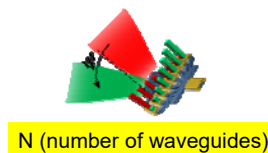
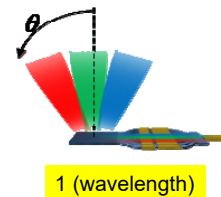
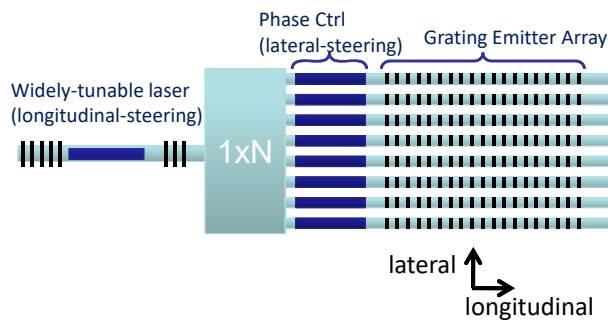
UCSB

2D-Beam Sweeping

DARPA-SWEEPER

MOC 2018

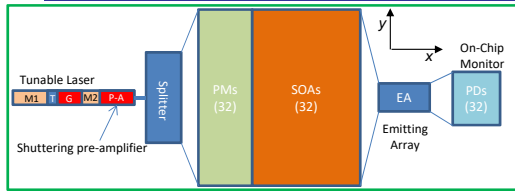
- Our approach: 1D array + grating
- Scaling as $N + 1$, not N^2



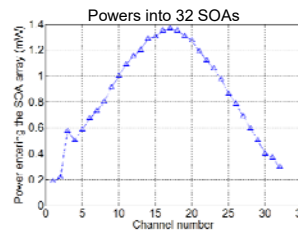
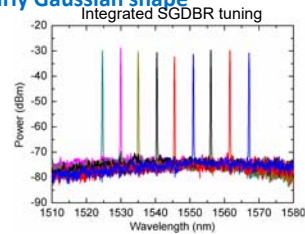
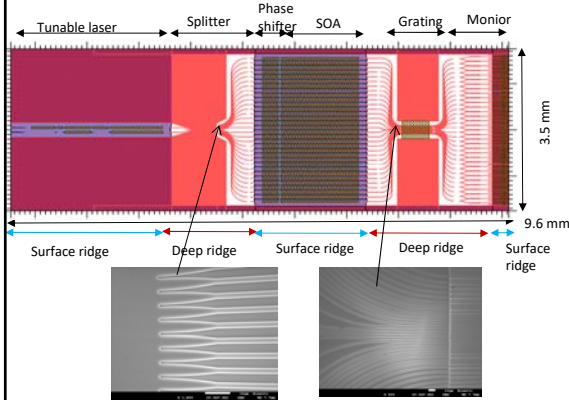
- Lateral beam-steering via phase-shifter array, ψ
- Longitudinal beam-steering via wavelength-tuned grating diffraction, θ

W. Guo, et al, *OFC '13*, Mar. 21, 2013

32 x N: Surface-emitting grating phased-array Optical Beam SWEEPER—InP-PIC



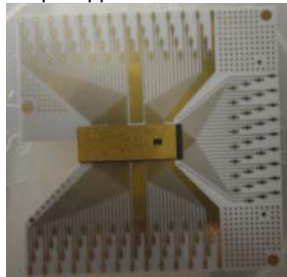
- Waveguide spacing varied to suppress lateral side lobes.
- Grating duty-factor weighted to extend effective length
- Nearly Gaussian shape



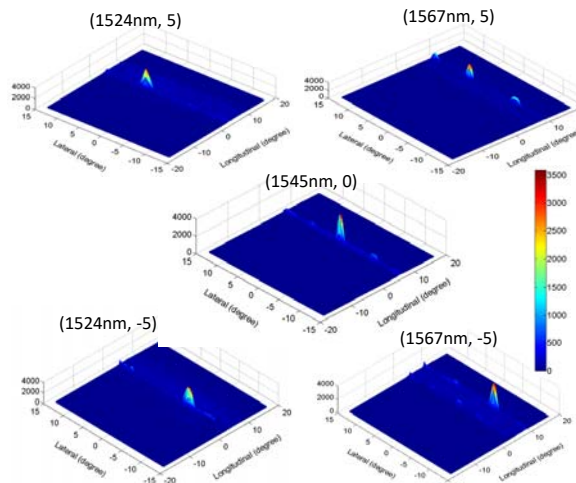
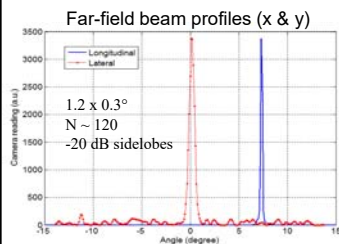
2D Beam Sweeping results (32 x N)

Flip-chipped PIC-on-carrier

- 2D beam steering demonstrated



110 good contacts



W. Guo, et al, OFC '13, Mar., 2013



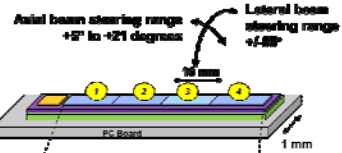
MOABB LIDAR Project (2016→)

Similar sweeping concept, but wider angles & larger arrays + LIDAR

Phase 1 Cell

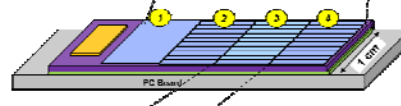
Demonstrates all key building blocks
Demonstrates full operation of 1x10 mm emission aperture cell

- 1 Transceiver
- 2 Spill/Phase Shifters
- 3 Gratings - Emitters
- 4 Phase Monitor



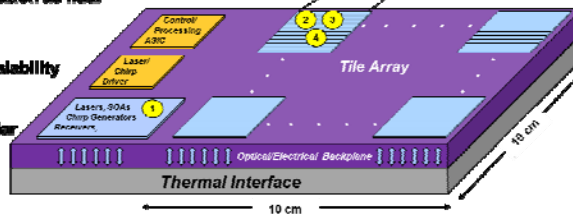
Phase 2 Tile

Demonstrates ability to generate arrays of cells operating as coherent apertures
Demonstrates 16 independent sensing channels
Demonstrates Phase 1 cell operation as lidar



Phase 3 Multi-Tile

Demonstrates large aperture scalability
Stacks PIC layers 2-4 vertically
Integrates PICs, ASSCS in 3D
Demonstrates Phase 2 tile as lidar



UNCLASSIFIED

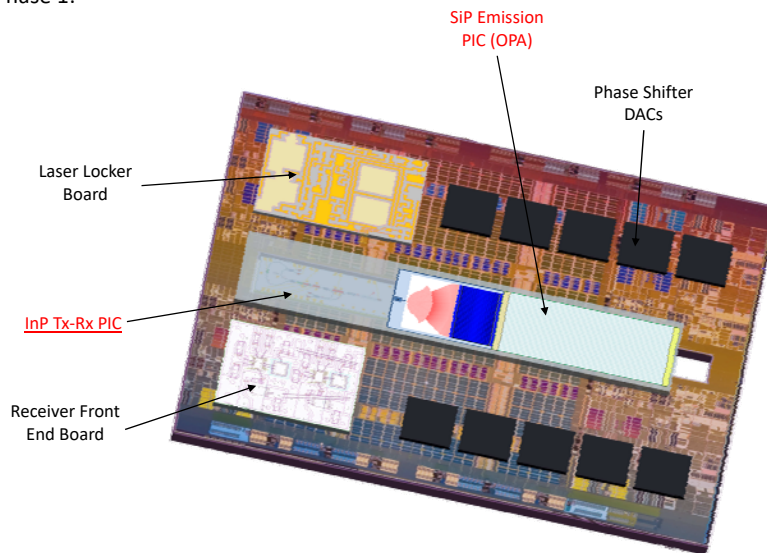
DISTRIBUTION STATEMENT B. Distribution authorized to U.S. Government agencies only. Other requests for this document shall be referred to DARPA.

37



MOABB Mock-up Showing InP and SiP PICs

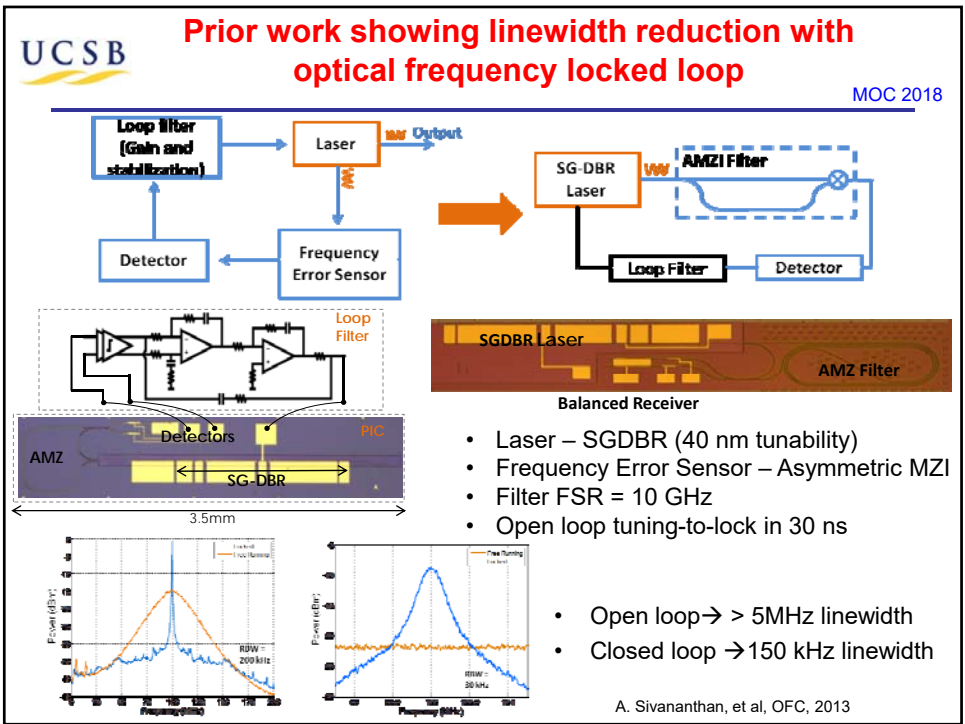
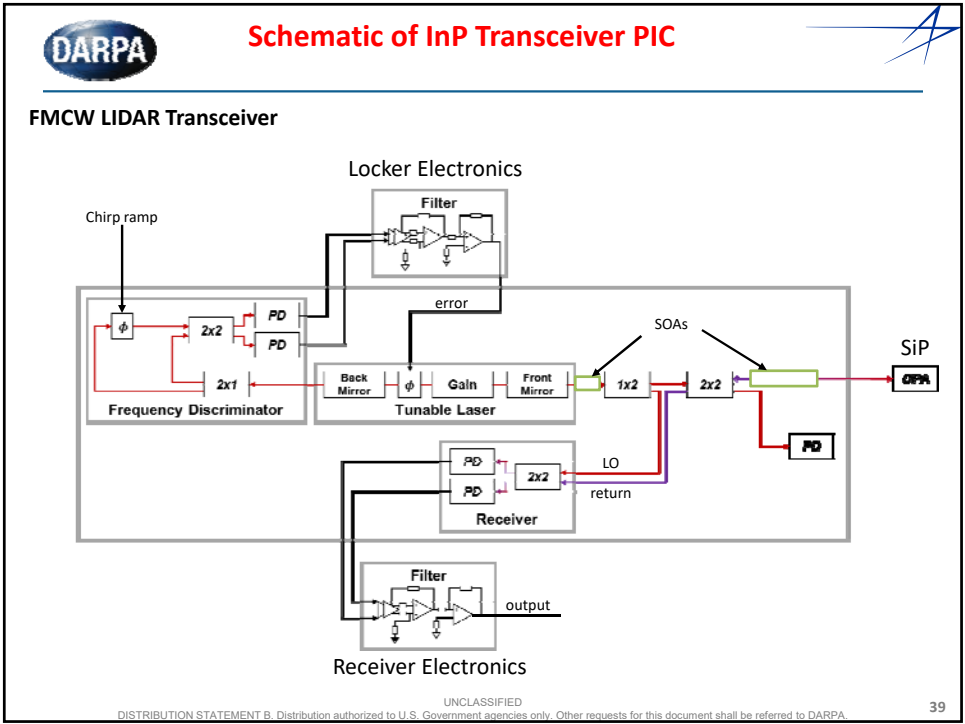
Phase 1:

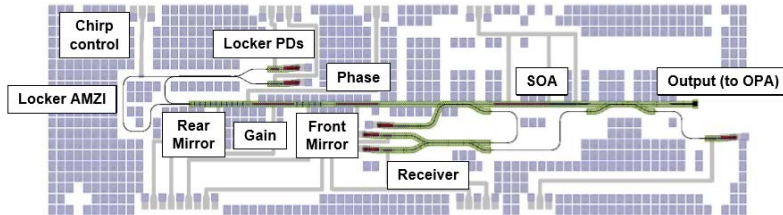


UNCLASSIFIED

DISTRIBUTION STATEMENT B. Distribution authorized to U.S. Government agencies only. Other requests for this document shall be referred to DARPA.

38

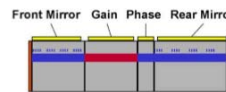




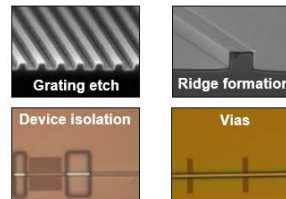
Design features

- ✓ **Fully integrated frontend transceiver**
 - Maximizes coupling between sections, avoids optical isolators
- ✓ **Sampled Grating DBR laser (SGDBR)**
 - Proven widely tunable laser technology
- ✓ **Dual use laser for transmitter and LO**
 - Balanced detection for common mode rejection
- ✓ **Asymmetric Mach-Zehnder interferometer (AMZI) locker**
 - Stabilizes wavelength and provides stable chirp for laser
- ✓ **Integrated semiconductor optical amplifiers (SOAs)**
 - In-situ monitoring, power amplifier, blanking during wavelength tuning, diode-based temperature sensor

Sampled Grating DBR laser

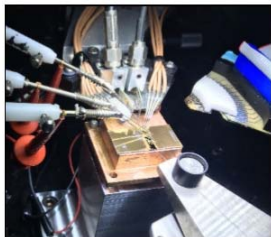


Critical Fabrication steps

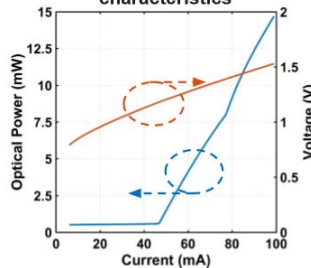


UNCLASSIFIED Distribution Statement B. Distribution authorized to U.S. Government employees only. All other rights reserved. All other rights reserved for the element shall be referred to DARPA.

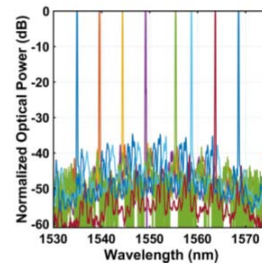
PIC on carrier under test



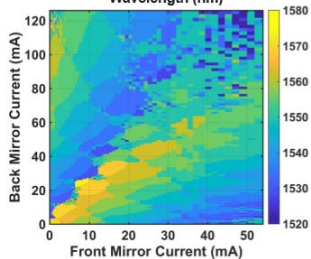
Light-current-voltage characteristics



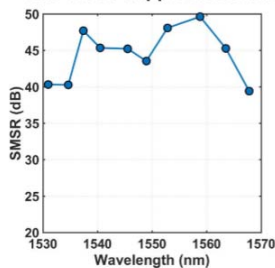
Overlaid lasing spectra



Wavelength tuning map



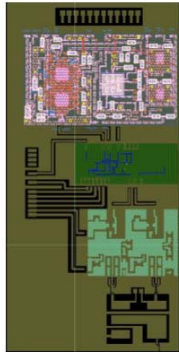
Side-mode suppression ratio



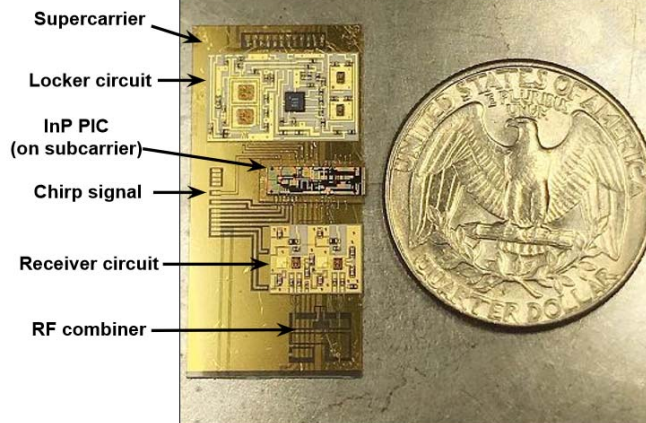
- Custom automated testbeds built for all measurements
- Typical laser performance:
 - Threshold current ~45-70 mA
 - Output power ~15 mW at 100 mA
 - Tuning range ~40 nm
 - SMSR ~40-50 dB
- Maps can provide lookup table for laser tuning

UNCLASSIFIED

Layout



Fabricated Module



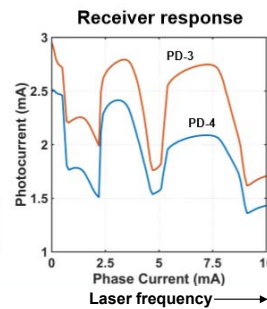
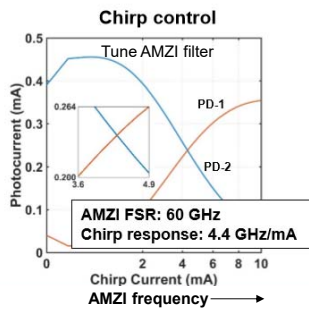
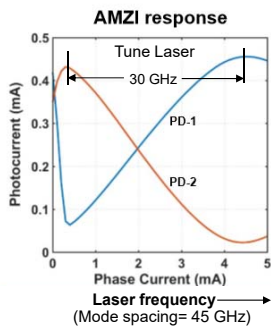
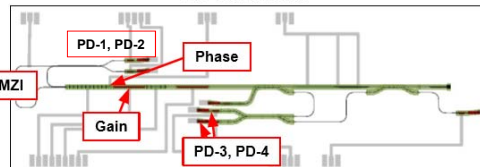
InP transceiver PIC mounted on AlN PIC subcarrier, then mounted on supercarrier with locker and receiver circuits/boards

UNCLASSIFIED

13

- Test 1: Laser and PIC DC characteristics**
 - SOA-1 used to measure laser LI characteristics
 - PD-1 and PD-2 used to measure AMZI response
- Test 2: Locking functionality (Tune laser)**
 - DC bias the laser
 - Sweep phase section and measure AMZI response
- Test 3: Chirp control (Tune filter)**
 - Sweep chirp control current
 - Measure chirp response with PD-1 and PD-2
- Test 4: Receiver functionality**
 - DC bias the laser and sweep phase
 - Measure receiver response with PD-3, PD-4

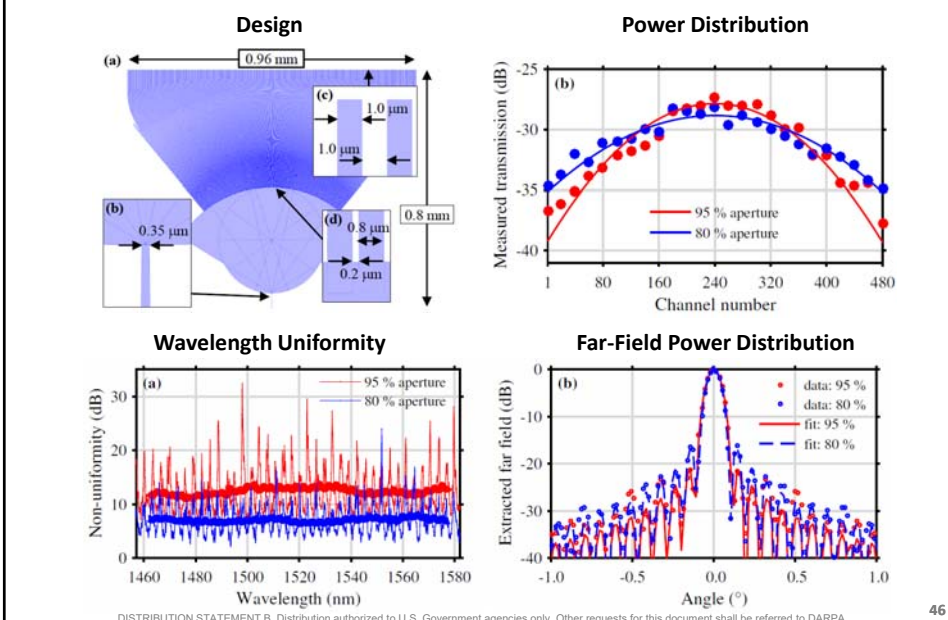
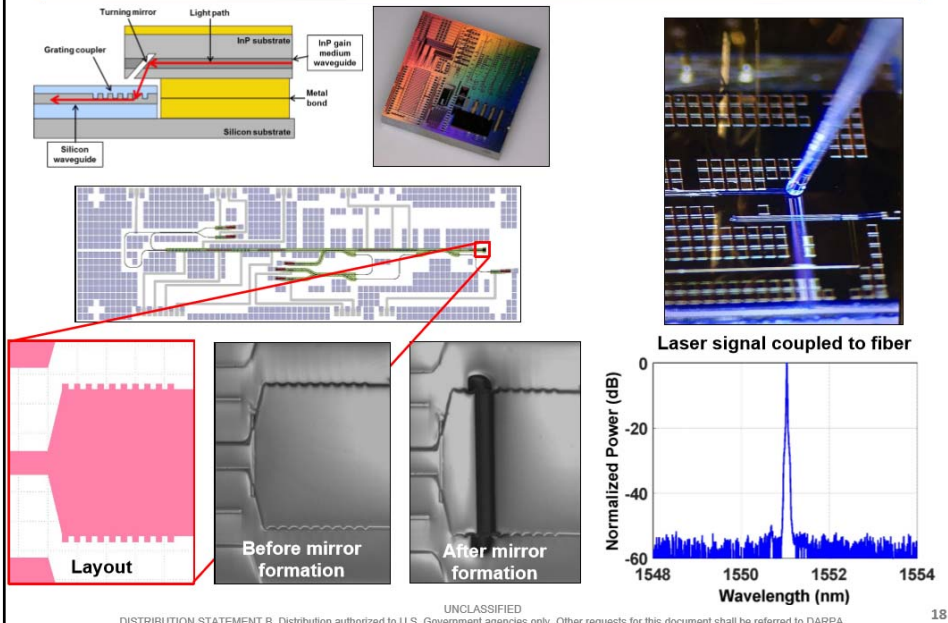
PIC Schematic



UNCLASSIFIED

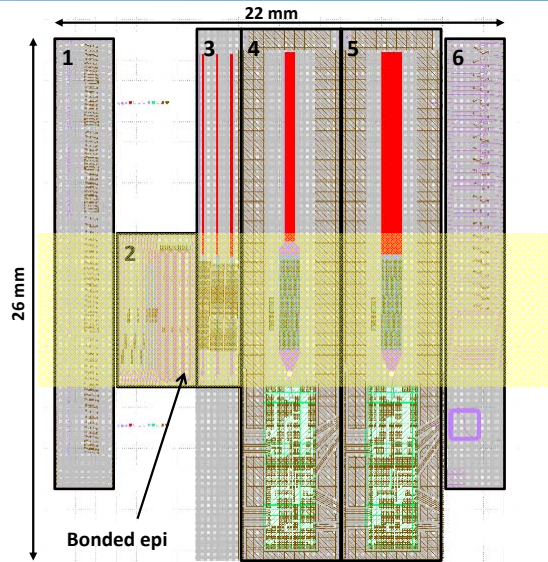
DISTRIBUTION STATEMENT B: Distribution authorized to U.S. Government agencies only. Other requests for this document shall be referred to DARPA.

17

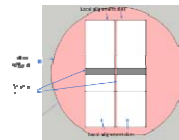




SiP-OPA full-run PIC



1. Deep etch: Directional couplers, ring resonators and loop mirrors test structures
2. Modulator test structures (MZI, loss spiral)
3. 32-channel devices (can be probed)
4. Reduced pitch 240-channel full device (to be bonded to interposer)
5. Standard pitch 240-channel full device (to be bonded to interposer)
6. Shallow etch: Directional couplers, ring resonators and loop mirrors test structures + loss spirals (both etch depths)



6 dies per 4 inch
(100 mm) wafer

UNCLASSIFIED
DISTRIBUTION STATEMENT B. Distribution authorized to U.S. Government agencies only. Other requests for this document shall be referred to DARPA.

47



Take-Aways

MOC 2018

- PICs are desirable for modest to high volume communication and sensing applications, where size, weight, power and cost (SWAP-C) reductions are desired.
- PICs are important because of the inherently stable phase relationships and possibly seamless interfaces between elements.
- PICs generally bring better reliability once properly designed; yield and some aspects of performance may be compromised, although other aspects can be improved.
- Although InP-PICs are currently being produced in higher volume, the use of SiP-PICs is growing more rapidly.

Indium Phosphide Photonic Integrated Circuits: Technology and Applications

Jonathan Klamkin
Electrical and Computer
Engineering Department
University of California Santa
Barbara
Santa Barbara, USA
klamkin@ece.ucsb.edu

Hongwei Zhao
Electrical and Computer
Engineering Department
University of California Santa
Barbara
Santa Barbara, USA
hwzhao@ece.ucsb.edu

Bowen Song
Electrical and Computer
Engineering Department
University of California Santa
Barbara
Santa Barbara, USA
bowen@ece.ucsb.edu

Yuan Liu
Electrical and Computer
Engineering Department
University of California Santa
Barbara
Santa Barbara, USA
yuan.liu@uemail.ucsb.edu

Brandon Isaac
Materials Department
University of California Santa
Barbara
Santa Barbara, USA
brandonjisaac@uemail.ucsb.edu

Sergio Pinna
Electrical and Computer
Engineering Department
University of California Santa
Barbara
Santa Barbara, USA
pinna@ece.ucsb.edu

Fengqiao Sang
Electrical and Computer
Engineering Department
University of California Santa
Barbara
Santa Barbara, USA
fsang@uemail.ucsb.edu

Larry Coldren
Electrical and Computer
Engineering and Department
University of California Santa
Barbara
Santa Barbara, USA
coldren@ece.ucsb.edu

Abstract—A summary of photonic integrated circuit (PIC) platforms is provided with emphasis on indium phosphide (InP). Examples of InP PICs were fabricated and characterized for free space laser communications, Lidar, and microwave photonics. A novel high-performance hybrid integration technique for merging InP devices with silicon photonics is also discussed.

Keywords—photonic integrated circuit, indium phosphide, silicon photonics, silicon nitride, hybrid integration.

I. INTRODUCTION

Photonic integrated circuit (PIC) technology continues to mature and expand in terms of functionality and performance [1]. Although silicon photonics (SiPh) has gained traction and promises low-cost and high-volume production, indium phosphide (InP) continues to be the most popular and advanced PIC platform [2], [3]. Also, currently all SiPh PICs utilize either InP or gallium arsenide (GaAs) lasers for optical sources and rely on external coupling or heterogeneous/hybrid integration.

Silicon nitride (SiN) has also received significant attention as a low-loss passive waveguide PIC platform [4], [5]. Lastly, lithium niobate (LN) continues to be used widely for high-speed modulators for telecommunications.

Figure 1 summarizes the primary PIC platforms illustrating common waveguide geometries used for each. The structure illustrated in Fig. 1(a) is referred to as a ridge or rib waveguide. A common waveguide core is indium gallium arsenide phosphide (InGaAsP) while the cladding material is InP. Depending on layer composition, thickness, and feature size, the waveguide core optical confinement is considered to be moderate for InP. This directly determines the size/compactness of passive components and is also an important consideration for the efficiency of active devices.

InP allows for the integration of all active components including lasers, semiconductor optical amplifiers (SOAs), photodetectors, and modulators. Depending on the complexity of the active-passive integration approach, low passive waveguide loss can also be demonstrated.

SiPh is based on silicon on insulator (SOI) technology and is illustrated in Fig. 1(b). Modulators based on pn junctions and germanium photodetectors have become mainstay active components for SiPh. The most common silicon device layer thickness is 220 nm and the buried oxide (BOX) layer is typically 2-3 μm . This platform is characteristic of very high index contrast (the refractive indices of the silicon core and oxide cladding are approximately 3.5 and 1.5, respectively at a wavelength of 1.55 μm) and therefore passive component sizes are extremely small. Unfortunately, modulation mechanisms in silicon are weak, therefore modulators are large in size despite the high index contrast. SiPh also lacks an inherent laser technology and therefore techniques have been developed to integrate compound semiconductor materials such as InP to provide gain.

SiN can be considered as an alternative to traditional glass waveguide technology that is based on doped silica. This is a passive PIC platform that could rely on hybrid or heterogeneous approaches to closely integrate active components. SiN is used as the core guiding material and silicon dioxide as the cladding material. Thicker waveguide cores (200-400 nm) can realize relatively strong optical confinement and in turn sharp waveguide bends and compact components [6]. Thinner SiN cores (40-100 nm) can realize more loosely confined waveguide modes and extremely low passive loss [7].

The next section will focus on the high-performance InP PIC platform, detailing the variety of components available as well as common active-passive integration techniques therein.

II. INDIUM PHOSPHIDE PICS

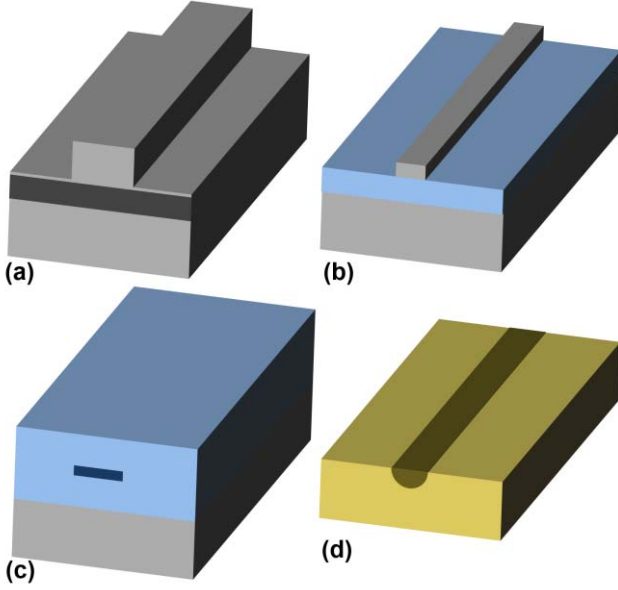


Fig. 1. Summary of PIC platforms: (a) InP, (b) SiPh, (c) SiN, (d) LN.

InP can realize lasers emitting in the common telecommunications bands between 1.26-1.625 μm . Additionally, high-performance modulators and photodetectors can be realized with this material system, therefore it represents an ideal PIC platform to reduce photonic system cost, size, weight and power (CSWaP).

Many InP lasers are based on strained multi-quantum well (MQW) active regions. The laser types that are available include distributed feedback (DFB) and several distributed Bragg reflector (DBR) variants [8]. One of the more mature widely tunable lasers is the sampled grating DBR (SGDBR) laser [9]. To effectively realize such a multi-section DBR

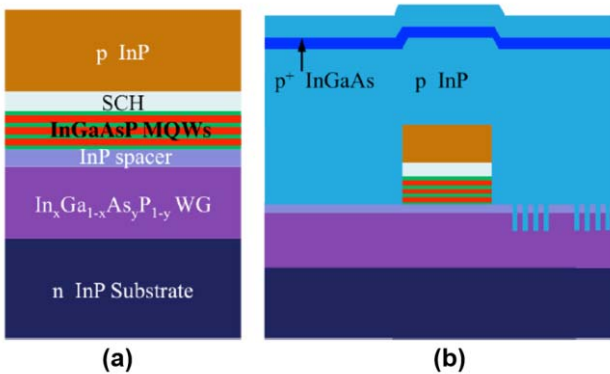


Fig. 2. Illustration of InP OQW PIC platform. (a) Cross section schematic of base epitaxial wafer. (b) Side view schematic after active passive-passive definition, grating formation, and p-cladding regrowth.

laser, an active-passive integration technique is required to selectively form regions for gain and regions that are optically transparent to the laser emission wavelength. The offset quantum well (OQW) platform provides a robust method for achieving this. Figure 2(a) shows a cross section schematic of

the base epitaxial structure whereby the quantum wells are deposited on top of a waveguide core in such a way that the quantum wells are offset spatially from the peak of the waveguide optical mode. For active-passive integration, the

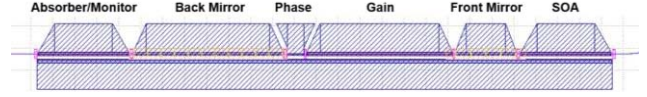


Fig. 3. Layout of multi-section SGDBR laser.

quantum wells are removed selectively. The DBR gratings are etched into the top of the waveguide layer and then the p-InP cladding and p-indium gallium arsenide (InGaAs) contact layers are deposited in a regrowth step. A side view schematic following this step is shown in Fig. 2(b). The remaining fabrication steps include ridge formation, passivation, and metal contact formation.

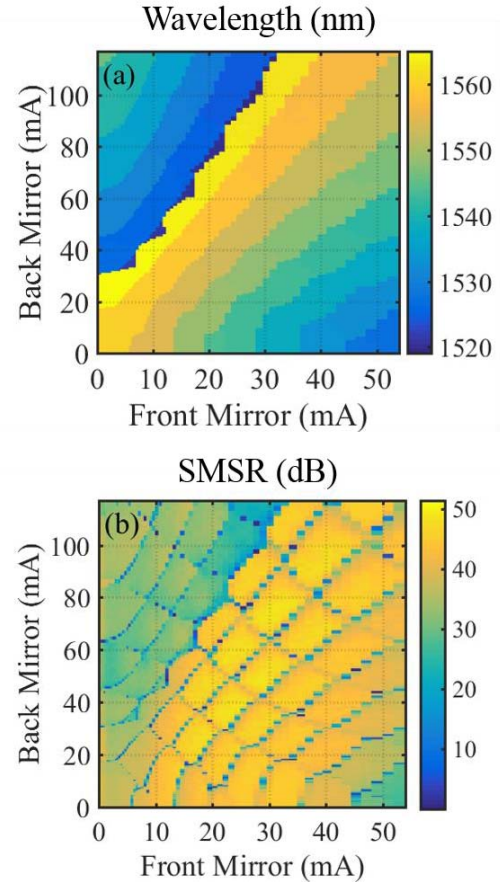


Fig. 4. SGDBR laser wavelength (a) and SMSR (b) as a function of applied back and front mirror currents.

InP PICs were initially developed primarily for telecommunications and have matured substantially due to the steady growth of this industry [10]. Other application areas have leveraged this technology, making use of the abundance of commercial-off-the-shelf (COTS) components. Examples are microwave photonics, and free space laser communications and sensing [11], [12]. These applications

would benefit greatly from PIC technology to reduce system CSWaP. This would allow for more frequent deployments and integration on smaller platforms.

Specifically, for space optical communications, InP PICs have been developed recently with the OQW platform and SGDBR laser sources [13], [14]. A layout schematic of an SGDBR laser is illustrated in Fig. 3. The laser consists

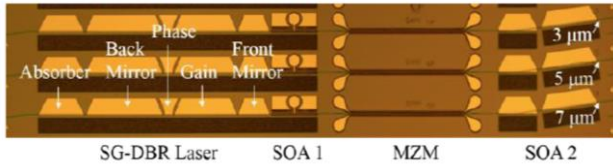


Fig. 5. Microscope images of InP PIC transmitters.

minimally of a gain section, a front SGDBR mirror, a back SGDBR mirror, and a gain section. Also common are to include an output SOA and a back absorber that can be used as a monitor photodetector. These lasers output well above 15 mW of optical power, and the power level is increased with the use of the output SOA. The lasers also tune over more than

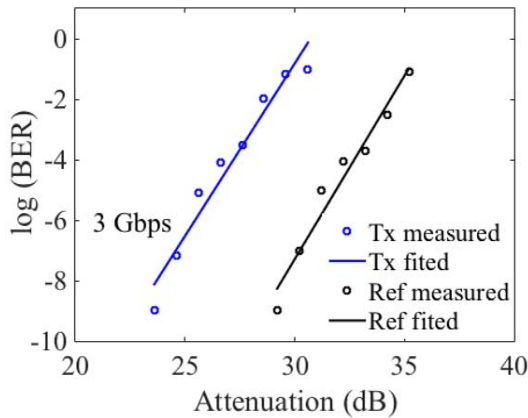


Fig. 6. BER measurements comparing PIC transmitter to reference.

45 nm and demonstrate high side-mode suppression ratio (SMSR) across this tuning range, as illustrated in Fig. 4. For high-speed transmitters, Mach-Zehnder modulators (MZMs) were integrated. The modulation mechanism is based on the Franz-Keldysh effect and utilizes the pn junction formed with the bulk InGaAsP waveguide core. As shown in Fig. 5, additional high-power two-section SOAs were incorporated at the output following the MZMs. The second SOAs in some cases have flared outputs with widths that are 5 μm or 7 μm to increase the saturation power level.

The transmitters were characterized in a free space link. A 3 Gbps non-return-to-zero (NRZ) pseudo random binary sequence (PRBS) was generated and applied to the MZM. The optical signal from the transmitter was collected by a lensed single mode fiber (SMF) and coupled to an optical collimator with a beam divergence angle of 0.016°, and then transmitted through air. At the receiver, an identical collimator collected the light. The distance between the collimators was 1.35 m.

An in-fiber variable optical attenuator (VOA) was used to emulate free space link attenuation. The bit error rate (BER) was measured for the PIC transmitter and compared to a reference consisting of an external cavity laser and high-speed LN modulator. The results are shown in Fig. 6, illustrating error free operation ($\text{BER} < 1 \times 10^{-9}$) for up to approximately 24 dB attenuation (180 m distance). With forward error correction ($\text{BER} < 2 \times 10^{-3}$), the equivalent link length can be up to 300 m (28 dB attenuation). In both cases, with a high-power booster amplifier the link distance can be increased significantly.

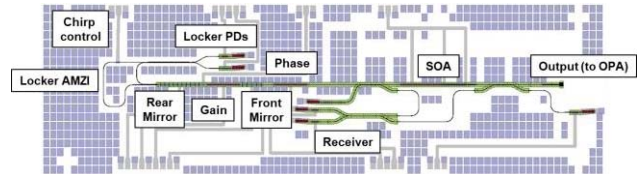


Fig. 7. InP PIC transceiver for beamsteering Lidar.

In addition to free space laser communications, InP PICs can enable a number of other emerging applications including Lidar, microwave photonics, and remote sensing. For some applications, the integration of InP with SiPh is desirable and can also facilitate packaging and electronic-photonic integration. Section III will discuss techniques to integrate InP lasers and PICs, such as those described, with SiPh.

An example of an InP PIC transceiver for a beamsteering Lidar system is shown in Fig. 7. This PIC comprises of a widely tunable SGDBR laser, a frequency discriminator for

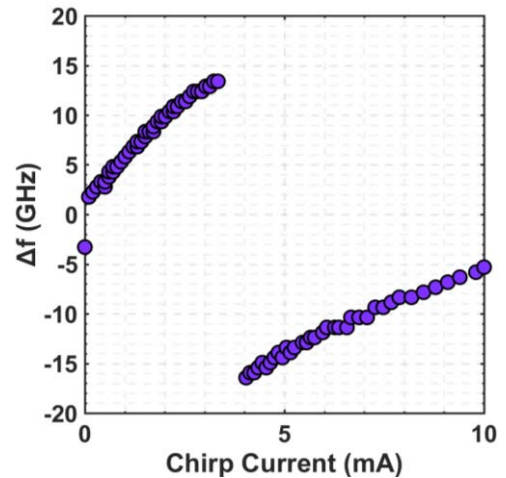


Fig. 8. Demonstration of locking functionality and application of chirp.

wavelength locking/stabilization, and a balanced receiver for coherent detection [15], [16]. This transceiver was designed to drive an optical phased array (OPA) for 3D mapping and other Lidar applications. Light from this PIC would couple to a SiPh circuit that includes a star coupler and a large array of phase shifters and (wavelength-dependent) grating emitters. 2D beam steering is achieved through the combination of the 1D phased array and wavelength tuning. The SGDBR laser is ideal for this application because of its wide tuning range. A frequency discriminator based on an asymmetric Mach-

Zehnder interferometer (AMZI) is used in conjunction with photodiodes (PDs) and an electronic circuit based amplifier/filter that drives the phase section of the laser to stabilize the wavelength between tuning steps. A chirp signal (frequency modulation) can be applied with a phase shifter implemented in one arm of the AMZI to enable a frequency-modulated continuous wave (FMCW) Lidar system. Figure 8 shows measurement results to demonstrate the locking functionality and application of chirp. First the laser is tuned to a specific wavelength using a lookup table (similar to the tuning map illustrated in Fig. 4). Then the AMZI-based locker would stabilize the wavelength, and following this the frequency modulation is generated by applied a small signal to the chirp control. The PIC also contains a balanced receiver that mixes a portion of the on-chip SGDBR laser power (serving as a local oscillator) with the return signal that is coupled through the same OPA.

III. HYBRID INTEGRATION FOR SiPH

For SiPh, several approaches to laser integration have been pursued including monolithic integration by heteroepitaxy, co-packaging, heterogeneous wafer bonding, and hybrid flip-chip

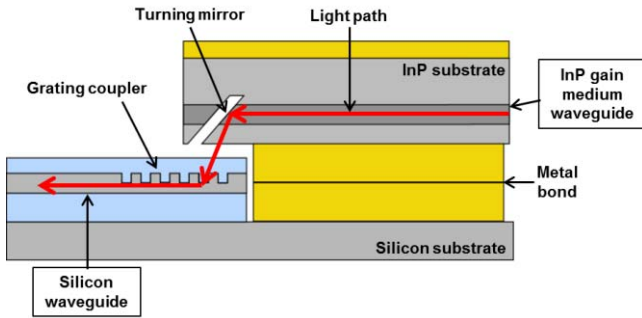


Fig. 9. 3D photonic integration platform.

integration. In addition to employing these techniques for integration of the laser source or sources, they can also enable the integration of full InP PICs on SiPh or SiN interposers. This is desirable for applications requiring the close integration of high-performance PICs with low-loss waveguide passive components, and to facilitate electronic-photonic integration and packaging.

Laser integration by heteroepitaxy of InP, GaAs and related compounds on silicon is promising for large-scale PICs. Although continuous wave (CW) lasing has been demonstrated, there are a number of challenges to overcome to improve reliability [17], [18].

Co-packaging involves the use of bulk optics to couple light from a semiconductor laser chip to a SiPh circuit. This technique has been utilized in industry [19]. It is advantageous because it allows for the use of qualified laser chips, but requires somewhat expensive assembly processes. This is also characteristic of limited scalability.

Heterogeneous approaches are based on wafer bonding and subsequent co-fabrication [20]. Typically, InP chiplets are bonded, the InP substrate is removed, and then mesas pin diode structures are fabricated to facilitate electrically pumped lasing.

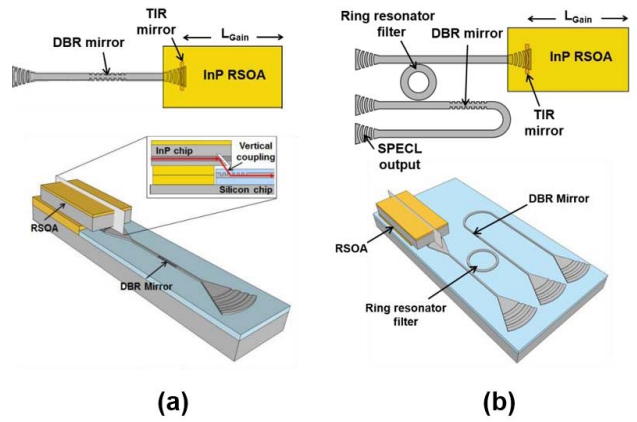


Fig. 10. SPECL with a DBR mirror only (a) and with both a DBR mirror and intra-cavity ring resonator filter (b).

The co-fabrication likely requires utilization of a silicon facility for the underlying SOI waveguide formation, and a separate facility for the InP fabrication. This platform does not require precision alignment of the InP chips for bonding. In addition to lasers and SOAs, the InP chiplets can be used for other active components including modulators and photodetectors, both of which arguably outperform their silicon counterpart. Although this technique is promising, co-fabrication is expensive and the performance is limited. Thick SOI waveguides are required to ensure coupling from the InP, as is a thick BOX layer for preventing substrate leakage. The BOX layer thermally isolates the InP active region leading to a high internal temperature under operation and low laser efficiency. Lastly, the mismatch in coefficient of thermal expansion potentially poses reliability issues [21].

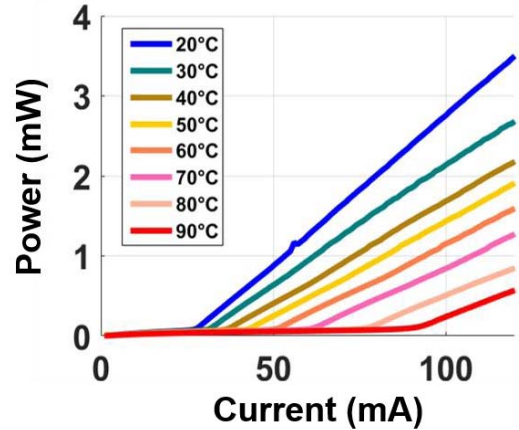


Fig. 11. Light-current characteristics for 3D hybrid laser at various operating temperatures.

Hybrid integration involves the close integration of separate laser chips and SiPh circuits [22]. In some cases, other intermediate chip-scale optics can be integrated on chip including isolators [23]. As for co-packaging, hybrid integration also uses fully fabricated laser chips, albeit perhaps with some customization, and avoids co-fabrication of dissimilar materials. Flip-chip integration can overcome

thermal issues since the InP chip can be directed bonded (or nearly directly bonded) to the silicon substrate, ensuring effective extraction of heat from the active region and dissipation into the highly thermally conductive silicon. A primary concern for planar butt-coupling of InP to SiPh is the alignment precision required because planar laser diodes are characteristic of large angular beam divergence, especially in the vertical direction [24]. The 3D hybrid integration approach overcomes some of these issues [25]. As illustrated in Fig. 7, InP devices (lasers or PICs) with fabricated with total internal reflection (TIR) turning mirrors to incorporate surface emission into the planar device. This is then flip-chip bonded to the

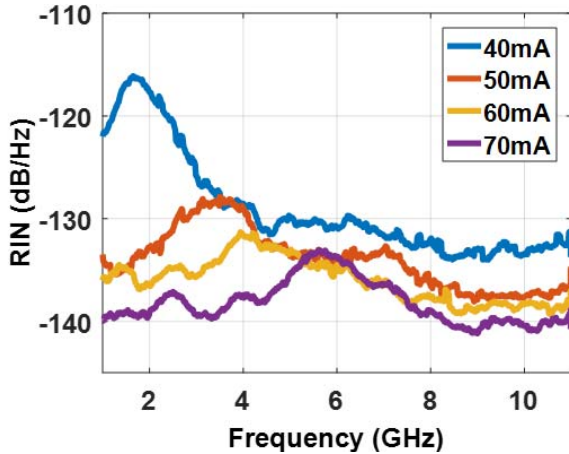


Fig. 12. RIN spectra for 3D hybrid laser at various operating current.

silicon and light is coupled into the SOI waveguide through a surface grating coupler, which is commonly employed for fiber coupling.

With this technology, either a standalone laser can be integrated, or a gain element can be integrated. For the latter, a reflective SOA (RSOA) can be integrated to provide gain, and feedback/filtering elements can be formed in the SiPh. Figure 8 depicts two types of such silicon photonic external cavity lasers (SPECLs), one that includes a single DBR mirror in the silicon, and the other that includes both a DBR mirror and an intracavity ring resonator filter [26]. Both lasers demonstrate single-mode lasing and some tunability because the DBRs and ring resonators in silicon include micro-heaters for thermal tuning.

Since the RSOAs were flip-chip bonded p-side down directly to the silicon substrate, heat generated in the InP active region is extracted effectively and dissipated in the silicon. In addition to perform thermal simulations to demonstrate this, an experiment was conducted to compare an InP device bonded to the top oxide cladding (and thermally isolated from the silicon substrate), to one bonded directly to the silicon. The latter demonstrated a thermal impedance that was a factor of three lower. Additionally, as illustrated in Fig. 9, these lasers operated at high temperature with an efficiency that is not severely degraded. Lastly, to provide an initial investigation into laser performance for communications applications, the relative intensity noise (RIN) was measured for a SPECL and the results are shown in Fig. 10. The RIN was less than -135 dB/Hz for a drive current of 70 mA.

Hybrid integration generally can also be leveraged to integrate not only lasers and SOAs, but also complex InP PICs such as those described in the previous section, and other high-performance active devices such as PDs. Figure 13 illustrates a concept for an optical beam forming network (OBFN) chip for high-frequency wireless communications and phased arrays

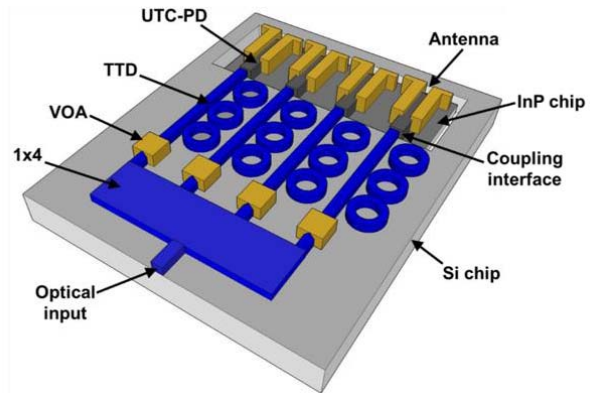


Fig. 13. OBFN chip concept.

[27]. For wireless, photonics is attractive for its broad bandwidth and immunity to electromagnetic interference [28]. The OBFN chip concept comprises all of the components required for signal generation, distribution, and radiation. The distribution network is based on an array of true time delay (TTD) elements for beamsteering to eliminate the beam squint issue associated with RF phase shifters. This TTD technology is now well developed and has been implemented on low-loss waveguide platforms on silicon [4], [29], [30]. Critical to such a system are the high-speed PDs required for mixing optical signals to generate the high-frequency signal to be radiated from the phased array antenna. InP-based uni-traveling-carrier photodiodes (UTC-PDs) are most ideal for this application for their ability to generate reasonable power levels while maintaining millimeter wave (mmW) class bandwidth and beyond [31], [32], [33]. To enable integration of such PDs with low-loss waveguides on silicon, as desired for the integrated OBFN concept, UTC-PDs were developed for integration with spot-size converters (SSCs) to enable hybrid integration and high efficiency coupling. Preliminary results have demonstrated 3-dB bandwidth as high as 67 GHz and 50 Gb/s on-off keying (OOK) operation. Future work will be focused on increasing the bandwidth and data rate further, as well as the hybrid integration of these PDs on silicon.

IV. CONCLUSIONS

InP PIC technology has been reviewed and some examples were described in detail, including a PIC transmitter for free space optical communications and a PIC transceiver for Lidar. A novel 3D hybrid integration approach was also discussed in the context of InP laser and PIC integration on SiPh. And lastly, a concept for integrating high-performance InP PDs for mmW communications and phase arrays was discussed.

ACKNOWLEDGMENT

The authors acknowledge the NASA Space Technology Mission Directorate (STMD) for support.

REFERENCES

- [1] Y. A. Vlasov, "Silicon CMOS-integrated nano-photonics for computer and data communications beyond 100G," *IEEE Communications Magazine*, vol. 50, no. 2, pp. s67-s72, 2012.
- [2] V. Lal, et al., "Extended C-Band Tunable Multi-Channel InP-Based Coherent Transmitter PICs," vol. 35, no. 7, pp. 1320-1327, 2017.
- [3] S. Arafin, L. A. Coldren, "Advanced InP Photonic Integrated Circuits for Communication and Sensing," *IEEE Journal of Selected Topics in Quantum Electronics*, vol. 24, no. 1, 2018.
- [4] Y. Liu, A. Wichman, B. Isaac, J. Kalkavage, E. Adles, J. Klamkin, "Ring Resonator Delay Elements for Integrated Optical Beamforming Networks: Group Delay Ripple Analysis," *Integrated Photonics Research, Silicon and Nanophotonics Conference*, paper IW1B.3, 2016.
- [5] C. G. H. Roeloffzen, L. Zhuang, C. Taddei, A. Leinse, R. G. Heideman, P. W. L. van Dijk, R. M. Oldenbeuving, D. A. I. Marpaung, M. Burla, K. -J. Boller, "Silicon nitride microwave photonic circuits," *Optics Express*, vol. 21, no. 19, pp. 22937-22961, 2013.
- [6] S. Dwivedi, B. Song, Y. Liu, R. Moreira, L. Johansson, J. Klamkin, "Demonstration of compact silicon nitride grating coupler arrays for fan-out of multicore fibers," *Conference on Lasers and Electro-Optics*, paper AT3B.4, 2017.
- [7] J. F. Bauters, M. J. R. Heck, D. D. John, J. S. Barton, C. M. Bruinink, A. Leinse, R. G. Heideman, D. J. Blumenthal, J. E. Bowers, "Planar waveguides with less than 0.1 dB/m propagation loss fabricated with wafer bonding," *Optics Express*, vol. 19, no. 24, pp. 24090-24101, 2011.
- [8] L. A. Coldren, S. W. Corzine, M. L. Masanovic, *Diode Lasers and Photonic Integrated Circuits*. Hoboken, NJ: John Wiley & Sons, 2012.
- [9] L. A. Coldren, G. A. Fish, Y. Akulova, J. S. Barton, L. Johansson, C. W. Coldren, "Tunable Semiconductor Lasers: A Tutorial," *Journal of Lightwave Technology*, vol. 22, no. 1, pp. 193-202, 2004.
- [10] T. L. Koch, U. Koren, "InP-based photonic integrated circuits," *IEEE Proceedings*, vol. 138, no. 2, pp. 139-147, 1991.
- [11] S. Iezekiel, M. Burla, J. Klamkin, D. Marpaung, J. Capmany, "RF Engineering Meets Optoelectronics: Progress in Integrated Microwave Photonics," *IEEE Microwave Magazine*, vol. 16, no. 8, 2015.
- [12] V. W. S. Chan, "Free-Space Optical Communications," *Journal of Lightwave Technology*, vol. 24, no. 12, pp. 4750-4762, 2006.
- [13] H. Zhao, S. Pinna, B. Song, L. Megalini, S. T. Suran Brunelli, L. Coldren, J. Klamkin, "Indium Phosphide Photonic Integrated Circuits for Free Space Optical Links," *IEEE Journal of Selected Topics in Quantum Electronics*, 2018.
- [14] H. Zhao, S. Pinna, B. Song, L. Megalini, S. T. Suran Brunelli, L. Coldren, J. Klamkin, "High-Power Integrated Indium Phosphide Transmitter for Free Space Optical Communications," *Conference on Lasers and Electro-Optics*, paper JW2A.52, 2018.
- [15] B. Isaac, B. Song, S. Pinna, S. Arafin, L. Coldren, J. Klamkin, "Indium Phosphide Photonic Integrated Circuit Transmitter with Integrated Linewidth Narrowing for Laser Communications and Sensing," *International Semiconductor Laser Conference*, 2018.
- [16] Y. Zhang, Y. -C. Ling, Y. Zhang, K. Shang, S. J. Ben Yoo, "High-Density Wafer-Scale 3-D Silicon-Photonic Integrated Circuits," *IEEE Journal of Selected Topics in Quantum Electronics*, vol. 24, no. 6, 2018.
- [17] L. Megalini, B. Bonef, B. C. Cabinian, H. Zhao, A. Taylor, J. S. Speck, J. E. Bowers, J. Klamkin, *Appl. Phys. Lett.* 111, 032105, 2017.
- [18] S. Chen, W. Li, J. Wu, Q. Jiang, M. Tang, S. Shutts, S. N. Elliott, A. Sobiesierski, A. J. Seeds, I. Ross, P. M. Smowton, H. Liu, "Electrically pumped continuous-wave III-V quantum dot lasers on silicon," *Nature Photonics*, vol. 10, pp. 307-311, 2016.
- [19] T. Pinguet, P. M. De Dobbelaere, D. Foltz, S. Gloeckner, S. Hovey, Y. Liang, M. Mack, G. Masini, A. Mekis, M. Peterson, T. Pinguet, S. Sahni, J. Schramm, M. Sharp, L. Verslegers, B. P. Welch, K. Yokoyama, S. Yu, "25 Gb/s silicon photonic transceivers," *International Conference on Group IV Photonics*, 2012.
- [20] A. W. Fang, H. Park, O. Cohen, R. Jones, M. J. Paniccia, J. E. Bowers, "Electrically pumped hybrid AlGaInAs-silicon evanescent laser," *Optics Express*, vol. 14, no. 20, pp. 9203-9210, 2006.
- [21] B. Song, L. Megalini, S. Dwivedi, S. Ristic, J. Klamkin, "High-Thermal Performance 3D Hybrid Silicon Lasers," *IEEE Photonics Technology Letters*, vol. 29, no. 14, pp. 1143-1146, 2017.
- [22] A. Rickman, "The commercialization of silicon photonics," *Nature Photonics*, vol. 8, pp. 79-82, 2014.
- [23] M. Mazzini, M. Traverso, M. Webster, C. Muzio, S. Anderson, P. Sun, D. Siadat, D. Conti, A. Cervasio, S. Pfnuer, J. Stayt, M. Nyland, C. Togami, K. Yanushefski, T. Daugherty, "25GBaud PAM-4 error free transmission over both single mode fiber and multimode fiber in a QSFP form factor based on silicon photonics," *Optical Fiber Communications Conference*, 2015.
- [24] N. Kobayashi, K. Sato, M. Namiwaka, K. Yamamoto, S. Watanabe, T. Kita, H. Yamada, and H. Yamazaki, "Silicon Photonic Hybrid Ring-Filter External Cavity Wavelength Tunable Lasers," *J. Lightwave Technol.*, vol. 33, no. 6, pp. 1241-1246, Mar. 2015.
- [25] B. Song, C. Stagarescu, S. Ristic, A. Behfar, J. Klamkin, "3D integrated hybrid silicon laser," *Optics Express*, vol. 24, no. 10, pp. 10435-10444, 2016.
- [26] B. Song, Y. Liu, S. Ristic, J. Klamkin, "Tunable 3D hybrid integrated silicon photonic external cavity laser," *Conference on Lasers and Electro-Optics*, paper AM4A.3, 2017.
- [27] J. A. Nanzer, A. Wichman, J. Klamkin, T. P. McKenna, T. R. Clark, "Millimeter-Wave Photonic for Communications and Phased Arrays," *Fiber and Integrated Optics*, vol. 34, no. 4, pp. 159-174, 2015.
- [28] G. Choo, C. K. Madsen, S. Palermo, K. Entesari, "Automatic Monitor-Based Tuning of RF Silicon Photonic True-Time-Delay Beamforming Networks," *IEEE/MTT-S International Microwave Symposium*, 2018.
- [29] Y. Liu, A. R. Wichman, B. Isaac, J. Kalkavage, T. R. Clark, J. Klamkin, "Ultra-Low-Loss Silicon Nitride Optical Beamforming Network for Wideband Wireless Applications," *IEEE Journal of Selected Topics in Quantum Electronics*, vol. 24, no. 4, 2018.
- [30] Y. Liu, A. R. Wichman, B. Isaac, J. Kalkavage, T. R. Clark, J. Klamkin, "Tuning Optimization of Ring Resonator Delays for Integrated Optical Beam Forming Networks," *Journal of Lightwave Technology*, vol. 35, no. 22, pp. 4954-4960, 2017.
- [31] J. Klamkin, A. Ramaswamy, L. A. Johansson, H. -F. Chou, M. N. Sysak, J. W. Raring, N. Parthasarathy, S. P. DenBaars, J. E. Bowers, L. A. Coldren, "High Output Saturation and High-Linearity Uni-Traveling-Carrier Waveguide Photodiodes," *IEEE Photonics Technology Letters*, vol. 19, no. 3, 2007.
- [32] Z. Li, H. Pan, H. Chen, A. Beling, J. C. Campbell, "High-Saturation-Current Modified Uni-Traveling-Carrier Photodiode With Cliff Layer," *IEEE Journal of Quantum Electronics*, vol. 46, no. 5, pp. 626-632, 2010.
- [33] B. Isaac, Y. Liu, B. Song, X. Xie, A. Beling, J. Klamkin, "Hybrid Integration of UTC-PDs on Silicon Photonics," *Conference on Lasers and Electro-Optics*, paper SM4O.1, 2017.

I. Photonic Integrated Circuits

B. Low-Power Optical-Phase-Locked Loops

Evolution of Chip-Scale Heterodyne Optical Phase-Locked Loops Toward Watt Level Power Consumption

Arda Simsek¹, Student Member, IEEE, Shamsul Arafin², Senior Member, IEEE, Seong-Kyun Kim³, Gordon B. Morrison, Leif A. Johansson, Member, IEEE, Milan L. Mashanovitch, Senior Member, IEEE, Larry A. Coldren, Life Fellow, IEEE, Fellow, OSA⁴, and Mark J. W. Rodwell, Fellow, IEEE

(Top-Scored Paper)

Abstract—We design and experimentally demonstrate two chip-scale and agile heterodyne optical phase-locked loops (OPLLs) based on two types of InP-based photonic-integrated coherent receiver circuits. The system performance of the first-generation OPLL was improved in terms of offset-locking range, and power consumption with the use of a power efficient and compact photonic-integrated circuit (PIC). The second-generation PIC consists of a 60-nm widely tunable Y-branch laser as a local oscillator with a 2×2 multimode interference (MMI) coupler and a pair of balanced photodetectors. This PIC consumes only 184-mW power in full operation, which is a factor of 3 less compared to the first-generation PIC. In addition, the sensitivity of these OPLLs was experimentally measured to be as low as $20 \mu\text{W}$. A possible solution to increase the sensitivity of these OPLLs is also suggested.

Index Terms—Heterodyne, integrated optics, optical phase-locked loop, photonic integrated circuits.

I. INTRODUCTION

OPTICAL phase-locked loops (OPLLs) have been of great interest for the last couple of decades due to the promising applications in the areas of communications, sensing and frequency control [1], [2]. These applications include short to medium range coherent optical communications [3], laser linewidth narrowing [4]–[6], terahertz signal generation [6], [7] and optical frequency synthesis [8]–[11]. With the improvements in the photonic integration, OPLLs became more attractive since they can offer small loop delay, which allows having OPLLs with loop bandwidths as large as 1.1 GHz [3]. However, these prior OPLLs consume almost 3 Watts of electrical power

[3]. This high-power consumption makes the use of OPLLs in practical applications questionable.

Therefore, realizing a low-power consumption OPLL is important to take advantage of recent advances in photonic integration. A chip-scale, compact, low power consumption OPLL can push the technology in the aforementioned application areas further forward. With the proper design of compact photonic integrated circuits (PICs), power consumption in such PICs, therefore OPLLs, can be lowered [12]. In this work, two chip-scale, highly-integrated OPLLs are designed and experimentally demonstrated using two different InP-based photonic integrated coherent receiver circuits.

After successfully achieving OPLLs with a reasonable offset locking range and low-power consumption, a detailed sensitivity analysis and some relevant experiments were performed. A minimum input optical power to demonstrate the phase-locking using our OPLLs was measured as $20 \mu\text{W}$ both theoretically and experimentally. A novel solution is proposed that can be implemented in such OPLLs in order to lock input power levels as low as nanowatts.

This paper is organized as follows. This paper begins with a short summary of OPLL system design together with the PIC design. We then present the experimental results for the first, and second generation OPLL. After this, the power budget for both OPLLs is given. Finally, the sensitivity analysis and a proposed solution for high sensitivity OPLL is provided.

II. OPTICAL PHASE-LOCKED LOOP SYSTEM DESIGN

A. PIC Design

Since two different types of PICs are used in this study for demonstrating heterodyne OPLLs, we have named them as gen-1 and gen-2 PICs for clarity. All active/passive components in these PICs are monolithically integrated on an InGaAsP/InP material platform. Details of the fabrication of such PICs can be found in [13], [14]. Microscope images of both PICs are shown in Fig. 1(a) and (b).

Out of two PICs, gen-1 PIC (see Fig. 1(a)) consists of 40 nm widely-tunable sampled-grating distributed-Bragg-

Manuscript received July 1, 2017; revised August 23, 2017 and September 16, 2017; accepted September 25, 2017. Date of publication October 1, 2017; date of current version February 24, 2018. This work was supported in part by the DARPA-MTO under the DODOS Project and in part by the National Science Foundation under Grant 1402935. (Corresponding author: Arda Simsek.)

A. Simsek, S. Arafin, L. A. Coldren, and M. J. W. Rodwell are with the Department of Electrical and Computer Engineering, University of California Santa Barbara, Santa Barbara, CA 93106 USA (e-mail: ardasimsek@ece.ucsb.edu; sarafin@ece.ucsb.edu; coldren@ece.ucsb.edu; rodwell@ece.ucsb.edu).

S.-K. Kim is with Teledyne Scientific and Imaging Company, Thousand Oaks, CA 91360 USA (e-mail: skkim910@gmail.com).

G. B. Morrison, L. A. Johansson, and M. L. Mashanovitch are with Freedom Photonics, LLC, Santa Barbara, CA 93117 USA (e-mail: gordon@freedomphotonics.com; leif@ece.ucsb.edu; mashan@ece.ucsb.edu).

Color versions of one or more of the figures in this paper are available online at <http://ieeexplore.ieee.org>.

Digital Object Identifier 10.1109/JLT.2017.2758744

U.S. Government work not protected by U.S. copyright.

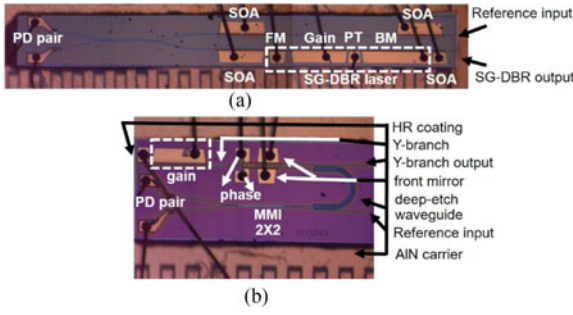


Fig. 1. (a) Microscope image of the gen-1 InP based PIC. (b) Microscope image of low power consumption gen-2 InP based PIC. (BM: back mirror, FM: front mirror, PD: photodiode, PT: phase tuner, SG-DBR: sampled-grating distributed-Bragg-reflector, and SOA: semiconductor optical amplifier.)

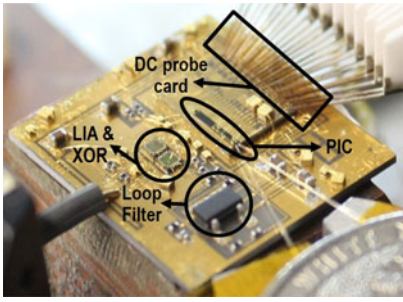


Fig. 2. OPLL system under measurement setup integrated on an AIN carrier including gen-1 PIC and control electronics.

reflector (SG-DBR) laser, 2×2 multimode interference (MMI) coupler, a balanced photodetector pair and a couple of semiconductor optical amplifiers (SOAs) on reference and local-oscillator (LO) optical paths. Reference optical signal was coupled into this PIC using the upper arm and amplified by two SOAs. SG-DBR laser output propagated in the lower arm. These two optical signals were combined in a 2×2 MMI coupler and mixed in a balanced photodetector pair to produce the beat note for the electronics part. The SG-DBR laser also has a second output from its backside for monitoring purposes.

Gen-2 PIC (see Fig. 1(b)) was designed for low power consumption. This PIC incorporates a widely tunable, compact Y-branch laser, formed between a high-reflectivity coated back cleaved mirror and a pair of Vernier tuned sampled-grating front mirrors, as well as a 2×2 MMI coupler and a balanced photodetector pair. The optical output from one of the front mirrors was connected to the MMI coupler, while the other output from another front mirror was used externally for monitoring the OPLL operation. The Y-branch laser has a compact cavity with short gain and mirror sections, requiring low current and therefore low drive power. It is tuned via Vernier effect and has been designed for high efficiency at 30 °C. The measured tuning range exceeds 60 nm with >50 dB side-mode suppression ratio [15].

B. Feedback Electronics Design and OPLL Assembly

Both OPLLs use SiGe (Silicon Germanium) based commercial-off-the-shelf (COTS) electronic ICs and loop filters built from discrete components as the control electronics. Fig. 2 shows an exemplary OPLL system assembled by mounting gen-1 PIC and electronic components on a patterned AIN carrier.

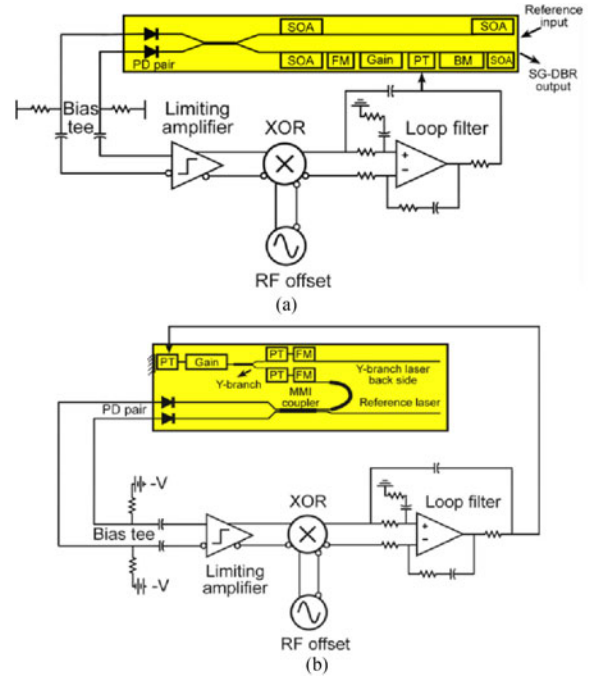


Fig. 3. (a) Circuit diagram of the first generation OPLL including gen-1 PIC in yellow and the control electronics. (b) Circuit diagram of the second generation OPLL including gen-2 PIC in yellow, and the control electronics. (BM: back mirror, FM: front mirror, PD: photodiode, PT: phase tuner, SG-DBR: sampled-grating distributed-Bragg-reflector, SOA: semiconductor optical amplifier.)

In this study, both OPLLs are designed to be heterodyne-type, which takes input offset frequency from external RF synthesizer and locks LO laser to the reference oscillator at this offset frequency. The second order loop filter with fast feedforward path was used in feedback electronics in order to get a high loop bandwidth. The circuit schematics of both OPLL systems can be seen in Fig. 3(a) and (b).

A limiting amplifier with 30 dB differential gain and 17 GHz 3-dB bandwidth, and a digital XOR gate functioning as a phase detector [16], together with an op-amp-based loop filter were used in the feedback electronics. The on-chip LO laser of the PIC was mixed via the external reference laser through the 2×2 MMI coupler and the PD pair to produce the beat note. This beat note then feeds the electronic ICs. First, it is amplified to logic levels through limiting amplifier and then mixed via external RF frequency synthesizer in order to produce an error signal. This error signal goes through the loop filter and feeds back to the phase-tuning section (PT) of on-chip LO laser. With sufficient feedback gain, this error signal becomes zero and LO laser is locked to external reference laser at a given RF offset frequency.

Open loop transfer function of an OPLL can be written as a product of gain, and the time constants of the loop [17]. Therefore, open loop transfer function of both OPLLs in this work can be expressed as follows:

$$T(s) = K_{PD} K_{CCO} \frac{1}{(\tau_{laser} s + 1)} e^{-\tau_d s} \times \left(\frac{\tau_2 s + 1}{\tau_1 s} \frac{1/R_{out}}{\tau_{op} s + 1} e^{-\tau_{dop} s} + \frac{C_{FF}}{2} \right)$$

where K_{PD} is the phase detection gain, K_{CCO} is the laser tuning sensitivity, τ_{laser} is the laser tuning frequency responsivity,

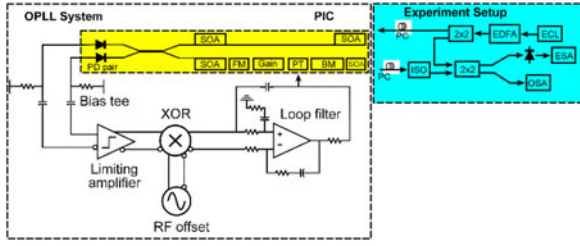


Fig. 4. Experimental setup for the first generation OPLL system. (ECL: external cavity laser, ESA: electrical spectrum analyzer, OSA: optical spectrum analyzer, PC: polarization controller, ISO: isolator.)

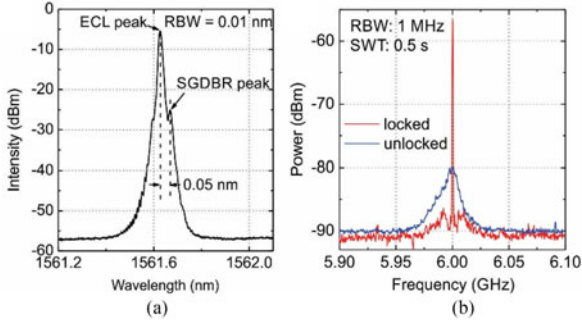


Fig. 5. (a) OSA spectrum when SGDBR is offset locked to the reference laser at 6 GHz offset, which corresponds 0.05 nm separation in optical domain. (b) Corresponding ESA spectrum when SGDBR is offset locked to the reference laser at 6 GHz offset, blue is before locking and red is after locking.

τ_1 is the loop filter pole, τ_2 is the loop filter zero, τ_{OP} is the op-amp parasitic pole, R_{out} is the voltage to current conversion resistance at the output, C_{FF} is the feed-forward capacitor and τ_{dop} is the op-amp delay, and τ_d is the total loop delay. Here K_{PD} is a constant value ($2 * V_{logic} / \pi$) due to the limiting amplifier, which makes the system loop bandwidth insensitive to the optical power level variations. This loop was designed to have a safe phase margin of around $50\text{--}60^\circ$ at unity gain crossover frequency for both OPLLs in order to realize a robust and stable system.

III. FIRST GENERATION OPLL EXPERIMENTAL RESULTS

The experimental setup, as shown in Fig. 4, was used in order to demonstrate the offset locking with the OPLL using the gen-1 PIC. The reference external cavity laser (ECL) was coupled into the PIC using lensed fiber from the back side of the PIC. It was then combined with the tunable on-chip SG-DBR laser output in the MMI coupler and mixed to form the desired beat note in the PDs. Light from the SG-DBR laser was coupled out from the lower arm for monitoring purposes. The superimposed optical spectra of the reference laser together with on-chip SG-DBR laser were measured by an optical spectrum analyzer (OSA). At the same time, the resulting RF beat-note was measured by an electrical spectrum analyzer (ESA) through a high speed photodiode.

This experiment shows offset-phase locking between the on-chip SG-DBR laser and the external cavity laser (ECL) as the reference. ECL used in this study has the optical linewidth of 100 kHz. Fig. 5(a) demonstrates the optical spectrum when the reference laser and the on-chip SG-DBR are offset locked at

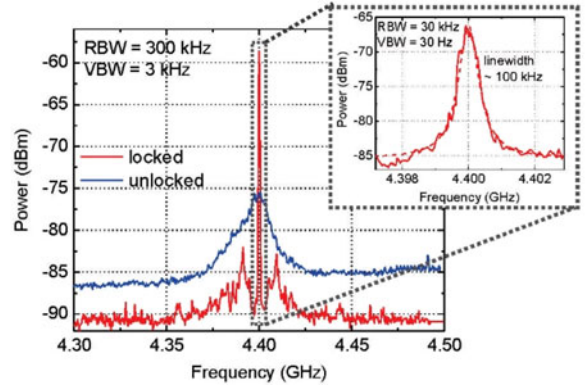


Fig. 6. ESA spectrum when SG-DBR is offset locked to the reference laser at 4.4 GHz offset. In this case, ECL and SG-DBR are decorrelated using a long fiber. Therefore, relative linewidth of the beat note is equal to 100 kHz, which is the linewidth of the ECL (reference laser).

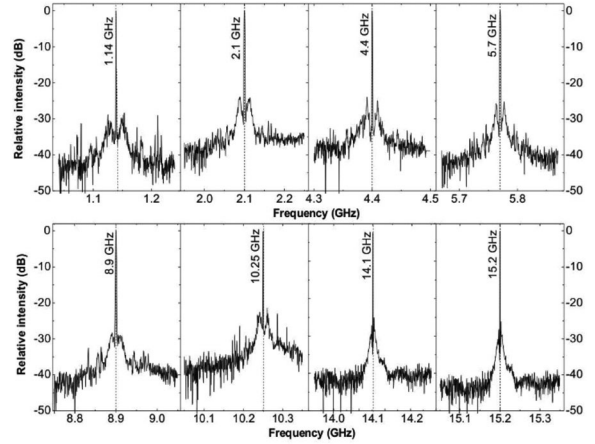


Fig. 7. Offset locking at multiple frequencies with the first generation OPLL at a RBW of 3 MHz.

6 GHz, which is determined by the RF frequency synthesizer. As can be seen in the figure, the separation between the two peaks are about 0.05 nm, which corresponds to 6 GHz frequency separation. In Fig. 5(b), the RF beat-note of the reference laser and the on-chip SG-DBR laser is presented both in locked and unlocked cases. The relative linewidth of the locked beat note at 6 GHz is in the order of sub-Hz, which is limited by the resolution bandwidth of the ESA. It should be noted that the optical linewidth of our free-running on-chip laser is 10 MHz.

In order to measure the absolute linewidth of the locked beat note, the measurement was performed after adding 20 km of fiber between the upper and lower external 2×2 couplers to decorrelate the ECL from the SG-DBR. In this case, one would expect to get a linewidth of the RF beat note equal to the optical linewidth of the ECL. Fig. 6 demonstrates this result. On-chip SG-DBR is offset locked at 4.4 GHz, but this time long fiber is added to decorrelate the ECL from the SG-DBR. In this case, the absolute linewidth of the locked beat tone was measured as 100 kHz, indicating the linewidth cloning of the SG-DBR to the ECL.

After proving the phase locking, the offset-locking range was demonstrated for different offset frequencies from 1.14 GHz up to 15.2 GHz as can be seen in Fig. 7. The higher the offset

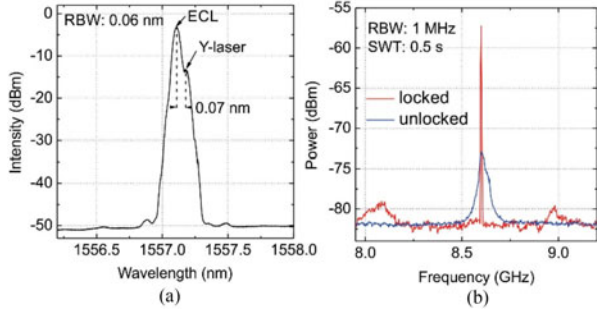


Fig. 8. (a) OSA spectrum when on chip Y-branch laser is offset locked to the reference laser at 8.6 GHz offset, which corresponds 0.07 nm separation in optical domain. (b) Corresponding ESA spectrum when Y-branch laser is offset locked to the reference laser at 8.6 GHz offset.

locking range, the easier it became for the OPLL to track the reference signal over a broad range of frequencies [18], [19].

IV. SECOND GENERATION OPLL EXPERIMENTAL RESULTS

Similar to the first generation OPLL, the experimental setup shown in Fig. 4 was used to demonstrate phase locking for the second generation OPLL. In this case, gen-1 PIC was replaced with the gen-2 PIC.

This experiment demonstrates phase locking between the on-chip Y-branch laser and the reference laser. Fig. 8(a) shows the optical spectrum when the reference laser and the on chip Y-branch laser are offset locked at 8.6 GHz, which is determined by the RF frequency synthesizer. As can be seen in the figure, the separation between the two peaks are about 0.07 nm, which corresponds to 8.6 GHz frequency separation. In Fig. 8(b), the RF beat-note between the reference laser and the on chip Y-branch laser is displayed both before the locking and after the locking. The relative linewidth of the locked beat note at 8.6 GHz is in the order of sub-Hz, which is limited by the resolution bandwidth of the ESA. The beat note has a relative linewidth in the order of a MHz before the locking, which is the unlocked Y-branch laser's linewidth [12].

With similar arguments presented for the first generation OPLL, one can add a long enough fiber at the output between the upper and lower external 2×2 couplers to decorrelate the ECL from the Y-branch laser and measure the actual linewidth of the beat note, which is equal to the linewidth of the ECL ~ 100 kHz.

As the next experiment, several offset frequencies from 1 GHz to 20 GHz were applied from the RF frequency synthesizer, and the same phase locking experiment was performed. Fig. 9 presents offset locking at several offset frequencies ranging from 1.6 GHz to 17.8 GHz.

In addition to the phase locking experiments, the residual phase noise spectral density of the OPLL system was measured when on chip local oscillator is offset locked to the reference laser. Since the loop parameters and order were not changed from the OPLL with gen-1 PIC to the gen-2 based OPLL, we only provide phase noise spectrum of the former one. Fig. 10 shows phase noise spectrum when on chip SG-DBR laser is offset locked to reference ECL at 2.5 GHz. This figure also demonstrates the ESA background and RF synthesizer phase

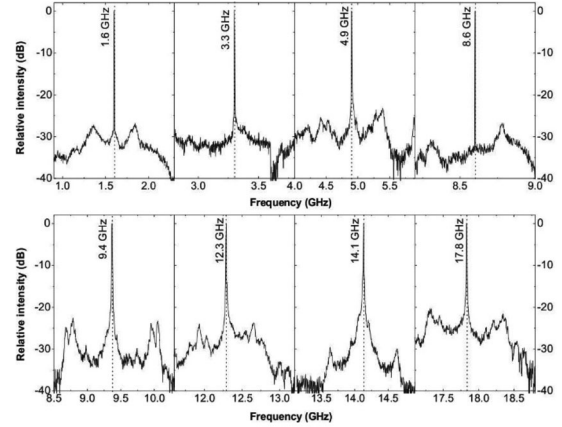


Fig. 9. Offset locking at multiple frequencies with the second generation OPLL at a RBW of 3 MHz.

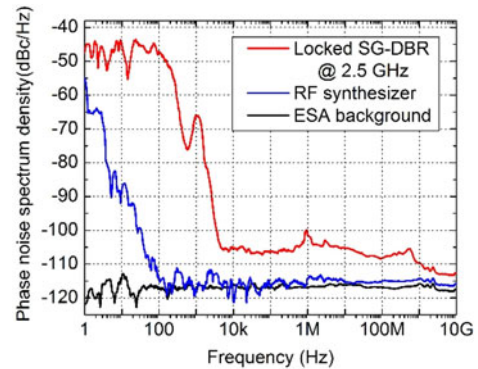


Fig. 10. Single-sideband residual phase noise of the heterodyne OPLL at 2.5 GHz offset locking. Phase noise results of the RF synthesizer at 2.5 GHz, and background is also shown here.

noise spectrum at 2.5 GHz. The phase noise variance is calculated to be 0.067 rad^2 from 1 kHz to 10 GHz offset interval. This corresponds to 14.8° standard deviation from the locking point. This OPLL achieves -100 dBc/Hz phase noise at an offset of 5 kHz. These results are comparable with the state of the art results in [20], [21].

For our OPLL system, the time domain equivalent of the phase error variance is equal to the timing jitter in the frequency range from 1 kHz to 10 GHz [22], which can be calculated as:

$$\text{Jitter} = \frac{\sqrt{0.067}}{2\pi \times 2.5 \times 10^9} = 16.48 \text{ ps}$$

This study is a proof-of-principle demonstration of optical phase locking to a reference laser with low power consumption. This system can be integrated with a better reference sources such as microresonator based optical frequency combs to synthesize arbitrary pure optical frequencies [10], [15]. Also, such narrow RF beat tones generated by beating on-chip laser with the comb lines can be used in a wide range of applications, including short to medium range optical communications, as well as broadband wireless communication in microwave photonic link technology.

TABLE I
POWER BUDGET FOR FIRST GENERATION PIC PROVIDING 10 mW OPTICAL
POWER AND OVERALL OPLL SYSTEM

| | Section | Current (mA) | Voltage (V) | Power (mW) |
|---|--------------------|--------------|-------------|-----------------|
| Gen-1 PIC | Gain(1) | 73 | 1.5 | 109.5 |
| | FM (1) | 30 | 1.5 | 45 |
| | PT (1) | 7 | 1.3 | 9.1 |
| | PD (2) | 1 | 2 | 4 |
| | BM (1) | 120 | 1.5 | 180 |
| | SOA (3) | 70 | 1.5 | 315 |
| | PIC-1 TOTAL | | | |
| Electronic ICs | LIA | 180 | 3.3 | 594 |
| | XOR | 130 | 3.3 | 429 |
| | Op-amp | 16 | 6 | 96 |
| Electronic ICs TOTAL | | | | 1119 |
| Total Power Consumption Gen-1 OPLL | | | | 1.78 (W) |

TABLE II
POWER BUDGET FOR SECOND GENERATION PIC PROVIDING 10 mW OPTICAL
POWER AND OVERALL OPLL SYSTEM

| | Section | Current (mA) | Voltage (V) | Power (mW) |
|---|---------|--------------|-------------|----------------|
| Gen-2 PIC | Gain(1) | 73 | 1.5 | 109.5 |
| | FM (2) | 20 | 1.3 | 52 |
| | PT (2) | 7 | 1.3 | 18.2 |
| | PD (2) | 1 | 2 | 4 |
| PIC-2 TOTAL | | | | 184 |
| Electronic ICs | LIA | 180 | 3.3 | 594 |
| | XOR | 130 | 3.3 | 429 |
| | Op-amp | 16 | 6 | 96 |
| Electronic ICs TOTAL | | | | 1119 |
| Total Power Consumption Gen-2 OPLL | | | | 1.3 (W) |

V. POWER BUDGET OF BOTH OPLLs

As mentioned, one of the primary objectives for this work was to realize a compact, chip-scale OPLL with Watt-level power consumption. In order to do this, one can improve the control electronics, PIC or both. In this work we proposed a novel, compact, low power consumption PIC as a possible solution to realize a chip scale, a Watt level OPLL. Tables I and II provides the power consumption of gen-1 PIC, gen-2 PIC, control electronics and overall OPLL systems. (Numbers in the parentheses for each section in the PIC part tell how many of them are integrated in the PIC, BM: back mirror, FM: front mirror, LIA: limiting amplifier, PD: photodiode, PT: phase tuner, SOA: semiconductor optical amplifier)

As can be seen from these tables gen-1 PIC consumes 660 mW, whereas gen-2 PIC consumes only 184 mW. Together

with the control electronics, the OPLL with gen-2 PIC only consumes record-low 1.3 Watts of electrical power.

VI. SENSITIVITY OF THE OPLL SYSTEM

For practical applications including coherent optical communications and optical frequency synthesis, OPLLs should be able to lock to input reference power levels in the order of μ Ws or even 10s of nWs. In this section, sensitivity analysis of the OPLL is given and experimental sensitivity results are reported. In addition to these results, a novel high gain transimpedance amplifier (TIA) is presented and possible OPLL is proposed using this TIA, which can lock to input power levels as low as 25 pW.

Both OPLLs in this work employs SiGe based COTS limiting amplifier, which has 30 dB differential gain. InP-based PICs have on chip tunable lasers, which produces reasonable amount of optical power. This is mixed with the reference input power through 2×2 MMI coupler and the PDs. The detected electrical signal is then fed into the limiting amplifier having a 50Ω common mode logic interface. In this system, the minimum required input current level from the balanced PD pair can be found as follows, where $V_{INPUT,MIN}$ represents the minimum required voltage level just before the limiting amplifier and $I_{BEAT,MIN}$ represents the minimum required beat current produced by the photodiodes:

$$\begin{aligned} Gain_{LIA} &= 30 \text{ dB} = 31.6 \\ V_{INPUT,MIN} &= \frac{300 \text{ mV}}{31.6} = 9.5 \text{ mV} \\ I_{BEAT,MIN} &= \frac{9.5 \text{ mV}}{50} = 0.19 \text{ mA} \end{aligned}$$

From the above equations, we found out that the minimum input current level for offset locking with the designed OPLLs is around 0.19 mA. Given the responsivity of the on-chip PDs is around 1 A/W, the minimum input beat power is around 0.19 mW. If we use this in the coherent detection equation, we can get the minimum required input power level from the reference laser as follows, where I_{BEAT} represents the beat current produced by the PDs, I_{LO} is the current produced by LO laser and I_{INPUT} is the current produced by the reference laser.

$$\begin{aligned} I_{BEAT} &= 2\sqrt{I_{LO}I_{INPUT}} \\ I_{INPUT,MIN} &= \frac{I_{BEAT,MIN}^2}{4I_{LO}} \\ I_{INPUT,MIN} &= 9 \mu\text{A} \end{aligned}$$

Therefore, the minimum input power required to offset lock this OPLL is theoretically about $9 \mu\text{W}$, which is close to the experimental results demonstrated in Fig. 11(b), in which the minimum input power level required to operate the OPLL system was found to be $20 \mu\text{W}$.

Fig. 11(a) and (b) demonstrates the pull-in range of the OPLL system with respect to offset locking frequency and input power levels respectively. Pull-in range varies from 1.4 GHz to 200 MHz depending on the offset frequency range. As expected, the pull-in range decreases with increasing offset frequencies, since the gain of the overall loop reduces. Similarly, decreasing input power levels reduces the pull-in range, and eventually at some point OPLL stops working with the certain input power levels. This minimum input power level was found to be $20 \mu\text{W}$, as can be seen in Fig. 11(b).

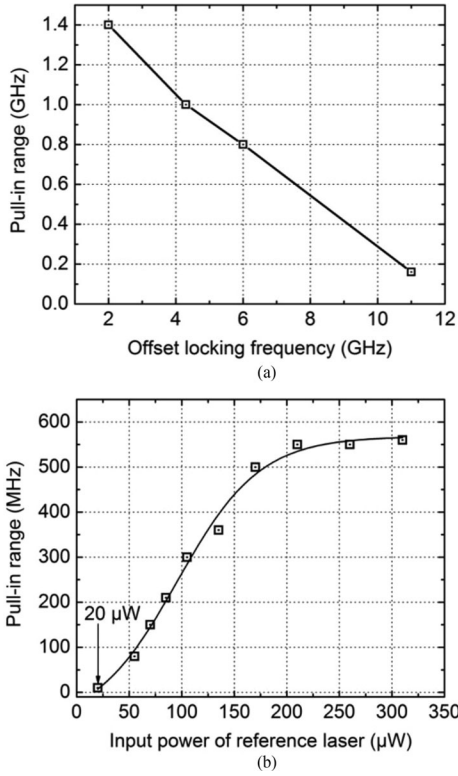


Fig. 11. (a) Pull-in range vs. offset locking frequency. (b) Pull in range vs. input power of the reference external cavity laser. Minimum input power required for locking was found 20 μW experimentally.

In order to improve the sensitivity of the OPLL further, an application specific transimpedance amplifier (TIA) with low noise, high gain and wide bandwidth using 130 nm SiGe HBT (Silicon Germanium Heterojunction Bipolar Transistor) process was designed. This chip was designed for 80 dB voltage gain and 120 dB-ohm transimpedance gain with 30 GHz 3-dB bandwidth. It has less than 10 $\text{pA}/\sqrt{\text{Hz}}$ input referred noise current density up to 20 GHz with respect to 50 fF photodiode capacitance according to the circuit level simulations. With this TIA minimum input power level of reference signal can be reduced to as low as 22.5 pW as follows, where each symbol is used the same way as explained previously:

$$\begin{aligned} \text{Gain}_{\text{TIA}} &= 120 \text{ dB}\Omega = 1 \text{ M}\Omega \\ I_{\text{BEAT,MIN}} &= \frac{300 \text{ mV}}{10^6 \Omega} = 0.3 \mu\text{A} \\ I_{\text{BEAT}} &= 2\sqrt{I_{\text{LO}} I_{\text{INPUT}}} \\ I_{\text{INPUT,MIN}} &= \frac{I_{\text{BEAT,MIN}}^2}{4I_{\text{LO}}} \\ I_{\text{INPUT,MIN}} &= 22.5 \text{ pA} \end{aligned}$$

Using this TIA, one can make a highly sensitive OPLL, which can be used in optical communications and optical frequency synthesis systems. Fig. 12 shows the proposed OPLL system using this novel TIA. The COTS SiGe limiting amplifier is replaced by this TIA in the proposed OPLL system. Please note that TIA gain was measured functionally to be 60 dB without DC restoration loop. With a proper DC restoration loop, one can get the simulated gain of 80 dB from the TIA. The study relating to the sensitive OPLL system with these high-performance TIAs is ongoing and will be reported in the future.

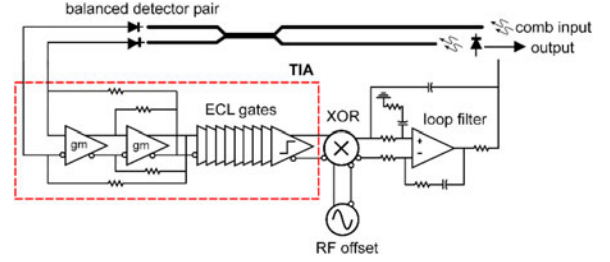


Fig. 12. Schematic of the sensitive OPLL with low noise, high gain transimpedance amplifier.

VII. CONCLUSION

In this paper, two chip-scale OPLLs were designed and demonstrated. By designing a novel, low power consumption InP-based photonic integrated receiver circuit, overall power consumption of the first generation OPLL was significantly reduced. The second generation OPLL consumes only 1.35 Watts of electrical power, which is the lowest power consumption reported for an OPLL to the best of author's knowledge. Both OPLLs have 500 MHz loop bandwidth, with 0.067 rad^2 phase noise variance, integrating from 1 kHz to 10 GHz. Offset locking ranges are 15.2 GHz and 17.8 GHz respectively. Minimum input power level required from the reference side for phase locking was measured to be 20 μW . Novel, application specific electrical IC was proposed for lowering the sensitivity of such OPLLs to as low as 25 pW.

REFERENCES

- [1] L. G. Kazovsky, "Balanced phase-locked loops for optical homodyne receivers: performance analysis, design considerations, and laser linewidth requirements," *J. Lightw. Technol.*, vol. 4, no. 2, pp. 182–195, Feb. 1986.
- [2] V. Ferrero and S. Camatel, "Optical phase locking techniques: An overview and a novel method based on single side sub-carrier modulation," *Opt. Exp.*, vol. 16, no. 2, pp. 818–828, Jan. 2008.
- [3] H. C. Park *et al.*, "40 Gbit/s coherent optical receiver using a Costas loop," *Opt. Exp.*, vol. 20, no. 26, pp. B197–B203, Dec. 2012.
- [4] S. Camatel and V. Ferrero, "Narrow linewidth CW laser phase noise characterization methods for coherent transmission system applications," *J. Lightw. Technol.*, vol. 26, no. 17, pp. 3048–3055, Sep. 2008.
- [5] S. Ristic, A. Bhardwaj, M. J. Rodwell, L. A. Coldren, and L. A. Johansson, "An optical phase-locked loop photonic integrated circuit," *J. Lightw. Technol.*, vol. 28, no. 4, pp. 526–538, Feb. 2010.
- [6] K. Balakier, M. J. Fice, L. Ponnampalan, A. J. Seeds, and C. C. Renaud, "Monolithically integrated optical phase lock loop for microwave photonics," *J. Lightw. Technol.*, vol. 32, no. 20, pp. 3893–3900, Oct. 2014.
- [7] R. J. Steed *et al.*, "Hybrid integrated optical phase-lock loops for photonic terahertz sources," *IEEE J. Sel. Topics Quantum Electron.*, vol. 17, no. 1, pp. 210–217, Feb. 2011.
- [8] D. T. Spencer *et al.*, "Towards an integrated-photonics optical-frequency synthesizer with <1 Hz residual frequency noise," in *Proc. Opt. Fiber Commun. Conf.*, 2017, pp. 1–3.
- [9] C. C. Renaud, C. F. C. Silva, M. Dueser, P. Bayvel, and A. J. Seeds, "Exact, agile, optical frequency synthesis using an optical comb generator and optical injection phase lock loop," in *Proc. IEEE/LEOS Summer Top. Meet.*, 2003, pp. WC1.3/67–WC1.3/68.
- [10] S. Arafin *et al.*, "Towards chip-scale optical frequency synthesis based on optical heterodyne phase-locked loop," *Opt. Exp.*, vol. 25, no. 2, pp. 681–695, Jan. 2017.
- [11] M. Lu, H. C. Park, E. Bloch, L. A. Johansson, M. J. Rodwell, and L. A. Coldren, "A highly-integrated optical frequency synthesizer based on phase-locked loops," in *Proc. Opt. Fiber Commun. Conf.*, 2014, pp. 1–3.
- [12] A. Simsek *et al.*, "A chip-scale heterodyne optical phase-locked loop with low-power consumption," in *Proc. Opt. Fiber Commun. Conf.*, 2017, pp. 1–3.

- [13] L. A. Coldren *et al.*, "High performance InP-based photonic ICs—A tutorial," *J. Lightw. Technol.*, vol. 29, no. 4, pp. 554–570, Feb. 2011.
- [14] M. Lu, "Integrated optical phase-locked loops," Ph.D. dissertation, Electr. Comput. Eng. Dept., Univ. California Santa Barbara, Santa Barbara, CA, USA, 2013.
- [15] S. Arafin *et al.*, "Power-efficient Kerr frequency comb based tunable optical source," *IEEE Photon. J.*, vol. 9, no. 3, pp. 1–14, Jun. 2017.
- [16] [Online]. Available: <http://www.adsantec.com/200-asnt5020-pqc.html>; <http://www.adsantec.com/83-asnt5040-kmc.html>
- [17] F. G. Agis *et al.*, "Ultrafast phase comparator for phase-locked loop-based optoelectronic clock recovery systems," *J. Lightw. Technol.*, vol. 27, no. 13, pp. 2439–2448, Jul. 2009.
- [18] K. Balakier, L. Ponnampalam, M. J. Fice, C. C. Renaud, and A. J. Seeds, "Integrated semiconductor laser optical phase lock loops (invited paper)," *IEEE J. Sel. Topics Quantum Electron.*, vol. 24, no. 1, Jan. 2018, Art. no. 1500112.
- [19] M. Lu *et al.*, "Highly integrated optical heterodyne phase-locked loop with phase/frequency detection," *Opt. Exp.*, vol. 20, no. 9, pp. 9736–9741, Apr. 2012.
- [20] R. J. Steed *et al.*, "Monolithically integrated heterodyne optical phase-lock loop with RF XOR phase detector," *Opt. Exp.*, vol. 19, no. 21, pp. 20048–20053, Oct. 2011.
- [21] M. Lu *et al.*, "An integrated 40 Gbit/s optical costas receiver," *J. Lightw. Technol.*, vol. 31, no. 13, pp. 2244–2253, Jul. 2013.
- [22] T. R. Clark, T. F. Carruthers, P. J. Matthews, and I. N. D. III, "Phase noise measurements of ultrastable 10-GHz harmonically modelocked fibre laser," *Electron. Lett.*, vol. 35, no. 9, pp. 720–721, Apr. 1999.

Arda Simsek received the B.S. degree in electrical engineering from Bilkent University, Ankara, Turkey, in 2014, and the M.S. degree in electrical and computer engineering in 2015 from the University of California Santa Barbara, Santa Barbara, CA, USA, where he is currently working toward the Ph.D. degree in electrical and computer engineering. His main research interests include RF and millimeter-wave-integrated circuits in silicon and III–V technologies for phased-array systems and optical phase-locked loops.

Shamsul Arafin (S'08–M'12–SM'17) received the B.Sc. degree in electrical and electronics engineering from Bangladesh University of Engineering and Technology, Dhaka, Bangladesh, in 2005, the M.Sc. degree in communication technology from Universitat Ulm, Ulm, Germany, in 2008, and the Ph.D. degree from the Walter Schottky Institut, Technische Universitat Munchen, Munich, Germany, in 2012. He was a Postdoctoral Research Scholar with the Device Research Laboratory, University of California Los Angeles, Los Angeles, CA, USA. He is currently an Assistant Project Scientist with the University of California Santa Barbara, Santa Barbara, CA. He has authored and coauthored more than 80 papers in leading technical journals and international conferences.

Seong-Kyun Kim received the B.S., M.S., and Ph.D. degrees from the College of Information and Communication Engineering, Sungkyunkwan University, Suwon, South Korea, in 2007, 2009, and 2013, respectively. He is currently a Postdoctoral Research Fellow in the Department of Electrical and Computer Engineering, University of California Santa Barbara, Santa Barbara, CA, USA. His current research interests include RF and millimeter-wave-integrated circuits for wireless communications and phased array.

Gordon B. Morrison received the B.A.Sc. degree (Hons.) in engineering physics from Simon Fraser University, Vancouver, BC, Canada, in 1997, and the Ph.D. degree in engineering physics from McMaster University, Hamilton, ON, Canada, in 2002. His doctoral work, under Prof. D. T. Cassidy, focused on modeling and characterization of gain-coupled DFB lasers. From 1998 to 2002, he spent more than a year with Nortel Networks, Toronto, ON, as a Graduate Student Researcher. From 2002 to 2003, he was a Postdoctoral Fellow with McMaster University, where he was involved in the development of a model for asymmetric-multiple-quantum-well gain and worked on process development for the quantum-well intermixing. In June 2003, he joined the Department of Electrical and Computer Engineering, University of California Santa Barbara, as a Visiting Assistant Research Engineer in Prof. L. Coldren's group, where he participated in the design, fabrication, and characterization of small footprint DBR EMLs using quantum-well-intermixing technology, and used photoluminescence spectroscopy to characterize and optimize photonic integrated circuits. In

2005, he joined ASIP (formerly III–V Photonics), Houten, The Netherlands, and in 2006, he joined Apogee Photonics (formerly ASIP/T-Networks), Allentown, PA, USA, where he worked on uncooled 1310 EML technology, 40G EA modulators, and monolithically integrated SOA/EA products. Apogee Photonics was acquired by CyOptics, Inc., Breinigsville, PA, and subsequently was acquired by Avago technologies. At CyOptics/Avago, he continued work on EML development while additionally focusing on design, characterization, calibration, and qualification of liquid crystal external cavity tunable lasers for coherent applications. In 2014, he joined Freedom Photonics LLC, Santa Barbara, CA, USA, as the Director of Engineering. He is the author or coauthor of more than 30 peer-reviewed journal papers.

Leif A. Johansson (M'04) received the Ph.D. degree in engineering from University College London, London, U.K., in 2002. He has been a Research Scientist with the University of California at Santa Barbara, Santa Barbara, CA, USA, and is the founder of Freedom Photonics, Santa Barbara. His current research interests include design and characterization of integrated photonic devices for analog and digital applications and analog photonic systems and subsystems.

Milan L. Mashanovitch (M'99–SM'13) received the Dipl.Ing. degree in electrical engineering from the University of Belgrade, Belgrade, Serbia, in 1998, and the Ph.D. degree in electrical engineering from the University of California Santa Barbara, Santa Barbara, CA, USA, in 2004. He cofounded Freedom Photonics LLC, Santa Barbara, in 2005, and he has been in many technical roles related to product development and program management since. In addition to Freedom Photonics, he was with the University of California Santa Barbara, both as a Researcher on photonic-integrated circuits, and as an Adjunct Professor teaching graduate level classes on semiconductor lasers and photonic ICs. He has coauthored nearly 130 papers, many invited, on photonic-integrated circuits and various photonic devices. He is one of the authors of the second edition of the *Diode Lasers and Photonic Integrated Circuits* (Wiley, 2012). He has chaired, served, or has served on technical committees for the *IEEE Avionics, Fiber Optics and Photonics Conference*, the *IEEE Microwave Photonics Conference*, the OSA's Integrated Photonics Research Conference, the International Semiconductor Laser Conference, and the Indium Phosphide and Related Materials Conference.

Larry A. Coldren (S'67–M'72–SM'77–F'82–LF'12) received the Ph.D. degree in electrical engineering from Stanford University, Stanford, CA, USA, in 1972. After 13 years in the research area with Bell Laboratories, he joined the University of California at Santa Barbara (UCSB), Santa Barbara, CA, in 1984. He is currently the Fred Kavli Professor of optoelectronics and sensors and holds appointments in the Department of Materials and the Department of Electrical and Computer Engineering. From 2009 to 2011, he was an acting Dean of the College of Engineering. In 1990, he cofounded Optical Concepts, later acquired as Gore Photonics, to develop novel vertical-cavity surface-emitting lasers (VCSEL) technology, and, in 1998, he cofounded Agility Communications, later acquired by JDSU (now Lumentum), to develop widely tunable integrated transmitters. At UCSB, he worked on multiple-section widely tunable lasers and efficient VCSELs. More recently, his group has developed high-performance InP-based photonic-integrated circuits and high-speed high-efficiency VCSELs. He has authored or coauthored more than a thousand journal and conference papers, eight book chapters, a widely used textbook, and 63 issued patents. He is a Fellow of the OSA, the IEEE, and the National Academy of Inventors, as well as a Member of the National Academy of Engineering. He received the 2004 John Tyndall Award, the 2009 Aron Kressel Award, the 2014 David Sarnoff Award, the 2015 IPRM Award, and the 2017 Nick Holonyak, Jr., Award.

Mark J. W. Rodwell received the Ph.D. degree from Stanford University, Stanford, CA, USA, in 1988. He holds the Doluca Family Endowed Chair in the Electrical and Computer Engineering with the University of California Santa Barbara (UCSB), Santa Barbara, CA. He also manages the UCSB Nanofabrication Lab. His research group develops nanometer and terahertz transistors, and millimeter-wave and submillimeter-wave-integrated circuits. The work of his group and collaborators has been recognized by the 2010 IEEE Sarnoff Award, the 2012 IEEE Marconi Prize Paper Award, the 1997 IEEE Microwave Prize, the 1998 European Microwave Conference Microwave Prize, and the 2009 IEEE IPRM Conference Award.

I. Photonic Integrated Circuits

C. GaSb-based PICS

MBE Growth of Quaternary AlGaAsSb/InGaAsSb Heterostructures for Tunable Lasers with 2.2-2.6µm Emission Wavelength

A.P. McFadden¹, S. Arafin¹, M. Pendharkar¹, L. Coldren¹ and C.J. Palmstrøm^{1,2}
¹Electrical and Computer Engineering, UC Santa Barbara, ²Materials Dept. UC Santa Barbara

Overview

This poster details the development of growth of the III-V semiconductor materials to be used for realization of the multiple quantum well lasers designed to emit between 2.2-2.6 µm. Thin films and heterostructures from the 'quaternary' In_xGa_{1-x}As_ySb_{1-y} and Al_xGa_{1-x}As_ySb_{1-y} material systems were grown by molecular beam epitaxy (MBE) at UCSB and characterized by reflection high electron diffraction (RHEED), optical microscopy, atomic force microscopy (AFM), X-ray diffraction (XRD), and photoluminescence (PL). Once satisfactory results were obtained from calibration growths and test structures, full p-n diode laser structures were grown according to the designs outlined below. These preliminary results are the first step towards development of sampled grading DBR lasers which to our knowledge have not been demonstrated using this material system.

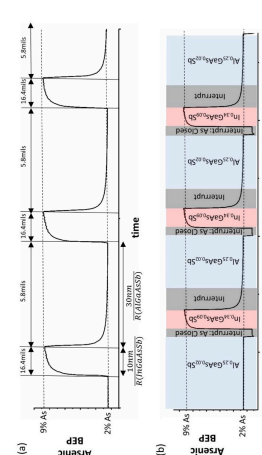
Objective

- The objective of this project is to fabricate sampled grading DBR lasers with full tunability between 2.2-2.6µm
- Three different laser structures are to be used to accomplish this
- The 2.6 µm emitting design shown makes use of InGaAsSb QWs with GaSb barriers
- Designs centered at 2.2 µm and 2.4 µm make use of InGaAsSb QWs with AlGaAsSb barriers

Methods: Materials Growth and Characterization

1. Materials Growth

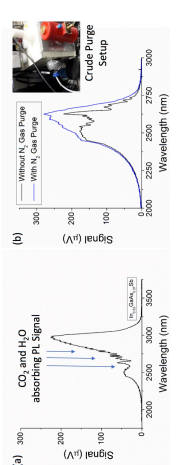
- Molecular beam epitaxy (MBE) was used to grow binary and quaternary compounds such as those listed in the laser structure shown above
- Typical III-V MBE of arsenides and antimonides makes use of a so called growth window
- In the growth window, excess group V material is desorbed from the sample surface and growth rate is determined by the group III flux
- Obtaining the desired composition in compounds with both arsenic and antimony is difficult due to the different vapor pressures and sticking coefficients of the group V elements
- Obtaining abrupt interfaces and uniform composition in heterostructures with varying Sb and As composition is difficult due to the 'memory effect' of As in the MBE chamber (see image to the right)



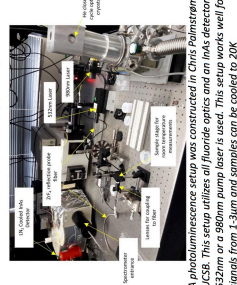
(a) Arsenic beam equivalent pressure (BEP) vs. time as the As shutter is opened and closed during growth of a MQW structure. The finite response time is due to the arsenic 'memory effect' through the valved cracker source. (b) Shutting sequence used for growth of MQW samples showing compensation of the memory effect.

2. Materials Characterization

- X-Ray Diffraction (XRD) was used to obtain lattice constants and information about crystal quality and abruptness of interfaces
- Photoluminescence (PL) was used to obtain emission wavelength. Material is optimized for narrow and bright PL.
- Atomic force microscopy (AFM) was used to obtain topographic images of material surfaces.



Strong atmospheric absorption is present near 2.6µm wavelength due to both water vapor and CO₂. (a) shows this effect clearly in the PL signal of a thick InGaAsSb calibration sample. (b) shows improvement with the use of a crude purge setup. A more sophisticated purge source was later employed.

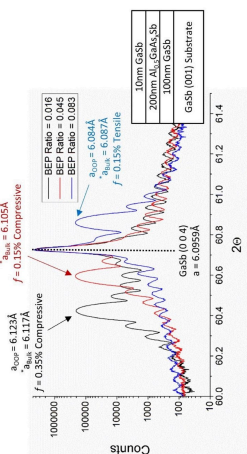


A photoluminescence setup was constructed in Chris Palmstrøm's lab at UCSB. This setup utilizes all fluoride optics and an InAs detector. Either a 532nm or a 980nm pump laser is used. This setup works well for PL signals from 1-3µm and samples can be cooled to 20K

Results: Structural Characterization and Photoluminescence

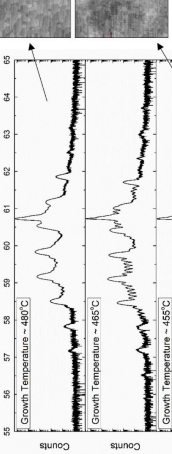
1. Lattice matching

- The proposed laser designs make use of thick (2µm) Al_xGaAsSb cladding layers
- The cladding layers need to be closely lattice matched (below 0.1%) to the GaSb substrates in order to reduce defects
- Lattice matching is accomplished by adding a small amount of arsenic (2-7%) to 'quasi-ternary' AlGaAsSb compounds

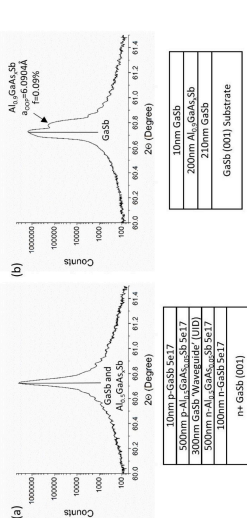


A calibration series was grown in order to determine the desired amount of arsenic for lattice matching of Al_xGaAsSb to the GaSb substrate at the optimized growth temperature. The figure shows the XRD of a MQW series grown at this temperature resulted in uninformative surface morphology. The figure above shows ω-2θ XRD of a MQW series grown with varying substrate temperatures. Growth at 485°C gives the sharpest thickness fringes indicating high quality films with abrupt interfaces. The AFM images at the right show a transition from step low to island like growth with decreasing growth temperature.

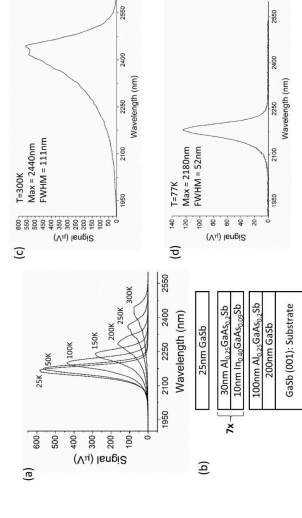
2. Multiple Quantum Wells



Earlier attempts (not shown) suggested that thick In_xGaAsSb films grew best at substrate temperatures around or below 450°C. However, it was found that heterostructure (MQW) growth at this temperature resulted in uninformative surface morphology. The figure above shows ω-2θ XRD of a MQW series grown with varying substrate temperatures. Growth at 485°C gives the sharpest thickness fringes indicating high quality films with abrupt interfaces. The AFM images at the right show a transition from step low to island like growth with decreasing growth temperature.



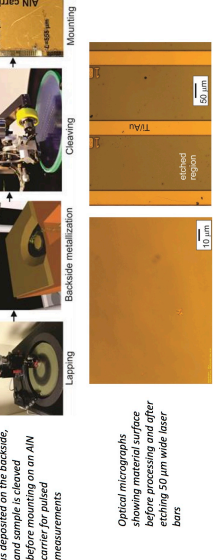
(a) PL lattice matched to a GaSb substrate were grown using the calibration series shown to the left for transport measurements. Lattice matching is near perfect. (b) First attempt at lattice matching for higher aluminum concentration cladding layers. The estimated flux required was extrapolated from the calibration series shown at the left resulting in lattice mismatch below 0.1%.



(a) Temperature dependent PL of a MQW calibration sample designed to emit at 2400nm at 300K. (b) layer structure of the PL calibration sample. (c) Room temperature PL. (d) PL at 77K showing FWHM of 52nm indicating high quality material

Broad Area Laser Characterization: Preliminary Results

- Broad area lasers were fabricated using contact lithography and dry etching



After dry etching laser bars, samples are thinned, metal is deposited on the backside, and sample is cleaved before mounting on an AlN carrier for pulsed measurements

Conclusions

- The desired composition was obtained in MBE growth films for all quaternary compounds in 2.2-, 2.4 and 2.6 µm laser designs
- The growth temperature of heterostructures and multiple quantum wells was optimized using XRD, AFM, and PL
- Unoptimized laser structures were grown and successfully fabricated into broad area lasers
- These results pave the way for MBE regrowth and processing efforts to realize widely tunable SGBDR lasers emitting between 2.2-2.6 µm

Recent Progress on GaSb-based Photonic Integrated Circuits

S. Arafin¹⁺, A. P. McFadden¹, M. Pendharkar¹, C. J. Palmström^{1,2} and L. A. Coldren^{1,2}

¹*Dept. of Electrical and Computer Engineering,*

University of California, Santa Barbara, CA-93106, USA

²*Dept. of Materials, University of California, Santa Barbara, CA-93106, USA*

Despite significant technological achievements in InP-photonic ICs with sampled-grating distributed Bragg reflector (SG-DBR) laser tuning technology near 1.55 μm over the past few decades, such platform in the short-wave infrared (SWIR) or mid-infrared (MIR) regimes has not yet reached its full potential. By employing an InGaAsSb/AlGaAsSb/GaSb gain material and necessary processing steps, we aim to develop photonic integrated circuits (PICs) technology in the GaSb material system. The proposed concept for an agile tunable PIC transmitter is shown in Fig. 1. The SG-DBR lasers are the tunable component and each is limited $\sim 6.5\%$ of the center wavelength in order to obtain a good side-mode suppression ratio using a simple cavity geometry; therefore, multiple SG-DBR lasers will be heterogeneously integrated together to cover the entire tuning range. Tunable light output from the SG-DBR cavity will be amplified in the semiconductor optical amplifier (SOA) to increase power to ~ 10 mW.

As can be seen in Fig. 1, the wavelength range from 2.2-2.8 μm can be covered with only four chips using broad bandwidth of the gain materials. Second, we integrate each chip with the desired phase modulator. Light will then be coupled from the GaSb PICs to the SOI combiner planar lightwave circuit (PLC). We suggest a simple non-dispersive 4×1 combiner as illustrated in Fig. 1. This combiner could be accomplished by the indicated “y-branch” structures or by 2×1 multi-mode interference (MMI) structures. Alternative to the non-dispersive combiner, a wavelength selective 4×1 MMI can also be thought of.

For the phase modulators, we propose current injection into the passive waveguide regions. The modulation depth is expected to be approximately π radians of phase modulation for a current input of 5 mA with a typical modulator length ~ 100 μm . The modulation is almost independent of modulator length for current densities in the 0.2-2 kA/cm^2 range. Higher bandwidths are possible by using reverse biased p - n junctions, also using the same passive regions of the platform.

The offset quantum-well (OQW) integration platform is chosen for processing SG-DBR lasers and compatible PICs because it requires a relatively simple process. A schematic cross-section of the layer structure of a GaSb-based offset quantum-well (OQW) integration platform is illustrated in Fig. 2(a). After growing the base structures, passive regions were formed by removing the multiple-QW active region from the base structure prior to the regrowth. Atomic steps were observed after MBE regrowth in both active and passive areas with and without MQWs, respectively. The film exhibits atomically smooth surface morphology with root-mean-square (RMS) roughness value of < 0.3 nm, as shown in Fig. 2(b)-(c). The presented concepts and encouraging materials growth results pave the way for the realization of transmitter PICs covering a large SWIR wavelength range using GaSb-technology.

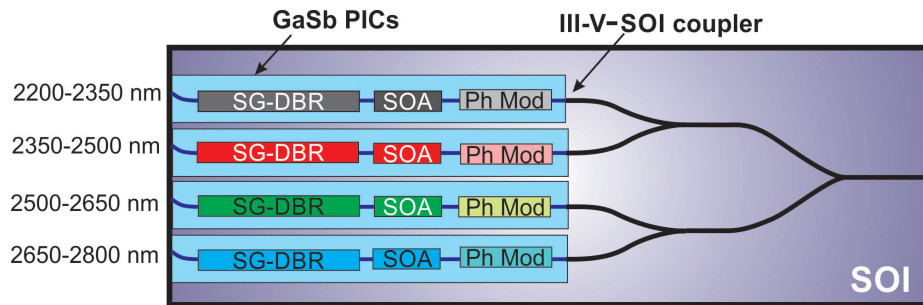


Figure 1: Hypothetical tunable laser design for 2.2–2.8 μm based upon GaSb Photonic ICs. GaSb chip lengths would be about 4 mm.

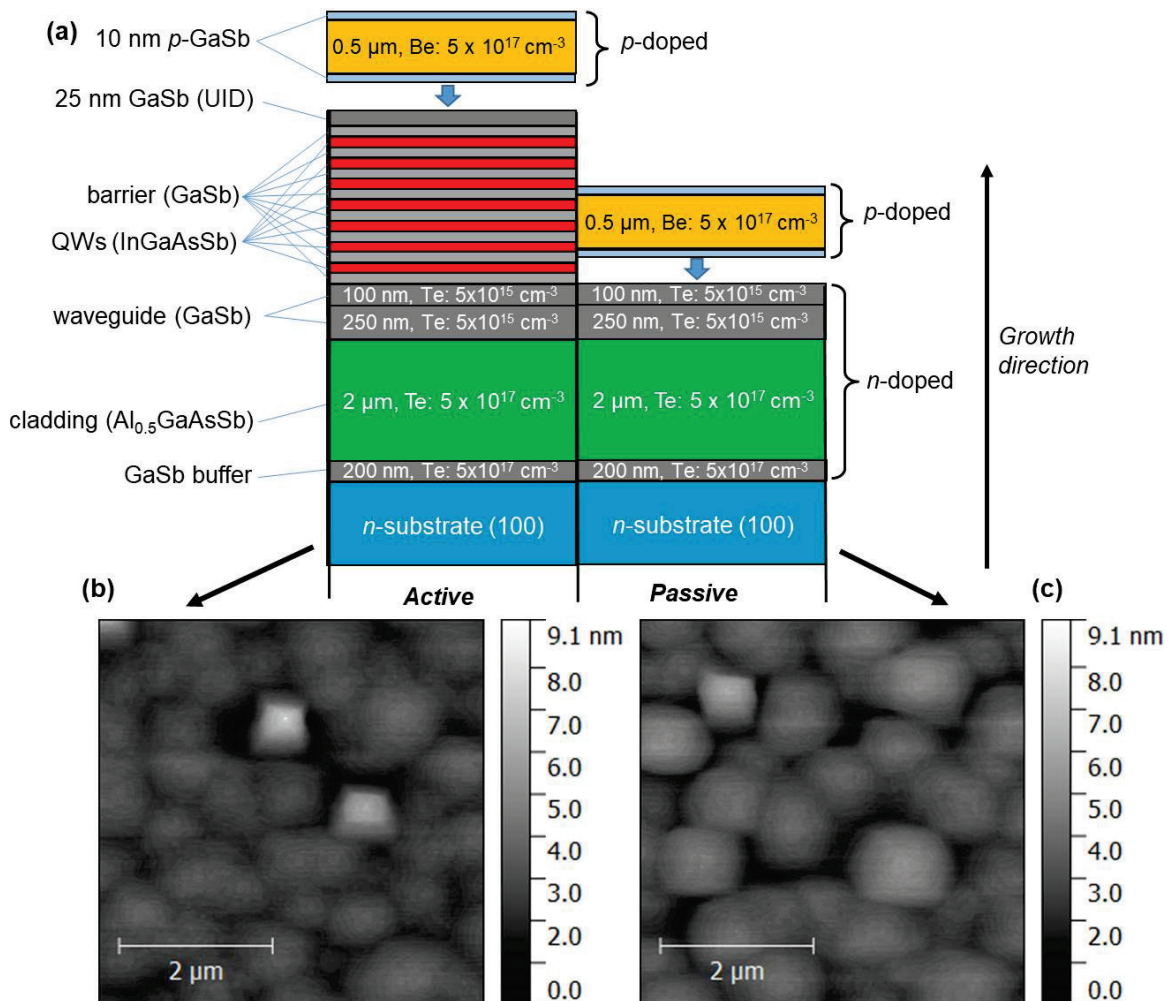


Figure 2: (a) Schematic cross-sectional view of offset quantum-well epitaxial structure – active (left), passive (right) regions with the regrown epilayers on top. 5 $\mu\text{m} \times 5 \mu\text{m}$ AFM images of the (b) active (with MQWs) and (c) passive areas (etched MQWs) after MBE regrowth.

I. Photonic Integrated Circuits

D. PICs for Free-Space Links and LIDAR

High-Power Integrated Indium Phosphide Transmitter for Free Space Optical Communications

Hongwei Zhao, Sergio Pinna, Bowen Song, Ludovico Megalini, Simone Suran Brunelli,
Larry Coldren and Jonathan Klamkin

Electrical and Computer Engineering Department, University of California Santa Barbara, Santa Barbara, CA 93106
hwzhao@ece.ucsb.edu

Abstract: An integrated indium phosphide transmitter is demonstrated for free space optical communications. The transmitter tunes from 1521 nm to 1565 nm, demonstrates performance up to 5 Gbps, and includes an output high-power semiconductor optical amplifier. © 2018 The Author(s)
OCIS codes: (200.2605) Free space optical communication; (250.5300) Photonic Integrated Circuits

1. Introduction

For deployment on small spacecraft, to enable low-cost and frequent missions that include high data rate downlink capability, free space optical communication systems require photonic components with low cost, size, weight and power (CSWaP), while demonstrating high output optical power and power-efficient modulation formats [1]. Indium phosphide (InP) is the most mature and high-performance photonic integrated circuit platform (PIC), and is therefore attractive for space applications where reliability and technology readiness are critical. This platform allows for the monolithic integration of all the required active components (e.g. lasers, semiconductor optical amplifiers (SOAs), modulators/pulse carvers), and passive components (e.g. waveguide interconnects, filters, couplers), thus enabling complex single-chip implementations of advanced transmitters and receivers [1-4]. In this work, we demonstrate an InP-based PIC transmitter comprising a widely tunable 1550-nm laser, a high-speed SOA, a high-speed Mach-Zehnder modulator (MZM), and a two-section high-power output SOA. The transmitter can be configured for various modulation formats including on-off keying (OOK), pulse position modulation (PPM), differential phase shift keying (DPSK), and frequency shift keying (FSK), and the high-power SOA obviates the need for an erbium-doped fiber amplifier (EDFA) especially for near-earth links.

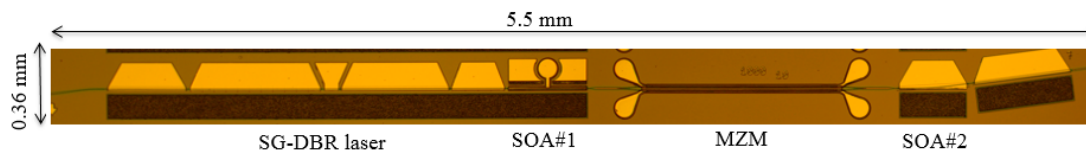


Figure 1. Microscope image of the fabricated InP-based PIC transmitter.

2. Transmitter fabrication and characterization

The PIC transmitter, of which the microscope image is shown in Fig. 1, consists of a widely tunable sampled grating distributed Bragg reflector (SG-DBR) laser, SOA, MZM, and high-power two-section SOA. The transmitter gain sections (used for the laser and SOAs) are based on an indium gallium arsenide phosphide (InGaAsP) multi-quantum-well structure grown on InP substrates by metalorganic chemical vapor deposition (MOCVD). The active/passive integration technique utilizes an offset structure with a single p-cladding regrowth as described in [5]. The sampled gratings in the laser section were defined by standard E-beam lithography and dry etched with chlorine-based ion beam etching. Photosensitive Benzocyclobutene (BCB) is used for its low dielectric constant to reduce parasitic pad capacitance for the high-speed SOAs and MZMs.

For characterization, the PIC was solder mounted to a ceramic carrier and wirebonded. The device submount was fixed to a temperature-controlled stage. Figure 2(a) shows the tuning characteristics of the SG-DBR laser. By controlling both the laser front and back SG-DBR mirror currents, the emission wavelength can be tuned from 1521 nm to 1565 nm, demonstrating a 44-nm tuning range, thus covering more than the entire C-band. The light-current-voltage (LIV) characteristics were measured by using the high-speed integrated SOA as a photodetector. As shown in Fig. 2(b), the laser exhibits a threshold current of 45 mA and an output optical power of 15 mW at a gain section current of 100 mA. The laser side mode suppression ratio (SMSR) is shown in Fig. 2(c) as a function of the laser wavelength, yielding an average value of 50.5 dB across the tuning range, with a maximum SMSR of 55 dB at wavelength near 1550 nm (see Fig. 2(d)).

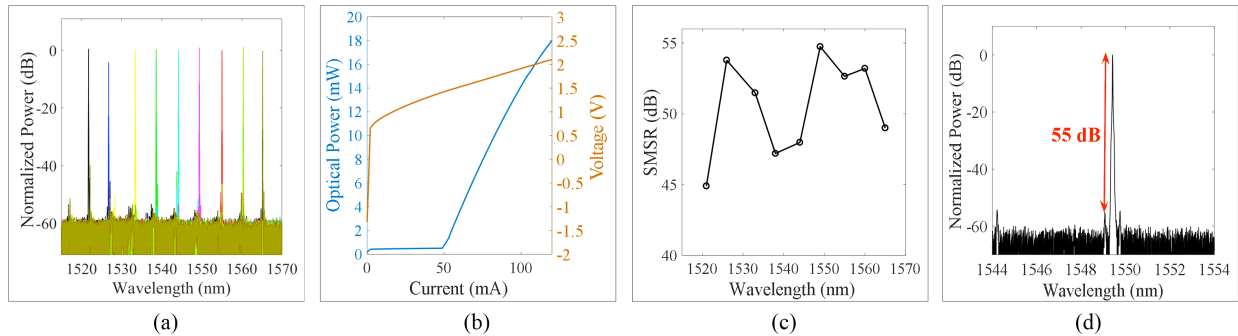


Figure 2. DC characterization of the SG-DBR laser: (a) Overlaid lasing spectra; (b) LIV characteristics; (c) SMSR versus wavelength; (d) Lasing spectrum near 1550 nm.

To characterize the performance of the high-speed MZM, a high-speed ground-signal-ground probe was contacted to a transmission line on the submount, and the transmission line was connected to the MZM through a wirebond. A bias-Tee was connected to the high-speed probe. Figure 3(a) and (b) show the modulation efficiency (transfer function) of the MZM under forward bias and reverse bias, respectively. As expected, the MZM is significantly more efficient under forward bias. This is attractive especially for applications where an MZM is used as a pulse carver (PPM configuration) for lower data rates. For higher data rates, reverse bias field-based modulation is preferable. Figure 3(c) shows the eye diagram for non-return-to-zero (NRZ) on-off keying (OOK) modulation with a forward bias of 1.22 V at 1Gbps; the measured extinction ratio (ER) was 13 dB. Figure 3(d) shows the NRZ OOK eye with a reverse bias of -5.7 V at 5Gbps. At this operating condition, the ER was measured to be 6.7 dB.

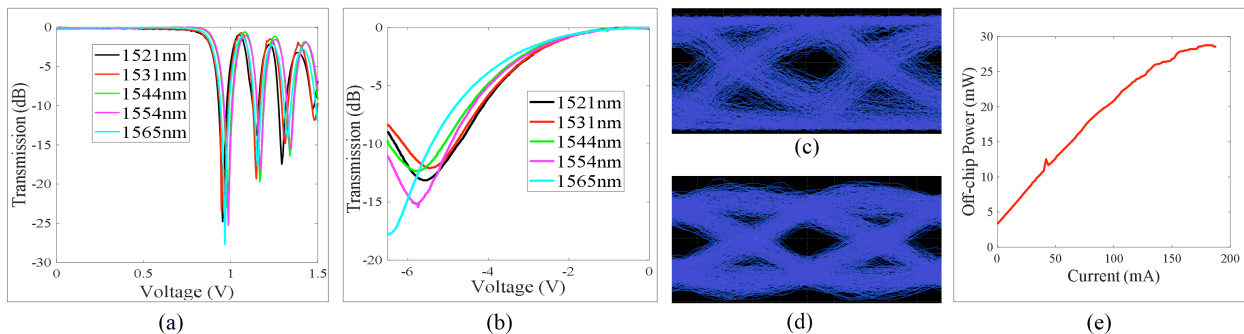


Figure 3. (a) MZM transfer function under forward bias; (b) MZM transfer function under reverse bias; (c) 1-Gbps NRZ OOK eye diagram with forward bias of 1.22 V; (d) 5-Gbps NRZ OOK eye diagram with reverse bias of 5.7 V; (e) Output optical power of the PIC transmitter versus current in the flared-waveguide section of the booster SOA for SOA#1 current of 130 mA and first section SOA#2 current of 90 mA.

Following the MZM is a two-section SOA where the second section has a flared waveguide width to reach a high output saturation level. With this booster SOA, the PIC transmitter could be used in some near-earth free space optical links without requiring an EDFA power amplifier. Figure 3(e) shows the output optical power of the PIC transmitter under conservatively low pumping conditions. Future measurements with anti-reflection coated devices and optimized heatsinking will increase the current levels for higher power.

3. Conclusions

An InP-based PIC transmitter was fabricated and characterized for free space optical communications. The SG-DBR laser demonstrates a 44-nm tuning range and high SMSR (on average 50 dB) across this range. The high-speed MZM demonstrated 1-Gbps operation under forward bias, and up to 5-Gbps operation under reverse bias, and the transmitter can be configured for various modulation formats to adapt to link and power requirements.

4. References

- [1] D. O. Caplan, "Laser communication transmitter and receiver design," *J. Opt. Fiber Commun.* vol. 4, pp. 225–362, 2007.
- [2] P. W. Juodawlkis, et al., "High-power, low-noise 1.5- μm slab-coupled optical waveguide (SCOW) emitters: physics, devices, and applications," *IEEE J. Quant. Elec.*, vol. 17, pp. 1698–1714, 2011.
- [3] V. Rosborough, et al. "Integrated transmitter for deep space optical communications," *2016 IEEE Avionics and Vehicle Fiber-Optics and Photonics Conference (AVFOP)*, Long Beach, CA, 2016, pp. 207-208.
- [4] V. Rosborough, et al. "Integrated Indium Phosphide Pulse Position Modulation Transmitter for Free Space Communications," in *Advanced Photonics 2016 (IPR, NOMA, Sensors, Networks, SPCom, SOF)*, paper ITu2A.3.
- [5] L. A. Coldren, et al. "High performance InP-based photonic ICs – a tutorial," *J. Lightw. Technol.*, vol. 29, pp. 554–570, 2011.

Vernier Transceiver Architecture for Side-Lobe-Free and High-Entendue LiDAR

Sergio Pinna^{1*}, Bowen Song¹, Larry A. Coldren¹ and Jonathan Klamkin¹

¹Electrical and Computer Engineering Dept., University of California, Santa Barbara, CA 93106 USA

*pinna@ece.ucsb.edu

Abstract: A Vernier-based LiDAR transceiver for high side-mode suppression optical phased arrays is proposed and investigated. This architecture enables side-lobe-free 180° viewing angle with multiple-wavelength waveguide spacing thereby easing fabrication requirements. © 2018 The Author(s)
OCIS codes: (000.010.3640) Lidar; (280.0280) Remote sensing and sensors; (280.3420) Laser sensors

1. Introduction

Automated technologies such as industrial robots, autonomous driving vehicles, and drones for defense applications require a high level of situational awareness for safe and effective operation [1, 2]. This is commonly achieved with a combination of passive and active sensors such as cameras, RaDAR, and LiDAR. Compared to RaDARs, LiDAR, owing to a very high carrier frequency, is characteristic of a narrow beamwidth, leading to superior angular resolution while maintaining a high range resolution not achievable with camera based sensors[3]. These attributes make LiDAR ideal for many applications where high resolution 3D performance is required such as environmental mapping and vehicle navigation. The most common LiDAR technology is based on scanning LiDAR whereby a single collimated beam scans the entire spatial volume to create a 3D map of the environment. The beam is commonly collimated with bulk optical components (lenses) and mechanically steered, leading to large size and weight, and, in harsh environments, reliability issues. To overcome these limitations, the development of optical phased array (OPA) solutions has come to the foreground. The principal challenge of OPAs is achieving sub-wavelength spacing for the array emitters, therefore these systems are prone to secondary lobes in the field of view. These lobes strongly limit system sensitivity and system entendue. Several techniques have been proposed to increase the unambiguous field of view, and these are based primarily on non-uniform OPA element spacing [4]. To date, these have demonstrated poor side-mode suppression ratio (SMSR) or require computationally heavy optimization methods to meet the desired OPA performance.

This work presents the simulation results of a novel Vernier-based LiDAR transceiver architecture capable of being fully integrated. The proposed scheme exploits two separated OPAs, one for the transmitter and one for the receiver, with wide (multi-wavelength) element spacing. Along with the potential for much simplified fabrication, this architecture enables high suppression of the sidelobes, thereby significantly increasing the system unambiguous field of view.

2. System description and simulation results

The Vernier-based LiDAR transceiver architecture is described schematically in Fig. 1(a). The transmitter laser is modulated by a Mach-Zehnder modulator (MZM) and coupled to the transmitter OPA. A portion of the transmitter laser light is directed to the receiver tunable coherent reception, thus improving system sensitivity while allowing simultaneous measurement of the target distance and velocity [5]. The receiver comprises a second OPA, which collects the light scattered by the target and routes it to the coherent receiver. The OPAs are composed of M transmitting elements and N receiving elements, respectively. M and N can be different or equal in value. The element spacing is respectively d_{tx} and d_{rx} , and are strictly different.

Studying a single OPA, the angular separation between two sidelobes, which corresponds to the OPA unambiguous field of view, is a function of the array element separation, d , and signal wavelength, λ , as described in Eq. 1. In order to avoid the presence of sidelobes within the total 180° field of view angle of the OPA, the maximum waveguide separation is equal to half of a wavelength, which, according to Eq. 1 would correspond to a waveguide separation $d < 750\text{nm}$ for $\lambda = 1550\text{nm}$.

$$\Delta\theta = \arcsin\left(\frac{\lambda}{2d}\right) \quad (1)$$

$$G(\theta) = G^{Tx}(\theta)G^{Rx}(\theta) \quad (2)$$

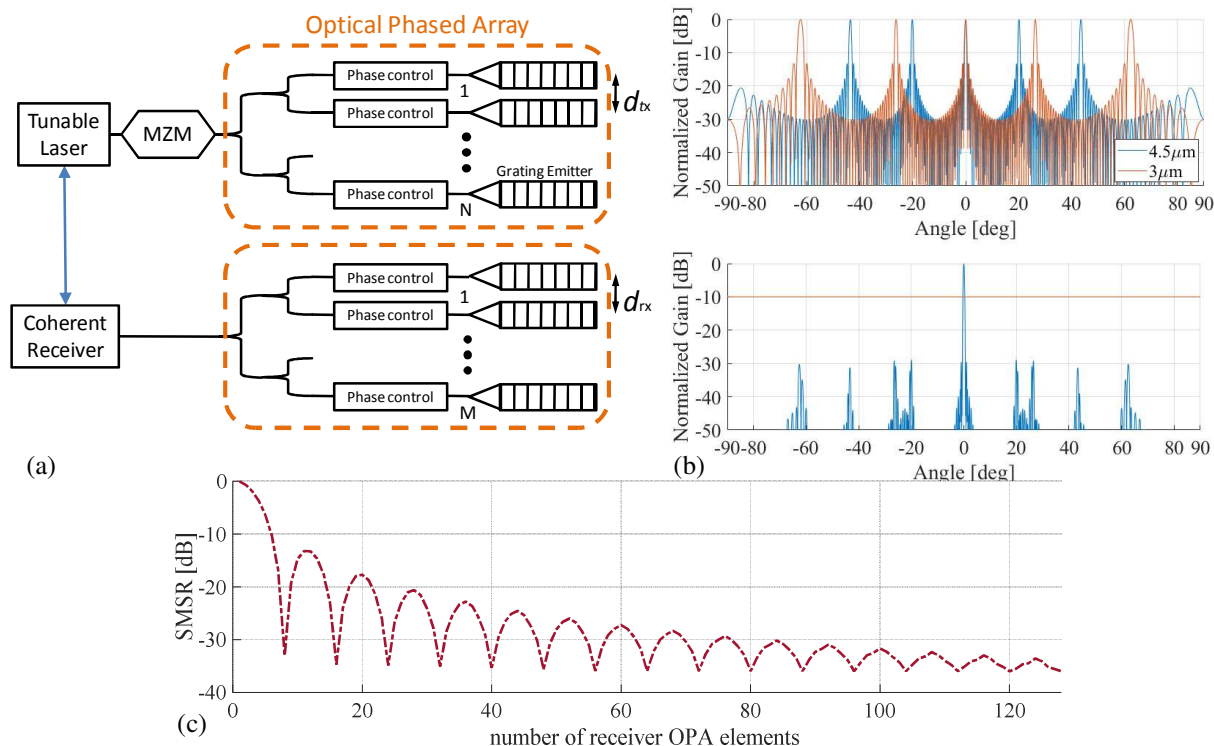


Figure 1: (a) Schematic of Vernier LiDAR architecture. (b) Radiation pattern for 3- μm spacing (red curve) and 4.5- μm spacing (blue curve) OPAs (top) and Vernier radiation pattern (bottom). (c) SMSR vs receiver radiating elements (transmitter elements = 128).

Considering a two OPA system, as the one proposed, the total gain associated with the transmitter and receiver chain (Eq. 2) is equal to the product of the transmitter and receiver gains. Based on Eq. 2, it is possible to design the two OPAs to yield a minimum of the transmitter gain where a sidelobe of the receiver is present, and vice versa, allowing for suppression of the unwanted sidelobes and expanding the sidelobe-free field of view of the system. This behavior is depicted in Fig. 1(b). The top plot shows the normalized gain as a function of the view angle for the two arrays (the transmitter and receiver OPAs) each one with 128 radiating elements and, respectively, a distance between the elements equal to 3 μm (red curve) and 4.5 μm (blue curve) for a wavelength of $\lambda=1550\text{nm}$. The two spacings, optimized to minimize the SMSR, yield radiation patterns with several sidelobes, with the two main lobes (0° angle) perfectly aligned, while the sidelobes, spaced about 20°, are slightly shifted with respect to each other. As a result, for the system gain reported in the bottom of Fig. 1(b), only the main lobe is preserved while the sidelobes are suppressed by more than 30dB. The OPA full width half maximum beam width (FWHM-BW) is 0.9°. As shown in Fig. 1(c) which reports the SMSR for a 128 elements transmitter OPA for different receiver OPA element count, good SMSR performance (SMSR>30dB) can be achieved even with significantly smaller receiver OPA, thus permitting a significant system size and cost reduction, at the cost of a slightly broadened beamwidth. This approach is therefore extremely promising for high performance and simplified fabrication enabled by the larger afforded emitter element spacing.

3. Conclusions

A novel LiDAR transceiver architecture based on the Vernier effect has been investigated. This scheme can be implemented in an OPA to enable side-lobe-free performance and high entendue with a waveguide spacing significantly greater than the signal wavelength, thereby simplifying fabrication. A SMSR greater than 25dB across the entire 180° viewing plane was theoretically demonstrated.

4. References

- [1] T. Ogawa et al., *Intelligent Vehicles Symposium (IV), 2011 IEEE*, pp. 734–739, 2011.
- [2] R. Rasshofer and K. Gresser, *Advances in Radio Science*, 3.B4, pp. 205–209, 2005.
- [3] D. D. Lichti and S. Jamtsho, *The Photogrammetric Record*, 21, 114, pp. 141–160, 2006.
- [4] Komljenovic, Tin, et al., *Optics Express* vol. 25.3 pp. 2511–2528, 2017.
- [5] Vercesi, V., et al., *Optics letters*, 40.7, pp. 1358–1361, 2015.

Integrated Indium Phosphide Transmitter for Free Space Optical Link

Hongwei Zhao, Sergio Pinna, Bowen Song, Ludovico Megalini, Simone Tommaso Šuran Brunelli, Larry Coldren and Jonathan Klamkin

Electrical and Computer Engineering Department, University of California Santa Barbara, Santa Barbara, CA 93106, USA
hwzhao@ece.ucsb.edu

Abstract: An integrated indium phosphide transmitter with 44-nm wavelength tuning range was demonstrated and inserted in a free space optical link. Error-free operation was achieved at 1 Gbps for an equivalent link length of 120 m. © 2018 The Author(s)

OCIS codes: (200.2605) Free space optical communication; (250.5300) Photonic integrated circuits

1. Introduction

Free space optical links can support much higher data rates than radio-frequency technologies and allow for greater flexibility in transmitter and receiver design and optimization [1]. Commercial-off-the-shelf (COTS) components provide a ready solution to assemble free space optical systems. However, communications from small spacecraft, where both performance and reliability are crucial, require optical components with lower cost, size, weight and power (CSWaP). The indium phosphide (InP) photonic integrated circuit (PIC) platform is attractive for free space links since it enables complex single-chip implementations of advanced transmitters and receivers [2-4]. In this work, an InP PIC transmitter was demonstrated comprising a widely tunable 1550-nm laser, a semiconductor optical amplifier (SOA) and a Mach-Zehnder modulator (MZM). With the fabricated PIC transmitter, a free space optical link was demonstrated; the bit error rate was measured at 1 Gbps and under different attenuation scenarios.

2. Transmitter Design and Characterization

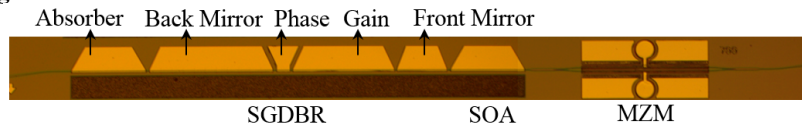


Fig. 1. Microscope image of fabricated InP PIC transmitter.

A microscope image of the fabricated InP PIC is shown in Fig. 1. The PIC consists of a widely tunable sampled grating distributed Bragg reflector (SGDBR) laser, SOA, and MZM. The PIC has a footprint of $4.4 \text{ mm} \times 0.36 \text{ mm}$. The indium gallium arsenide phosphide (InGaAsP) multiple quantum well structure was grown on an InP substrate by metalorganic chemical vapor deposition (MOCVD). The active/passive integration technique utilizes an offset structure with a single p-cladding regrowth [4]. The SGDBR laser consists of five sections: absorber, back mirror, phase section, gain section and front mirror. By tuning the injected current in the front/back mirrors, as shown in Fig. 2(a), the emission wavelength can be shifted from 1521 nm to 1565 nm. Figure 2(b) illustrates how the emission wavelength changes with the current applied to either the front or back mirror. Across the entire tuning range, the average side mode suppression ratio (SMSR) is 50 dB. A maximum SMSR of 55 dB was measured near 1550 nm, as shown in Fig. 2(c). The light-current-voltage (LIV) characteristics of the SGDBR laser (Fig. 2(d)) were measured by using the output SOA as a photodiode by applying a reverse bias and measuring the photocurrent. The threshold current of the laser is 45 mA and the optical power is 18 mW at a gain section current of 120 mA.

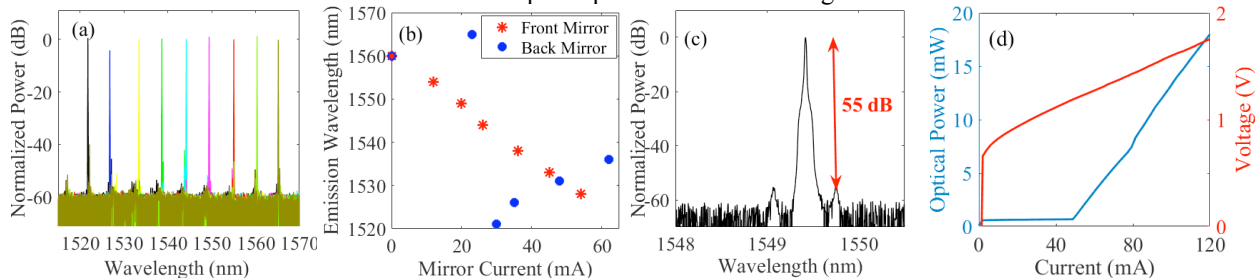


Fig. 2. SGDBR laser characteristics: (a) Overlaid lasing spectra; (b) Tuning characteristics; (c) Lasing spectrum near 1550 nm; (d) LIV characteristics.

The optical power from the SGDBR laser was boosted by a 400- μm -long SOA. Figure 3(a) shows the gain characteristics of the SOA at different input power levels. To measure the high-speed performance of the PIC

transmitter, a high-speed ground-signal-ground probe was contacted to the on-chip pads of the 700- μm -long MZM. The eye diagrams for 500 Mbps and 1 Gbps non-return-to-zero (NRZ) on-off keying (OOK) modulation are shown in Fig. 3(b), demonstrating an extinction ratio (ER) of 12.0 dB and 12.1 dB, respectively.

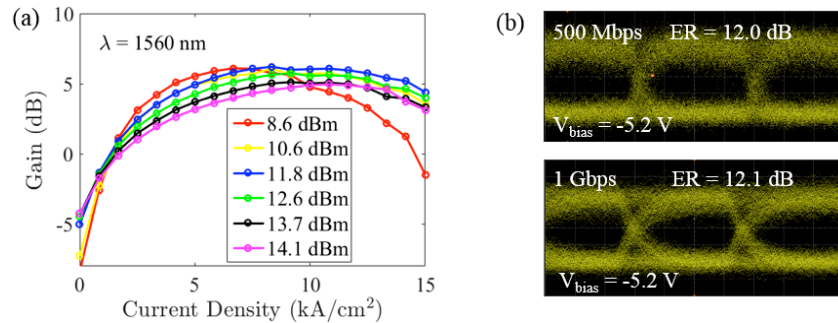


Fig. 3. (a) Gain as a function of SOA current density at different input power levels; (b) Eye diagrams for 500 Mbps and 1 Gbps NRZ OOK modulation.

3. Free Space Optical Link Demonstration

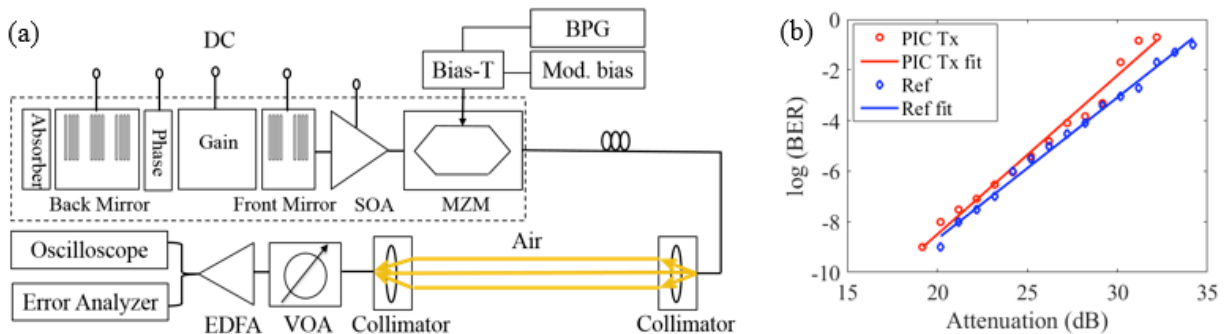


Fig. 4. (a) Schematic of free space optical link setup; (b) BER for 1 Gbps NRZ OOK transmission.

Utilizing the fabricated InP PIC transmitter, a free space optical link was constructed as shown in Fig. 4(a). The transmitter signal was collected by a single mode fiber (SMF) and coupled to an optical collimator, and then transmitted in air. At the receiver side, the light was collected by a second identical collimator (the two collimators are 1.35 m apart), and coupled to a SMF. An in-fiber variable optical attenuator (VOA) was used to simulate the geometric attenuation of the free space optical link. The equivalent length of the free-space transmission path, considering a beam divergence angle of 0.016° , spans from 0 m to 600 m (corresponding to from 0 dB to 34 dB of attenuation). At the receiver, an erbium doped fiber amplifier (EDFA) partially recovered the link loss and the signal was then detected by a PIN photodiode. Figure 4(b) shows bit error rate (BER) measurements at 1 Gbps as a function of the link attenuation. With the InP PIC (red), link operates free of errors ($\text{BER} < 1 \times 10^{-9}$) up to approximately 20 dB attenuation (120 m distance) and below the forward error correction limit ($\text{BER} < 2 \times 10^{-3}$), up to approximately 30 dB attenuation (400 m distance). Comparing the InP PIC performance with a reference 10 GHz commercial MZM and external cavity laser source (blue), the link power penalty associated with the integrated transmitter is less than 1 dB (at $\text{BER} < 1 \times 10^{-9}$).

4. Conclusions

A widely tunable InP PIC transmitter operating around 1550 nm was demonstrated for free space optical communications. The integrated SGDBR laser demonstrates a 44-nm tuning range and high SMSR (on average 50 dB) across the entire C band. Using the PIC transmitter, a free space optical link experiment was performed operating at 1 Gbps and demonstrating error free operation.

The authors acknowledge NASA for support through an Early Stage Innovations Award.

- [1] D. O. Caplan, "Laser communication transmitter and receiver design," *J. Opt. Fiber Commun.*, vol. 4, pp. 225–362, 2007.
- [2] V. Rosborough, F. Gambini, J. Snyder, L. Johansson, and J. Klamkin, "Integrated Indium Phosphide Pulse Position Modulation Transmitter for Free Space Communications," in *Proc. Integr. Photon. Res. (IPR)*, 2016, paper ITu2A.3.
- [3] J. Fridlander, S. Pinna, V. Rosborough, S. Estrella, L. Johansson, and J. Klamkin, "RZ-DPSK photonic integrated transmitter for space optical communications," in *Proc. SPIE Photonics West*, Jan., 2018, paper. 10524-34.
- [4] L. A. Coldren, S. C. Nicholes, L. Johansson, S. Ristic, R. S. Guzzon, E. J. Norberg, and U. Krishnamachari, "High Performance InP-Based Photonic ICs—A Tutorial," *J. of Lightw. Technol.*, vol. 29, no. 4, pp. 554-570, 2011.

Widely Tunable Integrated Laser Transmitter for Free Space Optical Communications

Hongwei Zhao, Sergio Pinna, Bowen Song, Simone Tommaso Šuran Brunelli, Brandon Isaac, Fengqiao Sang, Larry Coldren and Jonathan Klamkin

Electrical and Computer Engineering Department, University of California Santa Barbara, Santa Barbara, CA 93106, USA
hwzhao@ece.ucsb.edu

Abstract: Integrated laser transmitters are demonstrated for free space communications. The sampled grating DBR laser is tunable from 1521 nm to 1565 nm while maintaining >45 dB side mode suppression ratio. The transmitters demonstrate a 3-dB linewidth of 6.4 MHz and 7 Gbps data rate.

Keywords: Free space communication, photonic integrated circuits, sampled grating DBR laser, semiconductor optical amplifier, Mach-Zehnder modulator.

1. INTRODUCTION

Free space optical communications is of great interest recently for its promise to replace radio frequency systems for providing low-cost, reliable, high-speed connectivity for long-haul intersatellite and deep-space links [1, 2]. Compared to optical systems assembled with discrete commercial-off-the-shelf components, photonic integrated circuits (PICs) will dramatically reduce system cost, size, weight, and power (CSWaP) for free space links [3]. In our previous work, a 1-Gbps free-space optical link was demonstrated with a widely tunable indium phosphide (InP) PIC transmitter operating near 1550 nm, which is one of the key wavelengths utilized for space optical communications [4, 5]. Here the tuning characteristics and laser linewidth were studied and the InP PIC was implemented in a free-space optical link operating up to 7 Gbps.

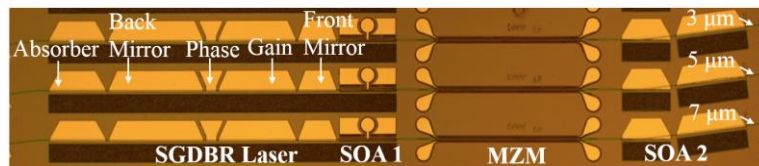


Fig. 1. Microscope image of fabricated InP-based PIC transmitters with different output booster SOA designs.

2. DEVICE CHARACTERIZATION

The InP-based PIC transmitter was fabricated with an indium gallium arsenide phosphide (InGaAsP) multi-quantum-well structure grown by metalorganic chemical vapor deposition (MOCVD). Figure 1 shows a microscope image of three different PIC transmitters. Each transmitter consists of a widely tunable sampled grating distributed Bragg reflector (SGDBR) laser, high-speed semiconductor optical amplifier (SOA), high-speed Mach-Zehnder modulator (MZM), and two-section output booster SOA. The ridge waveguide widths of the second section of the output SOAs are 3 μm , 5 μm and 7 μm , respectively, otherwise the three PICs are identical. With the flared waveguides, a higher output saturation power can be achieved. Each PIC transmitter has a footprint of 5.5 mm \times 0.36 mm. For characterization, the PIC was solder mounted to a ceramic carrier and wirebonded. The device submount was fixed to a temperature-controlled stage.

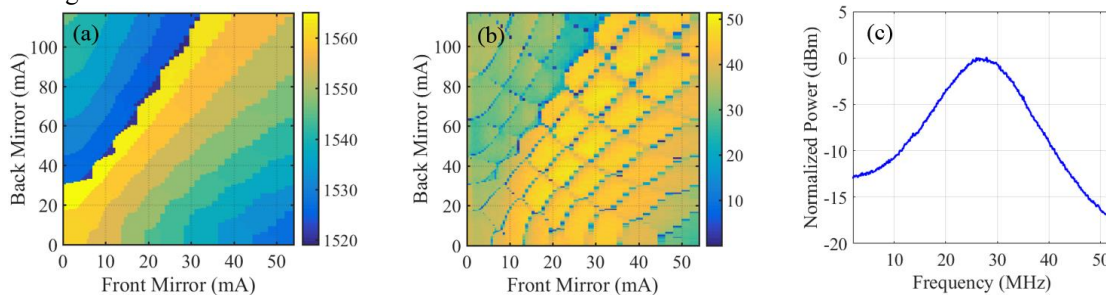


Fig. 2. DC characterization of the SGDBR laser: (a) Emission wavelengths (nm) as a function of currents applied to the front and back mirrors; (b) SMSR (dB) as a function of currents applied to the front and back mirrors; (c) Measured heterodyne laser linewidth spectrum demonstrating a 3-dB linewidth of 6.4 MHz.

As shown in Fig. 1, the multi-section SGDBR laser, consists of a back absorber, back SGDBR mirror, phase section, active gain section, and front SGDBR mirror. The emission wavelength can be tuned by adjusting the current applied to the front and back mirrors as well as the phase section. Without any tuning ($I_{\text{front mirror}} = I_{\text{back mirror}} = I_{\text{phase}} = 0$ mA), the emission wavelength is 1560 nm. Figure 2(a) shows the tuning characteristics of the SGDBR laser at a temperature of 15°C. The full tuning range is from 1521 nm to 1565 nm, covering more than the entire C band, which is most commonly used for free space laser communication. The side mode suppression ratio (SMSR) at different front and back mirror currents is demonstrated in Fig. 2 (b). As shown, greater than 45-dB SMSR was demonstrated over the entire tuning range. For the tuning maps generated (Fig. 2(a) and Fig. 2(b)), no current was applied to the phase section,

however, this could be leveraged for fine tuning and optimization of the wavelength precision and SMSR. For laser linewidth characterization, the self-delayed heterodyne method was utilized and the measurement results are shown in Fig. 2(c) demonstrating a 3-dB linewidth of 6.4 MHz.

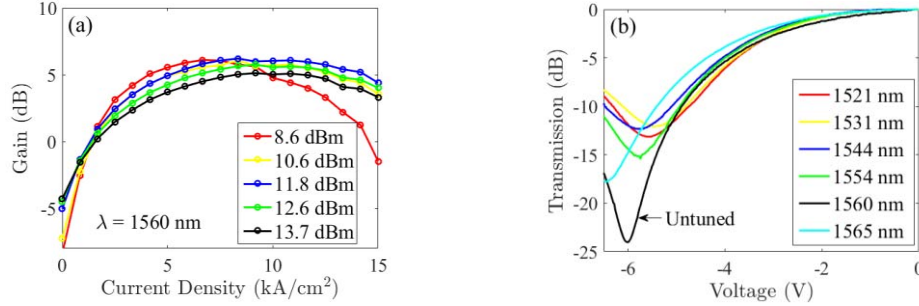


Fig. 3. (a) SOA gain as a function of current density at different input power levels; (b) MZM transfer function under reverse bias for different SGDBR laser wavelengths.

A 400- μm -long integrated high-speed SOA (SOA 1) follows the SGDBR laser. This can be used to compensate the insertion loss of the 1-mm-long MZM that follows. This SOA could also be used for modulating the SGDBR laser signal. The gain characteristics as a function of current density applied to SOA 1 are shown in Fig. 3(a). The transparency current of SOA 1 is approximately 15 mA. In conjunction with the MZM, this high-speed SOA can be utilized for pulse position modulation (PPM), which is commonly used for deep-space links [3]. Figure 3(b) shows the transfer function of the MZM under reverse bias. At a wavelength of 1560 nm, the DC extinction ratio (ER) is 24 dB with a V_{π} of -6.0 V.

A high-power two-section SOA (SOA 2) is used to boost the output signal. This comprises of a 350- μm -long curved waveguide section and a 500- μm -long flared waveguide. The output waveguide intersects the cleaved facet at an angle to minimize feedback to the laser cavity. The propagation loss of the curved waveguide is estimated to be 3 dB. The high-power SOA could obviate the need for an erbium-doped fiber amplifier (EDFA) especially for near-earth links. Figure 4(a) shows the output optical power of the PIC transmitter ($W_{\text{flare}} = 5 \mu\text{m}$) under conservatively low CW pumping conditions. The measured off-chip power is up to 14.5 dBm (28 mW). To characterize the RF performance of the modulator, one arm of the MZM was wire bonded to a 50- Ω RF feeding transmission line and on the other side to a 50- Ω load mounted to the ceramic carrier. Figure 4(b) shows the eye diagrams for non-return-to-zero (NRZ) on-off keying (OOK) modulation up to 7 Gbps at a bias of -2.2 V.

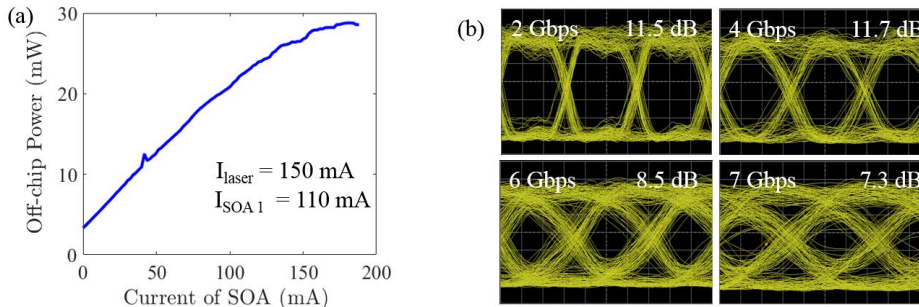


Fig. 4. (a) Output optical power of the PIC transmitter versus current in the flared-waveguide section of SOA 2 with a curved-waveguide section current of 90 mA; (b) Eye diagrams with NRZ OOK modulation.

3. CONCLUSION

An InP-based PIC transmitter was fabricated and characterized for free space optical communications. The SGDBR laser demonstrates a 44-nm tuning range and >45 dB SMSR across this range. The measured 3-dB linewidth is 6.4 MHz and off-chip optical power is 14.5 dBm. The high-speed MZM demonstrated up to 7 Gbps operation under reverse bias, and the transmitter can be configured for various modulation formats to adapt to link and power requirements.

ACKNOWLEDGMENT

The authors acknowledge support from the NASA Space Technology Mission Directorate.

REFERENCES

- [1] R.J. Cesarone, D.S. Abraham, S. Shambayati, and J. Rush, "Deep-space optical communications, visions, trends and prospects in Proc. Conf. Space Optical Systems and Applications, 2011, pp. 410-423.
- [2] D. O. Caplan, "Laser communication transmitter and receiver design," J. Opt. Fiber Commun. vol. 4, pp. 225—362, 2007.
- [3] V. Rosborough, F. Gambini, J. Snyder, L. Johansson, and J. Klamkin, "Integrated transmitter for deep space optical communications," in Conf. IEEE Avionics and Vehicle Fiber-Optics and Photonics (AVFOP), 2016, pp. 207-208.
- [4] H. Zhao, S. Pinna, B. Song, L. Megalini, S. T. Šuran Brunelli, L. Coldren, and J. Klamkin, "High-power integrated indium phosphide transmitter for free space communications," in Conf. on Lasers and Electro-Optics, 2018, paper JW2A.52.
- [5] H. Zhao, S. Pinna, B. Song, L. Megalini, S. T. Šuran Brunelli, L. Coldren, and J. Klamkin, "Integrated indium phosphide transmitter for free space optical link," in Advanced Photonics 2018 (IPR, NOMA, Sensors, Networks, SPPCom, SOF), paper ITu4B.6, in press.

3 Gbps Free Space Optical Link based on Integrated Indium Phosphide Transmitter

Hongwei Zhao, Sergio Pinna, Bowen Song, Ludovico Megalini, Simone Tommaso Šuran Brunelli, Larry Coldren and Jonathan Klamkin

Electrical and Computer Engineering Department, University of California Santa Barbara, Santa Barbara, CA 93106, USA

Email: hwzhao@ece.ucsb.edu / Phone: (857) 600-7938

In the last half century, advances in radio frequency (RF) and microwave technology have paved the way for space communications. Then in 2013, NASA demonstrated a two-way laser link between earth and a satellite in lunar orbit over 239,000 miles at a data rate of 622 Mbps, which is more than six times faster than previous state-of-the-art radio systems deployed to the moon [1]. The free space optical systems can be assembled with commercial-off-the-shelf (COTS) components. However, for deployment on small spacecraft, lower cost, size, weight and power (CSWaP) is required, while still demonstrating high output optical power and power-efficient modulation formats [2]. The indium phosphide (InP) photonic integrated circuit (PIC) platform is attractive for free space links since it enables complex single-chip implementations of advanced transmitters and receivers [3-5]. In this work, a free space optical link based on an InP PIC transmitter has been demonstrated. The transmitter is tunable from 1521 nm to 1565 nm, covering the entire C band. Error-free operation was achieved at 3 Gbps for an equivalent link length of 180 m (up to 300 m with forward error correction), and this distance can scale with the use of a high-power amplifier at the output.

The monolithic transmitter was fabricated on an n-type (001) InP substrate. The indium gallium arsenide phosphide (InGaAsP) multiple quantum well structure was grown on the InP substrate by metalorganic chemical vapor deposition (MOCVD). The active/passive integration technique utilizes an offset structure with a single p-cladding regrowth [6]. The InP PIC transmitter consists of a widely tunable sampled grating distributed Bragg reflector (SGDBR) laser, a high-speed semiconductor optical amplifier (SOA), a high-speed Mach-Zehnder modulator (MZM), and a two-section high-power output SOA. Figure 1(a) shows a microscope image of the fabricated PIC transmitter. The PIC has a footprint of 5.5 mm × 0.36 mm. SEM images at various stages of the fabrication process are shown in Fig. 1(b)-(e). The emission wavelength of the PIC transmitter can be shifted from 1521 nm to 1565 nm, as shown in Fig. 2. Across the entire tuning range, the maximum SMSR of 55 dB was measured near 1550 nm and the minimum SMSR of 45 dB at 1521 nm. The optical power from the SGDBR laser was boosted by a 400- μ m-long SOA (SOA 1), which can compensate the insertion loss in the following MZM. The two-section high-power output SOA (SOA 2) has a flared waveguide width to increase the saturation output power. To measure the high-speed performance of the transmitter, the chip was mounted on a high frequency ceramic submount. The eye diagrams for 1 Gbps and 3 Gbps non-return-to-zero (NRZ) on-off keying (OOK) modulation at a reverse bias of 3.9 V are shown in Fig. 3, demonstrating an extinction ratio of 13.4 dB and 16.8 dB, respectively.

The fabricated InP PIC transmitter was inserted in a free space optical link, as the setup shown in Fig. 4. A NRZ $2^{10} - 1$ pseudo random binary sequence (PRBS) was generated and used to drive the MZM through a bias-Tee. The optical signal from the transmitter was collected by a lensed single mode fiber (SMF) and coupled to an optical collimator (with a beam divergence angle of 0.016°), and then transmitted in air. At the receiver side, an identical collimator collected the light. The distance between the two collimators is 1.35 m. An in-fiber variable optical attenuator (VOA) was used to simulate the geometric attenuation of the free space optical link. The bit error rate (BER) measurements at 1 Gbps and 3 Gbps as a function of the link attenuation are shown in Fig. 5. At the data rate of 3 Gbps, the free space link operates free of errors ($BER < 1 \times 10^{-9}$) up to approximately 24 dB attenuation (180 m distance). With forward error correction ($BER < 2 \times 10^{-3}$), the equivalent link length can be up to 300 m (28 dB attenuation). At a lower data rate of 1 Gbps, the performance can be further improved. The corresponding link lengths at error free and forward error correction limit are 300 m and 400 m, respectively. A reference transmitter with a 10 GHz commercial MZM and an external cavity source was also tested in the link under the same setting.

In conclusion, a free space optical link with a widely tunable InP PIC transmitter around 1550 nm was demonstrated. Error-free operation was achieved at a data rate up to 3 Gbps with an equivalent link length of 180 m (up to 300 m with forward error correction).

- [1] R. Cesarone *et al.*, *Proc. Space Opt. System App.*, p. 410, 2011. [2] D. Caplan *et al.*, *J. Opt. Fiber Comm.* vol. 4, p. 225, 2007. [3] V. Rosborough *et al.*, *Advanced Photonics Congress*, p. ITu2A.3, 2016. [4] H. Zhao *et al.*, *CLEO*, p. JW2A.52, 2018. [5] H. Zhao *et al.*, *Advanced Photonics Congress*, p. ITu4B.6, 2018. [6] L. Coldren *et al.*, *J. Lightw. Technol.* 29 (4), 2007.

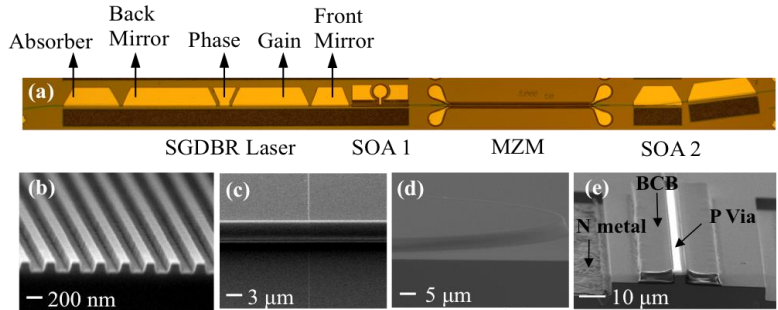


Fig. 1. (a) Microscope image of the InP PIC transmitter; (b)-(e) SEM images at various stages of the fabrication process: (b) The sampled gratings, (c) Dry etched waveguide ridge, (d) Sidewall of the BCB pattern, (e) Cross section of the high-speed SOA.

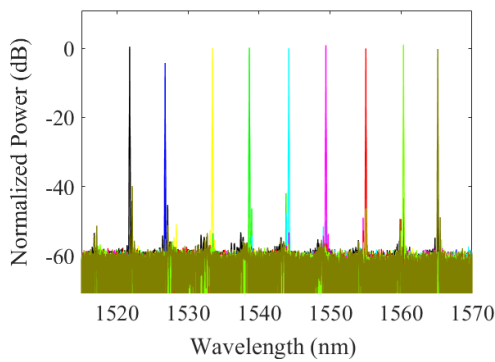


Fig. 2. Overlaid lasing spectra of the SGDBR laser.

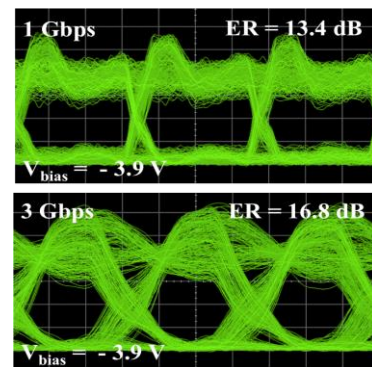


Fig. 3. Eye diagrams for 1 Gbps and 3 Gbps NRZ OOK modulation.

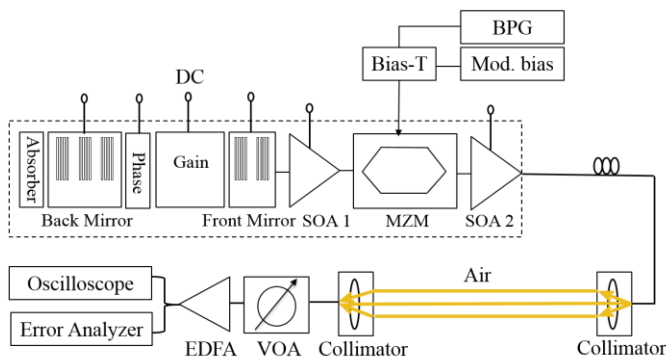


Fig. 4. Schematic of free space optical link setup.

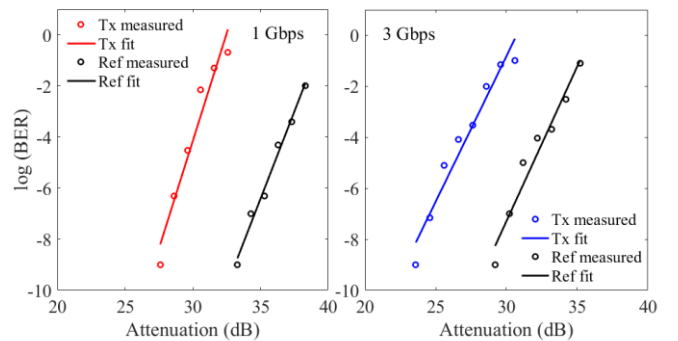


Fig. 5. BER for 1 Gbps and 3 Gbps NRZ OOK transmission.

Indium Phosphide Photonic Integrated Circuit Transmitter with Integrated Linewidth Narrowing for Laser Communications and Sensing

Brandon Isaac^{1*}, Bowen Song², Sergio Pinna², Shamsul Arafin³, Larry Coldren^{1,2}, Jonathan Klamkin²

¹Materials Department, University of California, Santa Barbara, California, 93106, USA

²Electrical and Computer Engineering Department, University of California, Santa Barbara, California, 93106, USA

*brandonjisaac@ucsb.edu

Abstract: An indium phosphide photonic integrated circuit transmitter with integrated linewidth narrowing capability is demonstrated. Frequency discrimination is achieved with an asymmetric Mach-Zehnder interferometer.

Introduction:

Tunable lasers have enabled significant advancements in communications and sensing applications [1]. Semiconductor diode lasers allow for reduced cost, size, weight, and power making them more widely deployable. Widely tunable semiconductor lasers, however, suffer from larger linewidth compared to short-cavity distributed feedback (DFB) lasers or external cavity lasers, thereby limiting their use in high-performance applications. Also for lidar applications, wide wavelength tuning can be utilized for beamsteering. We present an integrated solution for frequency locking and linewidth reduction of a widely tunable sampled grating distributed Bragg reflector (SGDBR) laser based on an indium phosphide (InP) photonic integrated circuit (PIC) platform that includes active/passive integration and two types of ridge waveguides to enable both low-loss and efficient active devices and sharp-bend-radius passive components. An integrated asymmetric Mach-Zehnder interferometer (AMZI) that taps excess light from the back SGDBR mirror is incorporated for frequency discrimination. The AMZI also includes a phase shifter to apply a frequency chirp. The PIC design and fabrication are discussed, and the components for linewidth narrowing are fully characterized including the laser, the AMZI discriminator, and the chirp phase shifter.

Design and Fabrication:

The PIC transmitter is comprised of an SGDBR laser and frequency discriminator. An external electrical circuit containing linear amplifiers and op-amps can provide the proportional and integral error correction respectively [1,2]. An SGDBR laser consists of a standard DBR laser modified by periodic blanking of the front and back grating mirrors at different sampling periods to produce Vernier-like mirror spectra. The output from the front SGDBR mirror is amplified by a semiconductor optical amplifier (SOA) and coupled off chip through an angled and cleaved facet. The PIC is designed to also alternatively couple light off chip vertically through a total internal reflection turning mirror (TIR), to enable hybrid integration with a silicon photonics optical phased array (OPA) [3]. Power is tapped from the back mirror for the AMZI frequency discriminator, which comprises multimode interference (MMI) couplers and a number of sharp bends. The path length difference of AMZI is designed for a free-spectral range (FSR) = $\frac{c}{n_{eff}\Delta L}$ of 60 GHz. Furthermore, one path contains a phase shifter for frequency chirping so that the laser can be tuned in frequency once it is stabilized. Two high-speed photodiodes (PDs) follow the AMZI for amplitude detection to generate an error signal for a feedback-loop based stabilization circuit. The sensitivity of the discriminator is higher for a smaller FSR, which is inversely proportional to the path length difference. However, increased path length difference leads to higher

passive optical loss, which reduces sensitivity. The 60-GHz FSR selected addresses this tradeoff.

The PIC transmitter layout and a microscope image of a fabricated chip are shown in Fig. 1. The PIC platform incorporates both surface ridge and deep ridge waveguides to allow for high-performance active components and sharp-bend-radii passive components, respectively. The SGDBR laser was designed for tuning over the wavelength range of 1520-1570 nm. The SGDBR mirrors were tailored for a front-to-

back mirror power splitting ratio of 7:1. For active/passive integration, the offset quantum wells were selectively removed. This was followed by formation of SGDBR gratings that were patterned with electron beam lithography and

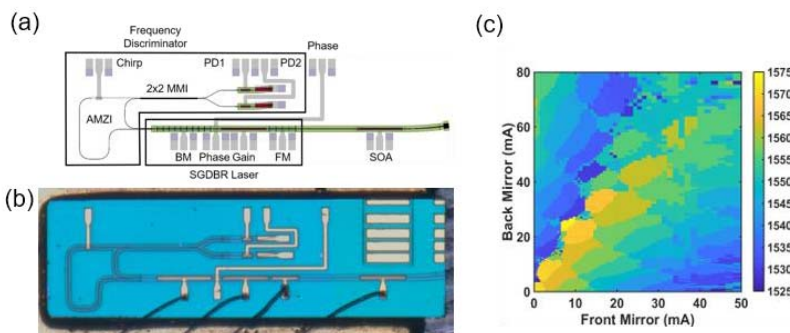


Figure 1 (a) Layout schematic of PIC showing SGDBR laser and frequency discriminator consisting of an AMZI, MMI couplers, and two photodetectors. (b) Microscope image of the fully fabricated PIC mounted on a carrier. (c) Wavelength tuning map of the SGDBR laser.

etched with reactive ion etching. Next the p-cladding was grown by metalorganic chemical vapor deposition. The remaining process steps were as follows: ridge waveguide formation based on inductively coupled plasma RIE (ICP-RIE) and wet chemical etching with a multi-step process to form both ridge types; device isolation with etching and ion implantation; vias and metal contact formation; sample thinning. A double taper structure was utilized to transition between surface ridge and deep ridge waveguides. The AMZI consists solely of deeply etched waveguides to achieve sharp bends and to reduce the overall footprint.

Experimental Results:

As illustrated in Fig. 1(c), the SGDBR laser demonstrated tuning from 1535-1570 nm. To evaluate the operation of the PIC transmitter, operation was first validated by measuring the laser light-current characteristic by sweeping the laser gain section current and measuring the photocurrent generated in the SOA following the laser and in the PDs (PD-1 and PD-2) as shown in Fig. 1(a). The photocurrent generated in the PDs was lower than expected, and this is attributed to higher than expected passive waveguide and passive component losses. As illustrated in Fig. 2(b), the PD signals were measured as the SGDBR laser phase section current was swept. As expected, the measured signals demonstrate the desired out-of-phase behavior and this measurement effectively tunes the laser. Instead to tune the AMZI filter, which would be performed to dynamically apply a frequency chirp to the stabilized laser, the photocurrent of the PDs was measured while sweeping the chirp phase shifter current (Fig. 2(c)). The inset of Fig. 2(c) shows a

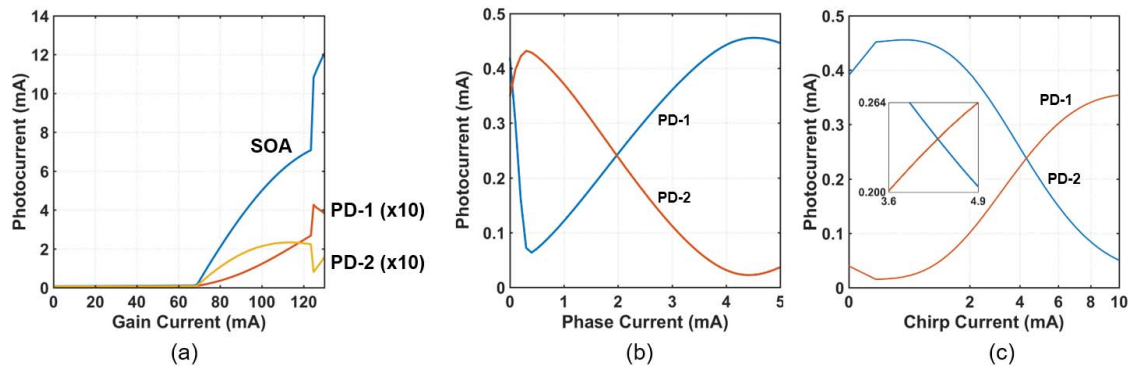


Figure 2 (a) Photocurrent detected out the front and back mirror from the SOA and balanced PDs respectively. (b) Photodetector response of discriminator as the current injected into the phase electrode is swept. (c) Photodetector response of the as the current injected into the chirp electrode in the AMZI is swept. The inset shows the linear region where a tuning efficiency of 4.4 mA/GHz is obtained.

closeup near the crossing point, and a tuning efficiency was estimated in this region to be 4.4 mA/GHz, illustrating the high efficiency attributed to current injection tuning in InP PICs. These measurements demonstrate the functionality of the PIC transmitter with integrated linewidth narrowing and frequency chirp capability. Future work will integrate a locker integrated circuit to demonstrate dynamic wavelength stabilization.

Conclusion:

We proposed and demonstrated an InP PIC transmitter with a widely tunable SGDBR laser and frequency discriminator based on a AMZI. The laser demonstrated 35 nm of wavelength tuning, showing potential for use with OPA-based lidars that utilize wavelength tuning for beamsteering. Locking functionality was demonstrated by measuring the out-of-phase signals generated by the AMZI frequency discriminator using the PDs. Chirp functionality was also demonstrated by first tuning the laser to a specific wavelength and then sweeping the chirp phase shifter current; a chirp efficiency of 4.4 mA/GHz was estimated. Experiments to demonstrate dynamic frequency locking and linewidth narrowing are in progress.

Acknowledgement

The authors acknowledge funding from DARPA AFOSR contract HR0011-16-C-0106 through a subcontract from Lockheed Martin. B. Isaac acknowledges support from the NSF GRFP.

References:

- [1] L. Coldren, G. Fish, J. Barton, L. Johansson, C. Coldren, "Tunable Semiconductor Lasers: A Tutorial" *Journal of Lightwave Technology* 22 (1) 2004
- [2] A. Sivanathan, H. Park, M. Lu, J. Parker, E. Bloch, L. Johansson, M. Rodwell, L. Coldren, "Integrated Linewidth Reduction of a Tunable SG-DBR Laser", *CLEO* (2013)
- [3] A. Sivanathan, H. Park, M. Lu, J. Parker, E. Bloch, L. Johansson, M. Rodwell, L. Coldren "Monolithic Linewidth Narrowing of a Tunable SG-DBR Laser" *OFC* (2013)
- [4] B. Song, C. Stagaescu, S. Ristic, A. Behfar, J. Klamkin, "3D integrated hybrid silicon laser," *Optics Express* 24(10), 10435-10444 (2016).

Indium Phosphide Photonic Integrated Circuits for Free Space Optical Links

Hongwei Zhao , Sergio Pinna, Bowen Song, Ludovico Megalini, Simone Tommaso Šuran Brunelli ,
Larry A. Coldren , *Life Fellow, IEEE*, and Jonathan Klamkin, *Senior Member, IEEE*

Abstract—An indium phosphide (InP)-based photonic integrated circuit (PIC) transmitter for free space optical communications was demonstrated. The transmitter consists of a sampled grating distributed Bragg reflector (SGDBR) laser, a high-speed semiconductor optical amplifier (SOA), a Mach-Zehnder modulator, and a high-power output booster SOA. The SGDBR laser tunes from 1521 to 1565 nm with >45 dB side mode suppression ratio. The InP PIC was also incorporated into a free space optical link to demonstrate the potential for low cost, size, weight, and power. Error-free operation was achieved at 3 Gb/s for an equivalent link length of 180 m (up to 300 m with forward error correction).

Index Terms—Free space communication, photonic integrated circuit, sampled grating DBR laser, semiconductor optical amplifier, Mach-Zehnder modulator, optical interconnect.

I. INTRODUCTION

FREE space laser communication is of great interest recently for providing reliable, high-speed connectivity for long-haul intersatellite and deep-space links [1]–[4]. In 2013, NASA demonstrated a two-way laser link between earth and a satellite in lunar orbits over 239,000 miles at a data rate of 622 Mbps, which is more than six times that of previous state-of-the-art radio systems flown to the moon. Commercial-off-the-shelf (COTS) components provide a ready solution to assemble free space optical systems. However, deployment of free space communication on small spacecraft, to enable low-cost and frequent missions that include high data rate downlink capability, requires photonic components with low cost, size, weight and power (CSWaP), while demonstrating high output optical power and power-efficient modulation formats [5]–[10]. Indium phosphide (InP) is the most mature and high-performance photonic integrated circuit (PIC) platform. It allows for the monolithic

Manuscript received February 1, 2018; revised June 19, 2018 and August 7, 2018; accepted August 13, 2018. Date of publication August 23, 2018; date of current version September 14, 2018. This work was supported by a NASA Early Stage Innovations Award. (*Corresponding author: Hongwei Zhao.*)

H. Zhao, S. Pinna, B. Song, S. T. Š. Brunelli, L. A. Coldren, and J. Klamkin are with the Department of Electrical and Computer Engineering, University of California Santa Barbara, Santa Barbara, CA 93106 USA (e-mail: hwzhao@ece.ucsb.edu; pinna@ece.ucsb.edu; bowen@ece.ucsb.edu; ssuranbrunelli@uemail.ucsb.edu; coldren@ucsb.edu; klamkin@ucsb.edu).

L. Megalini was with the Department of Electrical and Computer Engineering, University of California, Santa Barbara, CA 93106 USA. He is currently with Infineon Technologies, SiC High Power division, Villach 9500, Austria (e-mail: ludovico.megalini@infineon.com).

Color versions of one or more of the figures in this paper are available online at <http://ieeexplore.ieee.org>.

Digital Object Identifier 10.1109/JSTQE.2018.2866677

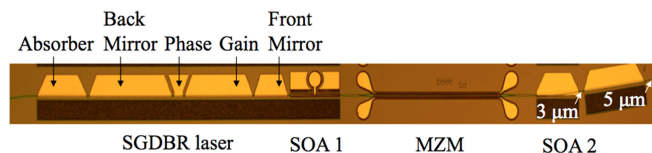


Fig. 1. Microscope image of fabricated InP-based PIC transmitter comprising of a five-section SGDBR laser (all sections are labeled in the figure), a high-speed SOA (SOA 1), a 1-mm long MZM, and a high-power two-section output booster SOA (SOA 2).

integration of all the required active components (e.g., lasers, semiconductor optical amplifiers (SOAs), modulators / pulse carvers), and passive components (e.g., waveguide interconnects, filters, couplers), thus enabling complex single-chip implementations of advanced transmitters and receivers [9]–[17]. Additionally, this platform is ideal for the telecommunication C band, which is the wavelength region of choice for free space optical communication. InP is therefore the platform of choice for space applications where reliability and technology readiness are critical.

Some previous works demonstrated that InP-based PICs can operate above 40 Gbps [18]–[20]. Our work here focuses on a few Gbps data rates, which is representative of state of the art for free space laser communication. For free space communications, it is desirable to achieve high energy efficiency and high output optical power. In this work, an InP-based PIC transmitter is demonstrated for free space optical links. The transmitter was tunable from 1521 nm to 1565 nm, covering the entire C band. The measured off-chip optical power was 14.5 dBm. The transmitter can be configured for various modulation formats including on-off keying (OOK), pulse position modulation (PPM), differential phase shift keying (DPSK), and frequency shift keying (FSK). The InP PIC was implemented in a free space optical link. Error-free operation was achieved at 3 Gbps for an equivalent link length of 180 m (up to 300 m with forward error correction).

II. INTEGRATION PLATFORM AND FABRICATION

The fabricated PIC transmitter is shown in the microscope image of Fig. 1. It consists of a widely tunable sampled grating distributed Bragg reflector (SGDBR) laser, a high-speed SOA (SOA 1), a Mach-Zehnder modulator (MZM), and a high-power two-section output booster SOA (SOA 2). The second section of SOA 2 has a flared waveguide for high output saturation power.

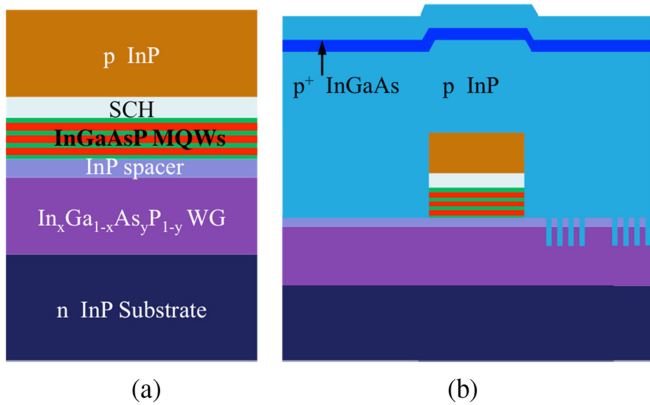


Fig. 2. (a) Epitaxial structure in the active region; (b) Sideview of the active/passive interface following regrowth.

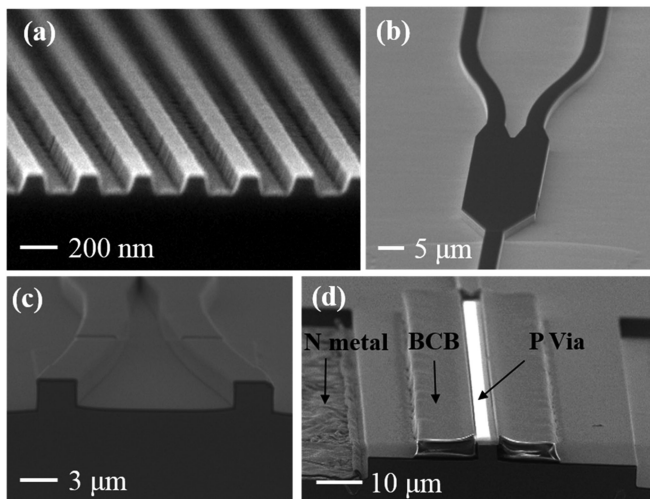


Fig. 3. SEM images at various stages of the fabrication process: (a) The sampled gratings of the front mirror of the laser; (b) Top view of a 1×2 MMI structure; (c) Cross section of a MMI with silicon nitride passivation; (d) Cross section of the high-speed SOA.

The waveguide at the output is angled with respect to the chip facet to reduce the reflectivity of this interface.

The epitaxial material structure was grown by metalorganic chemical vapor deposition (MOCVD) on an n-type (100) InP substrate. As shown in Fig. 2(a), the active region (used for laser and SOAs) consists of an indium gallium arsenide phosphide (InGaAsP) multi-quantum-well structure that is situated above an InGaAsP waveguide core layer [21]. The structure is designed to achieve a low confinement factor (4.2%) in the quantum well gain region, which is beneficial for providing SOAs with high saturation power. The active/passive integration technique utilizes an offset structure with the quantum wells being selectively removed by wet etching for passive waveguides and modulators. A sideview of the active/passive interface following the regrowth step is illustrated in Fig. 2(b), also showing the gratings etched into the waveguide core layer.

Fig. 3 shows scanning electron micrograph (SEM) images at various stages of the fabricated process. After the active/passive definition, the sampled grating mirrors were patterned by electron beam lithography and dry etched with chlorine-based ion beam etching (Fig. 3(a)). This was followed by a ‘blanket’ re-

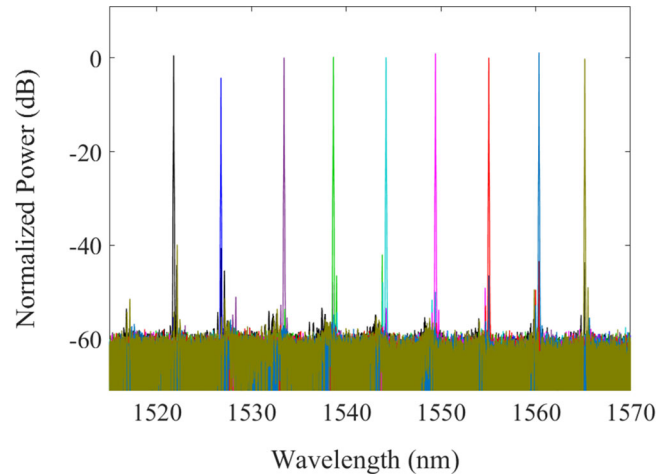


Fig. 4. Overlaid lasing spectra of the SGDBR laser.

growth of the InP cladding and p+ InGaAs contact layer [21], [22]. The waveguide ridges were then defined by dry etching and a cleanup wet etch to form smooth vertical sidewalls (Fig. 3(b) and (c)). Next, Ni/AuGe/Ni/Au n-contacts were deposited on the n InP substrate and annealed. The p+ InGaAs contact layer was removed between devices by wet etching to provide some electrical isolation. Photosensitive Benzocyclobutene (BCB) was used to reduce parasitic pad capacitance for the high-speed SOA and MZM (Fig. 3(d)). Ti/Pt/Au was deposited for p contacts and then annealed.

For backend processing, the fabricated samples were thinned to less than $180\text{-}\mu\text{m}$ thickness and then PICs were cleaved. Fabricated transmitters have a footprint of $5.5\text{ mm} \times 0.36\text{ mm}$. PICs were solder mounted to ceramic carriers and wire-bonded for characterization. Device submounts were fixed to a temperature-controlled stage.

III. DEVICE CHARACTERIZATION

A. SGDBR Laser

The widely tunable SGDBR laser, used as the integrated light source, consists of a rear absorber, back mirror, phase section, active gain section, and front mirror (see Fig. 1). The SGDBR laser has a 5-period front sampled grating mirror with $4\text{-}\mu\text{m}$ wide bursts and $68.5\text{-}\mu\text{m}$ period, a 12-period back sampled grating mirror with $6\text{-}\mu\text{m}$ wide bursts and $61.5\text{-}\mu\text{m}$ period [23], [24]. By controlling the injected current in the front and back mirrors, the emission wavelength can be tuned from 1521 nm to 1565 nm, demonstrating a 44-nm tuning range, thus covering more than the entire C-band. The tuning characteristics of the SGDBR laser are illustrated in Fig. 4, which presents the overlaid lasing spectra at various tuning conditions.

The light-current-voltage (LIV) characteristics were measured by using the reversed-biased high-speed integrated SOA as a photodetector. As shown in Fig. 5, the laser exhibits a threshold current of 45 mA and an output optical power of 15 mW at a gain section current of 100 mA; the peak power is well beyond 15 mW. The laser side mode suppression ratio (SMSR) across the tuning range is shown in Fig. 6, with a maximum SMSR of 55 dB at a wavelength near 1550 nm (see Fig. 7).

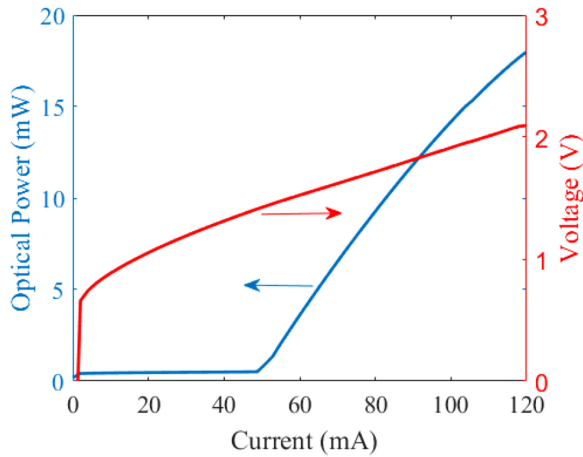


Fig. 5. SGDBR laser LIV curve (with CW current source) measured by using the SOA as a photodiode.

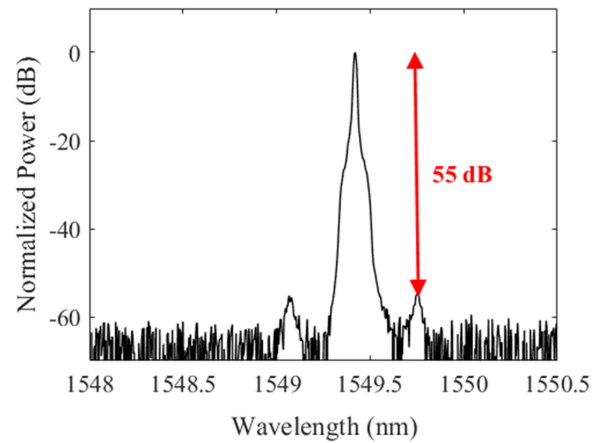


Fig. 7. Lasing spectrum near 1550 nm with a 55-dB SMSR measured by an optical spectrum analyzer with a resolution bandwidth of 0.02 nm.

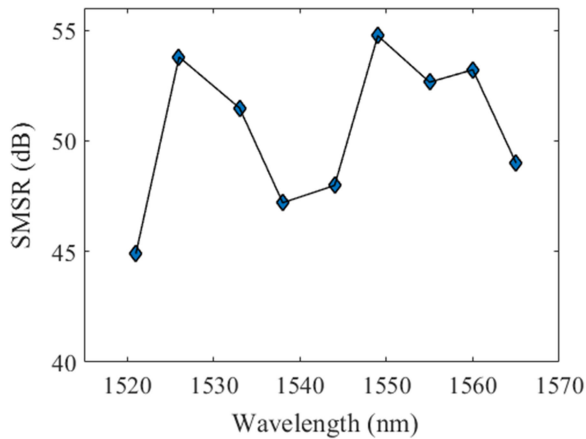


Fig. 6. Measured SMSR across the tuning range.

For laser linewidth characterization, the self-delayed heterodyne method was utilized and the measurement results are shown in Fig. 8 demonstrating a 3-dB linewidth of 6.4 MHz.

B. Mach-Zehnder Modulator

During the p-cladding regrowth, the zinc doping diffuses into the InGaAsP waveguide layer, significantly increasing the device capacitance. To address this issue, some of the waveguide layer adjacent to the fabricated ridge was removed with a low-power reactive ion etch step following ridge formation [25]. Then a BCB layer was patterned where metal pads would be later deposited in order to further reduce parasitic pad capacitance.

Fig. 9 and 10 report plots of the DC modulation characteristics (transfer functions) for the MZM under forward bias and reverse bias, respectively. Under forward bias, the MZM demonstrates an extinction ratio (ER) of 25 dB and half-wave voltage (V_{π}) lower than 0.25 V at 1554 nm with approximately a 0.7-V forward voltage bias. Under reverse bias, the ER is 15 dB with a V_{π} of -5.8 V. As expected, the MZM is significantly more

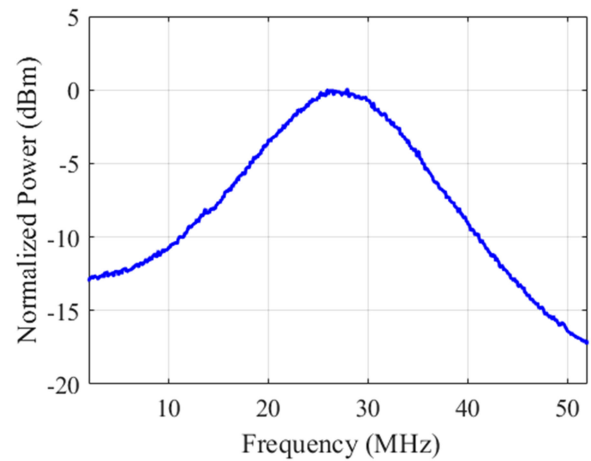


Fig. 8. Measured heterodyne laser linewidth spectrum demonstrating a 3-dB linewidth of 6.4 MHz.

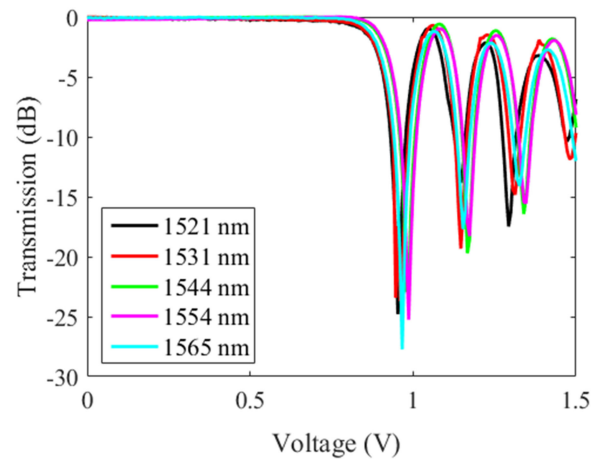


Fig. 9. MZM response under forward bias at various laser wavelengths.

efficient under forward bias. This is attractive especially for applications where an MZM is used for energy-efficient PPM for lower symbol rates. In this case, the MZM and high-speed SOA (SOA 1) would be simultaneously modulated by using two phase-aligned waveform generators.

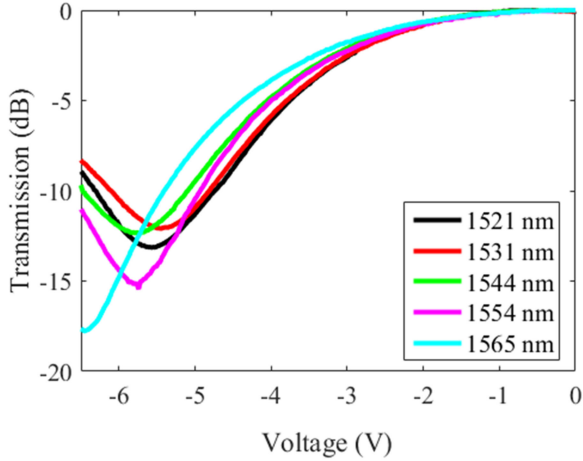


Fig. 10. MZM response under reverse bias at various laser wavelengths.

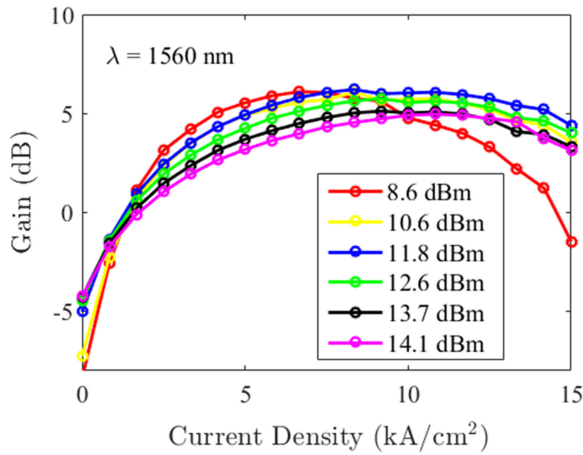


Fig. 11. Gain as a function of current density for the high-speed SOA ($3 \mu\text{m} \times 400 \mu\text{m}$) with different input power levels at a wavelength of 1560 nm.

C. Semiconductor Optical Amplifier

The PIC transmitter comprises of two SOAs: a high-speed SOA for amplification/modulation and a two-section booster SOA with curved/angled and flared ridge waveguides. SOA 1 is $3 \mu\text{m}$ wide and $400 \mu\text{m}$ long. It is placed after the laser and before the MZM, to compensate for modulator insertion loss, and could also be used for modulation. The gain characteristics of the high-speed SOA at different input power levels are shown in Fig. 11.

For SOA 2, it is constructed with two separate sections that can be pumped with different injection current levels, a scheme that may be utilized for optimizing power efficiency. The lengths of the two sections are $350 \mu\text{m}$ and $500 \mu\text{m}$, respectively. The second section linearly flares from $3 \mu\text{m}$ to $5 \mu\text{m}$, which reduces the optical power intensity thus enables an increased saturation power. This SOA at the transmitter output could potentially enable the PIC transmitter to be used in near-earth free space optical links without requiring an EDFA power amplifier.

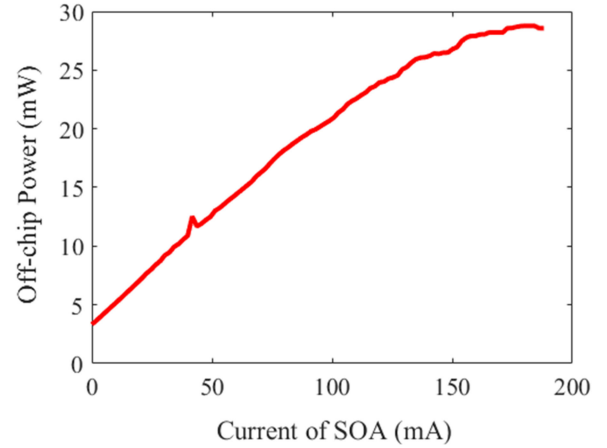


Fig. 12. Off-chip optical power of the PIC transmitter versus the current in the flared-waveguide section of the booster SOA.

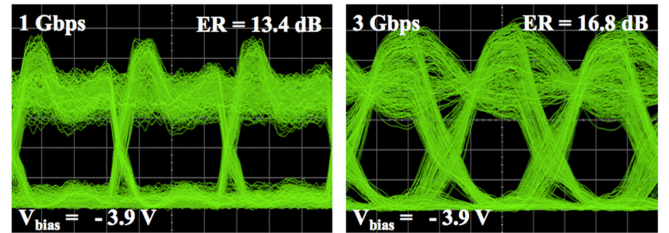


Fig. 13. Eye diagrams for 1 Gbps and 3 Gbps NRZ OOK modulation.

IV. FREE SPACE OPTICAL LINK

To evaluate the transmitter performance, first a static characterization was performed. The transmitter optical output was coupled to an integrating sphere to measure the off-chip power. Fig. 12 shows the off-chip power versus the current in the flared-waveguide section of the booster SOA. The current of the laser gain section, the SOA 1, and the first section of the SOA 2 are 150 mA, 110 mA and 90 mA, respectively. The maximum output power with the above DC biasing is 14.5 dBm (28 mW). The propagating loss of the curved and flared waveguides at the output is estimated to be 3 dB. The devices characterized were not anti-reflection (AR) coated, which would increase the coupled output power. Also, in future measurements with AR coated devices and improved heat sinking, it is expected that higher current levels can be achieved that will lead to higher measured output optical power.

To measure the high-speed performance of the transmitter, one arm of the MZM was wire bonded to a $50\text{-}\Omega$ RF feeding transmission line and on the other side to a $50\text{-}\Omega$ load mounted to the ceramic carrier. Fig. 13 shows the eye diagrams for 1 Gbps and 3 Gbps non-return-to-zero (NRZ) OOK modulation at a reverse bias of -3.9 V . The extinction ratios (ER) are 13.4 dB and 16.8 dB, respectively.

Utilizing the fabricated InP PIC transmitter, a free space optical link was constructed as shown in Fig. 14. A NRZ $2^{10} - 1$ pseudo random binary sequence (PRBS) was generated and applied to the MZM through a bias-Tee. The optical signal emitting

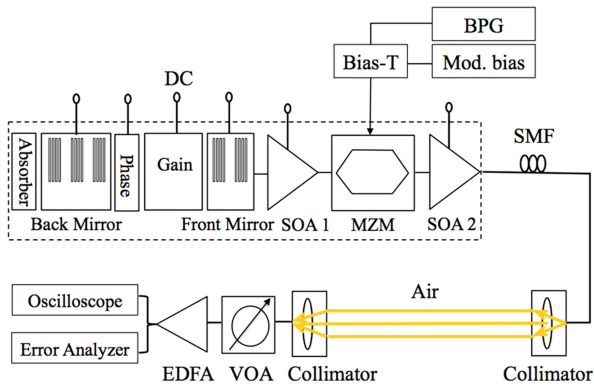


Fig. 14. Schematic of free space optical link setup.

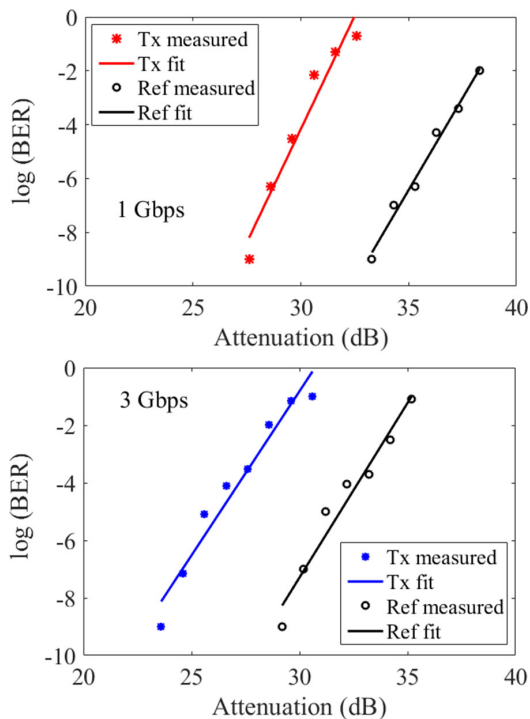


Fig. 15. BER for 1 Gbps and 3 Gbps NRZ OOK transmission.

from the transmitter was collected by a lensed single mode fiber (SMF) and coupled to an optical collimator (with a beam divergence angle of 0.016°), and then transmitted in air and collected by an identical collimator. The distance between the two collimators was 1.35 m. At the receiver side, an erbium doped fiber amplifier (EDFA) partially recovered the link loss and the signal was then detected by a PIN photodiode. An in-fiber variable optical attenuator (VOA) was used to simulate the attenuation of the free space optical link.

Bit error rate (BER) measurement results at 1 Gbps and 3 Gbps are shown in Fig. 15 as a function of the link attenuation. The free space link operates free of errors ($\text{BER} < 1 \times 10^{-9}$) up to approximately 24 dB attenuation (180 m distance) at the data rate of 3 Gbps. With forward error correction ($\text{BER} < 2 \times 10^{-3}$), the equivalent link length can be up to 300 m (28 dB attenuation). At a lower data rate of 1 Gbps, the performance can

be further improved. In this case, the corresponding link lengths at error free and forward error correction limit are 300 m and 400 m, respectively. A reference transmitter, consisting of a 10 GHz commercial MZM and an external cavity source, was also tested in the link under the same setting for comparison. The overall link length could be drastically increased with a booster high-power EDFA, which is commonly used in free space optical links.

In future work, other energy-efficient modulation formats, such as PPM at lower symbol rates, will be demonstrated for free space optical links. On the other hand, higher data rate up to 40 Gbps can be achieved with more compact modulator designs. Instead of using offset quantum wells, a quantum well intermixing technique would eliminate the tradeoff between modulation efficiency and insertion loss. Furthermore, efforts will be made to improve the output optical power. Structures with ultra-low optical confinement factor in the active gain region would enable lower local optical intensity inside the SOAs, thus allowing for higher output saturation power.

V. CONCLUSION

An InP-based PIC transmitter was fabricated and characterized for free space optical communications. The SGDBR laser demonstrates a 44-nm tuning range and >45 dB SMSR across this range. With the high-power output SOA, the measured off-chip power was 14.5 dBm. The InP PIC transmitter was inserted in a free space optical link. Error-free operation was achieved at a data rate up to 3 Gbps with an equivalent link length of 180 m (up to 300 m with forward error correction).

REFERENCES

- [1] H. Hemmati, A. Biswas, and I. B. Djordjevic, "Deep-space optical communications: Future perspectives and applications," *Proc. IEEE*, vol. 99, no. 11, pp. 2020–2039, Nov. 2011.
- [2] D. O. Caplan, "Laser communication transmitter and receiver design," *J. Opt. Fiber Commun.* vol. 4, pp. 225–362, 2007.
- [3] R. W. Kingsbury, D. O. Caplan, and K. L. Cahoy, "Compact optical transmitters for Cubesat free-space optical communications," in *Proc. SPIE, Free-Space Laser Commun. Atmos. Propag.*, 2015, Paper 9354.
- [4] R. J. Cesarone, D. S. Abrahams, S. Shambayati, and J. Rush, "Deep space communications visions trends and prospects," in *Proc. Int. Conf. Space Opt. Syst. Appl.*, 2011, pp. 412–425.
- [5] V. Rosborough, F. Gambini, J. Snyder, L. Johansson, and J. Klamkin, "Integrated transmitter for deep space optical communications," in *Proc. Conf. IEEE Avionics Veh. Fiber-Opt. Photon.*, 2016, pp. 207–208.
- [6] T. Su *et al.*, "Demonstration of free space coherent optical communication using integrated silicon photonic orbital angular momentum devices," *Opt. Express*, vol. 20, no.9, pp. 9396–9402, 2012.
- [7] J. Fridlander *et al.*, "RZ-DPSK photonic integrated transmitter for space optical communications," in *Proc. SPIE Photon. West*, 2018, Paper 10524-34.
- [8] V. Rosborough, F. Gambini, J. Snyder, L. Johansson, and J. Klamkin, "Integrated indium phosphide pulse position modulation transmitter for free space communications," in *Proc. Adv. Photon. (IPR, NOMA, Sensors, Networks, SPPCom, SOF)*, 2016, Paper ITu2A.3.
- [9] H. Zhao *et al.*, "High-power integrated indium phosphide transmitter for free space communications," in *Proc. Conf. Lasers Electro-Opt.*, 2018, Paper JW2A.52.
- [10] H. Zhao *et al.*, "Integrated indium phosphide transmitter for free space optical link," in *Proc. Adv. Photon. (IPR, NOMA, Sensors, Networks, SPPCom, SOF)*, 2018, Paper ITu4B.6.
- [11] L. A. Coldren *et al.*, "High performance InP-based photonic ICs—A tutorial," *J. Lightw. Technol.*, vol. 29, no. 4, pp. 554–570, Feb. 2011.

- [12] M. Smit *et al.*, "An introduction to InP-based generic integration technology," *Semicond. Sci. Technol.*, vol. 29, no. 8, pp. 083001–083004, 2014.
- [13] R. Nagarajan *et al.*, "Large-scale photonic integrated circuits," *IEEE J. Sel. Topics Quantum Electron.*, vol. 11, no. 1, pp. 50–65, Jan./Feb. 2005.
- [14] S. W. Corzine *et al.*, "Large-scale InP transmitter PICs for PM-DQPSK fiber transmission systems," *IEEE Photon. Technol. Lett.*, vol. 22, no. 14, pp. 1015–1017, Jul. 15, 2010.
- [15] S. C. Nicholes *et al.*, "The world's first InP 8x8 monolithic tunable optical router (MOTOR) operating at 40 Gbps line rate per port," in *Proc. Conf. Opt. Fiber Commun. Conf. Nat. Fiber Opt. Eng.*, 2009, Paper PDPB1.
- [16] P. W. Juodawlkis *et al.*, "High-power, low-noise 1.5- μm slab-coupled optical waveguide (SCOW) emitters: Physics, devices, and applications," *IEEE J. Sel. Topics Quantum Electron.*, vol. 17, no. 6, pp. 1698–1714, Nov./Dec. 2011.
- [17] J. W. Raring *et al.*, "40 Gbit/s photonic receivers integrating UTC photodiodes with high- and low-confinement SOAs using quantum well intermixing and MOCVD regrowth," *Electron. Lett.*, vol. 42, no. 16, pp. 942–943, 2006.
- [18] M. M. Dummer, J. Klamkin, A. Tauke-Pedretti, and L. A. Coldren, "40 Gb/s field-modulated wavelength converters for all-optical packet switching," *IEEE J. Sel. Topics Quantum Electron.*, vol. 15, no. 3, pp. 494–503, May/June 2009.
- [19] J. Summers *et al.*, "40 channels \times 57 Gb/s monolithically integrated InP-based coherent photonic transmitter," in *Proc. Eur. Conf. Opt. Commun.*, 2014, Paper P.2.5.
- [20] V. Lal *et al.*, "Extended C-band tunable multi-channel InP-based coherent transmitter PICs," *J. Lightw. Technol.*, vol. 35, no. 7, pp. 1320–1327, Apr. 2017.
- [21] L. C. V. Jayaraman, Z. M. Chuang, and L. A. Coldren, "Theory, design, and performance of extended tuning range semiconductor lasers with sampled gratings," *IEEE J. Quantum Electron.*, vol. 29, no. 6, pp. 1824–1834, Jun. 1993.
- [22] L. A. Coldren, "Monolithic tunable diode lasers," *IEEE J. Sel. Topics Quantum Electron.*, vol. 6, no. 6, pp. 988–999, Nov./Dec. 2000.
- [23] B. Mason, J. Barton, G. A. Fish, L. A. Coldren, and S. P. DenBaars, "Design of sampled grating DBR lasers with integrated semiconductor optical amplifiers," *IEEE Photon. Technol. Lett.*, vol. 12, no. 7, pp. 762–764, Jul. 2000.
- [24] J. S. Barton, E. J. Skogen, M. L. Masanovic, S. P. DenBaars, and L. A. Coldren, "A widely tunable high-speed transmitter using an integrated SGDBR laser-semiconductor optical amplifier and Mach-Zehnder modulator," *IEEE J. Sel. Topics Quantum Electron.*, vol. 9, no. 5, pp. 1113–1117, Sep./Oct. 2003.
- [25] J. S. Barton, "The integration of Mach-Zehnder modulators with sampled grating DBR lasers," Ph.D. dissertation, Dept. Elect. Comput. Eng., Univ. California, Santa Barbara, CA, USA, 2004.

Hongwei Zhao received the B.S. degree from the Huazhong University of Science and Technology, Wuhan, China, in 2008, and the M.S. degree from the Institute of Semiconductors, Chinese Academy of Sciences, Beijing, China, in 2011. She is currently working toward the Ph.D. degree at the Integrated Photonics Lab, Department of Electrical and Computer Engineering, University of California Santa Barbara, Santa Barbara, CA, USA. Her research interests include silicon photonics with emerging materials (such as graphene, indium tin oxide), and compound semiconductor photonic integrated circuits.

Sergio Pinna received the Ph.D. degree in innovative technologies from the Scuola Superiore Sant'Anna, Pisa, Italy, in 2014, and the B.Sc. and M.Sc. degrees in telecommunications engineering from the University of Pisa, Pisa, in 2008 and 2010, respectively. From November 2010 to December 2015, he was a Fellow with CNIT, National Photonic Networks Laboratory, Pisa. In 2014, he was a Visiting Researcher with the Integrated Photonics Laboratory, Boston University, Boston, USA. From January 2016, he was a Research Fellow with TeCIP Institute, Scuola Superiore Sant'Anna, Pisa, within the Digital and Microwave photonics group. In 2017, he joined the Integrated Photonics Laboratory, University of California Santa Barbara, as a Postdoctoral Research Associate.

Bowen Song received the B.Eng. degree from the School of Electronic Engineering and Optoelectronic Technology, Nanjing University of Science and Technology, Nanjing, China, in 2012, and the M.Sc. degree from Boston University, Boston, MA, USA, in September 2014. He is currently working toward the Ph.D. degree at the Department of Electrical and Computer Engineering, UCSB, Santa Barbara, CA, USA. He is from Shanxi, China. In early 2013, he joined the Wide Bandgap Semiconductor Laboratory, Boston University, working on developing nano-patterned sapphire substrate for AlGaIn-based deep UV LEDs. His current research interests include electronic-photonics integration, integrated photonics, and integrated Lidar.

Ludovico Megalini received the M.Sc. degree in ECE from UCSB, Santa Barbara, CA, USA, for which he had been awarded a Fulbright Scholarship; the M.Sc. degree in nanotechnology from ICT jointly awarded by Politecnico (IT), INPG (FR), and EPFL (CH), and had carried out the M.Sc. thesis project at MIT, Cambridge, MA, USA. He received the Ph.D. degree in materials from UCSB for his work on MOCVD growth, processing, and characterization of III-Nitride blue laser diodes. His past work experiences include positions as a Business Analyst with Accenture and as a Senior Process Engineer with Crossbar-Inc. He is currently working on SiC-based high-power T-MOSFETs at Infineon Technologies. His research interests include optoelectronics, high power devices and nanotechnology, including the design, heteroepitaxy growth, and fabrication of monolithically integrated lasers on silicon photonics and of high-power transistors.

Simone Tommaso Šuran Brunelli received the bachelor's degree in industrial engineering with a thesis on semiconductor quantum dots, and the master's degree in materials engineering with a thesis focused on atomic layer deposition, both from the Università degli Studi di Trieste, Trieste, Italy. He is currently working toward the Ph.D. degree at UCSB, Santa Barbara, CA, USA. After a fellowship with Elettra Sincrotrone working on carbon nanotube synthesis and photoelectron spectroscopy, he joined the Integrated Photonics Lab, UCSB. His current interests and duties revolve around metal organic chemical vapor deposition of III-V semiconductors for nanoelectronic and photonic applications including low-power tunneling transistors.

Larry A. Coldren (S'67–M'72–SM'77–F'82–LF'12) received the Ph.D. degree in electrical engineering from Stanford University, Stanford, CA, USA, in 1972. After 13 years in the research area with Bell Laboratories, he joined the University of California at Santa Barbara (UCSB) in 1984. He is currently the Fred Kavli Professor of optoelectronics and sensors and holds appointments with the Department of Materials and the Department of Electrical and Computer Engineering. From 2009 to 2011, he was the acting Dean of the College of Engineering. In 1990, he cofounded Optical Concepts, later acquired as Gore Photonics, to develop novel VCSEL technology, and, in 1998, he cofounded Agility Communications, later acquired by JDSU (now Lumentum), to develop widely tunable integrated transmitters. At UCSB, he worked on multiple-section widely tunable lasers and efficient vertical-cavity surface-emitting lasers (VCSELs). More recently, his group has developed high-performance InP-based photonic integrated circuits and high-speed, high-efficiency VCSELs. He has authored or coauthored more than a thousand journal and conference papers, eight book chapters, a widely used textbook, and 63 issued patents. He is a Fellow of OSA and the National Academy of Inventors, as well as a member of the National Academy of Engineering. He was the recipient of the 2004 John Tyndall Award, the 2009 Aron Kressel Award, the 2014 David Sarnoff Award, the 2015 IPRM Award, and the 2017 Nick Holonyak, Jr. Award.

Jonathan Klamkin received the B.S. degree from Cornell University, Ithaca, NY, USA, and the M.S. and Ph.D. degrees from the University of California Santa Barbara, Santa Barbara, CA, USA. From 2008 to 2011, he was a member of the Technical Staff with the Electro-Optical Materials and Devices Group, MIT Lincoln Laboratory, Lexington, MA, USA. From 2011 to 2013, he was an Assistant Professor with the Institute of Communication, Information and Perception Technologies, Scuola Superiore Sant'Anna, Pisa, Italy. From 2013 to 2015, he was an Assistant Professor of electrical and computer engineering (ECE) and materials with Boston University, Boston, MA, USA. In 2015, he joined the ECE Department, University of California Santa Barbara, where he is currently an Associate Professor. He is an Associate Editor for *Photonics Technology Letters* and the Vice Chair for the Microwave Theory and Techniques Society Subcommittee on Microwave Photonics. He was the Program Chair for the Integrated Photonics Research, Silicon and Nanophotonics Conference, in 2017, and is serving as the General Chair for the same conference, in 2018. He or his group members were the recipient of best paper awards at the 2006 Conference on Optoelectronic and Microelectronic Materials and Devices and the 2007 Microwave Photonics Conference, and the 2017 Asia Communications and Photonics Conference. He was the recipient of the NASA Early Career Faculty Award and DARPA Young Faculty Award. He is a senior member of the OSA.

I. Photonic Integrated Circuits

D. Signal Processing



Optics Letters

Optical dynamic memory based on an integrated active ring resonator

JIEJUN ZHANG,¹  ROBERT S. GUZZON,² LARRY A. COLDREN,² AND JIANPING YAO^{1,*} 

¹Microwave Photonics Research Laboratory, University of Ottawa, Ottawa, Ontario K1N 6N5, Canada

²Department of Electrical and Computer Engineering, University of California Santa Barbara, Santa Barbara, California 93116, USA

*Corresponding author: jpyao@eecs.uottawa.ca

Received 5 July 2018; revised 15 August 2018; accepted 16 August 2018; posted 27 August 2018 (Doc. ID 337960); published 21 September 2018

All-optical computing has been considered a solution for future computers to overcome the speed bottleneck encountered by the current electronic computers. High-speed optical memory is one of the key building blocks in realizing all-optical computing. In this Letter, we demonstrate an optical dynamic memory based on an amplified high Q -factor ring resonator that has the capability to achieve an infinite memory time. The optical memory uses an external pulse train to refresh the resonator, an operation in analogy to an electronic dynamic random-access memory widely used in modern computers, but at a speed that can be orders of magnitude faster. In our demonstration, a writing speed of 2.5 GHz is achieved with instant reading capability. The maximum writing speed can be as fast as 27.3 GHz if a shorter pulse is used. © 2018 Optical Society of America

OCIS codes: (210.4680) Optical memories; (200.4490) Optical buffers; (230.5750) Resonators; (250.4390) Nonlinear optics, integrated optics.

<https://doi.org/10.1364/OL.43.004687>

High-speed optical memory is one of the key building blocks for all-optical computing [1,2]. Commercial optical storage discs are playing an important role in cost-effective data storage. For example, a Blu-ray disc can store up to 25 gigabytes of data with single-layer patterning [3]. Recent advancements in data writing and storage techniques indicate a potential storage capacity of tens of terabytes per disk, making optical storage a strong competitor in the era of big data [4–6]. In contrast to the optical static memory based on disc patterning, optical dynamic memories that store photons to represent information have the potential of achieving much higher speeds for data reading, writing, and addressing. A high Q -factor optical resonator that can trap photons for a long time can be exploited to implement a dynamic optical memory. For example, an optical resonator with a Q -factor of 10^8 or higher can provide a photon storage time up to tens of nanoseconds [7]. However, the stored photons will eventually vanish due to the unavoidable loss in a resonator. Integrated amplifiers can be used in an optical resonator to partially compensate for the loss and to increase the photon storage time [7–9]. However, the photon

storage time still cannot be infinitely long, since the net gain in the resonator must be strictly less than unity to avoid lasing, making optical memories incompetent for all-optical computation.

Currently, dynamic optical memories are generally implemented with optical bistability devices, which can achieve ultra-fast read and write speed, as well as an infinite optical memory time [10–14]. Bistability optical memory can be switched between two output states by an optical control signal, with each state representing an optical logic. For example, an integrated optical memory based on optical bistability was reported in Ref. [13], in which an optical memory was realized by using an optical signal to switch the lasing direction of two microring lasers. The optical memory features an ultrashort switching time of 20 ps and a switching energy of 5.5 fJ. However, a constant optical probe is required for an optical bistability memory to both read the stored data and lock the memory in a specific memory state, which may result in high power consumption. In addition, electrical injection is generally required to sustain the stored optical signal.

In this Letter, we propose and experimentally demonstrate an optical memory based on an integrated active ring resonator that is optically refreshable. To achieve an extended memory time, a refreshing optical pulse that is in-phase with the stored signal is injected into the ring resonator to periodically refresh the stored information. The stored signal can be erased by injecting an optical pulse that is out of phase with the stored signal. The proposed optical memory integrates the merits of those based on a high Q -factor resonator with optical bistability, but without the need for a constant probe light. In contrast, a pulsed refreshing signal is used to periodically refresh the stored information, which can potentially have lower power consumption with an infinite memory time. The operation of the memory unit is in analogy to a dynamic random-access memory unit that is widely used in modern computers, in which a capacitor is used to store electrons that are refreshed electrically and periodically. In the proposed memory, information is carried by photons trapped in a resonator, in contrast to conventional optical memories based on optical bistability. The photons can carry more information encoded in polarization, wavelength, phase, and angular momentum and, thus, can potentially enhance the capability for all-optical computing.

Figure 1(a) shows the schematic of the proposed optical memory, and Figs. 1(b)–1(e) show the microscopic image of the fabricated chip which is wire-bonded to a carrier to facilitate electrical connection, and the scanning electron microscope (SEM) images of the key elements in the ring resonator. Four semiconductor optical amplifiers (SOA1–4) are incorporated to compensate for the coupling loss for the input signal, the refreshing signal, and the read-out signal, respectively. To enable a long memory time with a single refresh, two other SOAs (SOA5 and SOA6) are incorporated in the ring resonator to compensate for the round-trip loss. Two tunable couplers (TCs1–2) are used to change the coupling ratios between the bypass waveguides and the ring resonator. Each of the TCs consists of two multimode interferometer (MMI) couplers, and two phase modulators (PMs), as shown in Fig. 1. The coupling ratio of a TC can be tuned from 0 to 100% by changing the driving current that is applied to one of the PMs. The PM located in the ring modulator can be used to tune the resonance wavelength by applying a driving current.

A ring resonator can be used as an optical integrator. The transfer function of an optical integrator is given by [15]

$$H(\omega) = \frac{1}{j(\omega - \omega_0)}, \quad (1)$$

where $j = \sqrt{-1}$, ω is the angular frequency of the input signal, and ω_0 is the optical carrier frequency. An integrator is a band-pass filter with a π -phase jump at its central frequency. The integration of a positive pulse and a negative pulse can erase the information that is encoded in one of the two pulses. A ring resonator can be used to emulate an integrator with a finite integration time window due to its limited Q -factor. Based on the active ring resonator shown in Fig. 1, an optical integrator can be implemented by injecting a signal to be integrated from Port 1 and to get an integrated signal from Port 2. The response of the ring resonator is given by [16]

$$\frac{E_2}{E_1} = \frac{-\kappa_1^* \kappa_2 \sqrt{A} e^{j\phi/2}}{1 - \sqrt{A} t_1^* t_2^* e^{j\phi}}, \quad (2)$$

where t_1 , κ_1 , and t_2 , and κ_2 are the straight-through and cross-over coupling coefficients of TC1 and TC2, respectively; A is the round-trip optical power loss; ϕ is the round-trip optical

phase shift given by $\phi = \beta L$, in which β is the propagation constant of the waveguide; and L is the length of the ring resonator. By choosing proper coupling ratios of the TCs and reducing the round-trip loss, the response of a ring resonator can be configured to be close to that of an optical integrator within its free spectral range (FSR). The central wavelength of the integrator is equal to a resonance wavelength of the ring resonator, and the bandwidth is determined by the Q -factor of the ring resonator.

In our implementation, an optical pulse train with a central wavelength λ_c slightly shorter than a resonance wavelength of the ring resonator is launched via Port 1 as a refreshing signal. Due to a wavelength mismatch, the optical pulse train will be blocked from passing through Port 2. In this case, the ring resonator is considered to store an optical logic of “0.” To write an optical logic of “1” into the optical memory, an optical pulse with the same phase and a higher energy is launched via Port 4. The writing pulse is split into two parts by TC2, with most of the energy directed to Port 2 and the remaining coupled into the ring resonator. Due to the strong nonlinearity of the SOAs and the PM in the ring resonator, the coupled light will modify the resonance wavelength of the ring modulator [17] so that it will be shifted to λ_c . As a result, the ring resonator works as an integrator for the refreshing signal injected from Port 1. The output signals at Port 2 will be at a high optical power level, which is a sawtooth waveform corresponding to the integration of the refreshing pulse train. The optical memory is switched from optical logic “0” to “1.” However, due to the round-trip loss of the ring resonator, a single pulse in the refreshing pulse train can only sustain a high power level at Port 2 for a limited time. Thanks to the use of a pulse train as a refreshing signal, the next pulse will arrive and refresh the pulse recirculating in the resonator before it decays, thus extending the memory time for optical logic “1.” In addition, as a high optical power is confined within the ring resonator for “1,” the resonance of the ring resonator can be at around λ_c so that the refreshing pulse train can be continuously injected in the ring resonator, to make the resonator remain functioning as an integrator.

In the presence of strong nonlinearity, the internal electrical field is related to the injected optical electrical field E_1 [10]:

$$E_{\text{internal}} = \frac{\kappa_1 E_1}{1 - t_1^2 e^{2ikl - \alpha l}}, \quad (3)$$

where k and α are the optical-intensity-dependent refractive index and loss of the ring resonator, respectively. The refreshing pulse train can only be injected into the ring resonator when there is already an optical signal recirculating in it, which shifts the resonance wavelength of the ring resonator to align it with the wavelength of the incoming light. A refreshing pulse train has a lower optical power compared to that of a writing pulse. Hence, it cannot switch the ring resonator between two different states. The magnitude of a writing pulse, a refreshing pulse, and the required magnitude for optical switching are chosen based on the bistability response and the loss of the ring resonator, as shown in Fig. 2.

The optical memory unit is fabricated in the InP-InGaAsP material system. Figure 3 shows the experimental setup. A mode-locked laser (MLL) is used to generate the refreshing pulse train and the writing pulses. The MLL is locked to a microwave signal generator (SG) with an output frequency of 99.49 MHz. The MLL pulses are split by an optical coupler

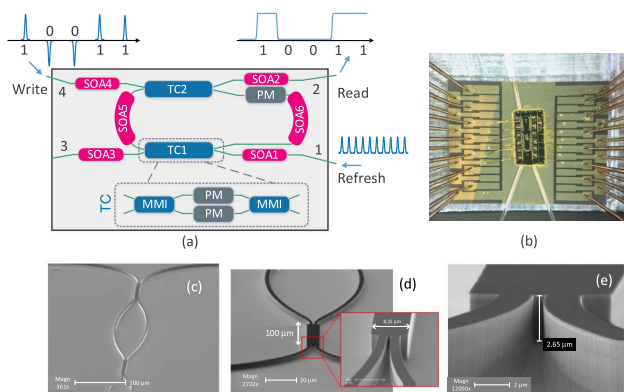


Fig. 1. (a) Schematic of the optical memory unit; (b) a photograph of the optical memory based on the InP/InGaAsP material system, wire-bonded to a polychlorinated biphenyl carrier; (c)–(e) SEM images of the TC, the MMI, and the waveguides. SOA, semiconductor optical amplifier; TC, tunable coupler; PM, phase modulator.

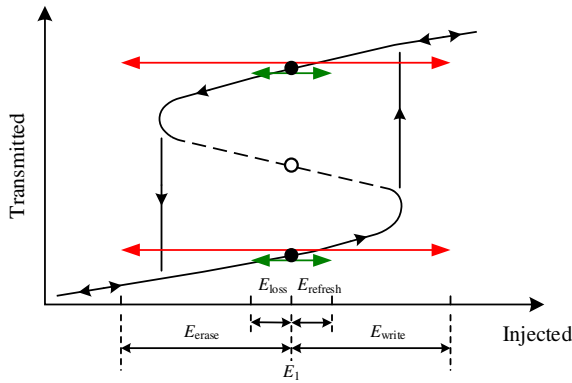


Fig. 2. Bistability response of the ring resonator from Port 1 to Port 2. The ring resonator has two possible output states at a given input of E_1 . The refreshing pulse $E_{refresh}$ is used to compensate for the loss of the ring resonator within the refreshing period E_{loss} . Strong writing and erasing pulses are used to switch the ring resonator between two output states.

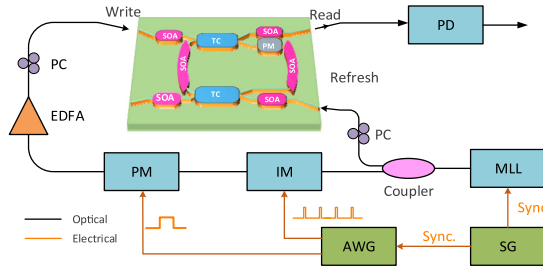


Fig. 3. Experimental setup. PD, photodetector; IM, intensity modulator; MLL, mode-locked laser; AWG, arbitrary waveform generator; SG, signal generator.

(OC), with one path directed to the refreshing port (Port 1) as the refreshing signal, and the other directed to an intensity modulator (IM) and a PM as a writing pulse with a phase of either “ π ” or “0.” The writing pulse is amplified by an erbium-doped fiber amplifier before being injected into the memory unit via the writing port (Port 4). Two polarization controllers (PCs) are used to optimize the optical coupling to the chip. A two-channel electrical arbitrary waveform generator (AWG) synchronized to the SG is used to generate two rectangular waveforms that are applied to the IM and the PM. The rectangular waveform applied to the IM has a repetition rate of 9.949 MHz and a duty cycle of 10%. The rectangular waveform applied to the PM has a duty cycle of 50% and a repetition rate of 2.487 MHz. The joint operation of the IM and the PM results in a writing pulse train with a repetition time of 100.5 ns and a π phase shift every two pulses. Figure 4 shows the pulse train from the MLL and the electrical waveforms that are applied to the IM and the PM.

To obtain a long memory time, it is critical to ensure that the second refreshing pulse is injected into the ring resonator before the first refreshing pulse fully decays. This can be achieved either by minimizing the round-trip loss or increasing the repetition rate of the refreshing pulse train. The round-trip loss is estimated to be 3.6 dB, excluding the coupling ratio of

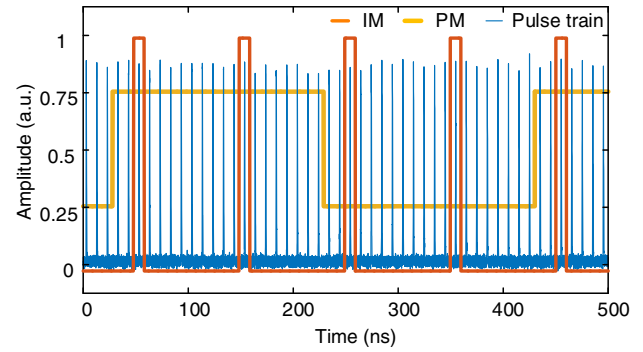


Fig. 4. Pulse train from the MLL fed to the refreshing port and the electrical signals applied to the IM and the PM.

the TCs. The two SOAs in the ring resonator can provide up to 20 dB of optical gain and, thus, can fully compensate for the round-trip loss. The optimum driving currents to the SOAs are chosen based on the coupling ratios of the TCs, and the net round-trip gain is kept below unity to avoid lasing. We first investigate the injection-power-dependent spectral response of the ring resonator. A continuous-wave light with a central wavelength at 1560 nm is launched into the memory via the refreshing port. As shown in Fig. 5(a), the measured resonance wavelength is redshifted by 15 pm when a light with a power of 16 dBm is injected. The wavelength shift is linearly proportional to the power increase.

Then we keep a constant injection power of 16 dBm and sweep the injection wavelength from 1559.79 to 1560.08 nm, as shown in Fig. 5(b). The resonance wavelength of the ring resonator is at around 1560.04 nm, and the FSR is around 218 pm. For the off-resonance injection wavelength from 1559.86 to 1559.99 nm, the resonance wavelength of the ring resonator does not change significantly. However, when a near-resonance wavelength from 1560.01 to 1560.03 nm is injected, the resonance wavelength is shifted dramatically and the peak of the spectral response drops, which agrees well with the prediction given by Eq. (3). The drop in the resonance peak is due to the saturation of the output SOA2 caused by the injected light. Thus, both the refractive index and the loss of the ring resonator are intensity dependent. Figure 5(a) shows a weaker nonlinearity within the ring resonator as compared with the case in Fig. 5(b), where the injection wavelength in Fig. 5(a) is far from the resonance wavelength which results in lower optical power confined in the ring resonator. An optical vector analyzer (OVA) is used to measure the transmission spectrum. Note that the power of the probe light from the OVA is low, so that no asymmetric spectral response with the resonance peak is seen.

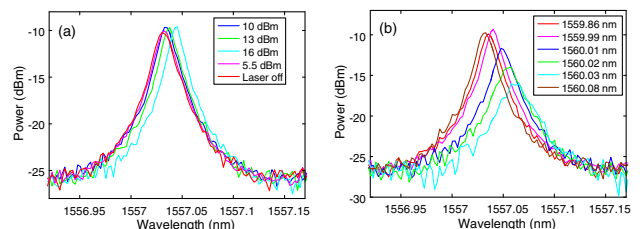


Fig. 5. Response of the ring resonator as a function of (a) the injecting optical power and (b) the injecting optical wavelength.

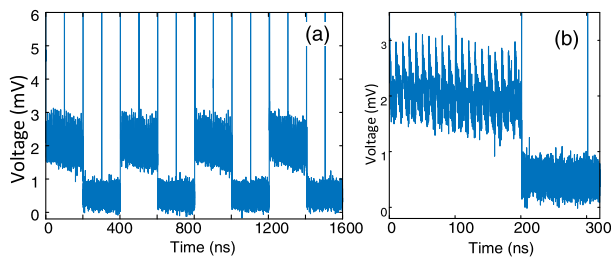


Fig. 6. (a) Detected waveform at the reading port when the writing and refreshing pulse trains illustrated in Fig. 4 are launched into the memory unit; (b) the zoom-in view of the waveform.

Then the ring resonator is tested as an optical memory. The bias current to the PM is tuned to find the optimum resonance wavelength corresponding to the central wavelength of the input optical signal. An optical writing pulse train with a periodic phase pattern of ["0", "0", " π ", " π "] and a refreshing pulse train with a repetition rate of 99.49 MHz are launched into the memory via the writing port and the refreshing port, respectively. The optical signal obtained at the reading port is sent to a photodetector (PD) and sampled by an electrical oscilloscope. Figure 6 shows the sampled waveform. The memory is originally in the "0" state. No optical power can be detected at the PD, as the optical pulses coming from the refreshing port are off-resonance and blocked by the ring resonator. When a negative pulse with π phase is injected as the writing signal, the ring resonator will be shortly excited to have highly confined optical power. However, the optical signal confined in the ring resonator cannot be refreshed by the refreshing pulse train, as they are of opposite phases. In contrast, when a positive writing pulse is injected, the ring resonator will be excited by the confined signal having the same phase with the refreshing signal. The memory is then repeatedly refreshed and, eventually, reaches a stable state where the refreshing power perfectly compensates for the loss of the ring resonator. The ring resonator is then switched to and held at the high-level state representing an optical logic "1." To erase the stored optical information, a negative writing pulse with a phase of π is injected via the writing port. Destructive interference will occur so that the confined optical power goes below the bistability region, as indicated in Fig. 2. The memory returns to the low level state corresponding to an optical logic of "0." A memory time of 100 ns is achieved, as shown in Fig. 6. In fact, the memory time of the ring resonator can be infinite, if the phase coherence between two consecutive pulses from the MLL is preserved, so that the latter can refresh the former. The experimental writing and reading speed is 2.5 GHz, which is determined by the MLL pulse width of 0.4 ns. Note that the nonlinearity excitation time is in the scale of picoseconds [18], and the ring resonator has an FSR of 27.3 GHz, which indicates that the acceptable pulse can be as short as 36.6 ps or a writing and reading speed of 27.3 GHz, exceeding the speed of any state-of-the-art electronic dynamic random-access memory units. If a ring resonator with a smaller size is used, the writing and reading speed can be further increased.

The power consumption of the memory is mainly from the power consumption due to the electrical bias to SOA5 and due to the optical pulses to refresh the memory, which are calculated to be 72.86 mW and 100 dBm, respectively. We believe that the total power consumption can be reduced to be below 100 mW if the fiber-to-chip coupling loss and the round-trip loss are minimized.

In summary, an optically refreshable optical dynamic memory based on an active ring resonator was designed, fabricated, and demonstrated. A memory time of 100.5 ns was demonstrated by refreshing the optical memory every 10.05 ns. An infinite memory time can be potentially achieved if a refreshing signal is injected constantly. In our demonstration, the writing and reading speed was 2.5 GHz. It should be noted that the writing and reading speed can be increased by using pulses with a narrower temporal width to write, read, and refresh the memory. The proposed optical memory is suitable for large-scale integration to achieve a high-speed and large-capacity optical dynamic random-access memory array, in which ring resonators with different diameters can be constructed to realize wavelength-multiplexed optical memory. The proposed device eliminates the bottleneck of limited memory time of an optical memory based on a high Q resonator and reduces the complexity by using optical refresh and, thus, can find applications for future high-speed all-optical computation.

Funding. Natural Sciences and Engineering Research Council of Canada (NSERC).

REFERENCES

1. A. E. Willner, S. Khaleghi, M. R. Chitgarha, and O. F. Yilmaz, *J. Lightwave Technol.* **32**, 660 (2014).
2. W. Liu, M. Li, R. S. Guzzon, E. J. Norberg, J. S. Parker, M. Lu, L. A. Coldren, and J. Yao, *Nat. Photonics* **10**, 190 (2016).
3. T. D. Milster, *Opt. Photon. News* **16**(3), 28 (2005).
4. E. Walker and P. M. Rentzepis, *Nat. Photonics* **2**, 406 (2008).
5. M. Gu, X. Li, and Y. Cao, *Light: Sci. Appl.* **3**, e177 (2014).
6. X. Li, Y. Cao, N. Tian, L. Fu, and M. Gu, *Optica* **2**, 567 (2015).
7. W. Liu, M. Li, R. S. Guzzon, E. J. Norberg, J. S. Parker, L. A. Coldren, and J. Yao, *J. Lightwave Technol.* **32**, 3654 (2014).
8. T. Zhong, J. M. Kindem, J. Rochman, E. Miyazono, A. Faraon, A. Ferrier, and P. Goldner, *Proc. SPIE* **9762**, 97620J (2016).
9. E. Miyazono, I. Craiciu, A. Arbabi, T. Zhong, and A. Faraon, *Opt. Express* **25**, 2863 (2017).
10. R. W. Boyd, *Handbook of Laser Technology and Applications (Three-Volume Set)* (Taylor & Francis, 2003), pp. 161–183.
11. B. S. Wherrett, *Appl. Opt.* **24**, 2876 (1985).
12. S. Smith, I. Janossy, H. MacKenzie, J. Mathew, J. Reid, M. Taghizadeh, F. Tooley, and A. Walker, *Opt. Eng.* **24**, 244569 (1985).
13. M. T. Hill, H. J. Dorren, T. De Vries, X. J. Leijtens, J. H. Den Besten, B. Smalbrugge, Y.-S. Oei, H. Binsma, G.-D. Khoe, and M. K. Smit, *Nature* **432**, 206 (2004).
14. T. Christopoulos, O. Tsilipakos, and E. E. Kriezis, *J. Appl. Phys.* **122**, 233101 (2017).
15. M. Ferrera, Y. Park, L. Razzari, B. E. Little, S. T. Chu, R. Morandotti, D. Moss, and J. Azaña, *Nat. Commun.* **1**, 29 (2010).
16. L. Chrostowski and M. Hochberg, *Silicon Photonics Design: From Devices to Systems* (Cambridge University, 2015).
17. W. Zhang, W. Li, and J. Yao, *Opt. Lett.* **41**, 2474 (2016).
18. H. Wang, K. Ferrio, D. G. Steel, Y. Z. Hu, R. Binder, and S. W. Koch, *Phys. Rev. Lett.* **71**, 1261 (1993).

II. Widely-Tunable VCSELs

Wide, Continuously Swept VCSEL Using a Novel Air-Cavity-Dominant Design

Pengfei Qiao¹, Kevin T. Cook¹, Jipeng Qi¹, Larry A. Coldren² and Connie J. Chang-Hasnain¹

1: EECS Department and Tsinghua-Berkeley Shenzhen Institute, University of California, Berkeley, CA 94720, USA

2: Department of Electrical and Computer Engineering, University of California, Santa Barbara, CA 93117, USA

Email address: cch@berkeley.edu

Abstract: We report electrically-pumped MEMS-VCSELs with a record 70 nm continuous wavelength sweep at 1057-nm with 600 kHz rate using a novel air-cavity-dominant design. Such devices are promising for swept-source OCT and 3D sensing applications. © 2018 The Author(s)

OCIS codes: (140.7260) Vertical cavity surface emitting lasers; (050.6624) Subwavelength structures; (230.4685) Optical microelectromechanical devices; (260.2110) Electromagnetic optics; (140.3600) Lasers, tunable.

1. Introduction

Wavelength-tunable lasers are important for many applications including optical fiber communications, optical coherence tomography (OCT), light detection and ranging (LIDAR), and high resolution laser spectroscopy. Vertical-cavity surface-emitting lasers (VCSELs) have exhibited advantages over edge-emitting lasers including lower cost, smaller footprint, and lower power consumption [1]. Using a microelectromechanical system (MEMS), one can vary the optical cavity length of a VCSEL and continuously tune/sweep the lasing wavelength without hops or hysteresis. Since the first MEMS-tunable VCSEL was reported in 1995 [2], many advances have been reported for center wavelengths at 850, 940, 980, 1060, 1310 and 1550 nm [3]. The 1060 nm tunable VCSELs are of interests for applications in short-wavelength division multiplexed (SWDM) fiber communications and swept-source OCT systems for ophthalmic and fiber endoscopic imaging. In an OCT, the axial resolution is inversely proportional to the tuning ratio (tuning range divided by center wavelength or $\Delta\lambda/\lambda_0$) and the field of view is proportional to the sweep rate. Hence, both continuously tuning ratio and sweep rate are important for these applications.

Previously a very wide tuning range for an electrically-pumped VCSEL was demonstrated at 1550 nm with 102 nm range (tuning ratio $\Delta\lambda/\lambda_0$ is 6.58%) but at a relatively slow speed of 215 Hz due to electrothermally tuning mechanism [4]. John et al. published a $\Delta\lambda/\lambda_0=6.1\%$ tuning ratio (63.8 nm) centered at 1046 nm with a 240 kHz sweep-rate [5]. Recently, we reported a new design leading to a record tuning ratio of 6.9% (73 nm) at the center wavelength of 1060 nm [3]. In that paper we introduced the concept of an air-cavity-dominant design with relatively low optical intensity in the semiconductor cavity at the center wavelength. Here, we explain with a clear model how this design works. Further, we demonstrate a dynamic tuning of 6.6% (70 nm) with a fast speed of 600 kHz, a record value for an electrically pumped VCSEL, to the best of our knowledge.

2. VCSEL Design

The schematic and the scanning electron microscopy (SEM) image of our 1060-nm MEMS tunable VCSEL are shown in FIG. 1. The device consists of a semiconductor portion, a top high-contrast grating (HCG) mirror, and an air gap in between forming an air cavity. An HCG is a single layer of high refractive index material with near-wavelength dimensions. They have shown to exhibit high reflectivity across a wide range of wavelengths [3], replacing traditional distributed Bragg reflectors (DBR) as top mirror for a VCSEL. The HCGs are lightweight and excellent for high speed wavelength tuning, and can be produced by simple fabrication methods with high tolerance.

The semiconductor portion (starting from the top) includes a semiconductor-air coupling (SAC) region, a couple of pairs of p-DBRs (with $\text{Al}_{0.9}\text{Ga}_{0.1}\text{As}$ low-index layer first, followed by high-index $\text{Al}_{0.12}\text{Ga}_{0.88}\text{As}$ layer), a quarter-lambda $\text{Al}_{0.98}\text{Ga}_{0.02}\text{As}$ layer for oxidation, a lambda-thick cavity with three quantum wells in the center, followed by 38.5 pairs of n-DBRs, all grown on a n-doped GaAs substrate. The SAC region consists of a few layers, collectively designed to control the coupling between the semiconductor and air cavities. The SAC region comprises, listed from the top, an InGaP etch stop, a GaAs contact, and a graded $\text{Al}_x\text{Ga}_{1-x}\text{As}$ layer, all of which combine to be the half-lambda window layer. The air gap is formed by selectively remove the GaAs sacrificial layer by selective wet etching. The fabrication process is similar to our 1060-nm SCD VCSELs in [3].

Conventional MEMS-tunable VCSELs have high reflection at the semiconductor-air interface and the optical field penetration into air is suppressed, referred as the semiconductor-cavity dominant (SCD) design. To extend the tuning range, researchers have applied a quarter-lambda thick anti-reflection (AR) layer with refractive index close to the geometric mean of the semiconductor refractive index and the refractive index of air. This configuration was

referred to as the extended-cavity (EC) design. In that case, the semiconductor and air cavities are perfectly matched. They resonate as one cavity, as if the original semiconductor cavity “extends” into the air region. Designs in [4, 5] belong to the EC case. The air-cavity-dominant (ACD) design is a case in which the semiconductor-air reflection is designed to be out of phase with the semiconductor cavity, causing the optical field to be confined more significantly in the air cavity at the center wavelength.

3. Semiconductor-Air Cavity Coupling

FIG. 2 shows the transfer-matrix calculated resonance wavelengths as functions of the air gap thickness for four longitudinal Fabry-Perot (FP) modes. The dominant lasing mode is determined by lowest threshold gain among all FP modes, as indicated by the green circled lines in FIG. 2, for SCD, EC, and ACD designs. From the cold-cavity simulation we observe significant improvement of the tuning range from 59 nm (SCD), to 79 nm (EC), and to 96 nm (ACD). Note the tuning range is limited by FP mode spacing (free spectra range FSR) at the tuning edges. The gray areas in FIG. 2 indicate the reflectivity of the hybrid top mirror is below 99.5%, hence unlikely to support lasing. The three configurations exhibit distinct shapes of their tuning curves, namely a mirrored S-shape for SCD, a straight line for EC, and an S-shape for ACD. The threshold material gain was calculated using transmission matrix method [6] for all three configurations. We find that the threshold material gain for ACD is only 6% higher than SCD at the tuning center.

We perform the finite-difference time-domain simulation of the field spectra at sampled observation points in the semiconductor cavity as a function of air gap thickness for SCD, EC and ACD (Fig. 3). The contour spectra confirm the shapes of the tuning curves in Fig. 2. Here we can identify two sets of asymptotic lines for each design. One can already conjecture that these are resonance lines dominated by the semiconductor and air cavities. Using the FP condition of the air cavity sandwiched between two effective mirrors, the wavelength tuning relation is derived as

$$\lambda_r(d) = \frac{2}{m}(d + L_{eff}) \quad (1)$$

where d is the air gap thickness, m is the FP mode number, and the tuning slope is $\Delta\lambda_r/\Delta d=2/m$. The blue and purple dashed lines in FIG. 3 correspond to semiconductor- and air-dominant resonances, respectively. For SCD, the purple and blue resonance lines are fitted with $L_{eff}=31.8$ and $0.6 \mu\text{m}$, respectively. For EC, the purple and blue lines are fitted with $L_{eff}=9.7$ and $3.2 \mu\text{m}$, respectively. Finally with ACD, it should be noted that the resonance lines reside on the blue lines instead of the purple lines. The fitting of purple and blue lines are $L_{eff}=13.0$ and $3.2 \mu\text{m}$, respectively, with all lengths assumed to be in air. Since the L_{eff} varies significantly, it is critical to understand the physical reasons.

We turned to the traditional method to determine the effective length in a multi-layer medium by taking derivative of reflection phase with wavelength [6] for the air and semiconductor cavities for each design. The effective cavity length looking from the center of the air cavity is thus

$$L_{eff} = -\frac{\lambda^2}{4\pi} \frac{d}{d\lambda} (\phi_{HCG}(\lambda) + \phi_s(\lambda)) \Big|_{\lambda=\lambda_r} \quad (2)$$

Where $\phi_{HCG}(\lambda)$ and $\phi_s(\lambda)$ are reflective phase for an HCG and the entire epitaxial structure below air gap. The penetration depth at the tuning center resonance of $\lambda_c=1060$ nm for HCG is $0.48 \mu\text{m}$ and relatively independent of wavelength. The effective length for the below-air region of SCD, EC, and ACD are sensitive to wavelength. The L_{eff} for SCD at the center and edge of tuning range are 32.1 and $1.8 \mu\text{m}$, respectively. The L_{eff} for EC at the center and edge of tuning range are $9.7 \mu\text{m}$, and $5.2 \mu\text{m}$ at the tuning center, respectively. The L_{eff} for ACD at the center and edge of tuning range are 3.2 and $12.6 \mu\text{m}$, respectively. These values agree well with the asymptotic L_{eff} values obtained from Eq(1) for blue and purple lines, and hence explained the effect of the SAC region in creating different $L_{eff}(\lambda)$, which in turn limits the FSR and thus the tuning range. Further, for ACD, both the value and change are much less with $3.2 \mu\text{m}$ at the center and $12.6 \mu\text{m}$ at the edge, resulting a larger FSR over a wide wavelength range.

4. Experimental Results

Previously, with a combination of thermal, current and electrostatic tuning, a single-mode continuous lasing across a 73-nm range was demonstrated in [3]. In this paper, with an optimized MEMS design, we obtain a continuous sweep with a DC tuning voltage of 30.2 V plus an AC tuning voltage of 5.2 V at 600 kHz sweep rate, as shown in FIG. 5. The full dynamic tuning range is 69.7 nm, spanning from 1022.5 nm to 1092.2 nm, which is a direct proof of the extended FSR by our ACD design, and is close to calculated tuning range of around 76 nm, showing the tuning range is FSR-limited instead of threshold-limited.

In summary, we demonstrated electrically pumped VCSELs with an ultrahigh tuning ratio of 6.6% using our novel ACD configuration. We investigate in-depth the mechanism of such large improvement over conventional and

AR-coated tunable VCSELs. The wavelength tuning characteristics reside on air-cavity dominant resonance lines, resulting in smaller effective cavity length. Our measurements of the ACD devices confirm our theory of the tuning ratio with MEMS resonance tuning at a fast speed of 600 kHz.

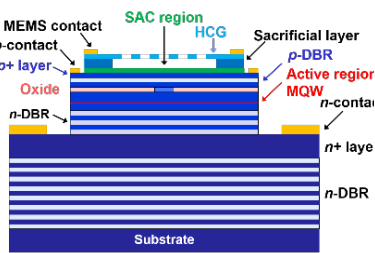


Figure 1. Schematic of a MEMS-HCG tunable VCSEL with an engineered semiconductor-air coupling (SAC) region.

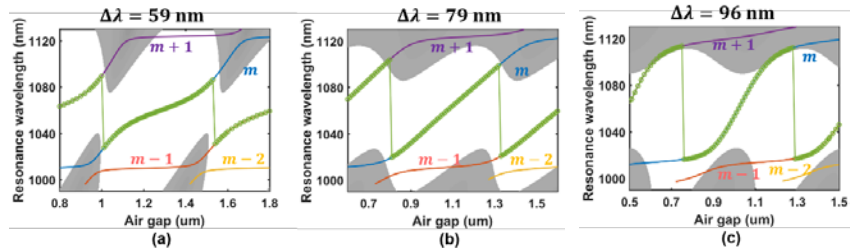


Figure 2. Resonance wavelengths versus air gap thicknesses for $m+1$, m , $m-1$, and $m-2$ longitudinal modes shown in purple, blue, red, and orange, respectively, for (a) SCD, (b) EC, and (c) ACD designs. The dominant resonance modes, determined by the lowest threshold gain, are shown as green circled lines, indicating tuning ranges of 59 nm, 79 nm, and 96 nm for SCD, EC, and ACD designs, respectively. Zero pairs of top DBR and 38.5 pairs of bottom DBRs are used. Shaded areas indicate hybrid top mirror reflectivity below 99.5%.

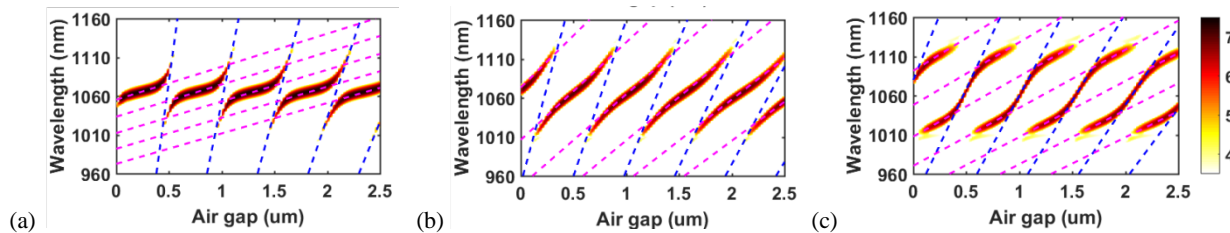


Figure 3. FDTD-simulated field spectra (log scale) as functions of the air gap thickness d using the (a) SCD, (b) EC, and (c) ACD designs. The high field intensities indicate the resonant wavelength for a given air gap value. Two pairs of top DBR and 38.5 pairs of bottom DBRs are used. The extracted tuning ranges are (a) 41 nm, (b) 59 nm, and (c) 76 nm. The blue and purple dashed lines are the air-dominant and semiconductor-dominant resonance lines, respectively.

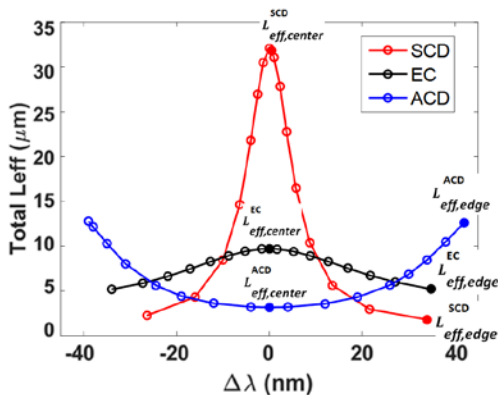


Figure 4. Total effective length calculation as a function of resonance wavelength for SCD, EC, and ACD designs looking from the center the airgap cavity, and again using effective lengths in air.

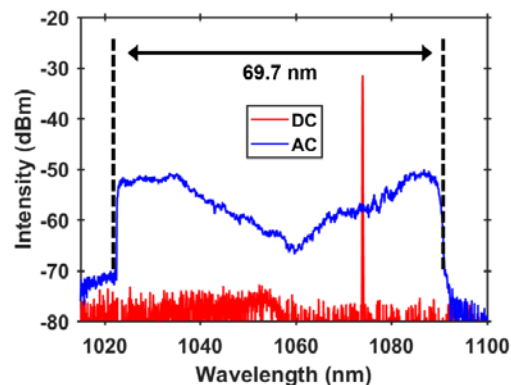


Figure 2. Measured swept VCSEL spectra for an ACD tunable VCSEL at 6 mA current injection under a constant DC bias (red) and with an additional 600 kHz AC (blue) tuning voltage.

References

- [1] F. Koyama, "Recent advances of VCSEL photonics," *IEEE J. Lightwave Technol.*, vol. 24, no. 12, pp. 4502-4513, 2006.
- [2] M. S. Wu, E. C. Vail, G. S. Li, W. Yuen and C. J. Chang-Hasnain, "Tunable micromachined vertical cavity surface emitting laser," *Electron. Lett.*, vol. 31, no. 19, pp. 1671-1672, 1995.
- [3] P. Qiao, K. T. Cook, K. Li, and C. J. Chang-Hasnain, "Wavelength swept VCSELs," *IEEE J. Sel. Top. Quantum Electron.*, vol. 23, no. 6, 1700516, 2017.
- [4] C. Gierl, T. Gruendl, P. Debernardi, K. Zogal, C. Grasse, H. A. Davani, G. Böhm, S. Jatta, F. Küppers, P. Meißner, and M.-C. Amann, "Surface micromachined tunable 1.55 μm -VCSEL with 102 nm continuous single-mode tuning," *Opt. Express*, vol. 19, no. 18, pp. 17336-17343, 2011.
- [5] D. D. John, C. B. Burgner, B. Potsaid, M. E. Roberson, B. K. Lee, W. J. Choi, A. E. Cable, J. G. Fujimoto and V. Jayaraman, "Wideband electrically pumped 1050-nm MEMS-tunable VCSEL for ophthalmic imaging," *J. Lightwave Technol.*, vol. 33, no. 16, p. 3461, 2015.
- [6] Larry Coldren, Scott Corzine, and Milan Mašanović, *Diode Lasers and Photonic Integrated Circuits*, J. Wiley, New York, New York 2012.

Air-Cavity Dominated HCG-VCSEL with a Wide Continuous Tuning

Jonas Kapraun¹, Jipeng Qi¹, Jiaying Wang¹, Philippe Tingzon², Kevin Cook¹, Emil Kolev, Larry A. Coldren³ and Connie J. Chang-Hasnain^{1*}

1: Department of Electrical Engineering and Computer Sciences and Tsinghua-Berkeley Shenzhen Institute, University of California Berkeley, Berkeley CA 94720, United States

2: Materials Science Engineering Program, University of the Philippines – Diliman

3: Department of Electrical and Computer Engineering, University of California, Santa Barbara, CA 93117, USA
*Author e-mail address: *cch@berkeley.edu*

Abstract: We present continuously tuned emission of 940-1000 nm wavelength from an electrically-pumped VCSEL without top DBR layers via an electrostatically controlled HCG mirror. Large tuning range results from a high optical intensity in the air cavity. © 2018 The Author(s)

OCIS codes: (140.7260) Vertical cavity surface emitting lasers; (140.5960) Semiconductor lasers

1. Introduction

Widely tunable lasers are highly desired for application such as optical coherence tomography (OCT), light detection and ranging (LIDAR) and dense wavelength division multiplexing (DWDM) application. Because of their compact design and low cost, wavelength tunable micro-electro-mechanical structure (MEMS) vertical cavity surface emitting lasers (VCSELs) are extremely promising for the mentioned application space.

In this paper, we present a new HCG tunable VCSEL design where we completely removed all distributed Bragg reflector (DBR) layers from the top mirror. The VCSEL top reflection is solely provided by a high contrast grating, which is freely suspended by a MEMS structure above the epitaxy layers via an air gap, forming an air cavity above the semiconductor cavity centered at the active layers. Recently, we reported VCSELs with a MEMS actuated high contrast grating (HCG) top mirror and 73 nm tuning range at 1060 nm [1]. In that paper, we discussed an interesting coupling mechanism formed between these two cavities, i.e. semiconductor and air cavity. The strong coupling led to a record tuning ratio of a VCSEL [1]. In this paper, we further removed the excess top DBR layers in [1] to reduce VCSEL drive voltage and resistance. We present experiment results with a wide 56 nm tuning range centered at 967 nm. This is the first demonstration that a VCSEL can lase entirely with the reflection of HCG and without any top DBRs. The lasing wavelength and the non-lasing Fabry Perot (FP) modes are measured as a function of tuning voltage and hence the air gap size. Excellent agreements are obtained between simulation and experimental data, showing a clear signature of the novel air-dominated cavity.

2. Device Structure

The presented HCG VCSEL was grown in-house by Metal-Organic Chemical Vapor Deposition (MOCVD) on a substrate of 33 pairs of distributed Bragg reflector from Landmark Optoelectronics Corp. TBA and TBP were used as group-V precursors. After desorption of the protective GaAsP layer terminating the DBR substrate [2], a GaAs buffer was grown. The active region is composed out of 5 InGaAs/GaAsP strain compensated quantum wells, surrounded by AlGaAs cladding. Then the oxidizable Al_{0.8}GaAs layer and a p-GaAs layer as laser top contact were grown. After this a 25nm thick InGaP layer serves as etch stop and is followed by 1.134 μm thick GaAs, to be selectively removed by wet etching to define the air cavity. The 278 nm thick n-Al_{0.6}GaAs HCG layer terminates the air cavity. A final n-GaAs cap layer serves as protection during fabrication. Being able to grow the described structure separately from the bottom DBR, reduced the total thickness of the grown structure to less than 2.5 μm, which resulted in a growth time of less than 2.5 hours. Additionally, the presented design eliminates any top DBR pairs, resulting in an increased free spectral range of 59 nm and simplifies the theoretical description of the device (micrograph shown in Fig. 1 (a)).

3. Electrostatic Tuning

After fabrication, the electrostatic tuning range was tested. Under application of a static reverse bias between n-doped HCG layer and the p-doped laser contact, the wavelength was tuned continuously for 56 nm from 1001 nm (at 0 V) to 945 nm wavelength (at 15.7 V). While maintaining >25dB side mode suppression ratio (Fig.1 (b)), almost the entire free spectral range of 59 nm was covered by static tuning. Fig. 1 (c) shows an exemplary LIV

characteristic near the center of the tuning range at 968nm. Here we observed a low threshold of 1mA and peak power of close to 0.7 mW.

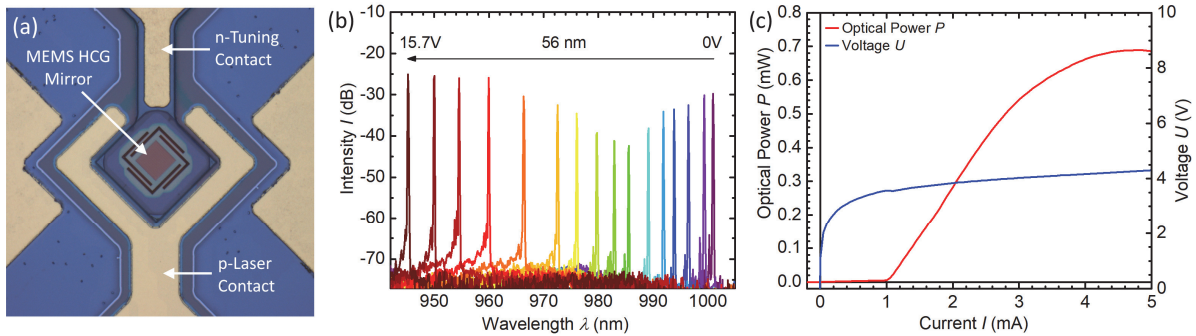


Fig. 1 Wavelength tunable laser: (a) Micrograph of an device; (b) Electroluminescence spectra showing 56 nm electrostatic tuning range; (c) Exemplary LIV curve near the center of the tuning range at 968nm and 14V tuning voltage.

In the following, the measured wavelength-tuning characteristic shall be compared to the simulated dependence of lasing wavelength on the air gap size. First, the emission wavelengths of the lasing mode (and non-lasing longitudinal modes) are obtained from the emission spectra at different tuning voltages. To relate the measured tuning voltages to the corresponding air cavity length the resonance frequency of the MEMS HCG mirror was determined, from the dependence of the dynamical tuning range as function of tuning frequency. The normalized change in wavelength range with AC tuning frequency is shown in Fig. 2 (a). A resonance frequency of 345 kHz and -3 dB frequency of 687 kHz were measured. Next, the spring constant k was calculated assuming a harmonic oscillator and resonance frequency $\omega = \sqrt{k/m}$, with the mass of the HCG mirror based on geometry. Fig. 2 (b) shows the length of the air cavity at static equilibrium as a function of tuning voltage. At 0 V the length of the air cavity equates to the thickness of 1134 nm of the sacrificial GaAs layer. The calculated pull-in voltage of 16 V fits very well to the experimentally observed range of pull-in voltages.

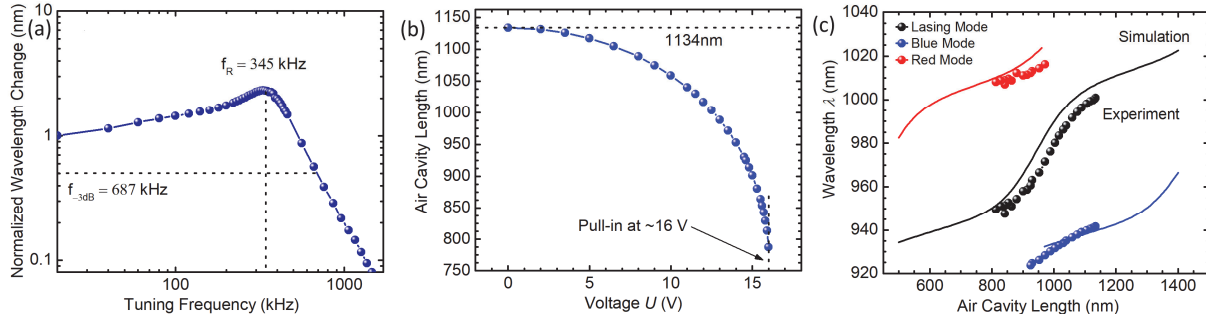


Fig. 2 Comparison of measured wavelength-tuning characteristic simulation (a) Measurement of the mechanical resonance of the MEMS HCG mirror; (b) Calculation of air cavity size as function of tuning voltage; (c) Experimental (dots) and simulated results (lines) for the wavelength of longitudinal modes of the air cavity. The fast change of lasing wavelength vs. air gap length is a clear signature of ACD design.

Finally, the emission wavelengths of the experimentally observed modes are plotted as function of the air cavity length in Fig. 2 (c). The experimental results (dots) are in very good agreement with the transfer matrix simulation (lines). The simulation parameters are within resolution of the SEM measurements of HCG period and epitaxial layer thicknesses. The stronger dependence of wavelength on the change in length of the air cavity (both in simulation and experiment), indicates the successful realization of an air-cavity dominant (ACD) design, which optimizes the free spectral range, and therefore the maximum tuning range of the device [1]. A further increase in free spectral range can be achieved by eliminating the more than 600 nm thick n-contact layer below the active region in parts or in total, which would increase the simulated tuning ratio to 7.1%. Further, by substituting the graded interface DBR by an abrupt interface AlAs/GaAs DBR to reduce the effective cavity length, we expect to increase the tuning ratio close to 9%.

4. References

- [1] P. Qiao et al., "Wavelength-Swept VCSELs" JSTQE **23**, 6 (2017)
- [2] J. Wang et al., "Precise Two-step Growth of 940-nm VCSEL on a GaAsP-capped DBR Wafer" CLEO, (2018), *Submitted*

Air Cavity Dominant VCSELs with a Wide Wavelength Sweep

KEVIN T. COOK,¹ PENGFEI QIAO,¹ JIPENG QI,¹ LARRY A. COLDREN,² AND
CONNIE J. CHANG-HASNAIN^{1,*}

¹*Department of Electrical Engineering and Computer Sciences and Tsinghua-Berkeley Shenzhen Institute, University of California at Berkeley, Berkeley, CA 94720, USA*

²*Departments of Electrical and Computer Engineering and Materials, University of California at Santa Barbara, Santa Barbara, CA 93106, USA*

*cch@berkeley.edu

Abstract: The wavelength tuning range of a tunable vertical-cavity surface-emitting laser (VCSEL) is strongly influenced by the design of the interface between the semiconductor cavity and the air cavity. A simplified model is used to investigate the origin of the dramatic differences in free spectral range (FSR) and tuning slope observed in semiconductor cavity dominant, extended cavity, and air cavity dominant VCSELs. The differences arise from the positioning of the resonant and antiresonant wavelengths of the semiconductor cavity with respect to the center wavelength. The air-cavity dominant design is realized by designing an antiresonant semiconductor cavity, resulting in a larger tuning slope near the center of the tuning range and a wider FSR toward the edges of the tuning range. The findings from the simplified model are confirmed with the simulation of a full VCSEL structure. Using an air-cavity dominant design, an electrically pumped laser with a tuning range of 68.38 nm centered at 1056.7 nm at a 550 kHz sweep rate is demonstrated with continuous wave emission at room temperature. This epitaxially design rule can be used to increase the tuning range of tunable VCSELs, making them more applicable in swept-source optical coherence tomography and frequency-modulated continuous-wave LIDAR systems.

© 2018 Optical Society of America under the terms of the [OSA Open Access Publishing Agreement](#)

1. Introduction

Wavelength-swept lasers are important components in modern optical communications, light detection and ranging (LIDAR), optical coherence tomography (OCT), and high-resolution laser spectroscopy. The most important performance criteria are wavelength tuning ratio ($\Delta\lambda/\lambda_C$) and sweep speed. Vertical-cavity surface-emitting lasers (VCSELs) with tuning capability [1] have exhibited many desirable attributes including wafer-scale fabrication and testing, continuous and wide tuning, smaller footprint, and lower power consumption. Using a microelectromechanical system (MEMS), the optical cavity length can be changed to continuously tune the lasing wavelength [2]. Since the first MEMS-tunable VCSEL reported in 1995, many advances have been reported for center wavelengths (λ_C) of 850 nm, 980 nm, 1060 nm, 1310 nm, and 1550 nm [3] [4] [5] [6] [7] [8] [9] [10]. Conventional MEMS-tunable VCSELs are designed with a high optical intensity concentrated in the semiconductor portion [3-5]. This configuration is referred to as semiconductor cavity dominant (SCD) design. The tuning ratio of a SCD design is limited to ~3.5% by the relatively small free spectral range (FSR).

To increase the tuning range, researchers have designed VCSELs with a $\lambda_C/4$ -thick anti-reflection (AR) layer with $n_{AR} = \sqrt{n_s}$ where n_s is the index of the topmost semiconductor layer. This configuration was referred to as the extended cavity (EC) design in [3]. In this case, the semiconductor and air cavities are perfectly matched. They resonate as one cavity, as if the semiconductor cavity “extends” into the air region. Previously, a very large static tuning range

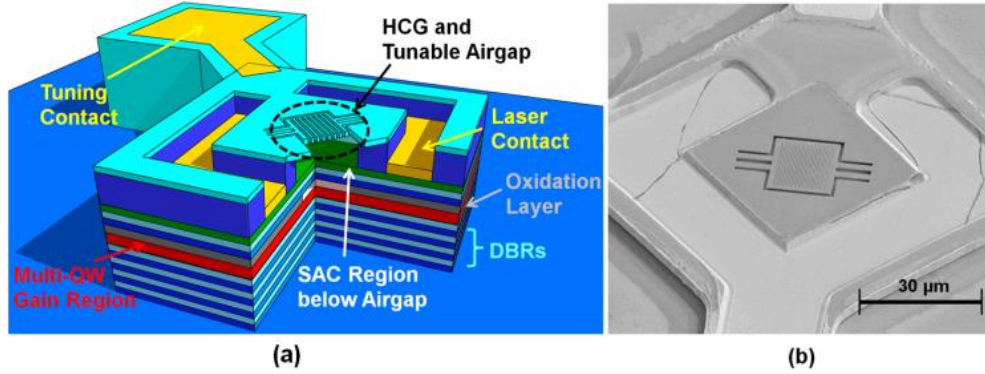


Fig. 1. (a) Schematic view of a MEMS-HCG tunable VCSEL with engineered semiconductor-air coupling (SAC) region. (b) Scanning electron microscope view of a fabricated 1060-nm MEMS-HCG tunable VCSEL.

of 102 nm centered at 1550 nm ($\Delta\lambda/\lambda_C = 6.6\%$) was reported for electrically-pumped EC VCSEL using electro-thermal tuning [4]. Limited by the thermal time constant, the tuning speed is shown to be relatively slow at 215 Hz with a smaller dynamic sweep range of 87 nm ($\Delta\lambda/\lambda_C = 5.6\%$). The EC design has also been implemented at a center wavelength of 1050 nm with a swept tuning range of 63.8 nm ($\Delta\lambda/\lambda_C = 6.1\%$) and a faster sweep rate of 240 kHz [5]. Both devices utilize dielectric distributed Bragg reflectors (DBR) with a high index contrast to minimize the effective length of the cavity, increasing the FSR at the cost of increased fabrication complexity due to additional deposition steps or multiple oxidation layers.

Recently, a third configuration called the air cavity dominant (ACD) design was reported, which forces the optical field to be confined more significantly in the air cavity at the center wavelength [6]. This design led to a record tuning ratio of 6.9% for an electrically-pumped VCSEL, while allowing more flexible choices of materials and thicknesses in the semiconductor-air coupling (SAC) region and the bottom DBR.

In this study, we investigate the origin of the increased tuning range of the ACD design and the impact of the design on threshold material gain. The swept operation of the device is demonstrated, exhibiting a swept tuning ratio of 6.5% at a sweep rate of 550 kHz. The high sweep rate is attributed to the lightweight high-contrast grating (HCG) used as the tunable mirror [7].

2. Underlying Physics of Tunable VCSELs

Error! Reference source not found. shows the schematic and the scanning electron microscopy (SEM) image of our 1060-nm ACD HCG tunable VCSEL. The device consists of a semiconductor portion, a top HCG mirror, and an air gap in between forming an air cavity. The semiconductor portion (starting from the top) includes a semiconductor-air coupling (SAC) region, two pairs of p-DBRs ($\text{Al}_{0.12}\text{Ga}_{0.88}\text{As}$ high-index layer first, followed by $\text{Al}_{0.9}\text{Ga}_{0.1}\text{As}$ low-index layer, $\text{Al}_{0.12}\text{Ga}_{0.88}\text{As}$ high-index layer, and $\text{Al}_{0.98}\text{Ga}_{0.02}\text{As}$ layer for oxidation), a $1\lambda_C$ cavity with five quantum wells in the center, followed by 38.5 pairs of n-DBRs, all grown on an n-doped GaAs substrate. One can identify two longitudinally coupled cavities: one centered at the active cavity with quantum wells and a second centered at the air gap between the HCG and the semiconductor. As described in [6], the SAC region dictates the difference between the three designs: SCD, EC and ACD.

To explore the underlying physics of the two cavities, we simplified the entire epitaxy stack to a $4\lambda_C$ semiconductor cavity with index n_s , a $\lambda_0/4$ SAC layer, and an air region of variable length (index 1), shown in Fig. 2(a). The semiconductor cavity was chosen to be $4\lambda_C$ to have a similar FSR to a realistic design. The structure is bounded on both sides by ideal reflectors which have Fresnel coefficients $r_1 = r_3 = 0.999 + 0i$ for all wavelengths. Here we consider only three refractive index values for the $\lambda_C/4$ SAC layer, $n_{\text{SAC}} = 1, n_{\text{AR}}, n_s$, representing SCD,

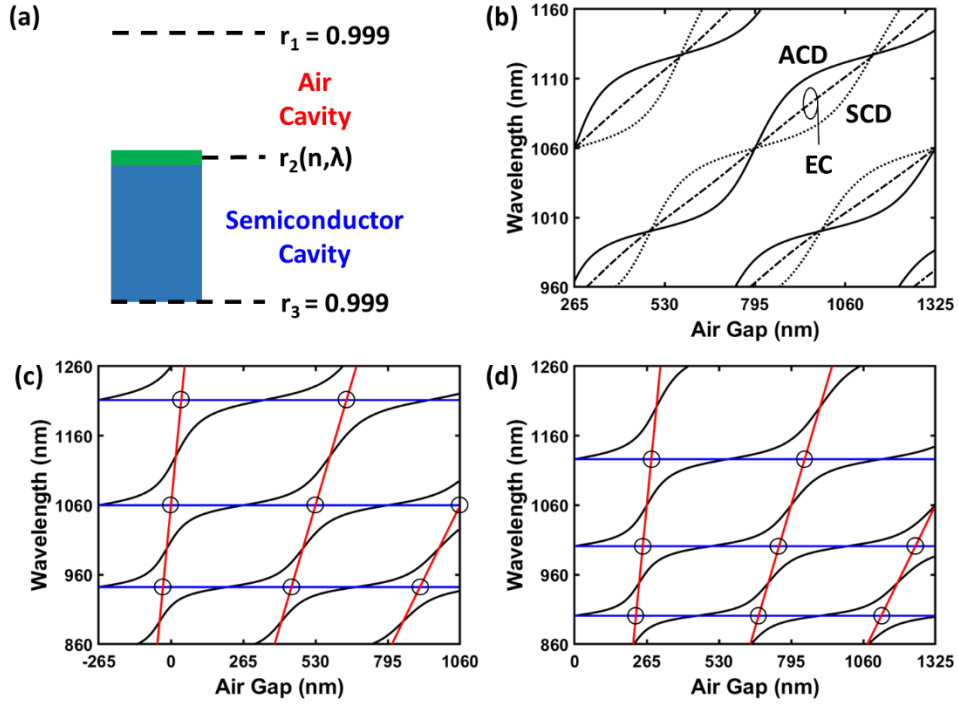


Fig. 2. Simplified coupled-cavity transfer-matrix analysis. (a) Illustration of simplified two coupled cavities with a semiconductor-air coupling (SAC) layer in-between. The $4\lambda_C$ semiconductor cavity with index n_s is shown in blue, the SAC layer with index n_{SAC} is shown in green, and the air cavity has an index of 1. The reflectors are indicated by dashed lines. (b) Comparison between SCD, EC, and ACD tuning characteristics with $n_{SAC} = 1$, n_{AR} , n_s respectively. The ACD design has the widest FSR when measured around the center wavelength of 1060 nm. (c) SCD and (d) ACD tuning curves plotted in black against semiconductor cavity modes in blue and air cavity modes in red. The circles indicate where the two families of lines cross, which resulted in anti-crossing in the (black) resonance lines of the full structures.

EC, and ACD cases, respectively. The resonances of the simplified coupled-cavity structure for the three cases are calculated using transfer matrix method by finding the wavelengths with zero round-trip phase for each air cavity length and are plotted as a function of air cavity length, as shown in Fig. 2(b), for all three cases. The EC case has Fabry-Perot (FP) wavelength linearly dependent on the air cavity length since the entire structure is one cavity. However, the SCD and ACD have distinctly different curvatures. This behavior is the same as shown in Figure 13 of [6] with a full VCSEL design.

To understand the curvatures of the SCD and ACD resonance lines, we examine the two cavities: the air cavity defined by r_1 and r_2 , and the semiconductor cavity defined by r_2 and r_3 . The FP resonances for the semiconductor cavity, computed by removing r_1 from the transfer matrix simulation described above and plotted in blue in Figs. 2(c) and 2(d), are horizontal lines since they do not depend on the air cavity length. The FP resonances for the air cavity between r_1 and r_2 , computed by removing r_3 from the simulation and plotted in red in Figs. 2(c) and 2(d), are linearly proportional to the air cavity length. Coupling between the semiconductor cavity and air cavity occurs when the two families of lines intersect each other, marked with circles on Figs. 2(c) and 2(d). The FP resonances of the full structure follows these two families of lines but avoid the crossings as shown by the black curved traces.

Figure 2(c) shows the case where $n_{SAC} = 1$. The semiconductor cavity is in resonance at $\lambda_C = 1060$ nm and thus a blue line is shown at the center wavelength 1060 nm. At an air gap of $-\lambda_C/4$, r_1 directly touches the semiconductor cavity. The full structure resonance lines are

coincident with the semiconductor cavity resonance lines. As the air gap increases, an avoided crossing causes the full structure resonance to follow the air cavity resonance. Eventually, the full structure resonance avoids a second crossing to switch back to following the semiconductor resonance line. Since there is a semiconductor resonance at λ_0 , the full structure resonance shows a low tuning slope at the center wavelength. This is the characteristic feature of an SCD design.

Figure 2(d) shows the case where $n_{SAC} = n_s$. Due to the $\lambda_c/4$ SAC refractive index, the FP wavelengths for the semiconductor cavity are shifted from those in the SCD case (Fig. 2(c)). In this ACD case, the semiconductor cavity is in *antiresonance* at λ_c , with the nearest FP modes located instead at 1130.7 and 997.6 nm. Again, the full structure resonance lines begin coincident with the semiconductor lines at an air cavity length of 0. The VCSEL resonance curves avoid the crossings between semiconductor and air resonances as air cavity length increases. Since the semiconductor cavity is in antiresonance at λ_c , the full structure resonance follows the air cavity resonance, resulting in a large tuning slope. This represents the ACD case. A stronger coupling between the semiconductor and air cavities in either an ACD or SCD design pushes the black lines apart, approaching the tuning characteristic for the EC case, in which the cavities are perfectly coupled.

The mathematical origin of the semiconductor resonances lies in the phase of r_2 . If $n_{SAC} < n_{AR}$, then the interface between the semiconductor cavity and the SAC layer dominates r_2 . The reflection phase into the semiconductor cavity, $\angle r_2(\lambda_c)$, is zero, and the semiconductor cavity is in resonance at λ_c . For the special case in which $n_{SAC} \approx n_{AR}$, the magnitude of r_2 is insignificant and the VCSEL cavity resonates as a unit. If $n_{SAC} > n_{AR}$, then the interface between the air cavity and the $\lambda_c/4$ SAC layer dominates r_2 . The reflection phase $\angle r_2(\lambda_c) = \pi$, the semiconductor cavity is in antiresonance at λ_c , and the design is ACD. Note this description is very general and applies to more complex designs, such as that depicted in Figure 1, which has two pairs of p-DBR between the $1\lambda_c$ cavity and the SAC, and the SAC consists of a window ($\lambda_c/2$) layer between the $\lambda_c/4$ n_{SAC} layer and air cavity.

For a typical tunable MEMS-VCSEL design, the air cavity length is chosen to be large enough to allow large tuning range with a maximum MEMS movement approximately 1/3 of the air gap. The FSR is thus the limiting factor in tunable VCSEL designs. As noted above, FSR is not constant with changing air cavity length. The range-limiting FSR is the shortest wavelength difference between the modes directly above and directly below the center wavelength, as these are the modes which are able to achieve threshold. In both ACD and SCD designs, the highest FSR is located near the intersections of the VCSEL cavity modes and the semiconductor cavity modes. Since the semiconductor cavity modes are off-center in an ACD VCSEL, the FSR is highest when the VCSEL resonance is far from the center of its tuning range. In contrast, the FSR of an SCD VCSEL is decreased as the VCSEL resonance moves away from the tuning center. The difference in FSR is illustrated in Fig. 2(b), which shows the VCSEL cavity modes for SCD, EC, and ACD designs. With this model, it is clear that to obtain a large tuning ratio, it is important to design an antiresonant semiconductor cavity with minimum length and reduce the coupling between the two cavities. In other words, it is best to let the air cavity dominate.

3. FDTD Simulation of Full Structure

The above simplified model is next verified by FDTD simulation of a realistic VCSEL structure without active layers. Fig. 3(a) shows the structure consisting of regions of $n_{high} = 3.483$ and $n_{low} = 2.988$, both $> n_{AR}$. From top to bottom, there is an HCG, a tunable air cavity, a SAC region, a 2-pair DBR, a $1\lambda_c$ high-index cavity, a 38.5-pair DBR, and a high-index substrate of infinite thickness. The SAC region contains a high-index $\lambda_c/2$ “window” layer on top of a low-index $\lambda_c/4$ layer with n_{low} . In this example, since there are limited choices of III-V epitaxy materials (refractive indices) for monolithic growth, we illustrate the coupling

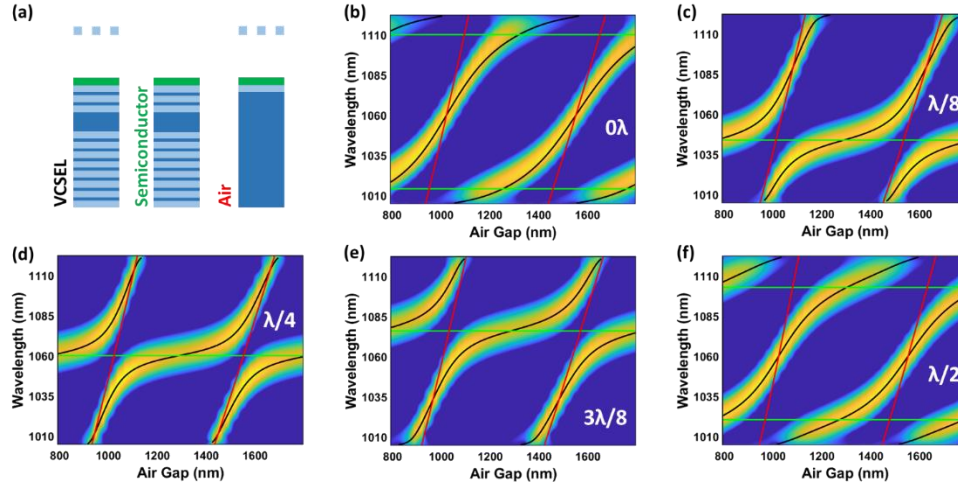


Fig. 3. FP Resonance as a function of air cavity thickness for a realistic VCSEL cavity using transfer-matrix and FDTD analysis. (a) Schematic of VCSEL structure, semiconductor cavity structure, and air cavity structure used to compute Fabry-Perot modes. The SAC region contains a high-index $\lambda_c/2$ “window” layer on top of a low-index $\lambda_c/4$ layer with n_{low} , both indices $>n_{AR}$. (b)-(f) Transfer matrix simulations for VCSEL modes (black), semiconductor cavity modes (green), and air cavity modes (red), inscribed on a resonance colormap from FDTD simulations of the full VCSEL structure. The thickness of the “window” layer is varied from 0 to $\lambda_c/2$, illustrating the shift from ACD at 0 to SCD at $\lambda_c/4$ and back to ACD at $\lambda_c/2$.

effect by changing the SAC “window” layer thickness instead, by adding or removing a $\lambda_c/4$ layer.

In this structure, r_1 is the reflectivity of the HCG (computed using rigorous coupled-wave analysis [7]), r_2 is the reflectivity of the SAC region, and r_3 is the reflectivity of the 38.5-pair DBR terminating in the substrate. The FDTD simulation in Figs. 3(b)–3(e) shows resonance lines of the entire structure as functions of air cavity length when the “window” layer is varied from 0 to $\lambda_c/2$. The color code indicates the strength of the cavity resonance (yellow is high Q and blue is low). The resonance for the air cavity, semiconductor cavity and the entire structure using transfer-matrix simulations are also plotted in the same plots for comparison. Excellent agreement is obtained between the two approaches.

Since the dominant interface contributing to r_2 is the interface between the “window” layer and the air gap, the semiconductor cavity is much more sensitive to changes in “window” layer thickness than the air cavity. As the thickness of the “window” layer increases, so does the wavelength of each semiconductor resonance. Meanwhile, the position and slope of the air cavity resonances remains almost constant. Since the tuning behavior is dominated by the semiconductor cavity resonance, any increase in the overall thickness of the semiconductor cavity corresponds to a shift in the tuning characteristic. When the thickness of the “window” layer is 0, the SAC simply consists of a low-index $\lambda_c/4$ layer (but the low index is still greater than n_{AR}). Hence, the semiconductor cavity is antiresonant with two semiconductor resonances at ~ 1010 and 1110 nm, as shown in Figure 3 (b). This is the ACD case. When the window has a thickness of $\lambda_c/4$, the semiconductor cavity is in resonance, resulting in an SCD tuning characteristic as shown in Figure 3 (d). With the window layer increased to $\lambda_c/2$, the device is again ACD, as show in Figure 3 (f).

4. Optical Confinement

The optical confinement factor is an important parameter to examine since it determines the threshold current density. The real VCSEL structure, described in section one and shown in Fig. 1, is used for this study. The top $\lambda_c/4$ portion of semiconductor is InGaP in the real device

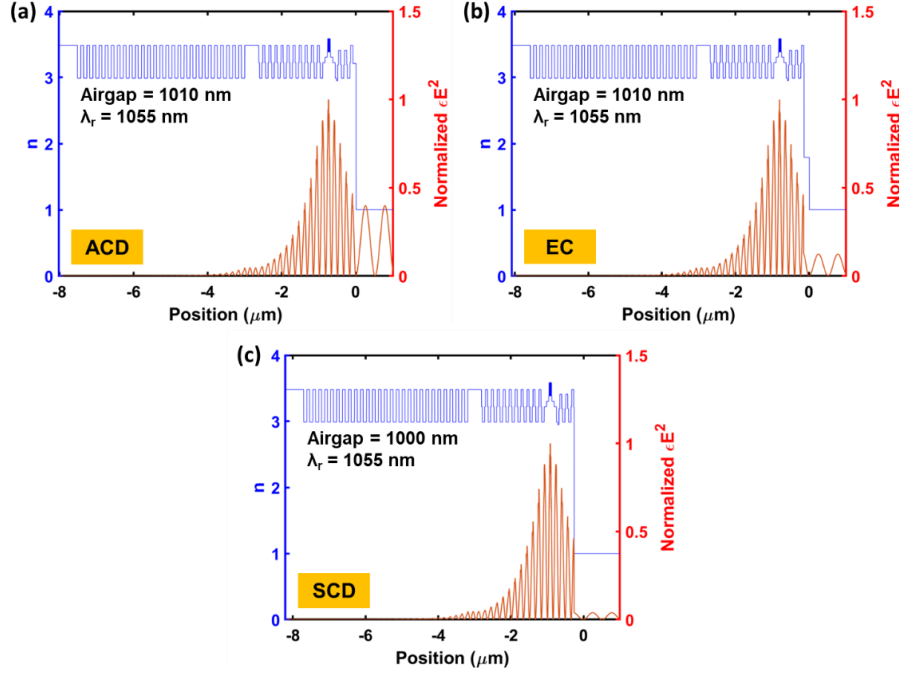


Fig. 4. Longitudinal electric energy density $\epsilon(z)|E(z)|^2$ profiles (red) calculated using the transfer-matrix method at tuning center where $\lambda_r=1060$ nm for (a) ACD, (b) EC and (c) SCD. The refractive index (blue) for each layer is also plotted for each case to show the simulated structure.

(ACD), but is changed to Al_2O_3 in the EC design and air in the SCD device for comparison here. The longitudinal electric energy density $\epsilon(z)|E(z)|^2$ profiles at tuning center wavelength for ACD, EC and SCD VCSELs are shown in Figs. 4(a), 4(b), and 4(c), respectively. At the tuning center, all three cases show the largest energy density inside the MQW region, which indicates a good field alignment. We indeed observe a relatively large energy distribution in the air cavity for ACD, in contrast to both EC and SCD. This confirms a strong coupling with the air cavity at the tuning center for the ACD case. Since ACD has more energy confined in the air sub-cavity, it should follow that the energy confinement factor for ACD is lower than EC and SCD.

To understand how the tuning impacts the laser threshold, we now calculate the effective cavity length observed from the semiconductor

$$L_{eff}(\lambda_r) = -\frac{\lambda_r^2}{4\pi n_g} \frac{\partial}{\partial \lambda} (\phi_{top}(\lambda) + \phi_{bottom}(\lambda)) \Big|_{\lambda=\lambda_r} \quad (1)$$

where $\phi_{top}(\lambda)$ and $\phi_{bottom}(\lambda)$ are reflective phases for the top and bottom mirrors seen by the semiconductor cavity. In this approach, we consider the layers beneath the central quantum well as our bottom effective mirror and the layers above as the top effective mirror. Note that the effective length of the ACD design is the largest for all three designs at the tuning center. However, the effective length for ACD stays relatively constant across the entire tuning range, whereas that of the SCD sharply increases as wavelength deviates from the center wavelength. Indeed, at the edges of the tuning range, the effective lengths of the SCD and EC devices become larger than that of the ACD device.

The threshold material gain is rigorously calculated using the transfer-matrix method [6] for all three configurations and plotted in Fig. 5(c). This calculation includes a uniform intrinsic loss of 20 cm^{-1} in every semiconductor layer. Finally, we calculate the confinement factor, as

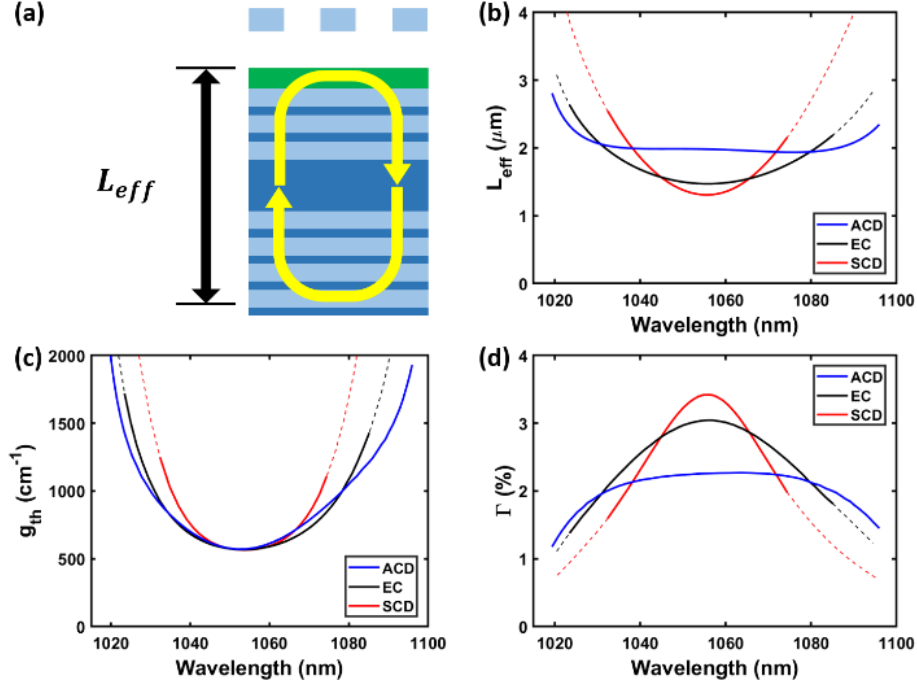


Fig. 5. Effective length is observed from the semiconductor cavity. (b) Total effective length L_{eff} as a function of resonance wavelength for SCD (red), EC (black), and ACD (blue) designs. (c) Threshold material gain g_{th} with uniform material loss $\alpha_i = 20 \text{ cm}^{-1}$ added to all semiconductor layers. (d) Confinement factor calculated with $\Gamma = \alpha_m/g_{th0}$.

depicted in Fig. 5(d), by calculating mirror loss and dividing by L_{eff} . The ACD device has the lowest confinement factor of all three cases due to the large portion of electric energy confined in the air. Despite the significantly lower confinement factor of the ACD device, the threshold material gain at the tuning center is only increased by 1% because the air is lossless.

The effective length and confinement factor calculations provide further insight into the threshold gain and FSR of the three designs. The FSR, which is inversely proportional to L_{eff} , is an important parameter at the tuning edge, where neighboring F-P modes may compete for the finite gain provided by the quantum wells. As shown in Fig. 5(b), the ACD design has the smallest effective length and thus the largest FSR at the tuning edge, confirming the trend noted in Fig. 2. The reduced effective length at the tuning edge in the ACD design also results in a higher confinement factor and lower threshold gain. As a result, using this novel ACD design, the threshold gain is not compromised significantly while the tuning range is largely extended.

5. Experimental Results

The device shown in Figure 1 is fabricated using process described in [6]. The GaAs sacrificial layer is removed by selective wet etching to form the $1.32 \mu\text{m}$ air gap. The SAC region of the actual device uses a design resembles the case shown in Fig. 3(f), with a $\lambda_c/2$ window layer composed of an InGaP etch stop and a GaAs contact layer on top of a $\lambda_c/4$ low-index layer.

Previously, with a combination of thermal, current and electrostatic tuning, a single-mode continuous lasing across a 73-nm range was demonstrated [6]. With an optimized MEMS design, we obtain a continuous sweep by applying a DC tuning voltage of 31.5 V plus an AC tuning voltage of $10.0 V_{pp}$ at the mechanical resonance frequency of 550 kHz, as shown in Fig. 6(a). Resonant excitation of the mechanical structure displaces the mirror further than the equivalent DC voltage, eliminating the need for a tuning voltage high enough to break down the semiconductor junction [8]. The full dynamic tuning range is 68.38 nm, spanning from

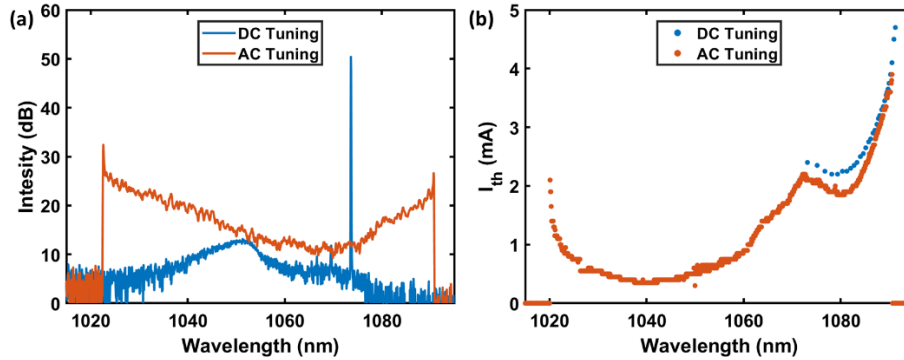


Fig. 6. (a) Measured swept VCSEL spectra for an ACD tunable VCSEL at 4.5 mA current injection under a constant DC bias (blue) and with an additional 550 kHz AC (red) tuning voltage. The swept spectrum covers a range of 68.38 nm, measured at -20 dB from the tuning edge peaks. (b) Threshold current measured with two different techniques. The curve in blue is measured by applying a series of DC tuning biases and measuring the threshold and wavelength at $1.1I_{th}$. The curve in red is measured by applying a DC tuning bias and sweeping the position of the HCG by applying a resonant AC signal, then measuring the emission spectrum at a series of laser drive currents.

1022.46 nm to 1090.84 nm, which is a direct proof of the extended FSR by our ACD design, and is close to the calculated tuning range of 76 nm. If the AC voltage is increased to displace the MEMS further, the next Fabry-Perot mode will begin to lase over the same range of wavelengths. This shows that the tuning range is FSR limited and not threshold limited.

The threshold current for each wavelength is determined using the swept spectrum. The DC tuning bias, AC amplitude, and AC frequency are set such that the movement of the mirror traces one period of the tuning curve. A series of DC currents, ranging from 0.1 mA to 4 mA in steps of 0.05 mA, is applied through the laser diode. For each DC current, the emission spectrum is measured. The threshold at each wavelength is then determined by numerically differentiating the spectral intensity with respect to laser diode current and locating the abrupt step corresponding to the threshold. The results of this measurement are shown in Fig. 6(b). For comparison, the threshold current is also measured at a series of DC tuning biases.

The shape of the measured threshold current plotted versus wavelength in Fig. 6(b) deviates from the shape of the simulated threshold material gain curve in Fig. 5(c) in several aspects. First, the minimum threshold is blue-shifted to 1040 nm due to differences in HCG dimensions caused by variation in the lithography and etch processes. The second deviation is the peak at 1075 nm. This peak corresponds to a transition between two transverse modes. Transverse mode suppression is achieved in non-tunable oxide VCSELs by placing an oxide aperture near a longitudinal intensity node of the desired Fabry-Perot mode. In a tunable VCSEL, the position of the oxide layer with respect to the mode changes with wavelength, which can cause different transverse modes to dominate at different wavelengths. In the future, different transverse control mechanisms such as multiple oxide apertures, ion implantation, or buried heterostructure can be used to eliminate higher order transverse modes during tuning. Chirped QWs could also be used to reduce wavelength dependence in threshold current.

6. Conclusion

In summary, we investigate the mechanism behind the ACD configuration's large tuning range improvement over SCD and EC tunable VCSELs, finding that an antiresonance in the semiconductor cavity at the center wavelength is the cause for the high tuning slope and wide FSR. Our measurements of ACD devices confirm our theory of tuning ratio enhancement, demonstrating electrically pumped VCSELs with a high tuning ratio of 6.5% with resonant MEMS tuning at 550 kHz.

References

References

- [1] C. J. Chang-Hasnain, "Tunable Vcsel," *J. Sel. Topics in Quantum Electron.*, vol. 6, no. 6, pp. 978-987, 2000.
- [2] M. S. Wu, E. C. Vail, G. S. Li, W. Yuen and C. J. Chang-Hasnain, "Tunable micromachined vertical cavity surface emitting laser," *Electronics Letters*, vol. 31, no. 19, pp. 1671-1672, 1995.
- [3] F. Sugihwo, M. C. Larson and J. S. H. Jr., "Micromachined widely tunable vertical cavity laser diodes," *IEEE J. Microelectromech. Syst.*, vol. 7, no. 1, 1998.
- [4] C. Gierl, T. Grundl, K. Zogal, H. A. Davani, C. Grasse, G. Bohm, F. Kuppers, P. Meisner and M.-C. Amann, "Surface micromachined MEMS-tunable VCSELs with wide and fast wavelength tuning," *Electron. Lett.*, vol. 47, no. 22, pp. 1243-1244, 2011.
- [5] D. D. John, C. B. Burgner, B. Potsaid, M. E. Roberson, B. K. Lee, W. J. Choi, A. E. Cable, J. G. Fujimoto and V. Jayaraman, "Wideband electrically pumped 1050-nm MEMS-tunable VCSEL for ophthalmic imaging," *Journal of Lightwave Technology*, vol. 33, p. 3461, 2015.
- [6] P. Qiao, K. T. Cook, K. Li and C. Chang-Hasnain, "Wavelength-Swept VCSELs," *IEEE J. Sel. Top. Quantum Electron.*, vol. 23, p. 1700516, 2017.
- [7] P. Qiao, W. Yang and C. J. Chang-Hasnain, "Recent advances in high-contrast metastructures, metasurfaces, and photonic crystals," *Adv. Opt. Photon.*, vol. 10, pp. 180-245, 2018.
- [8] T. Ansbaek, I. S. Chung, E. S. Semenova, O. Hansen and K. Yvind, "Resonant MEMS Tunable VCSEL," *IEEE Journal of Selected Topics in Quantum Electronics*, vol. 6, p. 19, 2013.
- [9] M. C. Y. Huang, Y. Zhou and C. J. Chang-Hasnain, "A Nanoelectromechanical Tunable Laser," *Nature Photonics*, vol. 2, pp. 180-184, 2008.

- [10] Y. Rao, W. Yang, C. Chase, M. C. Y. Huang, D. P. Worland, S. Khaleghi, M. R. Chitgarha, M. Zivadi, A. E. Willner and C. J. Chang-Hasnain, "Long-Wavelength VCSEL Using High Contrast Grating," *IEEE Journal of Selected Topics in QUantum Electronics, Special Issue on Semiconductor Lasers*, vol. 19, no. 4, 2013.
- [11] E. Haglund, J. Gustavsson, J. Bengtsson, A. Haglund, A. Larsson, D. Fattal, W. Sorin and M. Tan, "Demonstration of post-growth wavelength setting of VCSELs using high-contrast gratings," *Opt. Express*, vol. 24, pp. 1999-2005, 2016.
- [12] L. A. Coldren, S. W. Corzine and M. L. Mashanovitch, *Diode Lasers and Photonic Integrated Circuits*, Hoboken, NJ: John Wiley & Sons, 2012.
- [13] I. S. Chung, V. Iakovlev, A. Sirbu, A. Mereuta, A. Caliman, E. Kapon and J. Mork, "Broadband MEMS-Tunable High-Index-Contrast Subwavelength Grating Long-Wavelength VCSEL," *IEEE J. Quantum Electron.*, vol. 46, pp. 1245-1253, 2010.

Physics of Widely Tunable VCSELs with Coupled Cavities

Kevin T. Cook¹, Pengfei Qiao¹, Jipeng Qi¹, Larry A. Coldren², Connie J. Chang-Hasnain¹

¹Department of EECS, University of California, Berkeley

²Departments of EECS and Materials, University of California, Santa Barbara

Abstract: The behavior of a tunable VCSEL is governed by the resonances of a semiconductor cavity and an air cavity. By designing a semiconductor cavity which is antiresonant at the tuning center, the free spectral range is maximized at the edges of the tuning range.

Introduction

Vertical-cavity surface-emitting lasers (VCSELs) are the most commonly deployed light sources in optical communications due to their high direct modulation rate and low cost. VCSELs are also being deployed in new three-dimensional imaging applications such as optical coherence tomography (OCT), light detection and ranging (LIDAR), and structured illumination. Tunable VCSELs are deployed in swept-source OCT applications, where their wide tuning range and high sweep rate allow for high-resolution and high-throughput scans, respectively.

Tunable VCSELs generally comprise a fixed lower reflector, an active cavity, an air gap, and a movable upper reflector. The upper reflector – typically a high-contrast grating (HCG) or distributed Bragg reflector (DBR) – is supported by a microelectromechanical system with a thermal, electrostatic, or piezoelectric actuator to displace the reflector vertically [1] [2] [3]. The lasing wavelength is tuned by changing the length of the VCSEL cavity. In electrically pumped devices, the tuning range is limited by the free spectral range (FSR) of the VCSEL.

Due to the large refractive index contrast between semiconductor and air, the interface between the two can have a high enough reflectivity to divide the VCSEL into a system of two coupled cavities: one centered in the semiconductor and one in the air. Previous work to increase the FSR-limited tuning range of a VCSEL has focused on applying an antireflection (AR) coating at the interface in order to allow the VCSEL to resonate as one extended cavity (EC) [2] [4]. Recently, it has been shown that the tuning range can be extended even further without a significant increase in threshold material gain (g_{th}) by using an air cavity dominant (ACD) design [5].

Coupled Cavity Tunable VCSELs

A simplified structure is used in order to investigate the coupled cavity behavior of tunable VCSELs without AR coatings. This model consists of a semiconductor cavity with refractive index n_s and a variable length air cavity, all bounded by two idealized reflectors with $r = 0.999 + 0i$ for all wavelengths, as shown in Fig. 1. In all cases presented, the VCSEL is designed for emission at a center wavelength of $\lambda_c = 1060$ nm. Two cases are considered. In the semiconductor cavity dominant (SCD) case, the length of the semiconductor layer is set to $4\lambda_c$ so that the semiconductor cavity is resonant at λ_c and the VCSEL FSR is comparable to a realistic electrically pumped device. In the second case, which represents the ACD case, the length of the semiconductor layer is set to $4.25\lambda_c$ so that the semiconductor cavity is *antiresonant* at λ_c (the round-trip phase φ_{RT} is an odd multiple of π).

The resonances of each structure are calculated using the transfer matrix method by finding the wavelengths where φ_{RT} is a multiple of 2π . In addition to calculating the resonances of the entire VCSEL structure, the resonances of the constitutive semiconductor and air cavities are calculated by separating the simulation domain at the interface between air and semiconductor. These modes are plotted in Fig. 1 as a function of air cavity length. The semiconductor cavity modes, which are independent of the length of the air cavity, are shown in blue. The air cavity modes, which vary linearly with the air cavity length, are shown in red. Finally, the VCSEL modes are shown in black. The VCSEL modes follow the air and semiconductor cavity modes, avoiding crossings between the two.

The existence of two coupled cavities in a tunable VCSEL has an important consequence: the FSR of the VCSEL varies with wavelength and is limited by the cavity with the smallest FSR. Counterintuitively, this means that the VCSEL FSR is widest when the VCSEL mode is more confined within the cavity with the smallest FSR (the semiconductor cavity). Since an EC design has a much longer cavity than the semiconductor cavity alone, it has a lower FSR than one or both of the coupled cavity VCSELs at all wavelengths. Fig. 1(d) shows the VCSEL modes of all three designs for comparison. In order to capitalize on this increase in FSR, it is ideal to design a semiconductor cavity with modes that are far from λ_c by designing a semiconductor antiresonance at λ_c , as in an ACD VCSEL.

In order to illustrate the impact of increasing the FSR away from λ_c , a realistic VCSEL structure, including a lower DBR, a 1λ active cavity with multiple quantum wells, an oxidation layer, a contact layer, an airgap, and a movable HCG reflector, is considered in Fig. 2. In order to produce comparable SCD and ACD structures, the thickness of the contact layer is set to $\lambda_c/4$ and $\lambda_c/2$, respectively. In this analysis, the wavelength range is limited by the finite bandwidth of the semiconductor DBR. The air, semiconductor, and VCSEL cavities modes are shown in

red, blue, and black, respectively. In order to calculate g_{th} as a function of air cavity length, gain is added to the quantum wells until the round-trip loss reaches zero. The dominant VCSEL modes with the lowest g_{th} are plotted with solid lines. The SCD device (Fig. 2b) has a semiconductor cavity antiresonance at λ_c . The ACD device (Fig. 2c) has semiconductor cavity modes at the edge of the DBR band, which results in a wider VCSEL FSR where adjacent VCSEL modes can compete. As a result, the ACD VCSEL has a significantly wider tuning range.

Conclusion

A tunable VCSEL is a system of an air and a semiconductor cavity, coupled by the layers placed at the interface between the two. As the VCSEL mode oscillates between the semiconductor and air cavities, the FSR changes dramatically. By designing the semiconductor resonance wavelengths appropriately, the FSR can be maximized at the edges of the tuning range, where mode competition can take place.

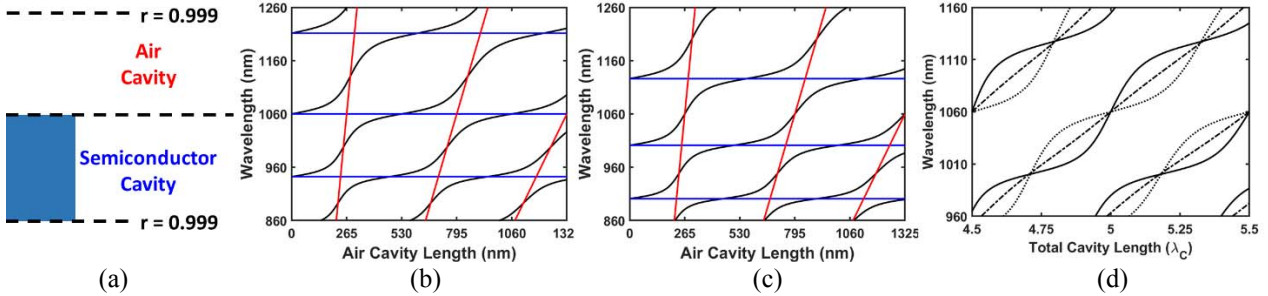


Figure 1. Simplified VCSEL structure used to investigate the underlying physics of SCD and ACD tuning curves. (a) Schematic of simulated structure. (b) SCD and (c) ACD resonance curves for air (red), semiconductor (blue), and VCSEL (black) cavities. The ACD semiconductor cavity modes are shifted to higher wavelengths due to the longer semiconductor cavity. (d) Comparison between SCD, EC, and ACD tuning curves.

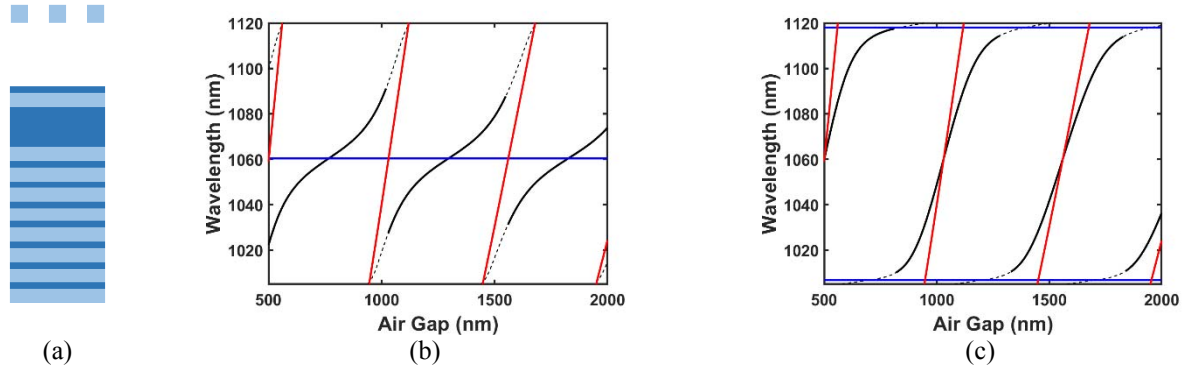


Figure 2. The tuning curve of a real coupled cavity VCSEL is bounded by the reflectance of the top and bottom reflectors. (a) Sketch of a realistic coupled cavity VCSEL with semiconductor DBR and HCG reflectors. (b) In an SCD VCSEL, the reflectance band contains a semiconductor cavity resonance at the center. The neighboring semiconductor cavity modes are outside of the band and the FSR enhancement is wasted. (c) In an ACD VCSEL, there is a semiconductor cavity antiresonance at the center of the reflectance band. The FSR enhancement increases the tuning range of the VCSEL.

References

- [1] M. S. Wu, E. C. Vail, G. S. Li, W. Yuen and C. J. Chang-Hasnain, "Tunable micromachined vertical cavity surface emitting laser," *Electronics Letters*, vol. 31, no. 19, pp. 1671-1672, 1995.
- [2] C. Gierl, T. Gruendl, P. Debernardi, K. Zogal, C. Grasse, H. A. Davani, G. Bohm, S. Jatta, F. Kuppers, P. Meissner and M.-C. Amann, "Surface micromachined tunable 1.55 μm -VCSEL with 102 nm continuous single-mode tuning," *Optics Express*, vol. 19, no. 18, pp. 17336-17343, 2011.
- [3] M. C. Y. Huang, K. B. Cheng, Y. Zhou, B. Pesala and C. J. Chang-Hasnain, "Demonstration of piezoelectric actuated GaAs-based MEMS tunable VCSEL," *IEEE Phot. Technol. Lett.*, vol. 18, no. 10, pp. 1197-1199, 2006.
- [4] F. Sugihwo, M. C. Larson and J. S. H. Jr., "Micromachined widely tunable vertical cavity laser diodes," *IEEE J. Microelectromech. Syst.*, vol. 7, no. 1, 1998.
- [5] P. Qiao, K. T. Cook, K. Li and C. Chang-Hasnain, "Wavelength-Swept VCSELs," *IEEE J. Sel. Top. Quantum Electron.*, vol. 23, p. 1700516, 2017.